Karlsruher Institut für Technologie

ETP-KA/2025-18

Beam monitoring system for therapeutic ion beams based on HV-CMOS active pixel sensors

Bogdan Topko

Zur Erlangung des akademischen Grades eines
DOKTORS DER NATURWISSENSCHAFTEN (Dr. rer. nat.)
von der KIT-Fakultät für Physik des
Karlsruher Instituts für Technologie (KIT)

angenommene

Dissertation

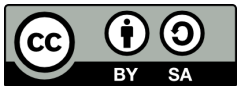
von

Spezialist Bogdan Topko
aus Jekaterinburg, Russland

Tag der mündlichen Prüfung: 31.10.2025

Referent:	Prof. Dr. Ulrich Husemann	Institut für Experimentelle Teilchenphysik
Korreferent:	Prof. Dr. Markus Klute	Institut für Experimentelle Teilchenphysik

Bogdan Topko:
Beam monitoring system for therapeutic ion beams based on HV-CMOS active pixel sensors
October 2025



This document is licensed under a Creative Commons
Attribution-ShareAlike 4.0 International (CC BY-SA 4.0):
https://creativecommons.org/licenses/by-sa/4.0/

Посвящается моей жене Юлии
(To my wife Iuliia)

Contents

I. Introduction and Basics 1

1. Introduction 3

2. Ion beam radiotherapy 7
- 2.1. Ion beam radiotherapy . . . 7
- 2.2. Heidelberg Ion Beam Therapy Center . . . 9
- 2.3. MRI-guided ion beam therapy . . . 10
- 2.4. ARTEMIS project . . . 12

3. Monolithic Active Pixel Sensors 13
- 3.1. Semiconductor physics . . . 13
  - 3.1.1. Crystal lattice and energy band structures . . . 13
  - 3.1.2. *pn*-junction . . . 15
  - 3.1.3. Metal–Oxide–Semiconductor Field Effect Transistor . . . 16
- 3.2. Signal generation in Silicon detectors . . . 17
  - 3.2.1. Interaction of charged particles with matter . . . 18
  - 3.2.2. Signal generation mechanism . . . 19
- 3.3. Detector signal processing . . . 21
  - 3.3.1. Charge-sensitive amplifier . . . 22
  - 3.3.2. Pulse shaper . . . 23
  - 3.3.3. Digital logic . . . 23
- 3.4. HV-CMOS technology . . . 24
- 3.5. Radiation damage of silicon detectors . . . 25
  - 3.5.1. Bulk damage . . . 26
  - 3.5.2. Surface damage . . . 27
  - 3.5.3. Mitigation techniques . . . 28

II. Main 31

4. Beam monitoring system for ion beam therapy 33
- 4.1. System description and requirements . . . 33
- 4.2. HitPix sensor family . . . 36
- 4.3. Data acquisition system . . . 39
- 4.4. Project milestones . . . 40

5. HitPix2 43
- 5.1. Sensor design . . . 43
  - 5.1.1. Pixel layout . . . 44
  - 5.1.2. Pixel electronics . . . 44
  - 5.1.3. Peripheral electronics . . . 46
- 5.2. HitPix2 characterization . . . 47
  - 5.2.1. Sensor probe station . . . 48
  - 5.2.2. Testing procedure . . . 48
  - 5.2.3. Current versus Voltage (I-V) test . . . 49
  - 5.2.4. Charge injection test . . . 50
  - 5.2.5. Adders readout test . . . 52

5.2.6. Latency scan test . . . 53
5.2.7. Characterization results . . . 54
5.3. Multi-sensor readout . . . 54
5.3.1. Readout architecture considerations . . . 54
5.3.2. 2 × 5 HitPix2 matrix . . . 55
5.3.3. Beam test setup . . . 56
5.3.4. ISO-MWPC detector . . . 57
5.3.5. Data comparison method . . . 58
5.3.6. Beam test results . . . 58
5.4. Performance at high particle rates . . . 62
5.4.1. Beam intensity scan . . . 62
5.4.2. Pileup and Baseline drop effects . . . 67
5.4.3. Infrared LED measurements . . . 69
5.4.4. Proton microbeam test . . . 70
5.5. Radiation hardness . . . 72
5.5.1. Experimental setup . . . 72
5.5.2. I-V measurements . . . 73
5.5.3. Detection efficiency . . . 75
5.5.4. Estimation of the tune voltage range for the pixel threshold . . . 76
5.6. Summary . . . 78

6. HitPix3 **81**
6.1. Sensor design . . . 81
6.1.1. Pixel layout . . . 83
6.1.2. Pixel electronics . . . 83
6.1.3. Peripheral electronics . . . 86
6.2. HitPix3 characterization . . . 88
6.2.1. Single sensor carrier design . . . 88
6.2.2. I-V test . . . 89
6.2.3. Latency scan measurement . . . 90
6.2.4. Experimental setups and Geant4 simulations . . . 90
6.2.5. CSA output calibration . . . 94
6.2.6. Charge injection measurements and pixel threshold tuning . . . 100
6.2.7. Limitations of the calibration procedure . . . 103
6.2.8. Counter and adder readout modes . . . 110
6.2.9. Pixel masking . . . 112
6.2.10. Performance at high particle rates . . . 113
6.2.11. Radiation hardness . . . 118
6.3. Probe station measurements . . . 122
6.3.1. Characterization process . . . 122
6.3.2. Wafer characterization results . . . 123
6.4. Multi-sensor readout . . . 124
6.4.1. 2 × 5 HitPix3 matrix design . . . 124
6.4.2. Measurement results . . . 127
6.5. HitPix4 design considerations . . . 129
6.5.1. General design . . . 130
6.5.2. Pixel design . . . 130
6.5.3. Peripheral electronics design . . . 131
6.6. Summary . . . 132

7. Beam monitor demonstrator **133**
7.1. Exploration of an assembly technology . . . 133
7.1.1. Optical characterization of HitPix2 sensors . . . 133
7.1.2. HitPix2 matrix design based on bump-bonding . . . 134
7.1.3. HitPix2 matrix design based on wire-bonding . . . 137
7.2. HitPix3 beam monitor demonstrator design . . . 139
7.2.1. HitPix3 sensor optical characterization . . . 141
7.2.2. 1×5 strip . . . 142
7.2.3. Motherboard . . . 143
7.2.4. Parallel readout of the 5×5 matrix . . . 145
7.2.5. Strip testing module . . . 147
7.3. Beam monitor production workflow . . . 148
7.3.1. Preparation phase . . . 148
7.3.2. Assembly phase . . . 149
7.3.3. Post-assembly phase . . . 151
7.3.4. Integration phase . . . 154
7.4. Beam test results . . . 159
7.4.1. Spot measurements . . . 159
7.4.2. Raster scan measurements . . . 170
7.5. MRI test results . . . 175
7.6. Full-scale beam monitor design considerations . . . 177
7.7. Summary . . . 178

III. Summary and Outlook **181**

8. Summary and Outlook **183**

IV. Appendix **187**

A. Monolithic Active Pixel Sensor **189**

B. HitPix2 **191**
B.1. HitPix2 sensor design . . . 191
B.2. Multi-sensor readout . . . 191
B.3. Performance at high particle rates . . . 191
B.4. Radiation hardness . . . 192

C. HitPix3 **197**
C.1. HitPix3 sensor design . . . 197
C.2. HitPix3 characterization . . . 197
C.3. Multi-sensor readout . . . 200

D. Beam monitor demonstrator **207**
D.1. Assembly technology exploration . . . 207
D.2. Beam monitor production workflow . . . 207
D.3. Beam test results . . . 208

Acronyms **217**

List of Figures **219**

List of Tables **227**

Bibliography **229**

Acknowledgments — Danksagung **237**

Part I.

Introduction and Basics

1 Introduction

Ion beam radiation therapy is a well-established technology of cancer treatment available at over 100 centers worldwide. Compared to the conventional radiation therapy based on photon irradiation, ion beam therapy provides a more conformal dose delivery to the tumor. This is achieved by modulating the beam energy at a particle accelerator to control the maximum dose position in the longitudinal projection of the tumor (the Bragg peak location of ion energy loss), and deflecting the focused beam with a magnetic raster-scanning system to control the maximum dose position in the lateral projection of the tumor (the beam center). Consequently, ion beam radiation therapy can minimize the damage to the surrounding healthy tissue.
The Heidelberg Ion Beam Therapy Center (HIT) utilizes this technology to treat approximately 700 patients each year with proton, helium and carbon ions. The center is one of the most advanced clinical facilities in the world, where for the first time an isocentric gantry was built to rotate the ion beam around the patient up to 360°. This allows to irradiate the tumor with ion beams from any direction, further minimizing the negative radiation effects on healthy tissue.
Despite the benefits of the ion beam radiation therapy, it faces serious challenges for clinical cases in which the dose application position may be shifted due to changes in the patient's anatomy, including the motion of a tumor or healthy organ, or changes in tumor volume. Shifts of the Bragg peak can lead to underdosing the tumor or overdosing the healthy tissue. To overcome this issue, a feedback system based on real-time Magnetic Resonance Imaging (MRI) can be used to directly monitor the tumor changes and to guide the ion beam delivery.
Adaptive RadioThErapy with MR-guided Ion beamS (ARTEMIS) is a research project focused on the development and clinical implementation of such a system at HIT. The developments and results presented in this thesis were done within the scope of "Adaptation of the beam application system and the monitoring system (BAMS)" – one of the ten sub-projects of ARTEMIS. A more detailed description of ion beam radiation therapy, the Heidelberg Ion Beam Therapy Center, future MRI-guided ion beam therapy and the ARTEMIS project are given in Chapter 2.
To ensure safe dose delivery, the beam parameters, such as beam position, size and intensity, must be continuously monitored during the treatment for both traditional and MRI-guided ion beam therapy. Therefore, a beam monitoring system must be installed between the beam exit window and the patient to track the beam parameters before the beam enters the patient's body. Additionally, this system must be able to send an interlock signal to the beam delivery system to immediately stop the irradiation, if any beam parameter deviates from the treatment plan. Moreover, the system must have a low material budget to minimize the changes in beam parameters due to beam interactions with the detector material.
The existing beam monitoring system at HIT consists of Ionization Chambers (ICs) and Multi-Wire Proportional Chambers (MWPCs), which is suitable for traditional ion beam therapy. However, its application is limited for the future MRI-guided approach. The acoustic noise produced by MRI scanners can cause vibration of the wires and membranes in the MWPC, degrading the chamber spatial resolution. Therefore, a new detector system is required to overcome this limitation.

The beam monitoring of therapeutic ion beams is a challenging task from a detector system design perspective, since it requires fast estimation of the beam parameters at high event rate to ensure accurate and safe treatment. Additionally, direct measurement of high-intensity ion beams demands significant radiation tolerance of the system.
The Institute of Experimental Particle Physics (ETP) and Institute for Data Processing and Electronics (IPE) of Karlsruhe Institute of Technology (KIT) jointly proposed a beam monitoring system design based on High-voltage CMOS (HV-CMOS) Monolithic Active Pixel Sensors (MAPSs), which have an advantage over the existing MWPC detectors due to their fast charge collection time and insensitivity to magnetic fields and acoustic noise. Moreover, this type of sensors utilize commercially available technology, used in Integrated Circuit (IC) production, to combine particle detector and readout electronics in a single silicon die, simplifying the final system construction and reducing its material budget. The proposed beam monitor will consist of individual HV-CMOS sensors integrated into a matrix with an active area of 26 cm × 26 cm.
The HitPix sensor family is a series of pixelated HV-CMOS sensors based on 180 nm commercial Complementary Metal–Oxide–Semiconductor (CMOS) technology, designed and developed by the ASIC and Detector Laboratory (ADL) at the IPE, KIT, aiming to develop a sensor for the proposed beam monitor. The HitPix sensor architecture is tailored for ion beam monitoring and includes frame-based readout, hit-counting pixels, on-sensor beam projection calculation and radiation tolerant design.
General working principles of a silicon detector, the HV-CMOS MAPS architecture description, and radiation damage effects in silicon detectors are detailed in Chapter 3. Chapter 4 gives an overview of the beam monitoring system requirements and the existing system used at HIT. The chapter also provides a detailed description of the proposed beam monitor design based on HV-CMOS MAPS, and the most important features of the HitPix sensor family.
The development of a new detector system is an iterative process, which includes intermediate steps in HitPix sensor design, the architecture of the multi-sensor assemblies and Data Acquisition (DAQ) system, followed by their evaluation in a laboratory environment and during ion beam tests. Section 4.4 describes the main project milestones and outlines the scope of this thesis within the project timeline.
Chapter 5 describes the design of the HitPix2 sensor – the second iteration of the HitPix family. The chapter gives an overview of the characterization campaign carried out to select valid sensors for various multi-sensor assemblies, the beam test results of a 2 × 5 HitPix2 matrix assembled from ten HitPix2 sensors, and other studies. The conducted studies were used to determine a necessary set of improvements for the next iteration of the HitPix sensor family – HitPix3.
The HitPix3 sensor was designed and produced with new features described in Chapter 6. To assess their functionality, a comprehensive evaluation, including laboratory and beam tests, was performed. The evaluation results are presented in section 6.2. The remaining part of the chapter describes a new characterization campaign dedicated to select valid sensors for the new multi-sensor assemblies, the design of an intermediate 2 × 5 HitPix3 matrix and its laboratory tests. Based on these results, a set of design considerations for the next HitPix4 sensor, which is foreseen as the main building block of the final beam monitor, was formulated and provided at the end of the chapter.
The next important step towards the final beam monitor and the main achievement of this thesis was the design and production of a beam monitor demonstrator based on 25 HitPix3 sensors integrated into a 5 × 5 matrix, which could fit the entire ion beams with a size larger than 20 mm for the first time. The beam monitor demonstrator was successfully tested during a beam test at HIT. Furthermore, the tested demonstrator was delivered to HIT for further evaluation regarding its potential integration into a beam quality control procedure. The exploration of the assembly technology for the demonstrator, its final design, and the analysis

of the beam tests are provided in Chapter 7. The design consideration for the final beam monitor are presented at the end of the chapter, based on the knowledge and experience gained from the overall studies conducted during this thesis.
The final Chapter 8 summarizes the results of this thesis.

2
Ion beam radiotherapy

Ion beam radiation therapy is a well-established technology of cancer treatment available at over 100 centers worldwide. The following chapter covers the advantages of this technology over conventional photon radiotherapy, introduces the Heidelberg Ion Beam Therapy Center, and provides an overview of future MRI-guided ion beam therapy.

2.1. Ion beam radiotherapy

Cancer treatment, commonly used in clinical practice, is divided into three main modalities: surgical resection, chemotherapy, and radiotherapy [DP16]. Surgical resection includes the physical removal of the tumor from the body [Nat25c]. Chemotherapy uses chemical agents that are injected into the patient's body to kill cancer cells, or prevent cell division [Nat25a]. According to [Nat25b], in radiotherapy, the same therapeutic effect is achieved by using particle radiation (photons, charged particles, or neutrons). It is divided into external and internal radiotherapy. External radiation therapy refers to the delivery of radiation from a source located outside the patient's body. Alternatively, radioactive material can be placed internally, near the tumor location inside the body and known as internal radiation therapy or brachytherapy. Depending on the clinical case, the combination of these modalities can be used to maximize the effectiveness of the treatment.
As described in [DP16], approximately two thirds of all cancer patients receive radiation therapy. Most of them are treated with X-rays (over 80 %), stereotactic radiosurgery or brachytherapy. Radiotherapy based on protons and heavier ions covers approximately 1 % of the treatments due to the higher cost of the production and maintenance of such clinical centers compared to centers based on photon radiotherapy. However, this number is increasing, due to the rapid growth of ion therapy facilities, which came into clinical operation in the last decade [Par25b]. This trend is expected to continue as more facilities, which are currently under construction [Par25c], or in the planning stages [Par25a], will become operational.
The reason for this trend is the advantages of ion beam radiotherapy in dose delivery to a tumor compared with photon radiotherapy, first described by Wilson in [Wil46]. The dependence of the relative deposited dose on penetration depth for photons with energy in the MeV range, proton, and carbon beams is shown in Fig. 2.1 on the left. According to [INT05], photon beams deliver dose to tissue through secondary charged particles produced in the interaction of photons with matter (photoelectric effect, Compton effect and pair production). Most of these charged particles travel along the photon beam path because of the dominance of the Compton effect for photon energies used in radiotherapy. If the photon beam energy lies within the MeV range, this leads to a smaller dose at the beam entrance (corresponds to the depth of 0 mm in the figure) than the maximum dose at a certain depth in the tissue, when charged particle equilibrium is reached. Beyond the maximum, the dose decreases exponentially, due to photon beam attenuation through photon absorption or scattering.
In contrast, ion beams deliver dose directly through the ionization energy loss. The mean energy loss per unit length of an ion is described by the Bethe equation [Nav+24] (more details

are given in section 3.2). For moderate particle energy, it is roughly inversely proportional to the ion velocity squared, leading to a small energy deposition at the beginning of the particle path in tissue and a characteristic peak at the end of the particle range. The peak is called the Bragg peak and is shown for carbon and proton beams in Fig. 2.1. The Bragg peak position shifts deeper in depth with increasing initial ion energy. Therefore, a more conformal irradiation of the tumor volume in longitudinal projection is achieved by modulating the beam energy and creating a Spread-out Bragg peak (SOBP), shown in Fig. 2.1 on the right. An additional advantage over photon beams (shown in the same plot for comparison) is the reduced dose to healthy tissue behind and in front of the tumor. For ions heavier than protons, the dose in the region behind the tumor is non-zero due to the nuclear fragmentation of beam particles [DP16], leading to a tail after the Bragg peak, shown for the carbon beam in Fig. 2.1 on the left.

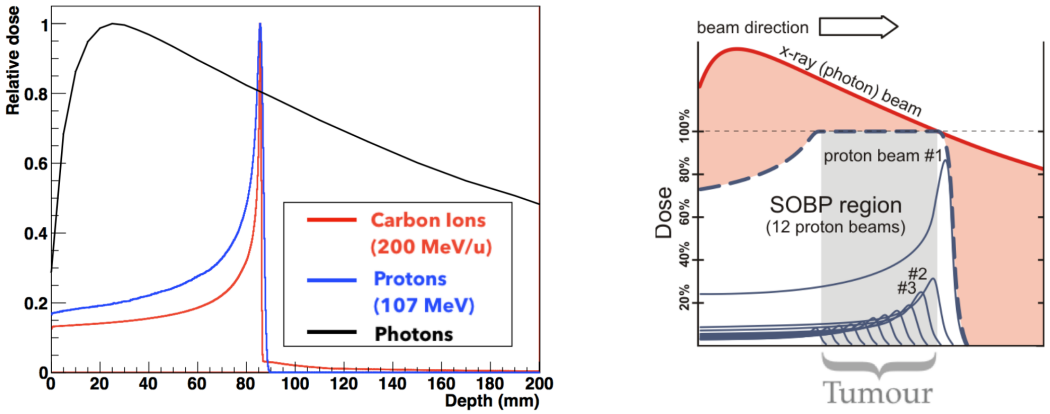


Figure 2.1.: Dependence of relative deposited dose on penetration depth (left) deposited with a photon with energy in the MeV range (black line), proton (blue line), and carbon (red line) beams. Spread-out Bragg peak (SOBP) region generated by proton beams at different energies (right). The gray region represents the tumor volume in longitudinal projection. From [Sim+20].

To maximize treatment effectiveness, the primary beam radiation field should conform to the tumor volume in both longitudinal and lateral projections. The magnetic raster-scanning and treatment planning systems, first developed at Helmholtzzentrum für Schwerionenforschung (GSI) [Hab+93; Krä+00; JKK22], are used for tumor volume scanning with an ion beam in three dimensions, as shown in Fig. 2.2.

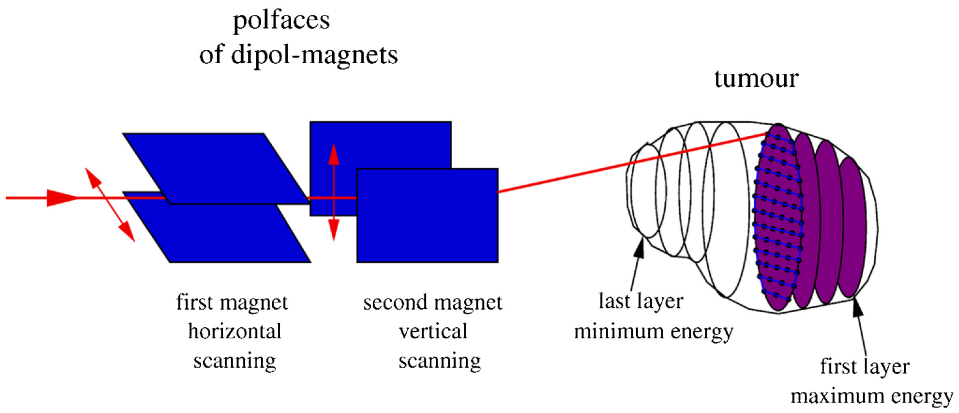


Figure 2.2.: Schematic view of the magnetic raster-scanning system. From [JKK22].

As described in [Krä+00; JKK22], the tumor location and volume, obtained with Computed Tomography (CT) or MRI, are used by the treatment planning system to split the target volume into layers, which are irradiated with ion beams that have the same energy. The magnetic raster-scanning system creates a grid of individual beam positions for each layer by deflecting ion beams. As a result, the dose is delivered to the tumor volume in the most conformal way, preserving healthy tissue around the tumor.

2.2. Heidelberg Ion Beam Therapy Center

The Heidelberg Ion Beam Therapy Center (HIT) is a clinical center that uses ion beams for cancer treatment. It was commissioned for patient treatment in 2009 [JKK22]. Today, HIT treats approximately 700 patients per year [Uni25c]. An illustration of the HIT facility is shown in Fig. 2.3.

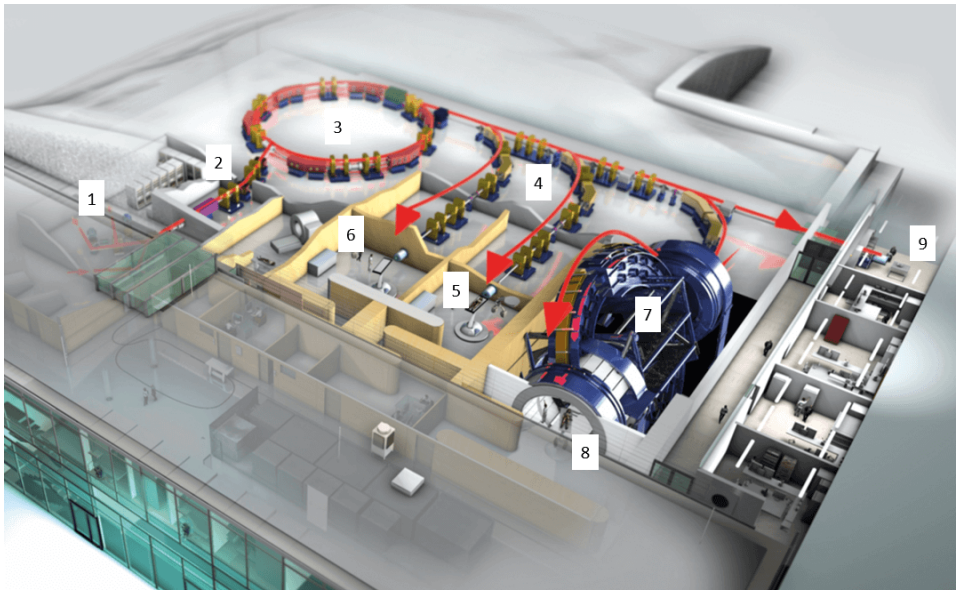


Figure 2.3.: Illustration of the Heidelberg Ion Beam Therapy Center facility. 1 - ion sources, 2 - linear accelerator, 3 - synchrotron, 4 - high-energy beam transport system, 5 and 6 - fixed horizontal beam treatment rooms, 7 - gantry, 8 - gantry treatment room, 9 - experimental area. From [Uni25a].

Proton, carbon, helium, and oxygen ions from ion sources (marked as 1 in the figure) are injected into the linear accelerator (linac, marked as 2 in the figure), which accelerates them up to an energy of $\sim$7 MeV u^{-1} [KOW09]. The first three types of ions are currently used for treatment, whereas the oxygen ions are available only for the experimental research [JKK22]. After acceleration in the linac, and stripping of all electrons, ions are injected into the compact medical synchrotron (marked as 3 in the figure) with circumference of $\sim$65 m designed by GSI [KOW09]. It accelerates the injected ions to the final energy within a range used for treatment. When ion beams reach the required energy, they can be delivered to the final four stations via the high-energy beam transport system (marked as 4 in the figure). Two of them are fixed horizontal beam treatment rooms (marked as 5 and 6 in the figure). The third station is a treatment room (marked as 8 in the figure) that uses the world's first isocentric gantry (marked as 7 in the figure), which allows to rotate the ion beam around the patient up to 360° [JKK22]. The last station (marked as 9 in the figure) is used for beam quality assurance and experiments. The accelerator control system is flexible and allows to select the predefined

beam parameters: ion type, energy, intensity, and size, defined as Full Width at Half Maximum (FWHM) at the isocenter (focal point). Each end station provides a magnetic raster-scanning system, presented in the previous section 2.1, to achieve maximal conformal treatment [JKK22]. The available range of nominal ion beam parameters used at HIT is shown in table 2.1.

Table 2.1.: Available range of nominal ion beam parameters used at HIT. The beam intensity unit **pps** stands for particles per second. The table data are taken from the actual List of Ion Beam Characteristics (LIBC) used at HIT.

Ion type	**proton**	**helium**	**carbon**
Energy (MeV u^{-1})	48.12 – 221.06	50.57 – 220.51	88.83 – 430.10
Size (FWHM in mm)	8.1 – 32.7	4.9 – 18.6	3.4 – 13.4
Intensity (pps)	8×10^7 – 3.2×10^9	2×10^7 – 8×10^8	2×10^6 – 8×10^7

2.3. MRI-guided ion beam therapy

This section summarizes the advantages and challenges of MRI-guided ion beam therapy and is based on recent review articles [Pha+22] and [LSY23].
Despite the treatment benefits of the Bragg peak in the deposited dose profile of an ion beam compared to a photon beam, ion beam radiotherapy faces serious challenges for some clinical cases. The Bragg peak location is highly sensitive to changes in the tumor or healthy organ anatomy, including motions of the tumor or healthy organ, changes in tumor volume, or its biological heterogeneity. These changes can lead to underdosing the tumor or overdosing healthy tissue. As a result, the planned dose profile for ion beams includes additional uncertainty margins to address these issues. An example of treatment plans for photon and proton radiotherapy is shown in Fig. 2.4.

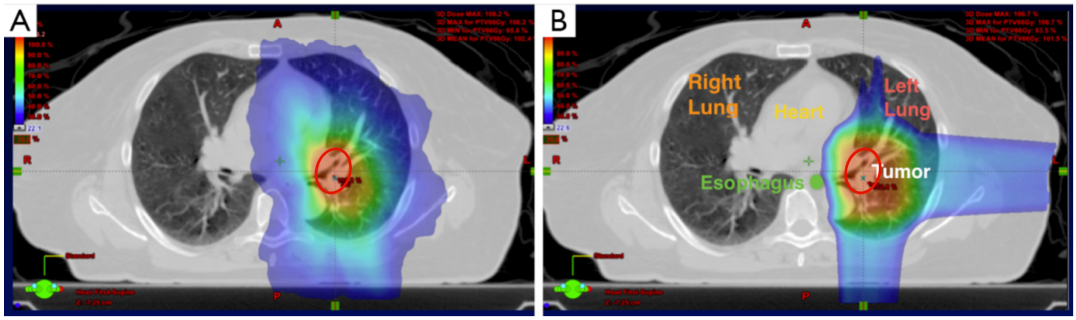


Figure 2.4.: Treatment plans for photon (A) and proton (B) radiotherapy. The tumor location and size are outlined with a red ellipse. The color scale corresponds to the applied dose. Modified from [GRG15].

As shown in [GRG15], the high-dose region (colored red) for the proton beam is less conformal to the tumor compared to the photon beam, due to the added uncertainty margins for the Bragg peak location. However, the low-dose region (colored light blue) is minimized for healthy organs (esophagus, heart, lung, and spinal cord) in the proton beam plan. These results are a trade-off between the higher conformal tumor irradiation achieved with photon beams and the better sparing of healthy organs achieved with ion beams. Hence, it prevents the full utilization of the ion beam therapy advantages in these cases.

Current methods for tumor motion compensation in ion beam radiotherapy include breath-hold techniques or beam gating. Tumor motion tracking can be performed by tracking external markers placed on the patient's body, fiducial markers inserted in or near the tumor, respiratory phase, or marker-less fluoroscopy. The gating system uses this information to stop beam delivery if the tumor moves outside the planned treatment region. However, using derivative information of the tumor location increases the uncertainty margins in the treatment plan.
To overcome this issue, a real-time imaging system can be used to directly monitor the tumor position and control the beam delivery, creating a feedback loop. This can be achieved with a basic technique like beam gating, or, more advanced, by adapting the beam energy to synchronize the Bragg peak position with the tumor movement.
As mentioned in section 2.1, treatment planning is based on the tumor location and size obtained with either CT or MRI. While photon CT is well established and widely used in clinical practice, it has several drawbacks that limit its use for ion beam guiding. Current CT systems provide low soft tissue contrast, which is critical for some types of cancer. Additionally, patients receive an extra dose from the imaging system, increasing the risk of radiation-induced second cancer. In contrast, MRI offers superior soft tissue contrast, real-time imaging capabilities, no extra dose delivery during imaging, and provides information for differential dose delivery to address the tumor inhomogeneity issue. These advantages make MRI-guided ion beam therapy a promising technology to significantly improve the quality of cancer treatment. Two possible configurations of such a system with horizontal fixed gantry are shown in Fig. 2.5. The main difference lies in the ion beam delivery relative to the MRI magnetic field: it can be delivered either parallel or transverse.

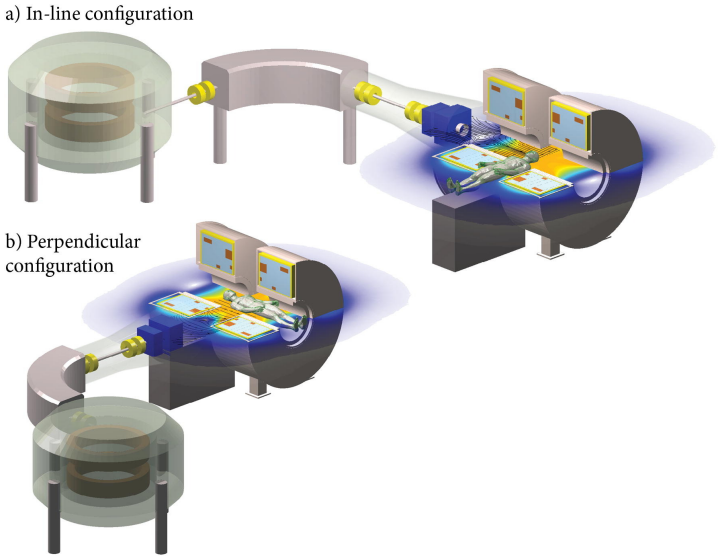


Figure 2.5.: Possible configurations of an MRI proton therapy system with horizontal fixed gantry beamline: In-line (a) and perpendicular (b) configurations in which the ion beam travels parallel or transverse to the MRI field, respectively. From [Pha+22].

Both configurations need to address several challenges to be used in clinical practice. The ion beam cannot be safely delivered through the scanner material because of significant particle scattering, which can be addressed by some form of magnet split, increasing the system cost. Furthermore, magnetic fields affect the entire ion beam trajectory, including the path inside a patient's body. This effect is deterministic and described by the Lorentz force. In the in-line configuration, the ion beam will be rotated around the central axis, whereas in the perpendicular configuration the beam trajectory will be bent from the central axis. This requires accurate

modeling of the beam behavior and a precise and fast beam monitoring system at the beam nozzle, which must be tolerant to the magnetic field and acoustic noise caused by a vibration of the gradient coils [Akb+23]. The time delay between MRI image acquisition and the gating system response must be short to resolve the tumor motion. For the system with dynamically adapted beam energy, timing becomes even more challenging, since the additional accelerator subsystems must be included in the feedback loop.

2.4. ARTEMIS project

Adaptive RadioThErapy with MR-guided Ion beamS (ARTEMIS) is a research project focused on the development and clinical implementation of a system for MRI-guided ion beam radiotherapy [Ger]. A visual concept of the system is shown in Fig. 2.5.

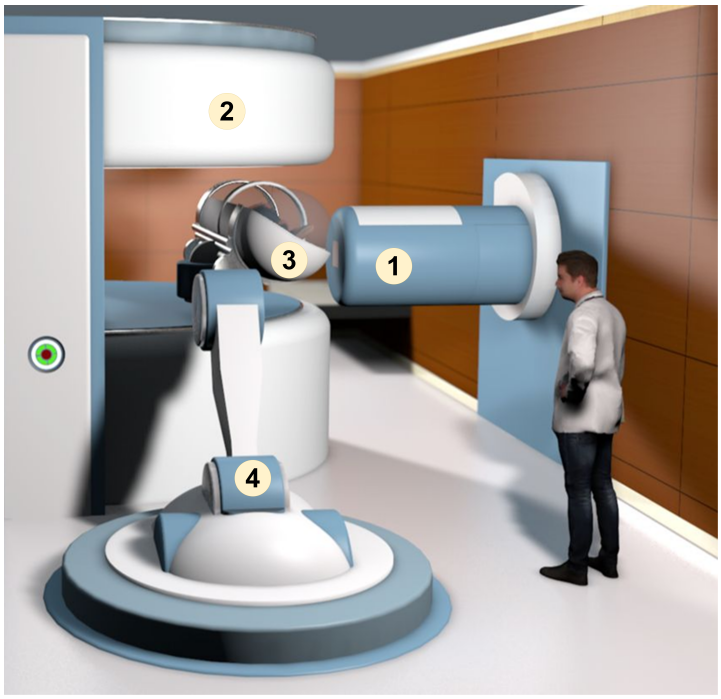


Figure 2.6.: Visual concept of the ARTEMIS project. 1 – fixed horizontal beam nozzle, 2 – MRI scanner, 3 – patient-rotating capsule, 4 – capsule position control device. Image courtesy of Heidelberg University Hospital.

In this system, the ion beam is delivered with a fixed horizontal beamline (marked as 1 in the figure) transverse to the magnetic field generated by the MRI scanner (marked as 2 in the figure). The patient is placed in the capsule (marked as 3 in the figure), which can be rotated up to 360° around its longitudinal axis and contains radiation-transparent (∼420 µm water equivalent thickness) radio frequency (RF) coils [Die+24]. These coils are used to excite the nuclear spin system in the human body and detect the MRI signal of the exited spins [Die+24]. The patient inside the capsule is positioned with respect to the MRI scanner and beam nozzle with a robotic arm of a position control device (marked as 4 in the figure).
The developments and results presented in this thesis were done within the scope of "Adaptation of the beam application system and the monitoring system (BAMS)" – one of the ten subprojects of ARTEMIS.

3
Monolithic Active Pixel Sensors

Monolithic Active Pixel Sensors are unique type of pixelated silicon detector that integrates readout electronic circuits within a sensing pixel by using a commercially available CMOS process. This architecture, characterized by high pixel granularity, low material budget and a simplified readout process, is expanding the CMOS application in fields of high-energy physics experiments and medical imaging. The following chapter covers a brief description of semiconductor physics, the signal generation mechanism in silicon detectors, a general approach for detector signal processing, an introduction to MAPS based on the HV-CMOS technology, and radiation damage effects in silicon detectors.

3.1. Semiconductor physics

The following section briefly explains the fundamentals of semiconductor physics, with a focus on silicon as a base material, and follows the detailed explanations presented in [Spi05].

3.1.1. Crystal lattice and energy band structures

In a silicon crystal, atoms form a periodic diamond cubic lattice in which four valence electrons of each silicon atom are covalently bonded to its neighboring atoms to complete their outer electron shells. A simplified view of an intrinsic silicon lattice structure is shown in Fig. 3.1 on the top left panel in which the lines represent covalent bonds between atoms.

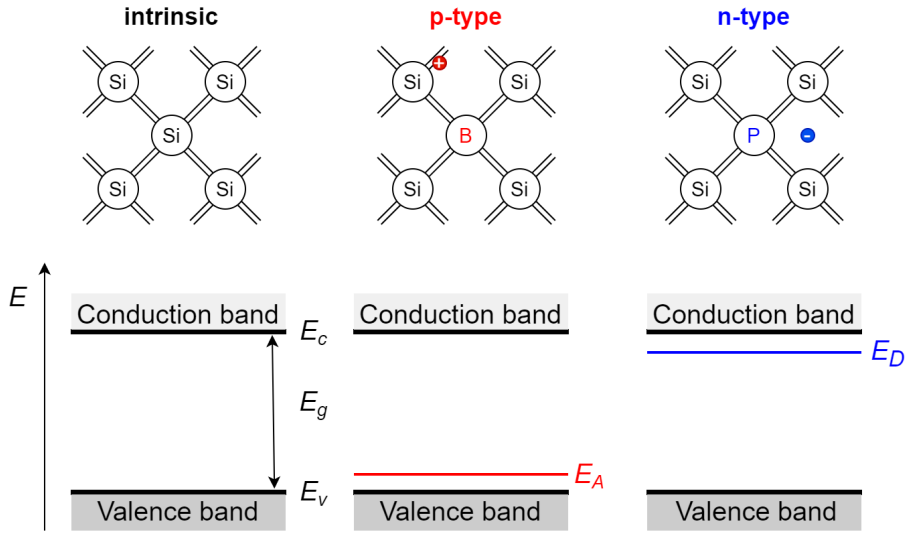


Figure 3.1.: Simplified views of lattices (top) and electronic energy band structures (bottom) of intrinsic (left), p-doped (center) and n-doped (right) silicon material. The illustration follows [Spi05].

Valence electrons of an isolated silicon atom occupy two s- and two p- orbitals. However, when a crystal lattice is formed, the atomic orbitals hybridize into sp^3-orbitals and overlap, resulting in the formation of continuous energy bands from the discrete atomic energy levels, due to Pauli exclusion principle. The simplified electronic energy band structure of intrinsic silicon is shown in Fig. 3.1 on the bottom left panel. In this structure, the valence band represents the states of electrons involved in the covalent bonds, while the conduction band represents the "free" electron states, which can travel through the lattice. The probability of an electron occupying a state with energy E is described by the Fermi-Dirac function 3.1 [Spi05]:

$$f_e(E) = \frac{1}{e^{(E-E_F)/kT} + 1}, \tag{3.1}$$

where k is the Boltzmann constant, T is the absolute temperature, and E_F is the Fermi level, defined as an energy state with the probability equal to one half.

The lowest energy level of the conduction band (E_v) and the highest energy level of the valence band (E_c) are separated by the energy band gap. It is formed by forbidden electron states in a crystal lattice, i.e. the probability of the electron occupying these states is significantly suppressed. As a result, the energy band gap E_g determines the minimum amount of energy required to transfer an electron from the E_v to E_c energy state, and is defined as the difference between them.

When a valence electron is excited with sufficient energy, it occupies a state in the conduction band and leaves a vacant state in the valence band. The vacant state can be filled with another electron in the lattice, creating a new vacant state at a different position and can be described as the motion of a positively charged quasiparticle, called hole.

The transition between states depends not only on the energy but also on the momentum. If states corresponding to E_v and E_c have different momentum (indirect semiconductors), the transition between the states will require the momentum conversation through the absorption or emission of a phonon (quasiparticle which describes the lattice vibration). This explains why the average ionization energy E_i of 3.61 eV required to form a single electron-hole pair in a silicon crystal at room temperature is larger than the band gap energy E_g of 1.12 eV.

The amount of "free" charge carriers in the semiconductor defines its electrical conductivity, which can be modified by introducing impurity atoms into the lattice structure. If an impurity atom has three valence electrons (an acceptor dopant), for example boron, it fills its outer electron shell with four electrons from the covalent bonds and one extra electron from a neighboring lattice atom, creating a hole (depicted as a red circle in the central top panel of the figure). Therefore, acceptor atoms create additional states, called acceptor energy level E_A, in the band gap close to the valence band, as shown in Fig. 3.1 on the central bottom panel. This allows a thermally excited valence electron to occupy this state, leading to hole movement in the lattice. A silicon crystal doped with acceptor atoms is called p-type silicon, since the majority charge carriers are *positively* charged holes.

In contrast, introducing an impurity atom with five valence electrons (a donor dopant), for example phosphorus, creates a lightly bound electron, depicted as a blue circle in the simplified lattice structures of Fig. 3.1 in the top right panel. This extra electron cannot occupy the valence band, since the phosphorus and neighboring silicon electron outer shells are already filled with four electrons. Therefore, donor atoms create an additional state, called donor energy level E_D, in the band gap close to the conduction band, as shown in Fig. 3.1 on the bottom right panel. The thermal excitation of an electron in this state is sufficient for transition into the conduction band, leading to electron movement in the lattice. A silicon crystal doped with donor atoms is called n-type silicon, since the majority charge carriers are *negatively* charged electrons.

3.1.2. *pn*-junction

When *p*- and *n*- doped regions are adjoined within a single silicon substrate, a special structure, called *pn*-junction (diode), is formed. After formation of the *pn*-junction, the mobile majority carriers (holes for the *p*-type region and electrons for the *n*-type region) thermally diffuse across the junction, leading to their depletion in the opposing regions. A simplified view of the *pn*-junction without applied external bias voltage is shown in Fig. 3.2 on the top left panel. The depletion of electrons in the *n*-type region forms a positive space charge of the exposed donor ions (shown as circles with a red cross in the figure). In contrast, the depletion of holes in the *p*-type region forms a negative space charge of the exposed acceptor ions (shown as circles with a blue minus in the figure). The accumulated space charges form a built-in electric field that counteracts the diffusion of majority carriers. This process lasts until the electrostatic potential energy of the built-in electric field, defined by the built-in voltage V_{bi}, becomes comparable to the thermal energy available to the carriers, reaching equilibrium if no external bias voltage is applied. The space charge region is also called a depletion region, since the concentration of the mobile majority carriers is significantly reduced. The value of V_{bi} and the depletion region width w depend on the initial donor N_D and acceptor N_A ion concentrations, the exact formulas may be found in [Spi05].

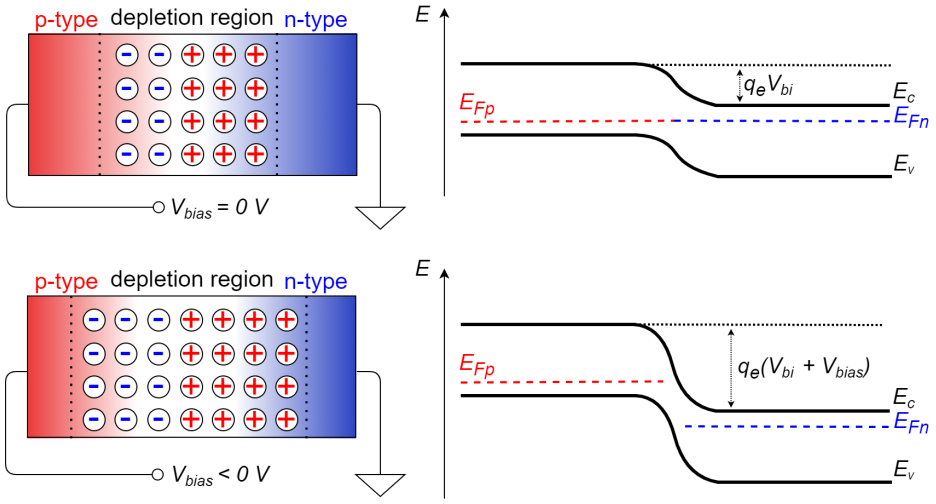


Figure 3.2.: Simplified view of the *pn*-diode (left) and its energy bands (right) in thermal equilibrium (top) and with applied reverse bias voltage (bottom). Vertical dashed lines in the simplified views represent the depletion region. The illustration follows [Spi05].

From an electronic energy band perspective, the Fermi levels E_{Fp} and E_{Fn} of the *p*-type and *n*-type regions are not the same and depend on the initial dopant concentrations. However, in thermal equilibrium, the energy bands are bent to adjust Fermi levels, resulting in a continuous transition of the energy bands from the *p*-type to the *n*-type region, as shown in Fig. 3.2 on the top right panel. The magnitude of bending in the depletion region equals the potential barrier defined by V_{bi}.

The depletion region width can be controlled by an external bias voltage V_{bias}. In forward bias mode, a high potential is applied to the *p*-region and a low potential to the *n*-region, reducing the potential barrier of the junction and narrowing the depletion region. Consequently, this increases the flow of the majority charge carriers (electrons from the *n*-region to the *p*-region,

and holes from the p-region to the n-region), resulting in an exponentially rising current, called diode forward current.
In reverse bias mode, a high potential is applied to the n-region and a low potential to the p-region, increasing the potential barrier and expanding the depletion region, as shown in Fig. 3.2 on the bottom. This reduces the flow of the majority charge carriers. However, the current across the junction is non-zero and equals a small leakage current consisting of three components: diffusion, generation, and surface currents. The diffusion current is based on the diffusion of the minority charge carriers (electrons in the p-region and holes in the n-region) into the depletion region, leading to their consecutive flow across the pn-junction. In contrast, the generation current is based on the thermal excitation of electron-hole pairs within the depletion region, which are then separated by the electric field. The number of thermally excited carriers increases with the density of defects in the crystal lattice because defects create additional energy states within the band gap. Furthermore, the generation current depends on the temperature and the applied reverse bias voltage (the size of the depletion region). The surface leakage current is based on conduction paths created by imperfections or contaminations of the surface. In high-quality devices with good surface passivation, generation current is the dominant mechanism for the total leakage current. For the purpose of particle detection, only the reverse bias mode is of interest, as will be explained in section 3.2.

3.1.3. Metal–Oxide–Semiconductor Field Effect Transistor

Another important semiconductor structure, fundamental to modern electronic circuits, is the Metal–Oxide–Semiconductor Field Effect Transistor (MOSFET), in which the channel conductivity is controlled by an applied electric field. The MOSFET can be implemented in two flavors: the n-channel MOSFET (nMOS), which uses electrons as charge carriers in an n-type conductive layer and the p-channel MOSFET (pMOS), which uses holes as charge carriers in a p-type conductive layer. This subsection is mainly based on [WH10; Spi05], which contain more detailed explanations of MOSFET working principles.
The MOSFET structure consists of a silicon substrate (bulk), the gate terminal (made of aluminum or polysilicon), which is insulated from the substrate by a very thin silicon dioxide layer, and implantation regions adjacent to the gate called the drain and source. The simplified structure of the nMOS transistor is shown in Fig. 3.3 in which the source and drain are implemented with $n+$ implants in a p-type substrate (for the pMOS the doping profile is reversed: $p+$ implants in an n-type substrate).
The connections to the drain, source, and bulk are implemented similarly to the gate with aluminum or polysilicon. For simplicity, the bulk and source terminals are usually considered shorted, and then the operational modes of the transistor will depend only on the voltages applied between the gate and the source V_{GS}, and between the drain and the source V_{DS} terminals.
In the initial state called cutoff mode, the V_{GS} is lower than the threshold voltage V_{TH} and V_{DS} is equal to 0 V, therefore, two diodes formed by the source-bulk regions and the drain-bulk regions are in equilibrium, and depletion regions are formed, as described in the previous subsection. The applied positive potential to the gate simultaneously attracts electrons from the bulk and pushes holes into the bulk, forming a depletion region under the gate oxide. In an ideal transistor, the depletion region prevents any current flow between the source and the drain I_{DS}, even if V_{DS} is greater than 0 V. However, in a real nMOS, the drain-source current I_{DS} is non-zero, due to the presence of a small leakage current. It depends exponentially on V_{GS} and is caused by electrons that diffuse from source to drain due to an electron concentration gradient [VDB73]. This operational mode of the transistor is called weak inversion and is actively used in the detector readout circuits, as explained in section 3.3.

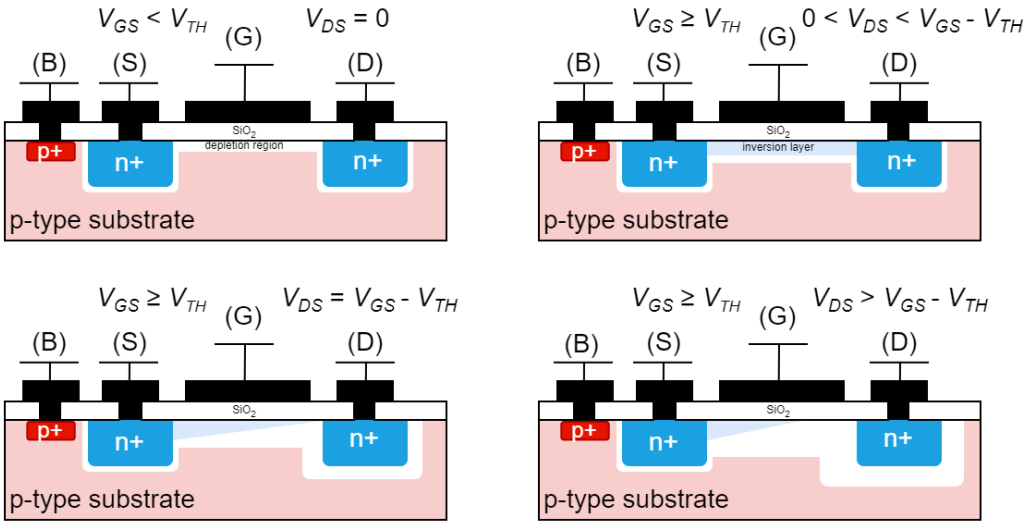


Figure 3.3.: Operational modes of the nMOS transistor: cutoff (top left), linear (top right), saturation at the point of inversion layer pinch-off (bottom left), saturation (bottom right). The letters B, S, G, and D stand for the terminals of bulk, source, gate, and drain of the transistor, respectively. The illustration follows [Ehr21].

When the gate-source voltage V_{GS} exceeds the V_{TH} (top right panel of the figure), the density of electrons attracted from the bulk is enough to form a conductive channel, known as the inversion layer. With a small positive drain-source voltage V_{DS} applied, electrons flow from source to drain, resulting in drain-source current I_{DS} (due to convention of the current direction, I_{DS} is opposite to the electron flow, i.e. I_{DS} flows from the drain to the source). This mode is called linear, because I_{DS} is proportional to the applied V_{DS} and the transistor can be considered as a voltage-controlled resistor.

The saturation of the drain-source current begins after V_{DS} reaches a value of $V_{\mathrm{GS}} - V_{\mathrm{TH}}$, when the inversion layer density is pinched off near the drain (bottom left panel of the figure). Nonetheless, the conduction continues, due to a high electric field between the inversion layer and the drain. At this point, the drain-source current I_{DS} is almost independent of applied V_{DS} and is primary defined by V_{GS}, which modulates the density of electrons in the inversion layer. In this mode, the transistor can be considered as a voltage-controlled current source. A further increase in V_{DS} slightly shifts the pinch-off point toward the source (bottom right panel of the figure), leading to a slight increase in I_{DS}, due to modulation of the channel length (the reduced length of the inversion layer decreases its resistance).

Examples of the drain-source current I_{DS} versus the drain-source voltage V_{DS} of the nMOS transistor at different values of $V_{\mathrm{GS}} - V_{\mathrm{TH}}$ are shown in Fig. 3.4. It is important to note that the presented curves do not reflect the channel-length modulation effect.

3.2. Signal generation in Silicon detectors

The detection of particles is based on their interaction with the detector material. This section briefly describes mechanisms of interaction of charged particles with matter and principles of signal generation in silicon detectors. The following section is based on the detailed information presented in [Nav+24; LR16] and [Spi05; Lut07; Har24].

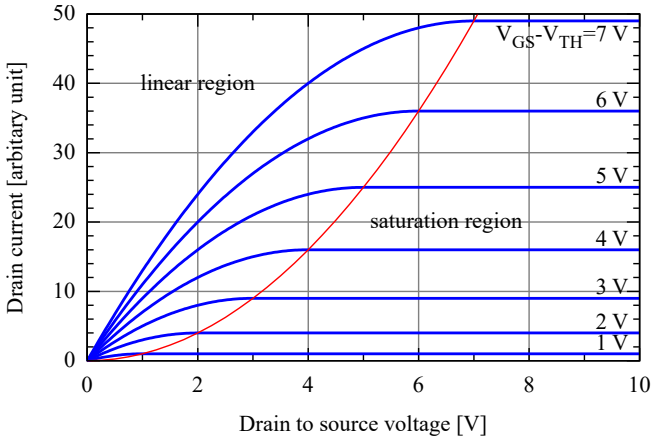


Figure 3.4.: Drain current versus drain to source voltage of an nMOS transistor at different values of $V_{\mathrm{GS}} - V_{\mathrm{TH}}$. The red curve represents the boundary between the linear and saturation modes. From [Wik11].

3.2.1. Interaction of charged particles with matter

A charged particle traveling in matter primarily interacts with the Coulomb fields of the atoms via electromagnetic forces, leading to energy loss. These particle interactions are based on ionization (excitation) and bremsstrahlung mechanisms. In an ionization (excitation) mechanism, energy is transferred from a charged particle to atomic electrons, exciting them to higher energy levels within an atom (excitation). If the transferred energy is sufficiently large, electrons are unbound from their atom (ionization). In a bremsstrahlung mechanism, a charged particle is decelerated by the electric field of the atomic nucleus, resulting in the emission of an electromagnetic wave. The main interaction mechanism depends on the particle type and its energy. Particles heavier than electrons primarily lose their energy by the ionization (excitation) mechanism, whereas electrons can lose their energy mainly by bremsstrahlung if their energy is higher than a critical energy, which depends on the target material. Within the scope of this thesis, only the ionization mechanism will be further covered, since it is the dominant energy loss mechanism for the energy range used in ion beam radiotherapy.
For a heavy particle with charge z and velocity v (given as a fraction of the speed of light $\beta = v/c$) the mean energy loss (stopping power) in a target material with atomic number Z and mass A is described by the Bethe equation 3.2 [Nav+24]:

$$-\langle\frac{dE}{dx}\rangle = 4\pi N_A r_e^2 m_e c^2 z^2 \frac{Z}{A}\frac{1}{\beta^2}\left[\frac{1}{2}\ln\left(\frac{2m_e c^2\beta^2\gamma^2 T_{\max}}{I^2}\right) - \beta^2 - \frac{\delta(\beta\gamma)}{2}\right], \tag{3.2}$$

where N_A is the Avogadro constant, m_e and r_e are the mass and classical radius of the electron, γ is the Lorentz factor, $T_{\max}$ is the maximum kinetic energy that can be transferred to an atomic electron in a single collision, I is the mean excitation energy of the target atom, and $\delta(\beta\gamma)$ is the correction factor of the density effect.
An example of mass stopping power (the stopping power is normalized to the density of the target material) for a positive muon in copper material as a function of $\beta\gamma = p/Mc$ is shown in Fig.3.5.
As discussed in [Nav+24], the mass stopping power follows the Bethe equation for $\beta\gamma$ in the range from 0.1 to 1000. In the region $\beta\gamma \leq 0.1$ several corrections must be introduced to take into account more complex interactions, since the incoming particle velocity becomes less than the orbital speed of atomic electrons. For the ultrarelativistic region $\beta\gamma \geq 1000$, energy loss

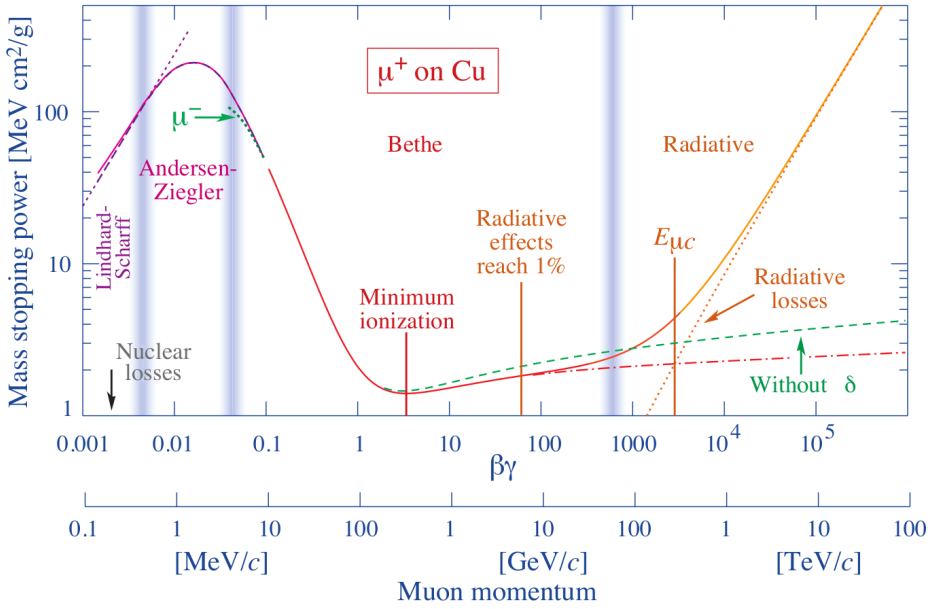


Figure 3.5.: Mass stopping power for a positive muon in copper as a function of $\beta\gamma = p/Mc$. The function follows the Bethe equation at $\beta\gamma$ in the range of 0.1 to 1000. The minimum ionization is achieved at $\beta\gamma \approx 3$. From [Nav+24].

via bremsstrahlung becomes dominant. The mean ionization energy loss reaches a minimum at $\beta\gamma \approx 3$. Particles within this energy range, called Minimum Ionizing Particles (MIPs), are often used as reference particles in detector system design to define an acceptable noise level of the system.

A charged particle path within a material consists of interactions with atomic electrons. The number of interactions and amount of energy transferred to electrons vary statistically. If the material thickness is much smaller than the particle range, the resulting energy loss distribution deviates significantly from the Gaussian shape. Hence, the observed Most Probable Value (MPV) is less than the mean energy loss predicted by the Bethe equation. This effect is shown in Fig. 3.6 for the energy deposition of 500 MeV pions in silicon with different thicknesses. The energy loss fluctuations in a thin absorber are described by the Landau-Vavilov-Bichsel function [Nav+24]. It takes into account events, when a large amount of energy is transferred to electrons, called δ-electrons, which can contribute to secondary ionization, resulting in a high-energy tail of the distribution.

As shown in Fig. 3.6, the MPV of the energy loss distribution increases with thicker material because a traversing particle can interact with more atoms. For silicon, the dependence of MPV on material thickness can be approximated by a logarithmic function, with MPV values of $\sim$ 76, 70, 60, and 50 electron-hole pairs per µm ($\frac{\text{e–h}}{\mu\text{m}}$) for sensor thickness of 300, 200, 50 and 25 µm [Har24]. The MPV values in electron-hole pairs units are obtained by normalizing them to the average ionization energy E_i of silicon.

3.2.2. Signal generation mechanism

When a MIP traverses an undepleted silicon detector with a thickness of 50 µm, it generates approximately 3000 electron-hole pairs (the most probable energy deposition). However, in the detector bulk volume of 1 cm × 1 cm × 0.005 cm at a temperature of 300 K the number of free carriers is around 7.3×10^7. Consequently, a significant portion of the ionization signal, created by MIP, is lost in recombination with thermally exited charge carriers within the bulk. In

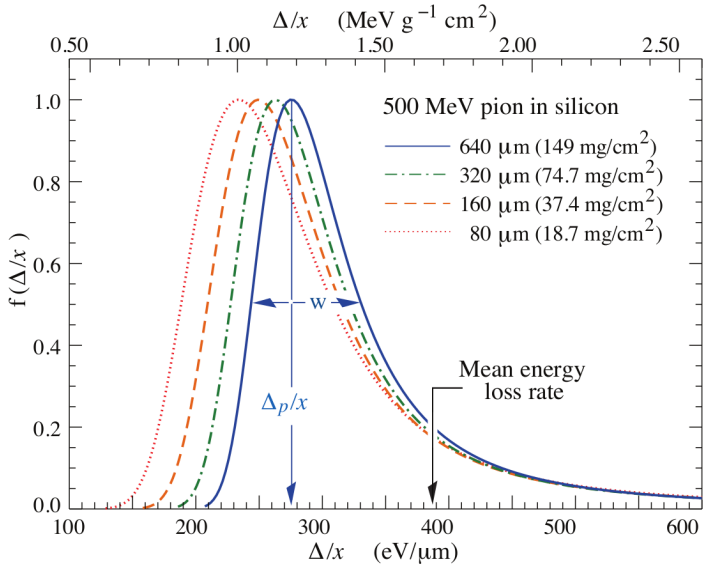


Figure 3.6.: Energy loss for 500 MeV pions in silicon with different thicknesses. Distributions are normalized w.r.t. the most probable value Δ_p/x. The width w stands for the full width at half maximum. From [Nav+24].

contrast, this loss is significantly reduced in the thin depletion region (a few µm depending on the doping concentration) in which the concentration of free carriers is much lower. Therefore, to fully utilize the detector volume, the external bias voltage V_{bias} is applied to increase the depletion region, as explained in subsection 3.1.2. The value of V_{bias} at which the depletion region reaches the detector backplane is called the full depletion voltage V_{fd}. A simplified view of a silicon detector based on p-type substrate is shown in Fig. 3.7.

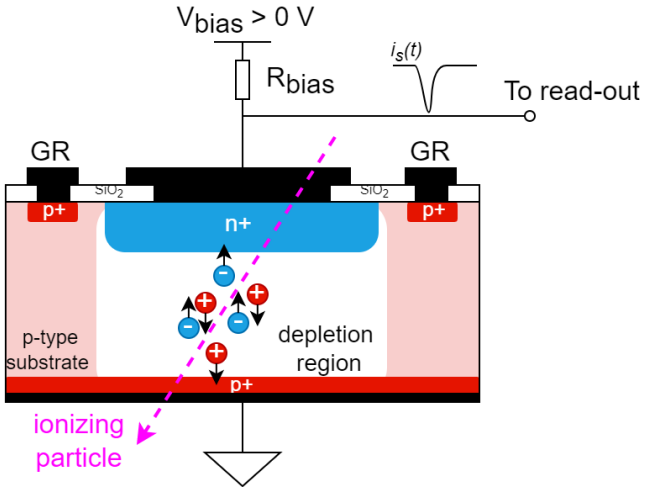


Figure 3.7.: Simplified view of signal generation in a silicon detector based on p-type substrate.

In the figure, the pn-junction of the detector is formed with the p-type silicon substrate and the heavily doped $n+$ implant. The silicon dioxide layer (white rectangles in the figure) provides an electrical insulation and surface passivation. The openings in the insulating layer are filled with an aluminum metallization layer (black rectangles in the figure) to create ohmic contacts with heavily doped $p+$ and $n+$ implants. To reverse-bias the pn-junction, high and low electric potentials are applied to the $n+$ implant and the detector backplane (the $p+$ implant on the

opposite side of the substrate), respectively. If the applied bias voltage significantly exceeds V_{fd}, the depletion region can extend to the detector edges. However, the edge regions have a higher concentration of free carriers, due to lattice dislocations, introduced during the mechanical extraction of the detector from the wafer after production. Hence, if the depletion region reaches the detector edges, the leakage current and noise of the detector increase. To prevent this, guard rings are implemented with $p+$ implants (marked as GR in the figure) to shape the electric field and suppress surface currents.
An ionizing particle (shown as a magenta arrow in the figure) passing through the detector interacts with atoms and generates electron-hole pairs along its path. The electrons (shown as blue circles) and holes (shown as red circles) are accelerated towards the $n+$ and $p+$ implants, respectively, by the electric field established in the detector volume. Consequently, the drift of charge carriers induces a current signal in an external readout circuit, as described by the Shockley–Ramo theorem and given in equation 3.3 [Spi05]:

$$i(t) = -q\vec{v}(t) \cdot \vec{E}_w, \tag{3.3}$$

where $i(t)$ is the induced current, q is the carrier charge, $\vec{v}(t)$ is the instantaneous velocity of the carrier and $\vec{E}_w$ is the weighting field, which is defined by the detector geometry.
The energy deposited in the detector by a traversing particle directly converts to the number of generated electron-hole pairs, i.e. to the deposited charge. It can be obtained by integrating the induced current signal $i(t)$ over time. The estimated height of such a signal generated by a MIP traversing the fully depleted silicon detector with a thickness of 50 µm is equal to $2Q_i/t_c = 0.96\,\mu\text{A}$ (assuming that the signal has a triangular shape and the collection time of 1 ns). To direct this signal into the external readout circuit, the bias resistor R_{bias} is introduced between the detector and the bias terminal. Additionally, a coupling capacitance C_c can be introduced between the detector *pn*-junction and readout electronics to reduce the influence of the detector leakage current, which comes from thermally generated carriers and surface effects. The C_c can be implemented on the detector with an additional SiO_2 layer between the aluminum metallization and the $n+$ implant, or with an external capacitor in the readout circuit.
Modern photolithography allows to create a pattern of *pn*-junctions with a few micrometers pitch on a single silicon die to measure the position of a traversing particle impact. The *pn*-junctions segmented as a series of equally spaced strips provide spatial information in one dimension, while a pixelated detector provides two-dimensional information.

3.3. Detector signal processing

As shown in the previous section, an ionization signal from a particle can be very small, therefore it should be amplified and processed to extract all relevant information for an experiment (deposited energy, hit position etc.). A general processing chain of a silicon detector signal is shown in Fig. 3.8. An ionization current signal $i_s(t)$ (blue pulse in the figure) from a detector is fed into a preamplifier, usually designed as a Charge-Sensitive Amplifier (CSA). The CSA generates an output voltage signal $v_{s1}(t)$ (red pulse in the figure) with an amplitude proportional to an input charge Q_i (integral of $i_s(t)$ over time). The next stage of the processing chain, called pulse shaper, is optional and may consist of several filter circuits to improve the Signal-to-Noise Ratio (SNR) and time resolution by changing the rise and fall times of the input signal, resulting in the signal $v_{s2}(t)$ (green pulse in the figure). The final stage contains digital logic circuits. They extract the required information from the detector signal, defined by the experiment, and transfer the information to a DAQ system. The following section briefly describes the working principles of CSA and pulse shaper, and lists common digital

logic components. The following section is based on the detailed information that can be found in [Spi05; Lut07].

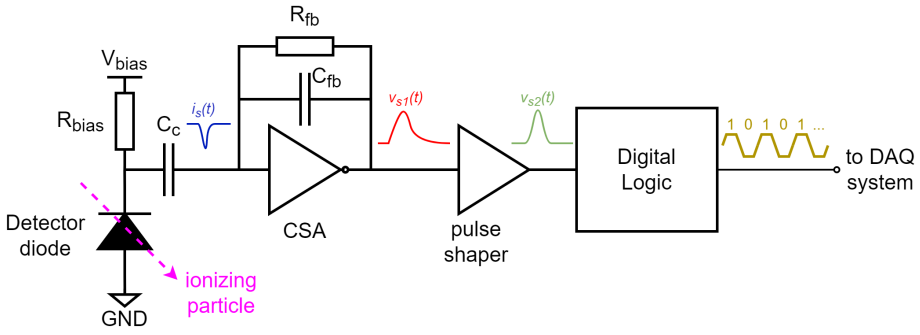


Figure 3.8.: General processing chain of a silicon detector signal.

3.3.1. Charge-sensitive amplifier

The first stage of the signal processing chain is a preamplifier, usually implemented as a CSA. It converts the ionization current signal from the silicon detector to the voltage output signal. The simplified schematic of CSA is shown in Fig. 3.9. For simplicity, the silicon detector can be considered as a current source for the signal and a capacitor for the depleted region connected in parallel. In the schematic, the detector (shown as the detector capacitance C_d in the figure) is connected to the inverting input of the amplifier with an open loop gain A. Due to the high input impedance of the amplifier, the signal current charges the feedback capacitor C_{fb}, resulting in the voltage output v_{out} given by equation 3.4 [Lut07]:

$$v_{\text{out}} = -\frac{Q_{\text{in}}}{C_{\text{fb}} + \frac{C_d + C_i + C_{\text{fb}}}{A}}, \tag{3.4}$$

where Q_{in} is the input charge, obtained by integrating the signal current over time, C_d is the detector capacitance and C_i is the input amplifier capacitance, usually dominated by the gate capacitance of the input transistor [Lut07].

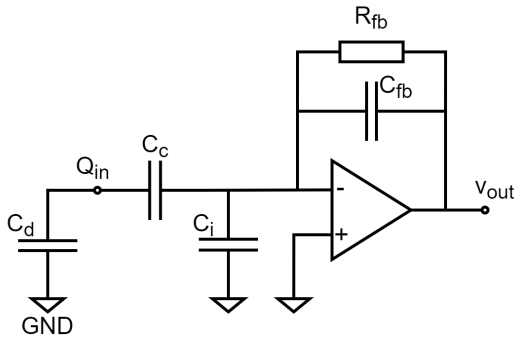


Figure 3.9.: Simplified schematic of the charge-sensitive amplifier. The illustration follows [Lut07].

In an ideal CSA with infinite gain A, the output voltage v_{out} is proportional to $-Q_{\text{in}}/C_{\text{fb}}$. However, according to [Spi05], in a real amplifier A is finite and frequency dependent, leading to a gain reduction at high frequencies. Furthermore, an additional gain reduction can occur due to the division of the input charge between the coupling capacitance C_c and C_i.

Several consecutive signals can cause saturation of the amplifier output, since the charge accumulates on the capacitor C_{fb}. To prevent this, a resistor R_{fb} can be introduced into the feedback circuit to discharge C_{fb} (continuous reset). The R_{fb} can be implemented by a MOSFET transistor in weak inversion mode to control the feedback capacitor discharge speed (proportional to the leakage drain-source current) with a gate voltage. Alternatively, an active reset circuit based on a MOSFET transistor operating in linear mode can be implemented. In this configuration, the transistor acts like a high-speed switch, which rapidly discharges the C_{fb}, when a reset signal is applied to the transistor gate.

3.3.2. Pulse shaper

An amplified signal can be processed with a chain of analog filters to improve the signal-to-noise ratio. The simplest chain can be implemented with a single high-pass (CR) and low-pass (RC) filter, as shown in Fig. 3.10.

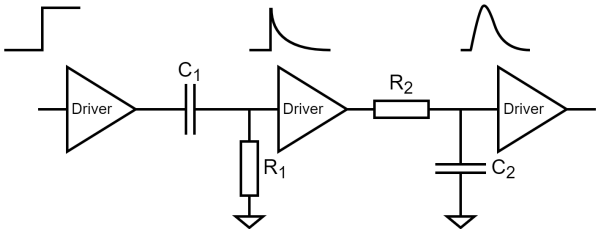


Figure 3.10.: Simplified schematic of the CR-RC pulse shaper. For the illustration purpose the output signal shape of the unit step input signal is shown after each stage. The illustration follows [Spi05].

The first high-pass filter attenuates the DC component and suppresses low-frequency noise in the signal. It shortens the duration of the signal by introducing a decay time constant $\tau_d = C_1 R_1$ [Spi05]. Without this shortening, the preamplifier signals with long tails overlap at high event rate (pileup). The second low-pass filter attenuates high-frequency noise to improve SNR and simultaneously increases the rise time, defined by the integration time constant $\tau_i = C_2 R_2$ [Spi05]. In the frequency domain, the time constants define the lower ($1/2\pi\tau_d$) and upper ($1/2\pi\tau_i$) cutoff frequencies. The output signal $v_{\mathrm{sh}}(t)$ of the CR-RC shaper in response to the unit step signal follows equation [Spi05]:

$$v_{\mathrm{sh}}(t) = \frac{\tau_d}{\tau_d - \tau_i}\left[e^{-t/\tau_d} - e^{-t/\tau_i}\right]. \tag{3.5}$$

The pulse shaper often uses more complex shapers with many filtering stages for better performance. However, the shaper design still relies on cutoff frequencies and their influence on the pulse shape: the upper cutoff frequency defines the signal rise time, and the lower cutoff frequency defines the signal duration [Spi05].

3.3.3. Digital logic

After the pulse shaper, a signal optimized w.r.t. SNR and possible pileup events is fed into the digital logic circuitry, which converts analog signals into digital signals for acquisition by the DAQ system. The exact implementation of the digital logic stage depends on the experimental requirements. The following list briefly describes the main functions that can be implemented within this stage.

1. **Threshold discrimination** is based on a comparator circuit in which a signal and an externally generated reference voltage are applied to its inputs. If the signal amplitude

exceeds the comparator threshold, the comparator output transits into a logic high state. The comparator transits back into a logic low state when the signal amplitude becomes lower than the comparator threshold. The binary signal of the comparator can be used to trigger the amplitude and timing measurements, or it can be used to count incoming particles, if the comparator output is fed into a counter circuit. The counter circuit can be implemented using a chain of D flip-flops in which the output of one flip-flop triggers the clock input of the next flip-flop and the first flip-flop of the chain is driven by the comparator output. As a result, the combined output states of all D flip-flops represent the binary value of the counter.

2. **Analog-to-Digital conversion** is based on an Analog-to-Digital Converter (ADC) that samples an analog signal at discrete time intervals and converts an amplitude of each sample into a digital number. As a result, the analog signal transforms into a series of digital values. The bit resolution and non-linearity of the ADC define the precision (how many bits are used to represent the digital value) and accuracy (how close is the digital value to the true analog value) of the digitization.

3. **Time-to-Digital conversion** is based on a Time-to-Digital Converter (TDC) that measures the time interval between two events by counting cycles of a high-frequency clock. A TDC is often used in the Time-Over-Threshold (TOT) method to measure signal amplitude indirectly from a time interval during which a signal exceeds a comparator threshold.

4. **Timing and synchronization** can be implemented with various timing circuits to measure the time-of-arrival of an incoming particle or to synchronize different detector components or external trigger signals.

To ensure the reliable data transmission and compatibility with other devices, the output signals of the digital logic stage follow certain electrical standards. These standards define the input and output voltage levels of a signal to represent the binary logic states. The Low-Voltage CMOS (LVCMOS) and the Low-Voltage Differential Signaling (LVDS) standards, used within the scope of this thesis, are presented in the Appendix in table A.1.

3.4. HV-CMOS technology

When a detector system is implemented with conventional strip or pixelated silicon detectors, the signal processing chain, presented in the previous section, is split between detector and readout electronics (hybrid system). In such a system, the strips or pixels are connected to a multichannel Application-Specific Integrated Circuit (ASIC) via wire bonds or bump bonds, respectively [Har24]. The ASIC usually consists of the preamplifier and pulse shaper stages, but some of them could have the integrated digital logic stage [Har24]. The hybrid system allows to separately optimize the ASIC and the sensor according to experimental requirements. However, this comes at the cost of increased complexity of detector assembly and readout, and the production costs. In case of hybrid pixel detectors, the bump-bonded ASIC additionally increases particle scattering in the system, which can be critical for some particle tracking applications.
The MAPS utilizes the commercial available CMOS technology, used in ICs production, to combine detector and readout electronics in a single silicon die. This simplifies the detector construction and reduces the material budget (especially if the detector thinning technique is used) and costs. However, as described in [GW18], modern ICs production implements electronic circuits in a thin epitaxial layer (few micrometers) based on a low-resistivity substrate.

Together with a restricted range of the applied bias voltage (a few volts for CMOS technology), these lead to a small depletion region around the charge collection node. Therefore, most of the deposited charge, generated by a traversing particle, is collected via diffusion, which is a significantly slower process compared to drift. Moreover, some portion of the signal is lost in recombination processes within the undepleted region. These factors limit MAPS application for experiments with expected high event rate or when precise measurement of arrival time or deposited energy is required.
To overcome the limitations of MAPS, the HV-CMOS technology is applied for pixellated particle detectors, first presented in [Per07]. The simplified cross-section of an HV-CMOS pixel in standard (STD) topology is shown in Fig. 3.11 on the left.

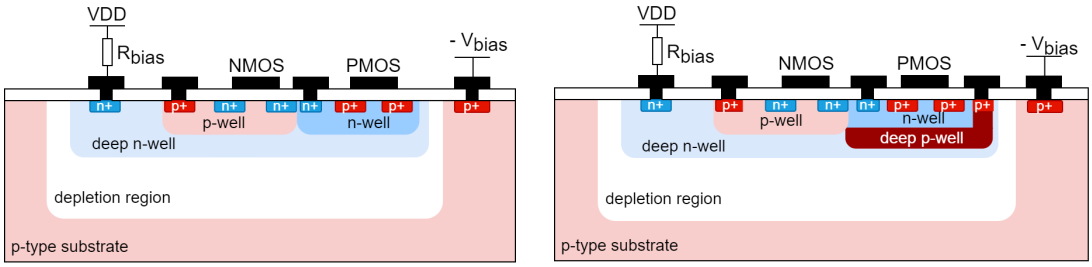


Figure 3.11.: Simplified cross-section of HV-CMOS pixel with standard (left) and isolated (right) topologies. Adapted from [Web21].

As described in [Per+21], a deep n-well forms a sensor diode together with a p-type substrate and hosts the pixel readout electronics. When the deep n-well is connected to the supply voltage V_{dd} of the pixel readout electronics via a bias circuit (marked as R_{bias} in the figure) and a high negative bias voltage V_{bias} is applied to the p-type substrate, the sensor diode is reverse-biased, creating a depletion region. Depending on the manufacturer capabilities and the initial substrate resistivity, the applied V_{bias} can reach more than $-100\,\mathrm{V}$ [Web+22] without breakdown, resulting in a depletion region thickness of $\sim 50\,\mu\mathrm{m}$ for a substrate with a resistivity of $300\,\Omega\,\mathrm{cm}$. Hence, the charge carriers generated by a traversing ionizing particle inside the depletion region are collected by drift, reducing the collection time and minimizing the charge loss. Moreover, by thinning the sensor to the depletion region thickness, the HV-CMOS pixel becomes fully depleted and can be used in precise measurements of a deposited energy.
The readout electronics of the HV-CMOS pixel, based on standard low-voltage nMOS and pMOS transistors, is implemented in the shallow p-well (for nMOS) and n-well (for pMOS). As explained in [Per07], in the STD HV-CMOS pixel topology, the $p+$ implants of the pMOS transistors are capacitively coupled to the deep n-well, which can result in parasitic crosstalk between the sensor diode and the readout electronics. Two topological modifications are possible to prevent this effect: the readout electronics can be placed in a separate deep n-well with the drawback of reducing the pixel fill factor (ratio of the pixel active area to the pixel total area). Alternatively, an additional deep p-well can be implemented to isolate the shallow n-well from the deep n-well. A simplified cross-section of the last topology, known as the isolated (ISO) HV-CMOS pixel topology, is shown in Fig. 3.11 on the right. The ISO topology has a pixel fill factor of almost $100\,\%$, but increases the pixel capacitance, which may limit its performance in detecting small signals [Web+22].

3.5. Radiation damage of silicon detectors

The main principle of particle detection is based on the particle interaction with the silicon detector material. However, some interactions can damage the silicon lattice (bulk damage),

the silicon dioxide or silicon dioxide-silicon interface (surface damage), leading to a degradation of the detector performance after some time in an intense radiation environment (high-energy physics experiments, direct ion beam monitoring or space applications). The following section briefly describes the main mechanisms of radiation damage in silicon detectors and their macroscopic effects, and is based on [Mol99; Har24; Lut07].

3.5.1. Bulk damage

Bulk damage is based on the atom displacement mechanism. If a traversing particle transfers enough energy to an atomic nucleus (Non-Ionization Energy Loss, NIEL), the nucleus can be displaced from its lattice site, creating a primary knock-on atom (PKA). If the PKA has enough kinetic energy, it creates additional displacement defects along its path. Several examples of silicon lattice defects induced by traversing particles are shown in Fig. 3.12. These defects include interstitial (silicon atom located in the interstitial space between lattice sites), vacancy (empty lattice site), or Frenkel pair (combination of interstitial and vacancy).

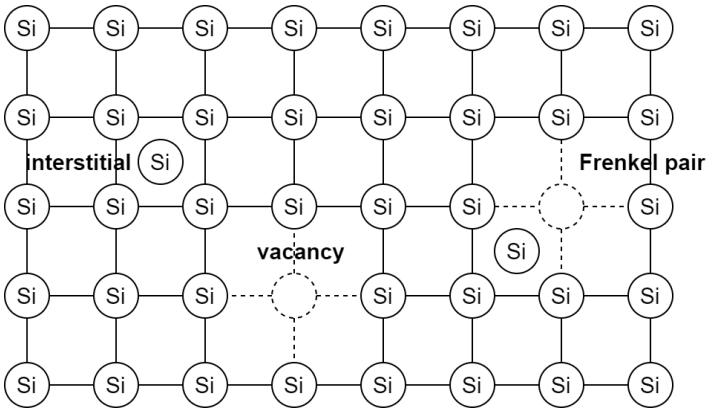


Figure 3.12.: Examples of silicon lattice defects (interstitial, vacancy and Frenkel pair) induced by a traversing particle. The illustration follows [Har24].

For silicon atoms, the displacement energy E_d is 25 eV, i.e. if a silicon atom has a recoil energy of E_d the probability of its displacement from the lattice site is around one half [Lut07]. The probability of PKA creation and PKA kinetic energy depend on the traversing particle type and energy, since an elastic scattering cross-section on silicon atoms depends on the incoming particle type, and transferred kinetic energy is strongly depend on the incoming particle mass [Lut07]. To quantify and compare the displacement damage in silicon caused by various particle types the NIEL hypothesis is used. It suggests that an amount of displacement damage in silicon is directly proportional to the NIEL, i.e. two different particles with same NIEL induce equivalent displacement damage. The experimental standard quantifies the displacement damage of silicon material in terms of the 1 MeV neutron equivalent fluence Φ_{eq}. It is calculated by multiplying the particle fluence Φ by the hardness factor κ, whose exact value was defined experimentally in various radiation studies for different particle types and energies [Har24].
Radiation-induced defects create additional energy levels in the energy band structure, changing the electrical properties of the initial material. Examples of defect level locations in the energy band structure are shown in Fig. 3.13.
According to [Har24], the defect energy levels created close to the middle of the band gap (left part of the figure), act as generation/recombination centers, increasing the detector leakage current in the depletion region. Many experimental studies confirmed that the increase of the silicon detector leakage current ΔI depends linearly on the equivalent 1 MeV neutron fluence Φ_{eq} and follows the equation 3.6:

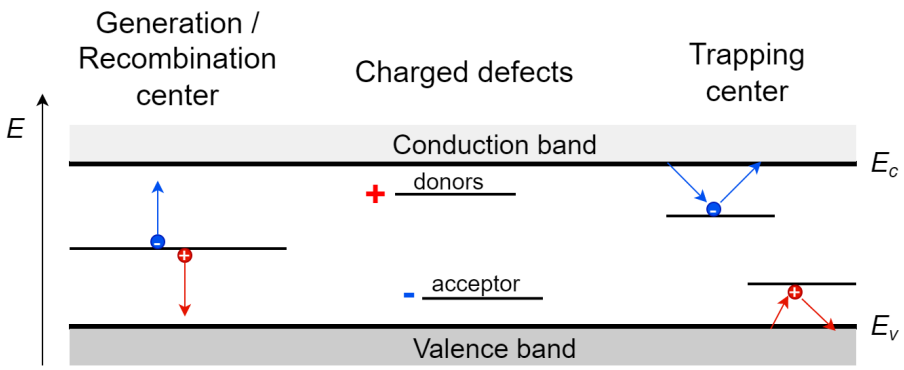


Figure 3.13.: Examples of defect levels locations in an electronic energy band structure and their macroscopic effects: creation of generation and recombination centers (left), charged defects affecting space charge region (center) and trapping centers (right). The illustration follows [Har24].

$$\Delta I = \alpha \Phi_{\text{eq}} V, \tag{3.6}$$

where α is the empirical damage constant, which depends on the particle type and energy, and V is the depleted volume of the detector. An increasing leakage current negatively affects the detector performance: it increases the shot noise (proportional to $\sqrt{I_{\text{leak}}}$) and power dissipation, leading to detector heating. Significant detector heating can form a positive feedback: a raising temperature increases the leakage current, which again heats the detector (thermal runaway), leading to detector breakdown.

As described in [Lut07], induced defects may change the effective doping concentration by deactivating dopants and creating charged defect states. These defects modify the space charge region of the detector. In the band gap, this corresponds to the creation of energy levels close to the conduction and valence band edges (central part of Fig. 3.13). On the macroscopic level, this is observed as a shift in the full depletion voltage V_{fd} of the detector.

Furthermore, the defect energy levels may act as trapping centers for electrons and holes generated by the incoming ionizing particle (right part Fig. 3.13). The trapping occurs when a charge carrier is captured by the defect and released after some time interval. If the delay is longer than the charge collection time, the detected signal is reduced, degrading the signal-to-noise ratio of the detector.

3.5.2. Surface damage

The surface damage is based on the ionization mechanism, since the displacement damage negligibly affects the silicon dioxide layer, which already has an irregular structure. When an ionizing particle traverses the silicon dioxide layer, it generates electron-hole pairs that can be captured by defects or recombine (the exact fraction depends on the oxide purity). The electrons in the oxide have higher mobility than the holes and can escape from the oxide layer, while the slow holes accumulate near the oxide-silicon interface, forming a positive buildup potential [Har24]. The accumulated positive potential attracts the electrons near the interface, creating a conductive channel and increasing the crosstalk between detector pixels (strips).

As explained in [Har24], additional negative effects of surface damage appear in MOSFET. For the heavily damaged nMOS transistor, the threshold voltage can shift to negative values due to buildup potential, resulting in the transistor being in a permanent “on” state. Furthermore,

in the p-well, the formed conductive channel increases the leakage current between adjacent $n+$ nodes, degrading the circuit performance.

3.5.3. Mitigation techniques

The performance degradation of a silicon detector system is an unavoidable process in an intense radiation environment. However, several techniques were developed across many experimental studies to control the detector system performance within defined specifications throughout the expected system lifetime. The following list briefly describes the main mitigation techniques and follows [Spi05; Har24]:

1. **Low operational temperature**. As discussed in subsection 3.5.1, an increased leakage current of a silicon detector after irradiation causes several negative effects on the system performance. The bulk leakage current exponentially depends on the temperature. Therefore, the simplest technique to reduce the leakage current is to keep the system at low temperatures, which should be estimated based on the initial leakage currents of detectors and the expected particle fluence during the system operational lifetime. However, depending on the experimental requirements, this method can be limited by the cooling infrastructure (available space, power consumption, minimal achievable temperature and increased material budget).

2. **Annealing**. Some radiation-induced defects, such as vacancies and interstitials, are very mobile at certain temperatures and can recombine, reducing the defect concentration and consequently the leakage current. This process, known as annealing, can be used to reduce the leakage current by heating a detector to a specific temperature during certain operational periods. However, this method is limited by the reverse annealing effect, characterized by an increased detector depletion voltage over a long time at the annealing temperature due to formation of new stable defects. Therefore, the optimal strategy includes only short annealing periods to exploit beneficial effects, while most of the time the system should be maintained at low temperatures to freeze the reverse annealing process.

3. **Control over bias voltage**. The detector bias voltage should be adjusted to compensate changes in the full depletion voltage after irradiation and to optimize the charge collection efficiency. However, this method can be limited by the sensor breakdown voltage and the power supply capabilities.

4. **Detector design optimization**. The detector design can be optimized with respect to the expected radiation environment. The p-type substrate can be used to prevent the type inversion effect of n-type substrate (caused by acceptor-like defects), which changes the electric field profile and degrades charge collection efficiency. Furthermore, selecting the proper detector pixel (strip) pitch and thickness can reduce the individual leakage current of the pn-junction and lower the full depletion voltage.

5. **Radiation hardened electronics**. Radiation-hardened components and a redundant readout system ensure that the detector signal processing chain remains functional after significant radiation damage. However, this can be limited by the available space on the readout ASIC die, since the radiation-hardened circuits and a redundant system require more space.

6. **Detector material**. The initial detector material can be changed to diamond or silicon-carbide, which have wider band gap and lower leakage currents compared to silicon, but at

the cost of a reduced charge yield. Furthermore, the production cost and available detector sizes limit the application of these materials for a large-scale detector construction.

Part II.

Main

4

Beam monitoring system for ion beam therapy

The beam monitoring of therapeutic ion beams is a challenging task for detector design. It requires fast estimation of the beam position, size and intensity at a high event rate, ensuring accurate and safe treatment. Furthermore, direct measurement of high-intensity ion beams demands significant radiation tolerance of the beam monitoring system. For application in MRI-guided ion beam therapy, the system also must be tolerant to magnetic fields and acoustic noise. The following chapter describes the requirements for this system and the concept of an ion beam monitor based on HV-CMOS active pixel sensors, introduces the HitPix sensor family featured for the ion beam monitor and the design of the data acquisition system. The project milestones are presented at the end of the chapter.

4.1. System description and requirements

An accurate and safe dose delivery to the target tumor volume can be achieved only if a beam monitoring system rapidly provides the beam position, size and intensity information to the beam control system for each raster spot in the treatment plan, as described in section 2.1. The requirements for the beam monitoring system at HIT are listed below and follow [Die+23; Web+22]:

1. **Beam position**. The position of an ion beam, defined as the center of gravity of the induced signals, must be measured in two dimensions (X and Y) orthogonal to the beam direction (Z) with accuracy and precision better than 200 µm.

2. **Beam size**. The size of the beam, defined as the Full Width at Half Maximum (FWHM) of a Gaussian distribution, must be measured in the X- and Y-dimensions with an accuracy and precision better than 400 µm.

3. **Beam intensity**. The intensity of the beam, defined as the number of particles in a given measurement time window, must be measured with an accuracy better than 0.5 %. The expected beam intensity depends on the particle type and can reach up to 3.2×10^9 pps (for protons) and 8×10^7 pps (for carbon ions). Together with two previous requirements, this ensures safe and accurate dose delivery according to a treatment plan.

4. **Timing requirements**. The beam parameters must be measured within a time window of 50 µs to 250 µs. The measured beam position and size must be transmitted to the beam control system within a delay (latency) of 100 µs. The updated beam intensity information must be delivered within a latency of 1 µs to 2 µs. These strict timing requirements are necessary to immediately stop the beam delivery, if one or more measured beam parameters significantly deviates from a treatment plan.

5. **Radiation tolerance**. The system must be tolerant to an annual 1 MeV neutron equivalent fluence of $\sim 1 \times 10^{15}\,\mathrm{cm}^{-2}$ at the beam isocenter expected for six operational days a week.

6. **Active area**. The system must cover a treatment field area of 200 mm × 200 mm with an adjustable beam size in the range from 3 mm to 33 mm to accurately measure ion beam parameters during the raster scanning of a tumor.

7. **Material budget**. The total material budget of the beam monitoring system must be less than 2 mm Water Equivalent Thickness (WET) to minimize the particle scattering in the system.

8. **MRI application**. The system must maintain operational stability in the presence of acoustic noise of ∼130 dB and magnetic fields in the range from 0.1 T (fringe) to 1.5 T (isocenter), which are typical for clinical MRI systems.

9. **Other mechanical constraint**. For the final integration of the system into the existing infrastructure, the outer dimensions of the system must not exceed a thickness of 5 cm and be able to fit into a beam nozzle volume with a diameter of 60 cm.

A photograph of the existing Beam Application and Monitoring System (BAMS) at HIT is shown in Fig. 4.1 on the left. It consists of three ICs and two MWPCs [Sch+15]. As described in [Die+23], the ICs (outlined with a yellow box in the photograph) are used to track the applied dose. The first IC downstream the beam controls the number of particles applied to the current raster point. Once the planned dose is reached, the beam is repositioned to the next raster point. The next two ICs provide independent dose measurements for cross-validation. A safety beam interlock signal is generated to prevent further irradiation if the difference between the IC measurements exceeds a certain threshold.

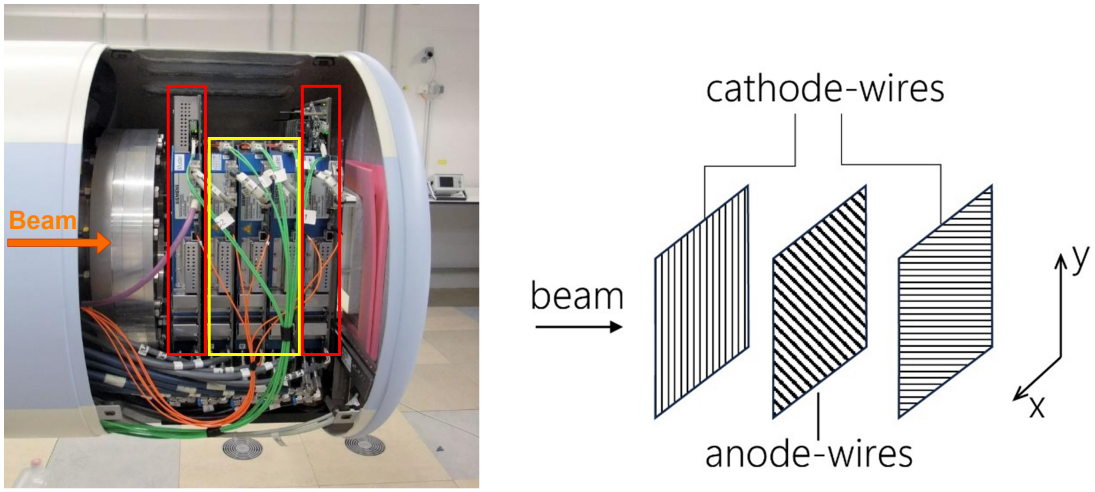


Figure 4.1.: The existing beam monitoring system at HIT (left) is based on two MWPCs (red boxes) and three ICs (yellow box) installed in front of the beam exit window. The orange arrow represents the beam direction. Simplified view of the internal MWPC structure (right). Photo courtesy of I. Perić, the simplified MWPC view from [Wit+25].

The position and size of the beam are measured with MWPCs (outlined with red boxes in the photograph). A simplified view of the internal MWPC structure is shown in Fig. 4.1 on the right. As described in [Par+12], the chamber consists of three parallel planes with equally spaced electrode wires made of tungsten. An anode plane with a wire pitch of 2 mm is rotated at 45° and placed between two orthogonal cathode planes with a wire pitch of 1 mm. This arrangement allows to simultaneously measure the beam position and size in the X- and Y-

directions. Furthermore, both MWPCs also contribute to the generation of the safety beam interlock signal if the position and/or size of the beam deviate from the plan beyond the tolerance limits defined by HIT. According to [Tes+16; Par+10; Eic+03; Rin11], the following operational tolerances are accepted at HIT for beam parameters deviations from the nominal (planned) values during the treatment at the isocenter: ± 1 mm for the lateral beam position, from -15 % to 25 % for the beam size, and ± 5 % for the total number of ions per raster point, while the instantaneous beam intensity measured in pps may vary up to ± 30 %.
However, application of the MWPCs for beam monitoring in MRI-guided ion beam therapy is limited. The acoustic noise produced by MRI scanners can cause vibration of the wires and membranes in the MWPC, degrading the chamber spatial resolution. Moreover, the relatively slow drift of ions in the chamber limits the detector response and increases its dead time, limiting the readout speed of the chamber and delaying the beam interlock signal [Die+23; Sch+15].
The silicon tracking detectors overcome the limitations of MWPCs, due to their fast charge collection time and insensitivity to magnetic fields and acoustic noise. However, an application of conventional silicon tracking detectors for high-intensity ion beam monitoring is a challenging task. Hybrid pixel detectors, widely used in high-energy physics experiments, introduce excessive material into the beam path [Ros+06; GW18], which could affect beam parameters due to significant particle scattering. MAPSs based on the LVCMOS technology and double-sided silicon strip detectors have limited capabilities at high event rate, the former due to the slow charge collection time via diffusion [GW18; Mag16] and the latter due to "ghost track" ambiguities [Sei19]. Furthermore, MAPSs and Low Gain Avalanche Detectors (LGADs) often have insufficient radiation tolerance for the direct ion beam monitoring at the high particle fluence [GW18; Mag16; Sac+20].
In contrast, HV-CMOS active pixel sensors integrate the detector and readout electronics in a single thin die (down to 50 µm), minimizing the material budget. The charge carriers, generated by the incoming particles in the sensor depletion region, are collected via drift, leading to short charge collection times. Moreover, studies of HV-CMOS prototypes, presented in [Web+22; Ben+18], demonstrated their high radiation tolerance up to 100 MRad of total ionizing dose and $1 \times 10^{15}\,\mathrm{cm}^{-2}$ of 1 MeV neutron equivalent fluence. The low material budget, radiation hardness, fast charge collection and high spatial resolution make the HV-CMOS active pixel sensor a promising solution for an ion beam monitor at HIT.
The general concept of a beam monitor based on HV-CMOS active pixel sensors was proposed in [Die+23]. The 3D rendering of the proposed beam monitor is shown in Fig. 4.2. In the monitor, the HV-CMOS sensors (marked with 2 in the figure) with an active area of $2\,\mathrm{cm} \times 2\,\mathrm{cm}$ and a thickness of 100 µm form a sensitive matrix of 13×13 sensors to cover the required sensitive area at HIT.
The sensors are mounted on a thin carbon fiber plate (marked with 1 in the figure) to simplify the assembly process and to ensure the mechanical support and thermal dissipation. The sensors are then interconnected via thin flex polyimide cables (marked with 3 in the figure) to the external electronics boards (marked with 4 in the figure). These connections between the sensor pads and the flex cable traces can be made using either wire- or tape-bonding technologies.
The electronics boards host Field-Programmable Gate Arrays (FPGAs) for sensor matrix configuration, output data sampling and fast estimation of the beam parameters. The boards are also responsible for electrical power delivery to the sensor matrix and data transfer between the beam monitor and the beam control system.
To ensure mechanical stability of the system, the sensor matrix and the electronics boards are mounted on a stabilizing frame (marked with 5 in the figure) with an opening under the sensitive area to prevent excessive particle scattering.

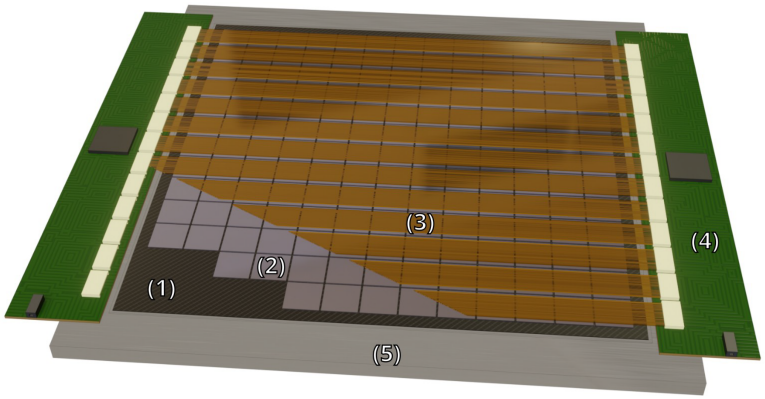


Figure 4.2.: 3D rendering of the proposed beam monitor based on 13 × 13 HV-CMOS active pixel sensors. 1 – thin carbon fiber plate, 2 – HV-CMOS sensor, 3 – polyimide interconnection cables, 4 – electronics boards, 5 – stabilizing frame. From [Die+23].

A dedicated Research and Development (R&D) program was initiated in 2019 to develop and produce an HV-CMOS active pixel sensor tailored for this beam monitoring system. Multiple sensor versions were designed and produced within the scope of the program. Together, they form the HV-CMOS sensor family, called HitPix, which is presented in the next section.

4.2. HitPix sensor family

The HitPix sensor family is a series of HV-CMOS active pixel sensors based on 180 nm commercial CMOS technology. The sensors are designed and developed by the ADL at the IPE, KIT. At the moment of writing this thesis, the family consists of three sensor versions: HitPix1, HitPix2 and HitPix3. Each sensor iteration explores pixel and readout architectures to optimize the performance in the ion beam. This section covers the design considerations and general sensor architecture common to all sensors and tailored for ion beam monitoring.
HitPix sensors are designed to address the system requirements presented in the previous section 4.1. The general concept of the sensor is shown in Fig. 4.3. The sensor consists of a square matrix of pixels with a size of 200 µm × 200 µm (shown as colored boxes in the figure) to ensure the accuracy and precision of the measured beam position (size) better than 200 µm (400 µm). To estimate the beam parameters at high event rates, each pixel contains a signal processing chain to count incoming particles within an adjustable time window. The time window is called a frame, and its duration can be configured from a few to thousands of microseconds.
The pixel counts can be read out row-by-row through the peripheral electronics located at the bottom of the sensor (shown as gray boxes in the figure). This readout mode is called counter mode. The data obtained in counter mode represents a detailed two-dimensional profile of the beam. The total sum of the particle counts at a given frame duration provides the beam intensity information, which together with a known beam energy, can be used to track the applied dose. However, in this mode, the readout speed of the sensor should reach a few Gbit s^{-1} for the final beam monitor to meet the timing requirements (latency of the measured beam position and size should be less than 100 µs). A high readout speed challenges the sensor and system design in power and thermal management, signal integrity, and fast beam parameters reconstruction. Therefore, a second readout mode is implemented in the sensor, called the adder mode. In this mode, the pixel counts are asynchronously summed along rows and columns to calculate the beam projections in two dimensions. The adder mode

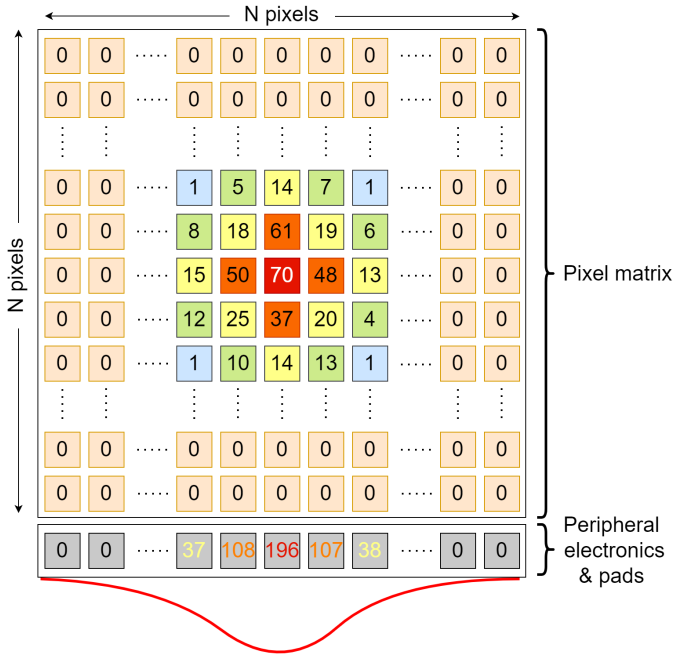


Figure 4.3.: General concept of a HitPix sensor with $N \times N$ pixels (colored boxes). The numbers in the pixels represent the particle counts within a given time window (frame). The column-wise projection of the beam profile (red line) calculated on the sensor is shown at the bottom in the peripheral electronics block (gray boxes).

effectively reduces the number of readout cycles by a factor equivalent to the number of pixel rows, relaxing the required readout speed to a few hundred of Mbit s^{-1} for the final beam monitor. It is important to note that the adder mode of HitPix1 and HitPix2 calculates a beam projection only column-wise, while in HitPix3 the beam profile projection is calculated in both dimensions. In Fig. 4.3, the calculated column-wise projection of a beam is shown as colored numbers in the peripheral electronics block. The peripheral electronics are designed to occupy approximately 4 % of the total sensor area to minimize the insensitive region, which is essential to fulfill the active area requirement for the final beam monitor assembled with 169 sensors.

To address the radiation tolerance requirement, the sensors are designed with the HV-CMOS technology (the advantages were explained in the previous section) and radiation-hardened electronic circuits. Additionally, the low material budget requirement can be achieved by thinning the sensor down to 100 µm thickness.

The internal HitPix pixel structure is shown on the left panel of Fig. 4.4. The pixel consists of a sensor diode connected to a Charge-Sensitive Amplifier (CSA). Its output is fed into the comparator circuit to perform the threshold discrimination, as explained in subsection 3.3.3. Next, a binary signal of the comparator is fed into the counter circuit to count the incoming particles. To perform the column- or row-wise projection calculation, the adder circuit asynchronously sums the pixel counter value and the adder value of the previous pixel.

The counter values of a single row can be accessed by selecting the row address and loading the values into the data shift register, located in the peripheral electronics block, as shown in the central panel of Fig. 4.4. The last sensor row also contains the beam projection onto the columns, which can be directly uploaded to the data shift register in the adder mode, as shown in the right panel of Fig. 4.4.

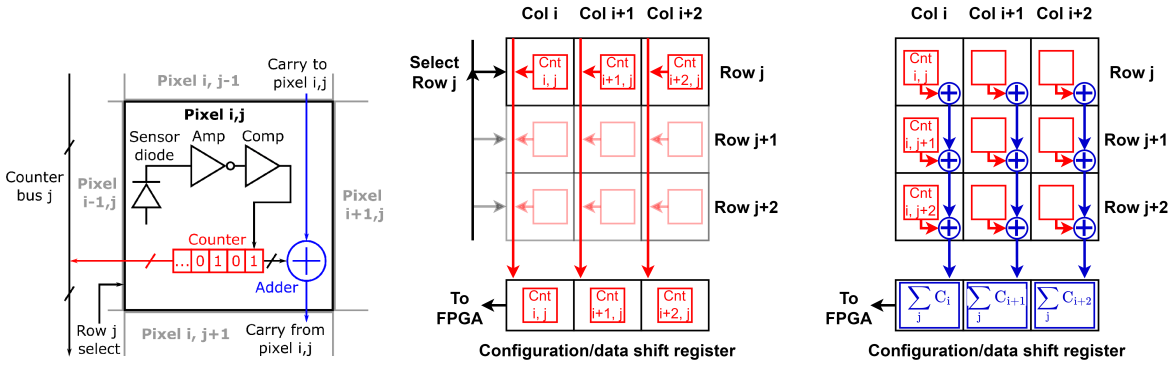


Figure 4.4.: Simplified HitPix sensor architecture. The internal pixel structure (left), the organization of the pixel matrix readout in counter (center) and adder (right) modes. Modified from [Die+23].

At HIT conditions, ion beams can varied in a wide energy range, as explained in section 2.2. Therefore, it is important to estimate the expected dynamic range of the signals generated in the sensor by the traversing particles for the sensor design. The dynamic range of the signals can be roughly estimated from the ion stopping power in silicon material as a function of the particle energy, as shown in Fig. 4.5. The stopping powers of protons (blue line in the figure) and carbon ions (orange line in the figure) are plotted alongside the stopping power of muons (green line in the figure) for comparison, since muons at $\beta\gamma$ of $\sim$3 are often treated as MIP in particle physics experiments, as explained in subsection 3.2.1.

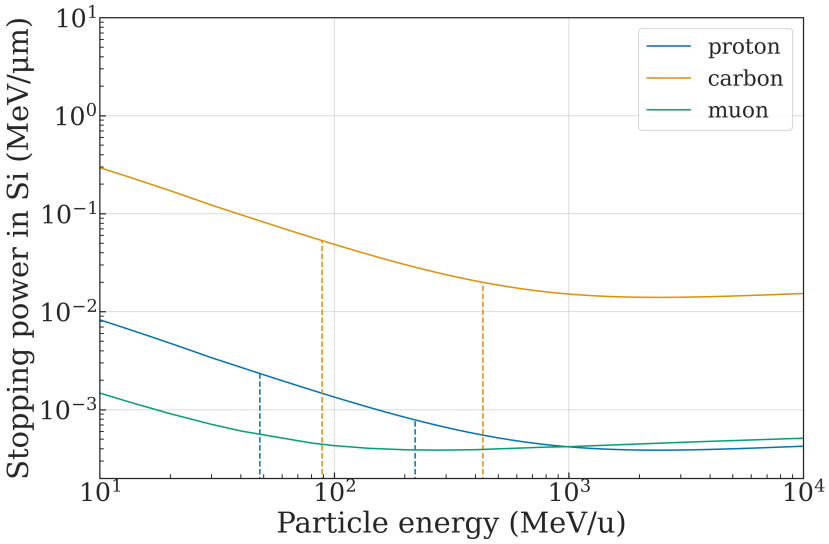


Figure 4.5.: Stopping power of protons (blue solid line), carbon ions (orange solid line) and muons (green line) in silicon material. The vertical lines represent the proton (blue dashed line) and carbon (orange dashed line) energy range used at HIT. The stopping powers for proton and carbon ion were calculated with the ATIMA software [Gei+]. The muon stopping power was taken from the tabulated data presented in [GMS01].

For the estimation, it is considered that the total energy loss of the particle is caused by the silicon atom ionization, since the nuclear stopping power component in the given energy range is negligible. From this figure, the mean energy loss of a MIP in silicon material equals

$388\,\mathrm{eV\,\mu m^{-1}}$ or $108\,\frac{\mathrm{e-h}}{\mu\mathrm{m}}$. The ion energy ranges used at HIT are shown in table 2.1 and marked with vertical dashed lines in the figure. Within these particle energy ranges the mean energy loss of a proton is larger than that for a MIP by factor of 2 to 6 ($216\,\frac{\mathrm{e-h}}{\mu\mathrm{m}}$ to $648\,\frac{\mathrm{e-h}}{\mu\mathrm{m}}$). For carbon ions, the factor is significantly larger and lies in the range from 52 to 136 ($5616\,\frac{\mathrm{e-h}}{\mu\mathrm{m}}$ to $14\,688\,\frac{\mathrm{e-h}}{\mu\mathrm{m}}$). The large deposited charge of therapeutic ions, especially carbon, relaxes the absolute noise requirements of the sensor. Therefore, the wide dynamic range of the particle signal is not a critical design consideration of the CSA, since the sensor measures particle counts and not signal amplitudes.

4.3. Data acquisition system

The HitPix sensor can be configured and read out via certain patterns of control signals applied to the sensor pads. Therefore, to control the data flow between a PC and the sensor, the DAQ system is designed. Its block diagram is shown in Fig. 4.6.

The entire system is controlled with a PC, which hosts the Graphical User Interface (GUI) program and the backend software for system configuration and sensor data storage and analysis.

The PC is connected to the main component of the DAQ system, the FPGA board. Within the scope of this thesis the Nexys Video Artix7 FPGA board [Dig20] was used. The firmware configures the FPGA to implement a simplified microprocessor with program memory. A set of predefined instructions may be uploaded to the program memory via a USB-UART interface. This ensures flexibility in the generation of HitPix control signals, the sensor configuration and output data sampling. The high-speed data transfer to the software backend is organized via USB interface (up to $190\,\mathrm{Mbit\,s^{-1}}$). The control and data signals are mapped to the board Low Pin-Count FPGA Mezzanine Card (LPC-FMC) socket for communication with the HitPix sensor. The available FPGA input-output resources allow to map up to 34 differential (68 single-ended) signals to the LPC-FMC [Dig20].

The GEneric Configuration and COntrol (GECCO) board, designed by F. Ehrler and R. Schimassek [Ehr21; Sch21], acts as an interface between the FPGA board, LV and HV power supplies, and the HitPix sensor. It delivers signals and electrical power to the connected sensor via a single Peripheral Component Interconnect Express (PCIe) x16 socket. Additionally, the GECCO board has eight small PCIe x1 sockets, which can be used to plug different functional cards for tasks such as generation of the reference voltage or a sequence of electrical pulses.

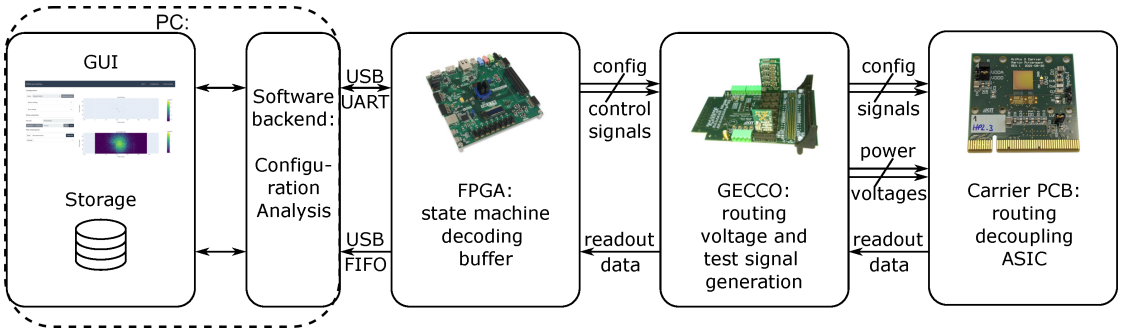


Figure 4.6.: Block diagram of the data acquisition system consisting of the main components: the PC, the FPGA board, the GECCO board, and the sensor carrier. Signals between components and their directions are indicated with arrows. Modified from [Die+23]. GUI screenshot from [Mar24].

A sensor is mounted on a custom-designed Printed Circuit Board (PCB), called the sensor carrier. The sensor carrier provides the routing of electrical power and signals to the sensor by wire-bonding the sensor pads to the exposed parts of the PCB traces. Moreover, the sensor carrier may include decoupling capacitors for the power rails, external pins for the direct measurement of the in-pixel CSA output signals, pull-up resistors for the LVDS signals and other functional elements, depending on the sensor requirements and desired functionality of the carrier. Additionally, the carrier features an edge connector compatible with the PCIe socket of the GECCO board.

The backend software and the FPGA firmware were initially designed and developed by M. Pittermann as part of his master's thesis [Pit22]. The author of this thesis modified and improved them to extend the system functionality for different devices, starting from HitPix2 multi-sensor assemblies to the HitPix3 5×5 beam monitor demonstrator, presented in this thesis. The GUI program was developed by P. Marchesi and B. Bartels within the scope of their master's theses [Mar24; Bar25] under the author's supervision.

4.4. Project milestones

As mentioned in section 4.1, the HitPix R&D project began in 2019. The following section briefly describes the main project milestones and outlines the scope of this thesis within the project timeline. The block diagram of the main project milestones is shown in Fig. 4.7.

The first stage of the project focused on the general design of the HV-CMOS active pixel sensor architecture for ion beam monitoring, followed by the production of the first HitPix1 sensor. The sensor had a small area of $5\,\text{mm} \times 5\,\text{mm}$ (24×24 pixels) and featured the one-dimensional column-wise calculation of the beam projection in the adder mode. Sensors were tested in a laboratory environment and the HIT beamline before and after applying significant radiation damage. The results proved that the proposed design and technology are suitable for the ion beam monitoring application. The detailed design of, and experimental results with, HitPix1 sensors can be found in [Web21; Web+22].

In the second stage of the project, the HitPix2 sensor was designed and produced with a larger sensor area of $10\,\text{mm} \times 10\,\text{mm}$ (48×48 pixels), while the projection calculation remained one-dimensional. The HitPix2 design description and initial measurement results can be found in [Web21; Pit22; Die+23]. The next stage of the project was concentrated on the assembly and testing of a detector system based on several HitPix2 sensors (a multi-sensor assembly), followed by comprehensive measurements of a HitPix2 sensor. Chapter 5 of this thesis covers the characterization campaign of the HitPix2 sensors, presents the beam test results obtained with the multi-sensor assembly and the studies of radiation-damaged sensors. The findings obtained at this stage formed the list of features for the next HitPix3 sensor design to improve its performance.

HitPix3 was designed and produced during the fourth stage. Although the sensitive area of HitPix3 remained unchanged ($10\,\text{mm} \times 10\,\text{mm}$), the important two-dimensional projection calculation was implemented for the adder mode. The HitPix3 sensor design and experimental results are presented in chapter 6 of this thesis.

The next two stages were carried out in parallel: first, to explore the assembly technologies for a 5×5 beam monitor demonstrator, which could fit the entire ion beams with a size larger than 20 mm for the first time, and second, to examine the HitPix3 performance in a small multi-sensors assembly. The first prototype of the 5×5 demonstrator based on HitPix2 sensors and the experimental results of the HitPix3 multi-sensor assembly are presented in the first part of chapter 7 and in chapter 6, respectively.

The knowledge gained from the last three stages was used to design and produce two 5×5 beam monitor demonstrators based on HitPix3 sensors. They were successfully tested in the laboratory. One of the demonstrators was additionally tested at the HIT beamline and was delivered to HIT for further evaluation regarding its potential integration into a beam quality control procedure. The beam monitor demonstrator design and measurement results are presented in the final chapter 7. This concludes the scope of the thesis within the project timeline.
However, the project will continue by the design of the next HitPix4 sensor, which will have the final sensor area of $20\,\text{mm} \times 20\,\text{mm}$ (96×96 pixels) and two-dimensional projection calculation. The sensor production will be followed by the well-established characterization procedure. The design considerations for HitPix4 sensor, based on the HitPix3 experimental results, are given at the end of chapter 6.
The project final stage consists of the development and production of full-scale beam monitors with a low material budget, presented in section 4.1. An extensive characterization at HIT is foreseen at this stage to allow the system to be further developed into a medical device.

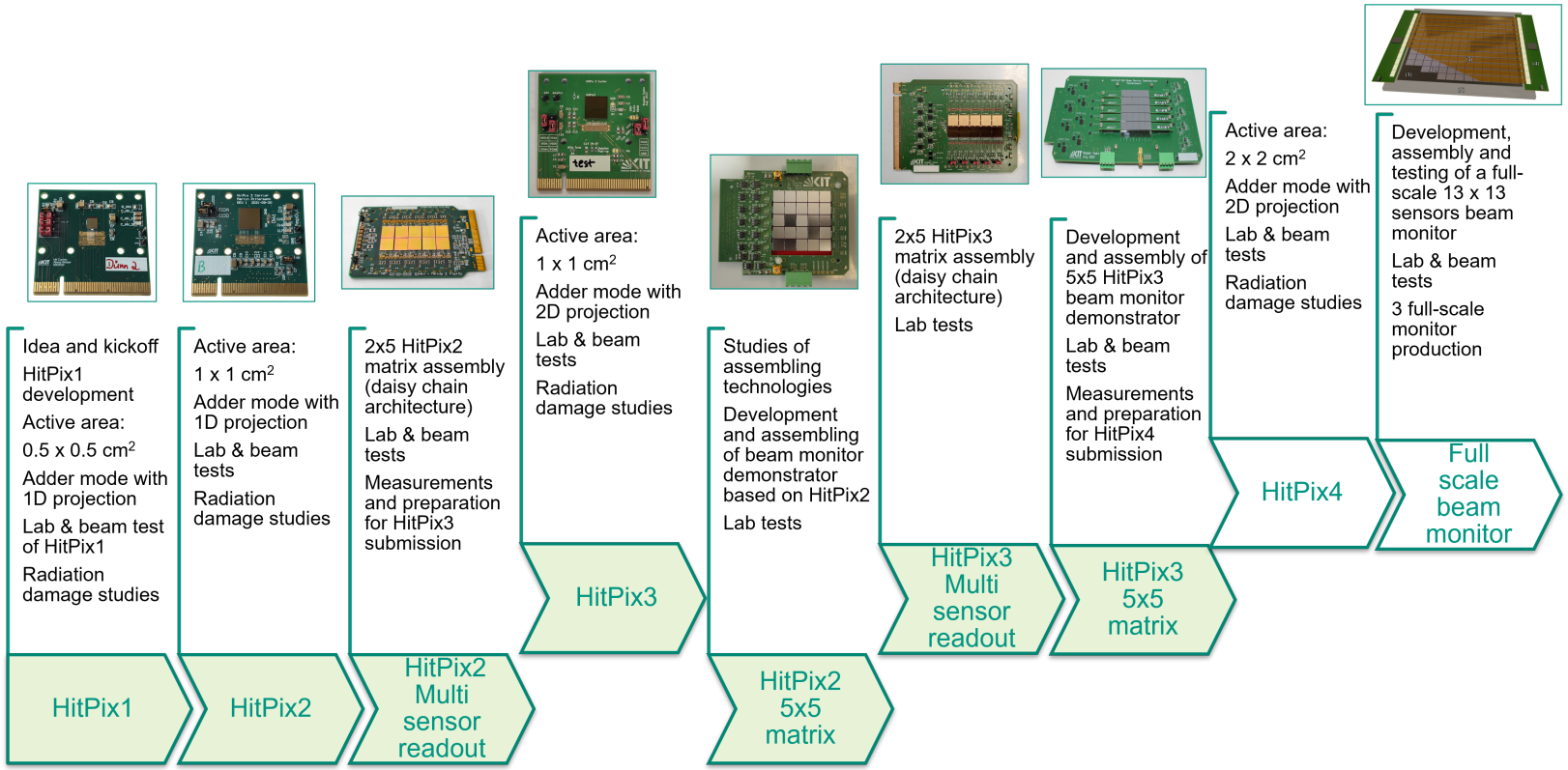


Figure 4.7.: Block diagram of the main project stages. The blocks filled with green color represent the completed milestones. The photograph of HitPix1 and HitPix2 single carriers are taken from [Pit22]. The 3D rendering of the full scale beam monitor is from [Die+23]

5 HitPix2

HitPix2 is the second iteration of the HitPix sensor family. As its predecessor HitPix1 it is based on the separated deep n-well pixel topology, but with a larger sensor sensitive area. The following chapter covers the HitPix2 sensor design, the sensor characterization process and results, the multi-sensor assembly, and the radiation hardness studies. The results were used to determine a necessary set of improvements for the next iteration of the HitPix sensor family – HitPix3.

5.1. Sensor design

HitPix2 sensors were designed and produced with a 180 nm HV-CMOS process at the TSI Semiconductors foundry. The sensor layout and its photograph are shown in Fig. 5.1.

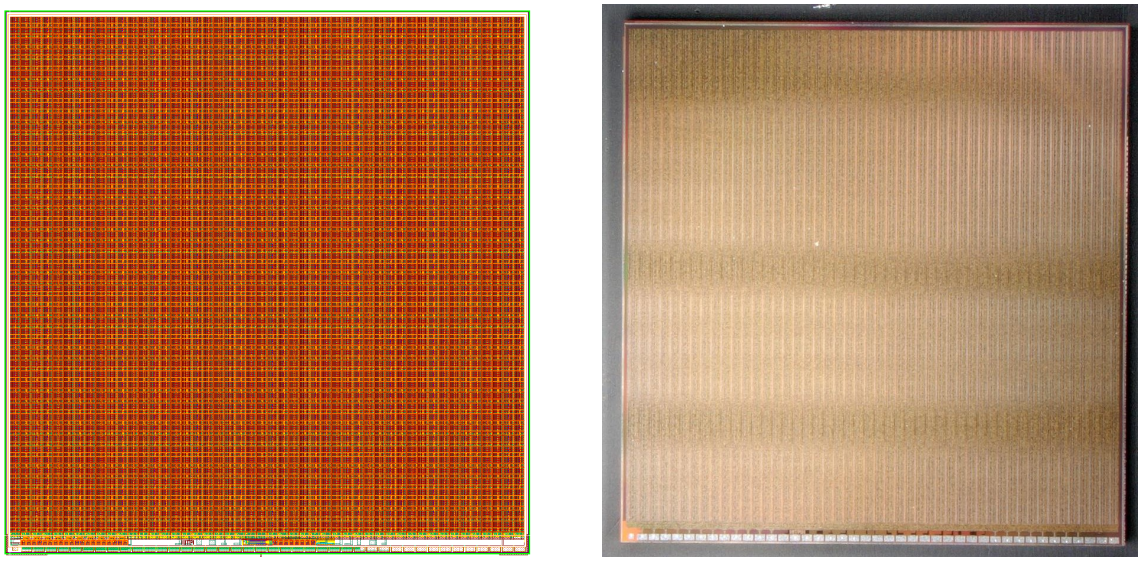


Figure 5.1.: The HitPix2 sensor layout (left) consists of a 48 × 48 pixel (orange), peripheral electronics (narrow yellow-green region) and connection pads are located at the bottom of the sensor [Web21]. Photograph of a HitPix2 sensor (right). Photo courtesy of L. Hahn.

The sensor has a total area of 9800 µm × 10 100 µm. The pixel matrix forms a sensitive area of 9600 µm × 9600 µm (or 93.1 % of the total area) and consists of 48 × 48 pixels with 200 µm × 200 µm size. The peripheral electronics and connection pads occupy a narrow region of 9600 µm × 420 µm (or 4.1 % of the total area) at the bottom of the sensor. The remaining 2.8 % of the total area is the region between guard ring and the sensor edges. The current layout allows to form multi-sensor assemblies with a minimal dead area between sensors. The previous HitPix1 sensor has only 4900 µm × 5200 µm total area with a 24 × 24 pixel matrix and the same pixel

size [Web+22; Web21]. As explained in section 4.2, the HitPix1 and HitPix2 have column-wise projection calculation and frame-based readout.

5.1.1. Pixel layout

The HitPix2 pixel cell can be divided into three functional blocks: sensor diode, analog and digital electronics, as shown in a simplified functional diagram in Fig. 5.2 on the left. The sensor diode collects the charge carriers generated by the passing ionizing particle. The analog electronics amplifies the induced current signal of the drifting charge carriers with a CSA and transforms it to a binary signal by a comparator. The comparator output is connected to the 8 bit counter of the digital electronics to count the number of particles that passed through the pixel. The counter value is also fed into the 14 bit adder to perform the column-wise projection calculation, as explained in 4.2. The actual layout of the HitPix2 pixel is shown in Fig. 5.2 on the right.

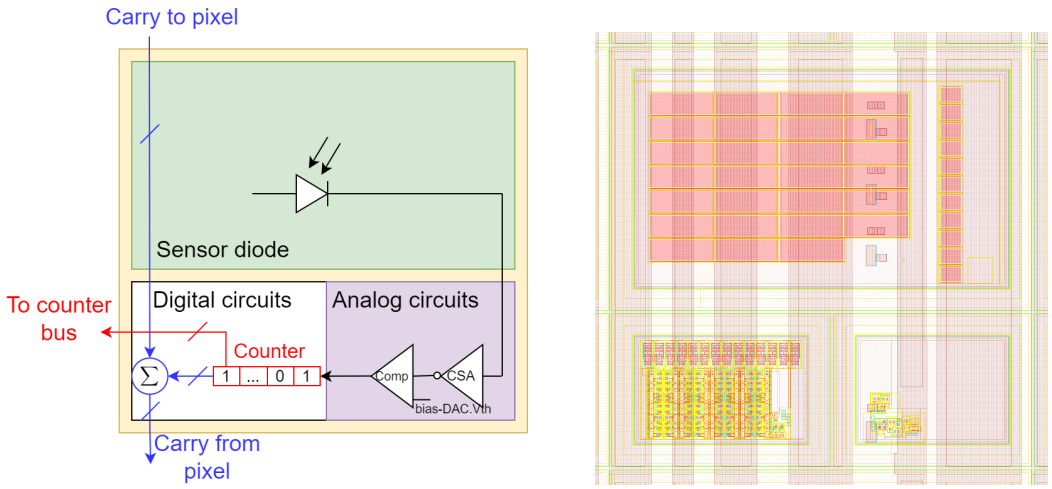


Figure 5.2.: Simplified functional diagram of the HitPix2 pixel (left) and its actual layout (right). The pixel layout courtesy of E. Trifonova.

The HitPix2 pixel cell has a separated deep n-well pixel topology (presented in section 3.4) as its predecessor HitPix1. Its simplified cross-section is shown in Fig. 5.3. The deep n-well of the pixel and the p-type silicon substrate form the sensing diode, whereas analog and digital circuits are located in the separated deep n-wells. As explained in [Web+22], the deep n-wells of the diode and the analog electronics part are connected to a positive supply rail voltage V_{dda} of 1.85 V to reduce a possible leakage current between them. The negative bias voltage V_{bias} is applied to a substrate contact to expand the depletion region of the pixel. The electronics deep n-wells occupy around 30 % of the pixel area, which can lead to a reduction of the ionization signal, since a charge collected with deep n-wells of the analog or digital electronics will not be amplified.

5.1.2. Pixel electronics

The pixel electronics of the HitPix2 sensor implements a general processing chain of a silicon detector signal previously discussed in section 3.3. A simplified schematic of the pixel electronics is shown in Fig. 5.4. The deep n-well biasing circuit (depicted as R_{bias} in the figure) is introduced between the V_{dda} supply rail and the deep n-well of the diode. Its high equivalent resistance forces the current signal induced by the particle to flow into the AC-coupled inverting input of

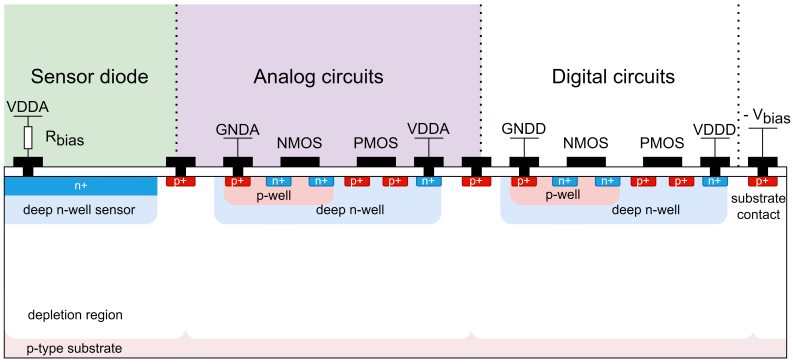


Figure 5.3.: Simplified cross-section of a HitPix2 pixel.

the CSA, since the coupling capacitance C_c forms the path of least impedance for the signal. For the ideal CSA, the output voltage signal v_{out} is proportional to $-Q_{\text{sig}}/C_{\text{fb}}$. In a real CSA, the capacitance of the sensor diode C_{diode} and equivalent input capacitance of the CSA C_{in} reduces the gain, as explained in [Web+22]. To prevent the CSA output saturation, caused by consecutive signals, the resistive feedback circuit (depicted as R_{fb} in the figure), based on transistors operating in the weak inversion mode, is introduced to discharge the feedback capacitor C_{fb} [Web21]. The CSA output is then AC-coupled via C_{ac} to a non-inverting input of comparator [Web+22], which converts the CSA output signal into a binary signal.

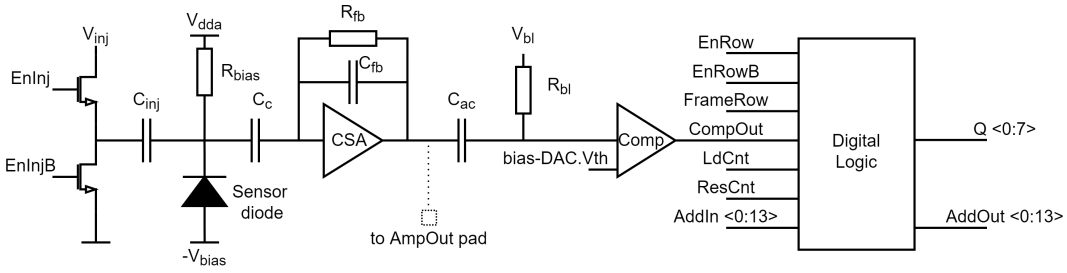


Figure 5.4.: Simplified schematic of HitPix2 pixel. An additional connection to the `AmpOut` pad (black dashed box) is implemented only for pixels in the row closest to the peripheral electronics. Adapted from [Web21] and [ZTP26].

The external baseline voltage V_{bl} is also applied at the comparator non-inverting input via controllable resistive circuit R_{bl} to form a constant and stable DC voltage level. The inverting comparator input is connected to the voltage level (Vth) common to all pixels of sensor and generated by the `bias-Digital-to-Analog Converter (bias-DAC)` block (more details in subsection 5.1.3). If the amplitude of the CSA output signal is higher than a threshold voltage of `bias-DAC.Vth` $- V_{\text{bl}}$, the comparator transits into a logic high state, and it transits into a logic low state, when the signal amplitude becomes lower than the threshold voltage.
The comparator output is connected to the 8 bit radiation hard ripple down counter, which decrements its maximum value of $2^8 - 1 = 255$ when the `FrameRow` signal is high, the comparator output is high and `EnRow` is low (the pixel row is not being read out). The `FrameRow` and `EnRow` signals are generated by the row control block at the sensor periphery. To reset all pixel counters, the externally generated signal `ResCnt` should be applied to the sensor pad. To read out the counter value, it should be latched with an externally generated signal `LdCnt`. The counter value can be read out only when the `FrameRow` signal is low and `EnRow` is high, which loads the latched value to a Parallel In Serial Out (PISO) register, introducing a read out dead time between frames.

Therefore, to satisfy the system timing requirements, a 14 bit adder is implemented in the same guard ring of the pixel cell as the counter (indicated in Fig. 5.2 on the left). The adder sums the pixel counter value with an adder value of the previous pixel. This allows to read out a beam profile within one readout cycle instead of the 48 row-by-row cycles, as discussed in section 4.2.
It is important to note a flaw in the counter design of HitPix1 and HitPix2 sensors, first discovered and reported in [Pit22]. Due to this flaw, the `ResCnt` signal resets the counter values to 0 instead of 255 and the first detected hit overflows the counter value to 255, and all consecutive hits decrement its value. While this unconventional behavior can be addressed during the decoding of the counter data, it limits the adder bit range because adder data can be decoded without ambiguity only if the total number of hits in the projection column does not exceed 255.
Each pixel also contains the injection circuits to test the pixel response to a given input charge. The pixel can be selected for the test by applying the enable signal `EnInj` via configuration of the PISO register (more details in subsection 5.1.3). When a pixel is selected, an external short injection voltage pulse V_{inj} is applied to the `Inj` pad of the sensor, generating the current pulse proportional to C_{inj} and dV_{inj}/dt.
Furthermore, the pixels in the row closest to the peripheral electronics have an additional connection between CSA output and sensor `AmpOut` pad, which allows to directly measure the amplifier output. The detailed transistor level schematics of the analog and digital circuits may be found in [Web21; Web+22; Per+21].

5.1.3. Peripheral electronics

The peripheral electronics of HitPix2 sensors is used to configure and read out a sensor. It consists of three main parts: PISO shift registers, row control block and `bias-DAC` block, similar to HitPix1 [Web21].
A PISO shift register consisting of 14 bit radiation hard Scan Flip-Flops (ScanFFs) is implemented for each pixels column to control its readout and configuration. A simplified schematic of a single ScanFF is shown in Fig. 5.5. It consists of two inverting multiplexers and three level-sensitive D-latches. The first multiplexer, controlled by the external signal `PSel`, selects either the counter bit C_i or the adder bit A_i. The second multiplexer, controlled by `PEnable`, selects either the input data bit SIn_i or the output of the first multiplexer. The selected bit is propagated through two latches by the external two-phase clock signal `Clk1` and `Clk2`. When SIn_i contains a configuration bit, it is propagated through the third latch by the external signal `LdConfig`.

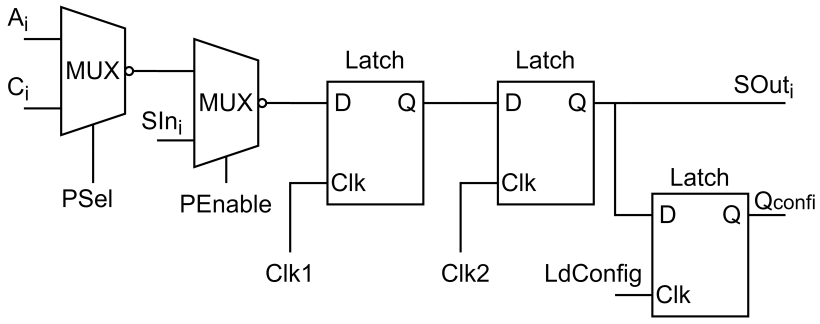


Figure 5.5.: Simplified schematic of single HitPix2 scan flip-flop. Adapted from [Web21].

All 48 PISO shift registers are connected in series to form a single configuration/data shift register with a size of $14 \times 48 = 672$ bit, as shown in Fig. 5.6. The input SIn_0 of the first ScanFF

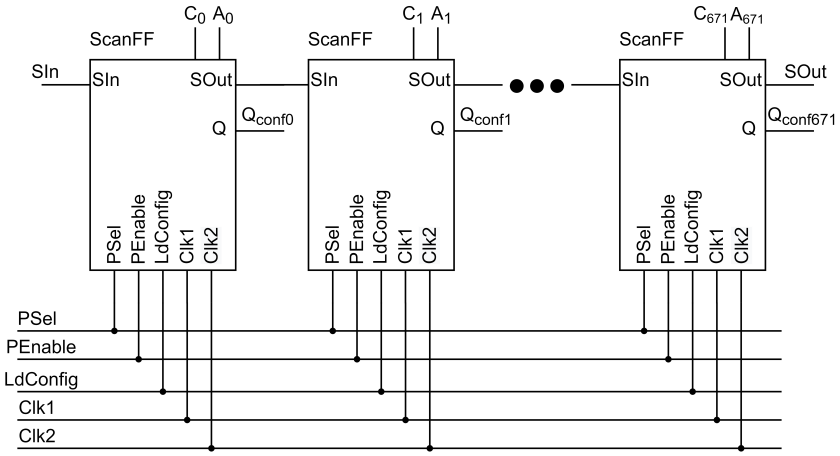


Figure 5.6.: Simplified schematic of HitPix2 configuration/data shift register. Adapted from [Web21].

connects to the `SIn` sensor pad. The output SOut_{671} of the last ScanFF drives LVCMOS and LVDS output buffers, each of them is connected to the corresponding sensor pads [Web21].

Six configuration bits $\mathrm{Q_{conf}}\langle 8{:}13\rangle$ of the configuration/data shift register encode the row address. They, together with an external signal `Frame`, are fed into the row control block, which generates `EnRow` and `FrameRow` signals for the corresponding row. Every 7th configuration bit $\mathrm{Q_{conf}}\langle 7{::}14\rangle$ corresponds to enable injection signal `EnInj`. Every 6th configuration bit $\mathrm{Q_{conf}}\langle 6{::}14\rangle$ selects the test output of the in-pixel CSA in the row closest to the peripheral electronics for its direct measurement via the `AmpOut` pad.

The `bias-DAC` block provides specific voltages and currents to many sensor components to adjust the sensor operation. These voltages and currents are generated by Digital-to-Analog Converters (DACs) with bit resolutions in a range of 6 bit to 8 bit. The configuration data of the `bias-DAC` block is stored in a separate Serial In Parallel Out (SIPO) shift register with a size of 74 bit. To configure this shift register, separate sets of pads and control signals (`SInDAC`, `SOutDAC`, `LdDAC`, `Clk1DAC`, `Clk2DAC`) are used. A detailed bit assignment of the `bias-DAC` block shift register is presented in the Appendix in table B.1. More details of the peripheral electronics design may be found in [Web21].

5.2. HitPix2 characterization

Several dozens of sensors are produced in a single silicon wafer. The wafer can contain sensors with completely different designs (Multi-Project Wafer run), to optimize the cost of small production series. After production, the wafer is diced with a diamond saw to extract individual sensors. The produced sensors can have defects such as faulty circuits in pixels or peripheral electronics induced during the manufacturing phase. Moreover, cracks and scratches on the sensor surface can be induced during the mechanical extraction of sensors from the wafer. The fraction of sensors without defects defines the production yield, which is usually less than 100 %. Only fully functional sensors can be used in multi-sensor assemblies, otherwise, even a single defective sensor may drastically decrease the assembly performance (an example of 1×5 HitPix2 matrix with a defective sensor may be found in [Pit22]). In the worst case, it can make the assembly completely nonfunctional. The following section covers the HitPix2 sensors characterization campaign dedicated to the assembly of 2×5 and 5×5 matrices. The

campaign was carried out in 2022-2023 mostly by L. Hahn within the scope of her bachelor's thesis under the author's supervision. The detailed campaign results may be found in [Hah23].

5.2.1. Sensor probe station

Characterization of a sensor requires connections for power supply, DAQ control and data readout at the sensor pads. Simultaneously, it should be performed with minimal invasion to the pads to allow the sensor final assembly. This excludes wire-bonding of the sensor to a PCB carrier, since the wire bond feet will partially remain at the pads after testing. In the worst case, it can make a tested sensor unusable for the final assembling.
The probe station, designed and produced by the ADL at the IPE, KIT [BLP18], provides an effective way to test a large number of sensors without wire-bonding. It is achieved by using tiny probe needles to contact the sensor pads. The needles are located at a special PCB called probe card (designed by F. Ehrler). The needles pitch matches exactly the pitch of the pads. Each needle is soldered to a corresponding PCB trace, which ends at a custom PCIe connector for the connection with a GECCO board (as explained in chapter 4.3). A photograph of a HitPix2 sensor under the probe card is shown in Fig. 5.7.

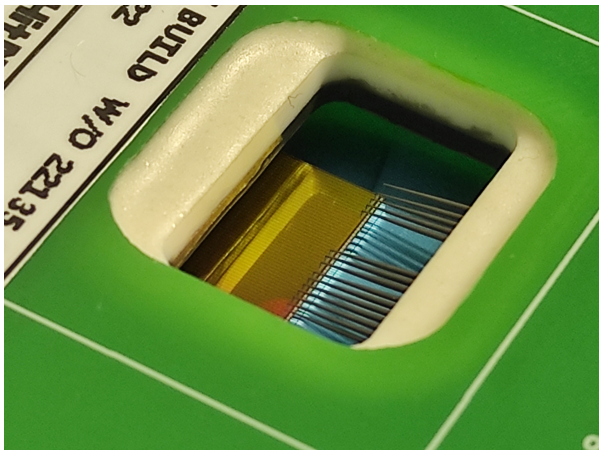


Figure 5.7.: HitPix2 sensor under the probe card needles.

A photograph of the probe station and its coordinate system are shown in Fig. 5.8. During the test, several sensors are fixed on a special membrane, which prevents their movements. Next, the membrane is positioned and fixed at the vacuum jig (sensor fixation membrane and vacuum jig are marked as 3 in the figure). After that, the alignment between sensor pads and probe needles (marked as 2 in the figure) is achieved by controlling the sensor position with mechanical stages containing step motors (marked as 5 in the figure) in the X- and Y-directions and rotation angle ϕ and optical control through the microscope (marked as 1 in the figure). Power supply and data flow from/to the sensor are established with FPGA and GECCO boards (marked as 4 in the figure), which are connected to a probe card.

5.2.2. Testing procedure

The testing procedure was designed to verify functionalities of HitPix2 sensor in-pixel and peripheral electronics. The flowchart of the procedure is shown in Fig. 5.9.
A group of 5 to 8 sensors are fixed on the membrane and installed at the probe station as described in the previous subsection 5.2.1. In the next step, a first sensor in the group is aligned with probe needles. The contact between sensor pads and probe needles is established by moving the aligned sensor along vertical Z-direction with a speed of a few $\mu m\,s^{-1}$ and

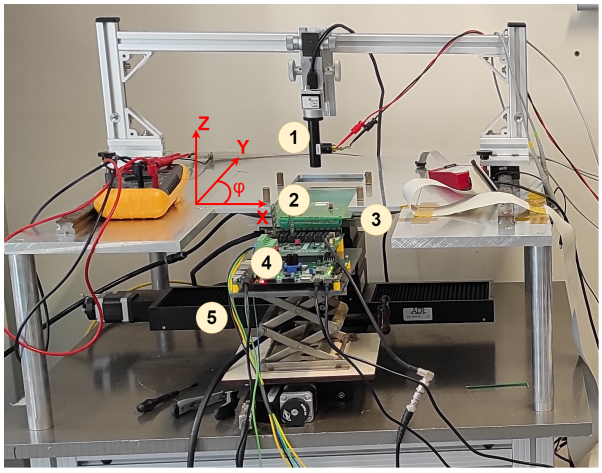


Figure 5.8.: ADL-KIT chip probe station. 1 - High resolution microscope, 2 - probe card, 3 - vacuum jig and sensor fixation membrane, 4 - FPGA and GECCO boards, 5 - mechanical stages with step motors. The red arrows represent the coordinate system of the setup.

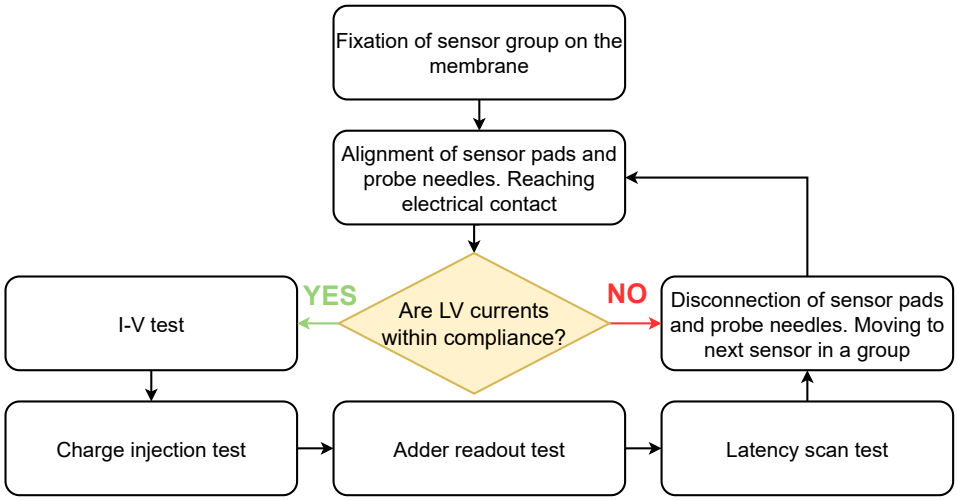


Figure 5.9.: Flowchart of HitPix2 sensors testing procedure.

monitoring the value of the LV power supply current I_{ddd}. A I_{ddd} current of 0 mA corresponds to no contact between pads and needles, whereas $I_{\mathrm{ddd}} \geq 5$ mA corresponds to an established contact. Next, all three LV currents I_{ddd}, I_{dda} and I_{ssa} are checked to be within a compliance upper limit of 300 mA each (any LV current of a fully functional sensor does not exceed 150 mA). If the sensor passes the compliance check, the following sequence of tests is performed: I-V, charge injection, adder readout and latency scan. Descriptions and examples of measurement results of each step in this sequence are given in the following subsections. If one of the sensor LV currents failed the compliance check, the sensor is immediately marked as malfunctional. After the testing sequence or failed LV current compliance check, the contact between pads and needles is released and the next sensor in a group is aligned for the tests.

5.2.3. I-V test

The design of the HitPix2 sensor allows to bias the pixel diode below −100 V to increase its depletion region [Web+22; Web21], which is a main advantage compared to MAPS based on

LVCMOS technology, as explained in section 3.4. Therefore, a current versus voltage (I-V) test is used to verify that the tested sensor has a breakdown voltage below −100 V. During the test, the bias voltage is decreased from 0 V to −130 V with a −1 V step. If a sensor has a breakdown voltage above −100 V it is marked as malfunctional. Since the probe station is not protected from the environmental light, the measured current is a sum of leakage and photo currents. Examples of the measured I-V curves of functional and malfunctional HitPix2 sensors are shown in Fig. 5.10 in which the malfunctional sensor has an early breakdown voltage around −80 V.

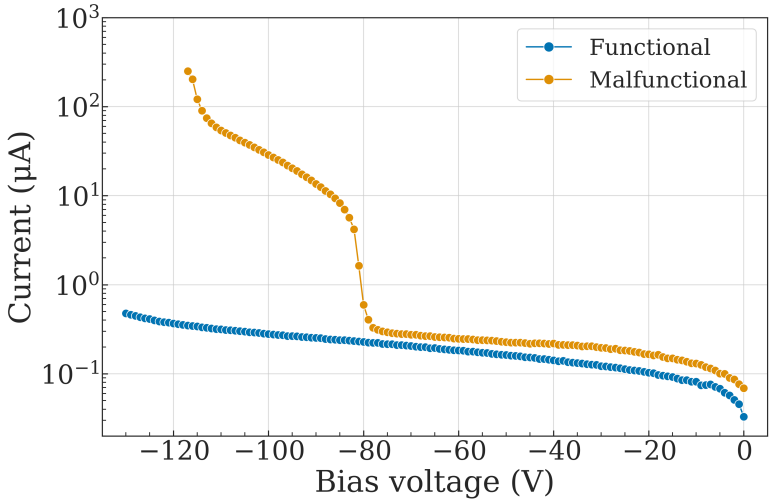


Figure 5.10.: Example of a measured I-V curves for functional (blue points) and malfunctional (orange points) HitPix2 sensors at room temperature. The current is plotted in absolute values.

5.2.4. Charge injection test

Each HitPix2 pixel contains an injection circuit to test the pixel response to a given input charge, as explained in subsection 5.1.2. This feature is used in the charge injection test to validate the in-pixel electronics functionality. During a single measurement, a known number of voltage pulses is applied to the `Inj` pad. The pulse duration and amplitude are controlled by the FPGA and the GECCO board injection card [Ehr21]. The injection voltage amplitude is varied from 0 V to 1.2 V in 30 steps and the pixel responses are recorded at fixed values of `bias-DAC.Vth`. As explained in subsection 5.1.2, the in-pixel comparator transits into a logic high state if the CSA output signal is higher than a comparator threshold voltage of `bias-DAC.Vth` − V_{bl}. For brevity, the `bias-DAC.Vth` will be referred as a threshold voltage throughout this thesis, since the V_{bl} is usually kept at the constant level unless mentioned otherwise.
The measurement is repeated for a set of threshold voltages from 160 DAC units to 190 DAC units in 26 steps at fixed bias V_{bias} and baseline V_{bl} voltages of −50 V and 1.1 V, respectively. The pixel efficiency is then calculated as the ratio of detected hits to the number of injected pulses. An example of a single pixel response of functional and malfunctional sensors at a fixed threshold voltage are shown in Fig. 5.11. The pixel response of an ideal sensor would follow a unit step function. In a real sensor, the noise of the sensor diode and in-pixel electronics is non-zero and follows a Gaussian distribution, which smears the transition region. As a result, the mean and standard deviation of the underlying Gaussian distribution defines the pixel threshold and noise. Therefore, the pixel threshold and noise can be calculated as the injection voltage value at which the pixel efficiency is equal to 50 % and the transition region width, respectively.

It is important to distinguish between the threshold voltage (`bias-DAC.Vth`) and the pixel threshold. The former refers to the voltage applied to the in-pixel comparator inverting input, whereas the latter is the characteristic of the pixel response to a given input signal. The pixel threshold depends on pixel settings such as the CSA gain. For two pixels with different CSA gains set to the same threshold voltage, the pixel threshold will be higher for the pixel with smaller CSA gain, since a larger input signal should be induced in that pixel to be detected.

Each pixel response of a functional sensor is fitted with an error-function, called S-curve, to extract the pixel threshold and noise values, which are depicted as a vertical orange line and orange bands, respectively in Fig. 5.11 on the left. The pixel response of the malfunctional sensor does not follow the error-function and the shape of the distribution can vary from pixel to pixel significantly, indicating a problem with the in-pixel electronics. However, the response cannot point out the exact source of the problem, since several components are involved during the measurements: injection circuit, CSA, comparator and counter. Nonetheless, sensors with such behavior cannot be used in the multi-sensor assembly.

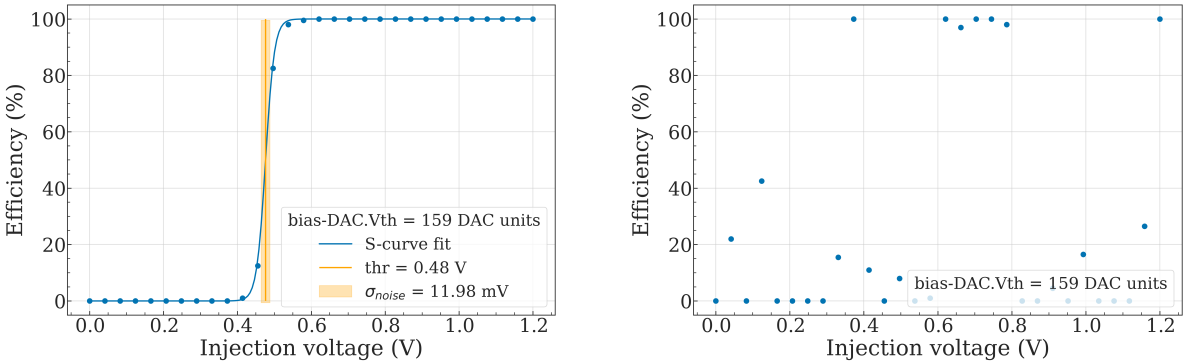


Figure 5.11.: Example of charge injection measurements of functional (left) and malfunctional (right) HitPix2 sensors. The pixel response of a functional sensor is fitted with an error function. The vertical orange line and orange bands represent the pixel threshold and noise values, respectively.

The pixel threshold distributions of a functional sensor at different threshold voltages are shown in Fig. 5.12 on the left. For illustrative purpose, only 8 distributions of the 26 threshold voltages are plotted. As explained in subsection 5.1.2, the threshold voltage is common to all pixels in a sensor. Therefore, for an ideal sensor, the distribution would follow a delta function. However, for a real sensor, the manufacturing variations of pixels could influence in-pixel electronics properties: injection capacitance C_{inj}, CSA gain, voltage offsets of the comparator inputs etc. This smears the ideal distribution to a Gaussian one. To estimate the mean pixel threshold value μ_{thr} and the pixel threshold standard deviation σ_{thr}, all pixel threshold distributions are fitted with a Gaussian function.

The dependence of μ_{thr} on threshold voltage is shown in Fig. 5.12 on the right. It follows a linear function in a wide range of threshold voltages, as expected, since the threshold voltage is generated with a linear 8 bit DAC. It can be seen that σ_{thr} becomes larger at the higher threshold voltages. This can be explained by a non-linearity of the injection circuit which saturates at high injection voltages. Furthermore, the number of the pixel response fitting points with 100 % efficiency becomes smaller at high threshold voltages, which could influence the goodness of the S-curve fit.

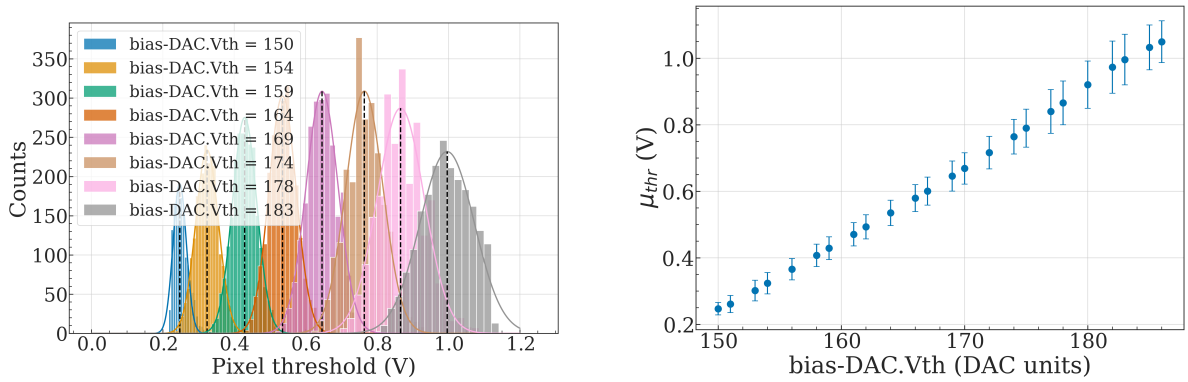


Figure 5.12.: Pixel threshold distributions (left) and mean μ_{thr} of these distributions (right) of a functional sensor at different threshold voltages. Error bars represent the standard deviation of the measured distribution σ_{thr}.

5.2.5. Adders readout test

Another important feature of the HitPix2 sensor is the adder mode, which allows to perform a one-dimensional beam projection calculation on the sensor with adder circuits implemented inside each pixel. To verify their functionality, the adders readout test is performed.
In a single measurement, 1000 frames are recorded at fixed threshold voltage, V_{bias} and V_{bl} settings. The bias voltage V_{bias}, and the baseline voltage V_{bl} are set to $-50\,\text{V}$ and $1.1\,\text{V}$, respectively. The frame duration t_{frame} is set to $5\,\text{ms}$. The measurement is repeated for a set of threshold voltages from 160 DAC units to 190 DAC units in 26 steps. An example of measured averaged number of adder counts per frame of functional and malfunctional sensors is shown in Fig. 5.13.

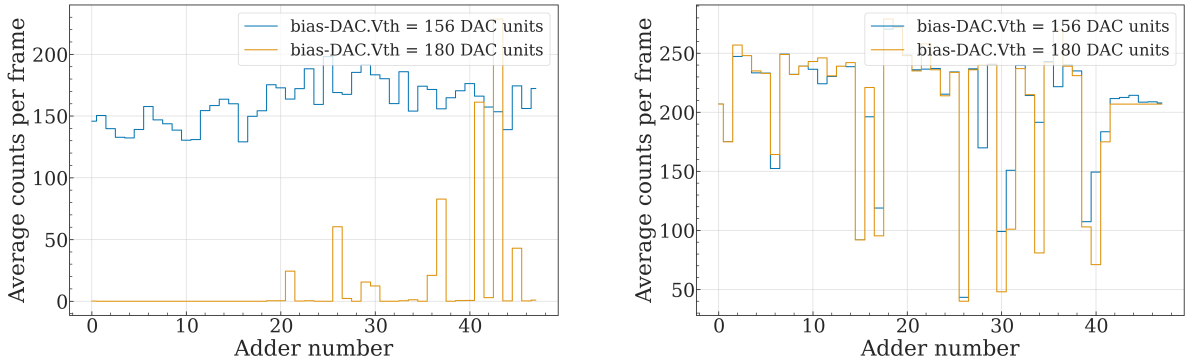


Figure 5.13.: Example of averaged number of adder counts per frame of functional (left) and malfunctional (right) sensors.

Averaged number of adder counts per frame of functional and malfunctional sensors are plotted at two threshold voltages. The frame of a functional sensor at the low threshold voltage of 150 DAC units consists of pedestal noise, because some fraction of pixels in a sensor column has a threshold lower than the noise level. At the higher threshold voltage of 180 DAC units most of the adders have zero average counts. The remaining pedestal noise in eight adders indicates that even at high threshold voltage some pixels may still generate fake hits. In contrast, the averaged adder frame of the malfunctional sensor is almost insensitive to changes in threshold voltage. This confirms the charge injection test results, indicating a problem with in-pixel electronics of the malfunctional sensor.

The adders performance of the functional sensor is sufficient to confirm the adders functionality, allowing it to be used in multi-sensor assembly prototypes. During beam measurements, the pedestal value calculated from frames without a beam can be used to correct the influence of fake hits in the frames containing a beam. However, for the final beam monitor system, the new sensor design must include a pixel masking feature, which allows to disable individual noisy pixel output.

5.2.6. Latency scan test

The HitPix2 sensor can be configured and read out through a configuration/data shift register located at the sensor peripheral electronics. To ensure its functionality, the latency scan test is used.
During the test, a randomly generated bit sequence with a size of 672 bit is shifted into the configuration/data shift register and read out back through the sensor LVDS output buffer at fixed readout speed and sampling latency. The readout speed corresponds to the frequency of the two-phase clock `Clk1` and `Clk2`. The sampling latency corresponds to the time delay between the `Clk2` pulse and arrival of the data signal at the FPGA input. The number of error bits is calculated by comparing the initial sequence with the read sequence. The procedure is repeated ten times and the numbers of error bits are summed. An example of a measured latency scan is shown in Fig. 5.14. The green area in the plot corresponds to readout speed and sampling latency values without an error.

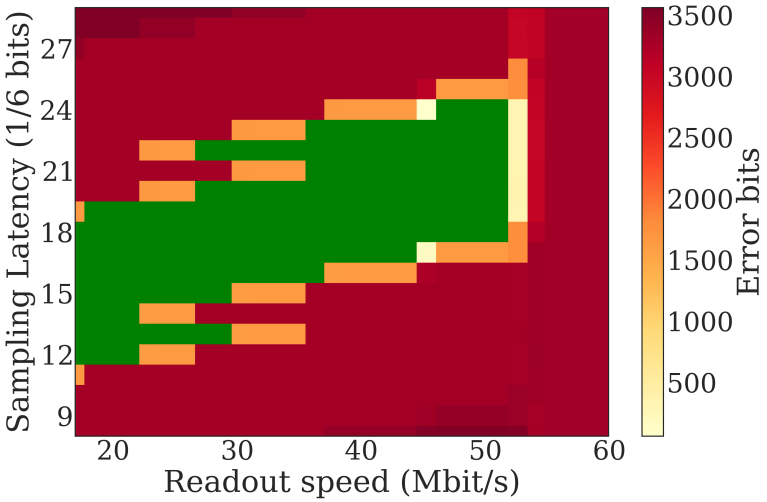


Figure 5.14.: Example of a measured latency scan. The green area corresponds to readout speed and sampling latency values without an error.

During the HitPix2 sensor evaluation presented in [Pit22], it was shown that the maximum readout speed of the configuration/data shift register and the active clock duty cycle are limited to 58 Mbit s^{-1} and 33 %, respectively, by parasitic capacitance and resistance of the long clock lines of the register. At the probe station, the maximum readout speed of all tested sensors varied in the range from 17 Mbit s^{-1} to 58 Mbit s^{-1}. This large variation can be explained by different quality of contact between probe card needles and sensor pads. To confirm this, several sensors with a small maximum readout speed were wire-bonded to single sensor PCB carriers (designed by M. Pittermann [Pit22]) and tested again. The maximum readout speed of these sensors increased to 49 Mbit s^{-1} and higher. Therefore, in this test, a malfunction of the configuration/data shift register can only be stated if there is no combination of readout speed and sampling latency, which yields zero error bits. However, every tested sensor had at least

one combination in which the shift register can be read out without error bits. Hence, it can be concluded that malfunctioning of the sensors is not related to the sensor peripheral readout electronics.

5.2.7. Characterization results

In total, 153 sensors were tested and only 52 of them passed all tests, leading to a total production yield of 34 % detailed in table 5.1. The sensors were produced on p-type substrates with different resistivities ρ of 20 Ω cm, 300 Ω cm and 5000 Ω cm to find an optimal substrate in terms of radiation hardness. This is covered in section 5.5.

Table 5.1.: Results of HitPix2 characterization campaign at the probe station.

Wafer	ρ (Ω cm)	# tested	# func.	# malfunc.	yield (%)
Wafer 1	20	16	7	9	44
Wafer 4	5000	25	0	25	0
Wafer 5	5000	44	9	35	21
Wafer 7	300	41	19	22	46
Wafer 10	300	27	17	10	63
Total	-	153	52	101	34

The characterization campaign results concluded that the primary source of sensor malfunction was a problem with the in-pixel electronics (the detailed measurement results may be found in [Hah23]). No functional sensors were found among 25 tested sensors from wafer 4, which had a resistivity of 5000 Ω cm and was thinned to a thickness of 300 µm. The remaining wafers were not thinned and had an approximate thickness of 850 µm. Wafer thinning can cause mechanical damage to the sensors, reducing yield. However, wafer 5, which was also based on the high resistivity substrate, had a significantly lower yield than the other three unthinned wafers. Therefore, the malfunctioning of sensors from wafer 4 cannot be directly attributed to the sensor thinning procedure.
Valid sensors from wafer 10 were used to assemble 2×5 matrix, which is presented in next section 5.3, and other assemblies. Sensors from wafer 7 and 1 were used for the 5×5 matrix wire-bonding assembly and wafer 5 sensors were used in the bump-bonding assemblies. They are presented in section 7.1. Additionally, the malfunctional sensors were used in various mechanical mock-ups to test assembly technology before valid sensors were used.

5.3. Multi-sensor readout

The final beam monitoring system should reliably measure two beam parameters: position and size, as discussed in section 4.1. The single sensor area is not sufficient to cover the entire treatment field of 200 mm × 200 mm at HIT. Therefore, a multi-sensor assembly should be used to fulfill the sensitive area requirement. Validated HitPix2 sensors were selected to assemble a prototype of a multi-sensor matrix. Its performance was estimated during a beam test at HIT.

5.3.1. Readout architecture considerations

The multi-sensor assembly, consisting of N sensors, can be read out using either a daisy chain or a bus architecture. Their simplified views are shown in Fig. 5.15. In both architectures,

sensor control signals are distributed to all sensors via the bus, the only difference is how the data is propagated during the readout process.

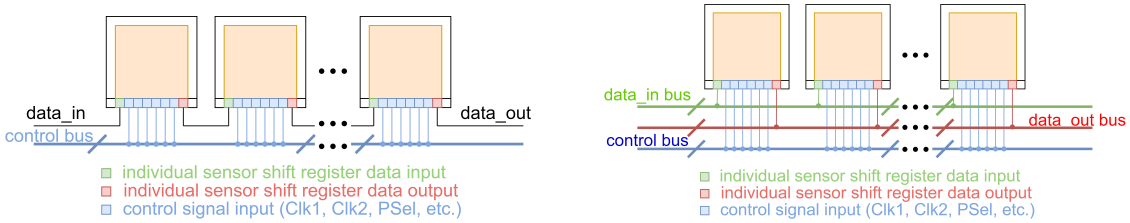


Figure 5.15.: Simplified view of a daisy chain (left) and a bus (right) readout architecture. The simplified view of a daisy chain from [Top+24].

In a daisy chain architecture, the configuration/data shift register output of one sensor directly connects to the shift register input of the next. This creates a single, larger shift register N times the size of an individual sensor shift register. During the readout, the data is propagated through the entire chain. The daisy chain simplifies the readout logic and the PCB design. However, a single damaged sensor in the chain can result in the loss of the chain data. Moreover, a chain consisting of many sensors could limit the maximum readout speed, since the clock signal will be delayed for the sensors at the end of the chain, leading to potential errors in the data.
In a bus architecture, the input and output of the configuration/data shift register of all sensors are connected in parallel to the corresponding data buses. Each sensor can be read out through the data bus individually. The bus architecture allows to read out a selected subset of sensors, increasing the speed of the data processing, but at the cost of increased complexity of the readout logic and the PCB design. A selection of the sensor subset for readout can be achieved either by performing the full-system data readout to determine a region of interest, or through an alternative measurement, such as monitoring of the changes in sensor bias currents, which will be higher for sensors under beam due to the additional current induced by traversing particles.
The daisy chain architecture was selected for all multi-sensor assemblies presented in this thesis, because of its advantages. The chain integrity issue was resolved by assembling only sensors which passed all probe tests. The potential control signal delay issue was resolved by keeping the chain short (only five sensors per chain). The final system consisting of 13 sensors per chain may be split into two individual chains. In the scope of a beam monitoring task, the main advantage of the bus architecture is diminished, because the entire matrix should be read out for every frame. Otherwise, the beam misbehavior, such as unexpected changes in beam position or shape, can be missed, if only a subset of the sensors are being read out.

5.3.2. 2 × 5 HitPix2 matrix

Ten valid HitPix2 sensors were selected to assemble the 2×5 matrix which is shown in Fig. 5.16. Five sensors in each matrix row are mounted on the PCB carrier and wire-bonded to the carrier bonding pads to form a daisy chain. The PCB was designed by M. Pittermann within the scope of his master's thesis [Pit22]. Power supply, control and data signals are delivered to the matrix through the GECCO board via custom PCIe connector. Power rails and control signals are delivered to both matrix rows in parallel. Each matrix row has individual traces for configuration/data LVCMOS `SIn`, LVDS `SOut` and `bias-DAC` LVCMOS `SInDAC` signals. The daisy chain is organized via the LVCMOS output buffer of sensor configuration/data shift register connected to the input buffer of the next. The row data is read out through the LVDS shift register output buffer of the last sensor in the row.

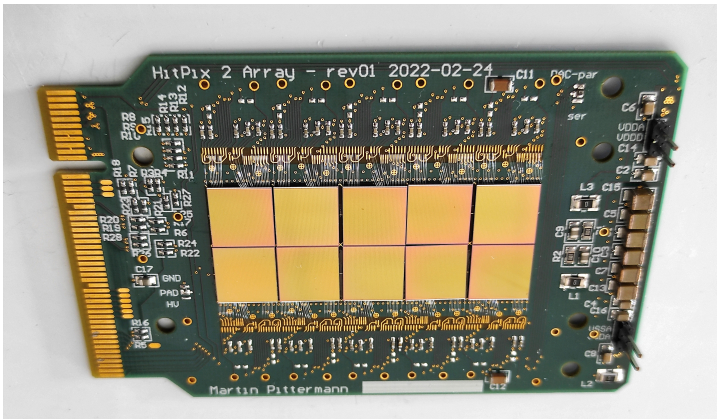


Figure 5.16.: Assembled 2×5 HitPix2 matrix. The PCB was designed by M. Pittermann.

The maximum readout speed of the matrix is limited to $22\,\mathrm{Mbit\,s^{-1}}$, due to missing pull-up resistors in a LVDS `SOut` trace for one of the matrix rows. The other row can be correctly read out up to $36\,\mathrm{Mbit\,s^{-1}}$. This value is lower than that for the single sensor readout speed of $58\,\mathrm{Mbit\,s^{-1}}$, due to the propagation delay of 23 ns between falling edge of `Clk2` of one sensor and LVCMOS `SIn` of next sensor in the chain, which was measured and reported in [Pit22]. Since the clock is delivered to both matrix rows in parallel, the slowest row limits the entire matrix readout speed. After identification of this problem, it was recommended to redesign data and control signal buffers according to the LVDS standard to increase the readout speed for the next HitPix3 sensor.
Sensors in the matrix were mounted manually, leading to local sensor rotations and gap variations between neighboring sensors. Without alignment, these effects bias the reconstruction of beam position and size. To compensate this, the entire matrix was measured with a microscope to create a local matrix coordinate map of each pixel center, which is shown in Fig. 5.17.

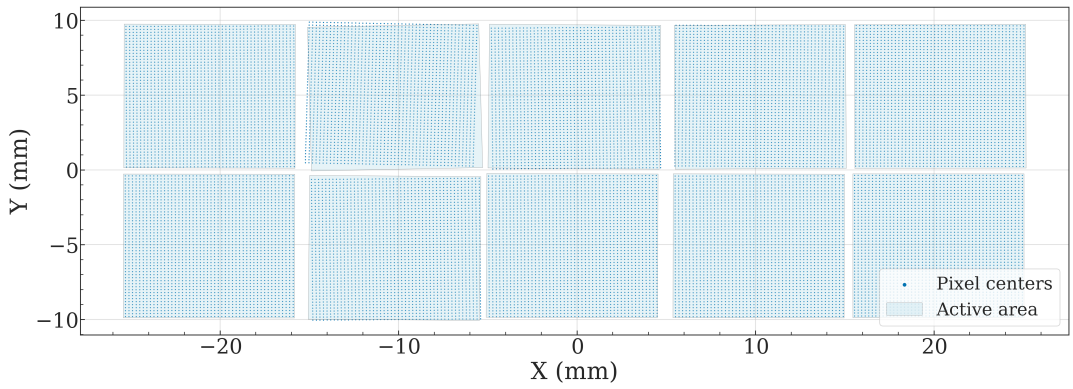


Figure 5.17.: Pixel coordinate map of 2×5 HitPix2 matrix.

The coordinate origin (0,0) of the map is located at the matrix geometrical center. The map X- and Y-axes are aligned with the axes of the existing beam monitoring system at HIT, with the Z-axis pointing downstream the beam path.

5.3.3. Beam test setup

The 2×5 HitPix2 matrix was installed and tested at the HIT beamline in September 2023. The experimental setup is shown in Fig. 5.18 on the left. To position the matrix at the beamline

isocenter (focal point), the laser-based alignment system available at HIT (pink lines in the photographs) was used. The 2×5 HitPix2 matrix position was controlled via step motors in a modified mechanical stage. The initial version of the mechanical stage was developed by U. Elicabuk within the scope of his master's thesis [Eli21].

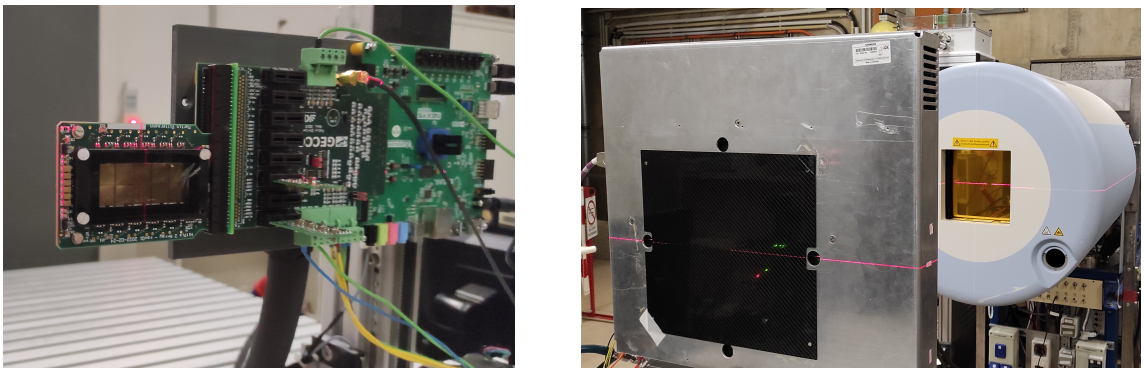


Figure 5.18.: 2×5 HitPix2 matrix (left) and reference ISO-MWPC (right) installed at the isocenter of HIT beamline. The HitPix2 matrix and ISO-MWPC are shown in views downstream and upstream the beam, respectively. The pink lines represent the laser-based alignment system.

To evaluate the matrix performance for the beam position and size reconstruction, the existing isocentric-MWPC (ISO-MWPC) detector, produced by Siemens Healthineers (Germany), was used as a reference detector (right photograph in Fig. 5.18). Since only one detector can be located at the isocenter, the 2×5 HitPix2 matrix and ISO-MWPC were measured independently using the same set of beam parameters and compared after the beam test. Due to variations in the beam optics and fluctuations in the number of particles extracted from the synchrotron (as reported in [Sch+15]), the measured beam parameters may deviate within the tolerances defined by HIT, which are detailed in section 4.1.

5.3.4. ISO-MWPC detector

The isocentric-MWPC detector is a part of the existing beam monitoring system at HIT and is used for the beam quality assurance at the beamline isocenter. Its parameters and geometry are identical to the MWPCs installed within the beam nozzle, which are detailed in section 4.1. Raw beam profile information is not available for the ISO-MWPC detector. Instead, the beam position and size information for each measurement cycle is provided by the integrated TwinCAT Ether-CAT system (Beckhoff Automation GmbH, Germany) [Rin+13; Wit+25]. According to [Wit+25], the beam position μ and FWHM measured with the ISO-MWPC are calculated with equations 5.1 and 5.2, respectively:

$$\mu = \frac{\sum_{i=1}^{n}(Q_i - C) \cdot i \cdot d}{\sum_{i=1}^{n}(Q_i - C)}, \tag{5.1}$$

$$FWHM = 2\sqrt{2\ln 2} \cdot s \cdot \sqrt{\frac{\sum_{i=x_{\text{start}}}^{x_{\text{end}}}(Q_i - C) \cdot (i \cdot d - \mu)^2}{\sum_{i=x_{\text{start}}}^{x_{\text{end}}}(Q_i - C)}}, \tag{5.2}$$

where Q_i is a measured charge of channel i, C is a constant cutoff offset equals 10 % of the maximum signal in a profile [Par+10], d is the wire pitch of 2 mm, n is the total number of channels, x_{start} and x_{end} define a dynamically adjusted window for the beam size calculation (the exact window size depends on the beam settings), and s is an empirical scaling factor of

1.17. The purpose of this scaling factor is not provided in [Wit+25]. One possible explanation is that it is used to compensate for the beam size calculation within the dynamically adjusted window. Only positive values are used in the beam parameters calculation after the cutoff value is applied to the measured profile data.

5.3.5. Data comparison method

To extract the beam parameters from the 2×5 HitPix2 matrix data, each non-empty frame was fitted with a 2D-Gaussian function, given in equation 5.3:

$$f(x, y) = A \exp\left(-\frac{(x-\mu_x)^2}{2\sigma_x^2} - \frac{(y-\mu_y)^2}{2\sigma_y^2}\right), \tag{5.3}$$

where A is the height of the Gaussian, μ_x, μ_y are the coordinates of the center, and σ_x, σ_y are the standard deviations in the X- and Y-directions, respectively. The beam size defined in FWHM is then calculated as $2\sqrt{2\ln 2} \cdot \sigma$ in the corresponding direction without an empirical scaling factor of the ISO-MWPC.
Since measurements with the 2×5 matrix and ISO-MWPC were done independently, only mean values of reconstructed beam position and size can be compared against the system requirements. Therefore, the beam position and size distributions, measured using the 2×5 matrix and the ISO-MWPC, were fitted with a 1D-Gaussian function 5.4 to extract the mean values.

$$f(p) = A_p \exp\left(-\frac{(p-\langle\mu_p\rangle)^2}{2\sigma_p^2}\right), \tag{5.4}$$

where A_p is the height of the Gaussian, $\langle\mu_p\rangle$ and σ_p are the mean and standard deviation of the measured beam parameter p.
As reported in [Wit+25], where beam size measurements were performed with five different types of detectors, the ISO-MWPC systematically provided the smallest beam sizes across all detectors tested with proton and carbon beams. This can be explained by using the cutoff offset in equation 5.2, which suppresses the influence of particles with large scattering angles on the estimated beam size. Hence, to directly compare the size of the proton beam reconstructed with the ISO-MWPC and 2×5 HitPix2 matrix, the matrix cutoff value was calculated as 10 % of the 2-D Gaussian height $\langle A \rangle$ averaged over all frames. For the carbon beam, the cutoff value was calculated as 10 % of the averaged maximum counts over all frames, because of the lower number of counts per pixel, leading to poorer fitting results. After that, the cutoff value was subtracted from all pixel counts. Mean beam positions and sizes were compared with and without applied cutoff value to the 2×5 matrix data. Noisy pixels with an average pixel hit rate above 0.05 per frame without beam were masked during the analysis.

5.3.6. Beam test results

Proton and carbon beams were measured with the 2×5 HitPix2 matrix and ISO-MWPC at four beam focus settings and fixed intensity and energy. The beams were delivered in three spills with approximate duration of 5 s per spill. The nominal beam parameters used in the measurements are detailed in table 5.2.
The following operational parameters of the 2×5 matrix were fixed for all measurements: $V_{\text{bias}} = -100\,\text{V}$, $V_{\text{dda}} = 1.85\,\text{V}$, $V_{\text{bl}} = 0.93\,\text{V}$. The threshold voltage and frame duration t_{frame} were set to 143 DAC units and 350 µs, respectively. All measurements were performed at room temperature. The sensors were read out in counter mode.
An example of a measured beam profile with the 2×5 matrix in one frame without cutoff applied is shown in the top plot of Fig. 5.19. The orange cross and ellipse in the figure represent

Table 5.2.: Nominal beam parameters in the measurements with 2×5 HitPix2 matrix. The table data are taken from the actual List of Ion Beam Characteristics (LIBC) of HIT. F1, F2, F3 and F4 represent different beam size (FWHM) settings.

Ion	Energy (MeV u^{-1})	Intensity (pps)	F1 (mm)	F2 (mm)	F3 (mm)	F4 (mm)
proton	221.06	2×10^8	8.1	9.7	11.1	12.6
carbon	430.10	5×10^6	3.4	5.5	7.8	9.8

the estimated beam position and FWHM with 2D-Gaussian fit. The color palette for the counts is in logarithmic scale to visualize the contribution of particles with large scattering angles in the measured beam profiles.

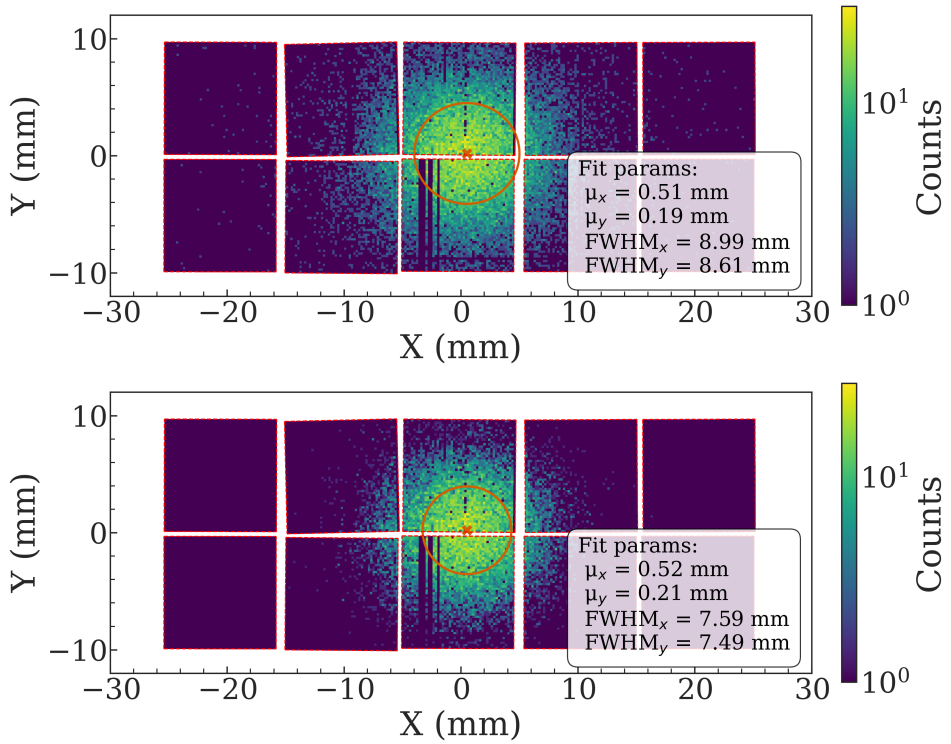


Figure 5.19.: Proton beam profile measured using the 2×5 HitPix2 matrix in one 350 µs frame (**counter mode**) without (top) and with (bottom) cutoff applied in the local coordinate system. Red dashed lines enclose the active areas of the sensors. The orange cross and ellipse represent the estimated beam position and FWHM with 2D-Gaussian fit, respectively. Nominal beam FWHM = 8.1 mm.

An example of a measured proton beam profile with cutoff applied is shown in the bottom plot of Fig. 5.19. It can be seen how the contribution of particles with large scattering angles is suppressed, leading to a smaller beam size and almost unchanged beam position estimated with 2D-Gaussian fit.

Measurements with an 8.1 mm size proton beam were used to align the 2×5 matrix and ISO-MWPC local coordinate systems. Without alignment, a systematic offset of each local detector coordinate system position with respect to the isocenter, would bias comparisons between results from two detectors. The systematic offset (x_{align}, y_{align}) was calculated as a

difference between mean beam position ($\langle\mu_{xref}\rangle$, $\langle\mu_{yref}\rangle$) measured with the ISO-MWPC and the beam position ($\langle\mu_x\rangle$, $\langle\mu_y\rangle$) measured with the 2×5 matrix without cutoff applied. After that, (x_{align}, y_{align}) was added to all pixel coordinates for all measurements.
Figure 5.20 shows the measured distributions of proton beam size $FWHM_x$ and $FWHM_y$ using the ISO-MWPC and 2×5 matrix without and with cutoff applied for different beam focus settings. All distributions follow the same trend: the beam size becomes larger at higher beam focus setting. As expected, the beam size measured with the 2×5 matrix without cutoff applied is larger than that for the ISO-MWPC.

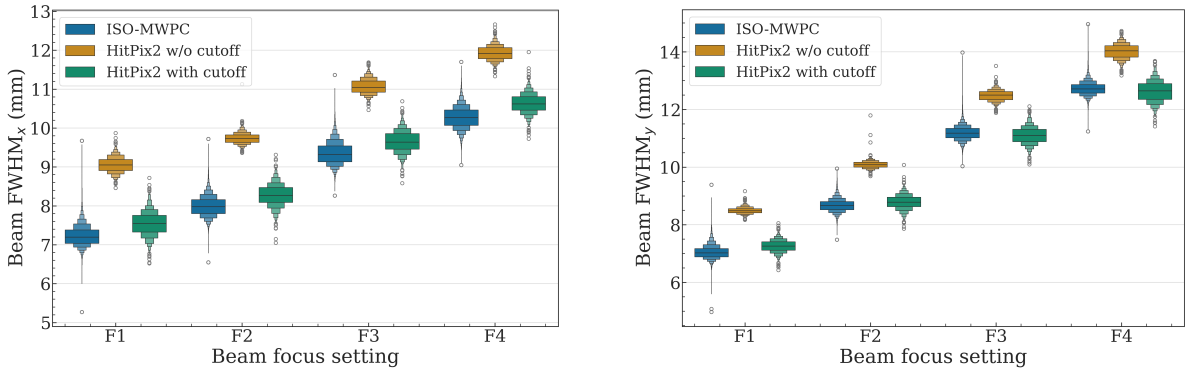


Figure 5.20.: Measured distributions of proton beam size $FWHM_x$ (left) and $FWHM_y$ (right) using the ISO-MWPC (blue color), 2×5 HitPix2 matrix without (orange color) and with (green color) cutoff applied for different beam focus settings.

The mean proton beam size in the X- and Y-directions and their standard deviations were estimated on the measured distributions, as explained in subsection 5.3.5. These results are presented in tables 5.3 and 5.4. In the tables, the focus setting column shows the focus name and the nominal beam FWHM. The next three columns show the estimated parameters. Columns Δ_{FWHM} and $\Delta_{FWHM_{cut}}$ show differences between mean beam size measured with the ISO-MWPC and 2×5 matrix without and with cutoff applied, respectively.

Table 5.3.: The $\langle FWHM \rangle$ of the measured proton beam size in the X-direction using the ISO-MWPC and 2×5 HitPix2 matrix. Units: mm.

Focus setting	$\langle FWHM_{xref} \rangle$	$\langle FWHM_x \rangle$	$\langle FWHM_{xcut} \rangle$	Δ_{FWHM}	$\Delta_{FWHM_{cut}}$
F1: 8.1	7.18 ± 0.24	9.04 ± 0.22	7.54 ± 0.32	-1.86	-0.36
F2: 9.7	7.97 ± 0.26	9.72 ± 0.15	8.27 ± 0.28	-1.75	-0.30
F3: 11.1	9.31 ± 0.30	11.04 ± 0.21	9.65 ± 0.30	-1.73	-0.34
F4: 12.6	10.26 ± 0.29	11.91 ± 0.21	10.62 ± 0.25	-1.65	-0.36

Table 5.4.: The $\langle FWHM \rangle$ of the measured proton beam size in the Y-direction using the ISO-MWPC and 2×5 HitPix2 matrix. Units: mm.

Focus setting	$\langle FWHM_{yref} \rangle$	$\langle FWHM_y \rangle$	$\langle FWHM_{ycut} \rangle$	Δ_{FWHM}	$\Delta_{FWHM_{cut}}$
F1: 8.1	7.01 ± 0.20	8.48 ± 0.11	7.26 ± 0.22	-1.47	-0.25
F2: 9.7	8.66 ± 0.21	10.09 ± 0.13	8.79 ± 0.25	-1.43	-0.13
F3: 11.1	11.18 ± 0.24	12.49 ± 0.21	11.09 ± 0.31	-1.31	0.09
F4: 12.6	12.71 ± 0.22	14.03 ± 0.29	12.64 ± 0.40	-1.32	0.07

The Δ_{FWHM} in the X- and Y-directions are larger than 1 mm, due to the influence of particles with large scattering angles. However, the $\langle FWHM_x \rangle$ and $\langle FWHM_y \rangle$ are still within the tolerance of $-15\,\%$ to $25\,\%$ from the nominal beam size, accepted at HIT. Across all measured proton beam settings, the beam size is reconstructed by the 2×5 matrix with an accuracy ($\Delta_{FWHM_{cut}}$) and precision ($\sigma_{FWHM_{cut}}$) better than the 0.4 mm required for the final beam monitoring system, defined in section 4.1.

Figure 5.21 shows the measured distributions of proton beam position μ_x and μ_y using the ISO-MWPC and 2×5 matrix without and with cutoff applied at different beam focus settings. The measured beam positions are in good agreement for both detectors.

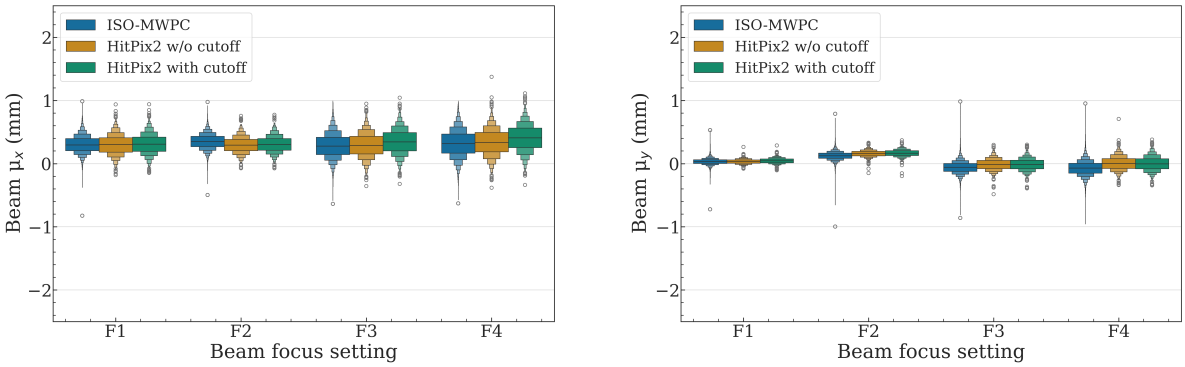


Figure 5.21.: Measured distributions of proton beam position μ_x (left) and μ_y (right) using the ISO-MWPC (blue color), 2×5 HitPix2 matrix without (orange color) and with (green color) cutoff applied different beam focus settings.

The mean beam position in the X- and Y-directions and their standard deviations were estimated on measured distributions, and the values are presented in tables 5.5 and 5.6. In the tables, the focus setting column shows the focus name and the nominal beam FWHM. The next three columns show the estimated parameters. Columns Δ_μ and $\Delta_{\mu_{cut}}$ show differences between mean beam position measured with the ISO-MWPC and 2×5 matrix without and with cutoff applied, respectively. Across all measured proton beam settings, the beam position is reconstructed by the 2×5 matrix with an accuracy (Δ_μ and $\Delta_{\mu_{cut}}$) better than the 0.2 mm required for the final beam monitoring system, defined in section 4.1. The precision (σ_{μ_x} and $\sigma_{\mu_{xcut}}$) of the beam position reconstructed by the 2×5 matrix in the X-direction is slightly exceeds the 0.2 mm requirement for the beam focus settings F3 and F4. In contrast, the precision in the Y-direction (σ_{μ_y} and $\sigma_{\mu_{ycut}}$) is better than 0.2 mm for all settings. However, the same effect is observed for the reference ISO-MWPC. Therefore, this effect can be attributed to the beam delivery of the low intensity proton beams with a large beam size, rather than the performance of the 2×5 matrix.

Table 5.5.: The $\langle \mu \rangle$ of the measured proton beam position in the X-direction using the ISO-MWPC and 2×5 HitPix2 matrix. Units: mm.

Focus setting	$\langle \mu_{xref} \rangle$	$\langle \mu_x \rangle$	$\langle \mu_{xcut} \rangle$	$\Delta\mu$	$\Delta\mu_{cut}$
F1: 8.1	0.30 ± 0.14	0.30 ± 0.17	0.31 ± 0.17	0.00	−0.01
F2: 9.7	0.35 ± 0.12	0.29 ± 0.14	0.30 ± 0.14	0.06	0.05
F3: 11.1	0.27 ± 0.20	0.29 ± 0.21	0.34 ± 0.21	−0.02	−0.07
F4: 12.6	0.32 ± 0.23	0.34 ± 0.23	0.41 ± 0.23	−0.02	−0.09

Table 5.6.: The $\langle\mu\rangle$ of the measured proton beam position in the Y-direction using the ISO-MWPC and 2×5 HitPix2 matrix. Units: mm.

Focus setting	$\langle\mu_{\text{yref}}\rangle$	$\langle\mu_{\text{y}}\rangle$	$\langle\mu_{\text{ycut}}\rangle$	$\Delta\mu$	$\Delta\mu_{\text{cut}}$
F1: 8.1	0.03 ± 0.04	0.03 ± 0.04	0.04 ± 0.04	0.00	-0.01
F2: 9.7	0.13 ± 0.06	0.16 ± 0.05	0.17 ± 0.06	-0.03	-0.04
F3: 11.1	-0.06 ± 0.09	-0.01 ± 0.10	-0.01 ± 0.10	-0.05	-0.05
F4: 12.6	-0.07 ± 0.11	0.00 ± 0.12	-0.01 ± 0.12	-0.07	-0.06

For the carbon beams configured with a minimal focus setting F1, the beam position (size) were reconstructed with a similar accuracy of ∼0.05 mm (∼0.2 mm), and a precision of ∼0.12 mm (∼0.15 mm) in the X- and Y-direction. However, at the higher focus settings, the beam shape significantly deviates from a 2D-Gaussian model due to the known effect of the carbon beams extraction process and the beam optics [KOW09; Par+12]. The cumulative beam profiles measured using the 2×5 HitPix2 matrix at beam focus settings F2, F3 and F4 are shown in the Appendix in Fig. B.1. These results confirmed the deterioration of the beam shape and that the deviation from a Gaussian shape increases with higher focus settings. Although the 2D-Gaussian fit can provide values close to the ISO-MWPC results, it does not accurately capture the beam shape (average coefficient determination of the fit of ∼0.28), and, therefore, these beams were not used for a direct comparison between the 2×5 matrix and the ISO-MWPC.
Overall, it can be concluded that the multi-sensor 2×5 matrix based on HitPix2 sensors meets the HIT beam monitoring system requirements in beam position and size reconstruction.

5.4. Performance at high particle rates

At the HIT conditions, the beam intensity varies depending on the ion type used. For carbon beams, the intensity ranges from approximately 2×10^6 pps to 1×10^8 pps (particles per second). Proton beams cover an even higher intensity range from approximately 8×10^7 pps to 4×10^9 pps [Sch+15]. The final beam monitoring system should be capable of accurately measuring these widely varying intensities. First measurements of HitPix2 sensors with proton and carbon beams at different intensities revealed a significant limitation of the sensor counting capability for high-intensity beams [Pit22; Die+23]. The studies, presented in this section, are focused on identifying the origin of this limitation to improve the pixel hit rate capability in the next iteration of HitPix sensor family – HitPix3.

5.4.1. Beam intensity scan

Proton and carbon beams were measured with a single HitPix2 sensor at six beam intensity settings (I3, I5, I7, I8, I9 and I10) and fixed energy and focus during the beam test at HIT in September 2022. The nominal beam energy and focus for the proton beam were 221.06 MeV u^{-1} and 8.1 mm, and for the carbon beam 430.10 MeV u^{-1} and 3.4 mm. Beam intensity settings for proton and carbon beams are detailed in table 5.7.
The following parameters of HitPix2 sensor were fixed for all measurements: $V_{\text{bias}} = -50\,\text{V}$, $V_{\text{dda}} = 1.85\,\text{V}$, $V_{\text{bl}} = 1.10\,\text{V}$. The threshold voltage and frame duration t_{frame} were set to 175 DAC units and 30 µs, respectively. All measurements were performed at room temperature. The sensor was read out in counter mode.
The total number of hits per frame of carbon and proton beams measured with the HitPix2 sensor at different beam intensities are shown in Fig. 5.22. The zoomed spill structure of the

Table 5.7.: Nominal beam intensity settings for proton and carbon beams at HIT. Units: pps. The table data are taken from the actual LIBC of HIT.

Intensity setting	proton	carbon
I1	8.0×10^7	2.0×10^6
I2	1.2×10^8	3.0×10^6
I3	2.0×10^8	5.0×10^6
I4	3.2×10^8	8.0×10^6
I5	4.0×10^8	1.0×10^7
I6	6.0×10^8	1.5×10^7
I7	8.0×10^8	2.0×10^7
I8	1.2×10^9	3.0×10^7
I9	2.0×10^9	5.0×10^7
I10	3.2×10^9	8.0×10^7

low-intensity beams are shown in the Appendix in Fig. B.2. In the plots, the orange and magenta horizontal lines represent the expected and measured ⟨Total hits per frame⟩.
For carbon beams, the measured spill structures have a ramp-up at the beginning of the spill and fluctuation with stable average around the ⟨Total hits per frame⟩, as expected from measurements presented in [Sch+15]. The relative difference between expected (calculated from the nominal value) and measured ⟨Total hits per frame⟩ is below 27 % up to intensity settings I7 with a minimum value of 1 % for intensity I3, whereas at the highest intensity I10 this value reaches 78 %.
For proton beams, the measured spills have similar structure only up to intensity setting I7. However, the relative difference between expected and measured ⟨Total hits per frame⟩ is already 75 % for the lowest beam intensity I3 and reaches 85 % for the beam intensity I7. Furthermore, beyond this setting, the spill structure measured by the sensor degrades: after the initial ramp-up, the measured intensity rapidly decreases to a level even lower than that observed at the I3 setting. This sensor behavior was not expected and can be attributed to the high-voltage compliance settings of the power supply: when the current in a bias circuit exceeds a certain threshold, the HV power supply reduces the bias voltage. This reduction narrows the depletion zone, reduces the signal amplitude of incoming particles, and consequently decreases the number of detected hits. During this beam test, the drop in the bias voltage was not realized because the bias current monitoring was not yet implemented.
The plots in Fig. 5.22 show only the integral characteristic of the sensor. To assess the HitPix2 counting capability on the pixel level, measured and expected pixel hit rates should be estimated by taking into account the beam position and shape. The following algorithm was used for this purpose:

1. **Calculate intensities** I_k based on the number of particles from the measurement plan and the measured total spill duration for each intensity setting k, where $k \in \{3, 5, 7, 8, 9, 10\}$.
2. **Select** N_{frames} **frames from the first spill** for each intensity setting I_k.
3. **Extract beam parameters** $\mu_{\text{x}jk}, \mu_{yjk}$ and $\sigma_{\text{x}jk}, \sigma_{yjk}$ based on the sample mean and the standard deviation for each frame j and beam intensity setting k.
4. **Average beam parameters** over all frames $\langle \mu_{\text{x}k} \rangle$, $\langle \mu_{\text{y}k} \rangle$ and $\langle \sigma_{\text{x}k} \rangle$, $\langle \sigma_{\text{y}k} \rangle$ for each intensity setting k
5. **Calculate standard deviation of beam parameters** across all frames $\sigma_{\mu_{\text{x}k}}$, $\sigma_{\mu_{\text{y}k}}$ and $\sigma_{\sigma_{\text{x}k}}$, $\sigma_{\sigma_{\text{y}k}}$ for each intensity setting k

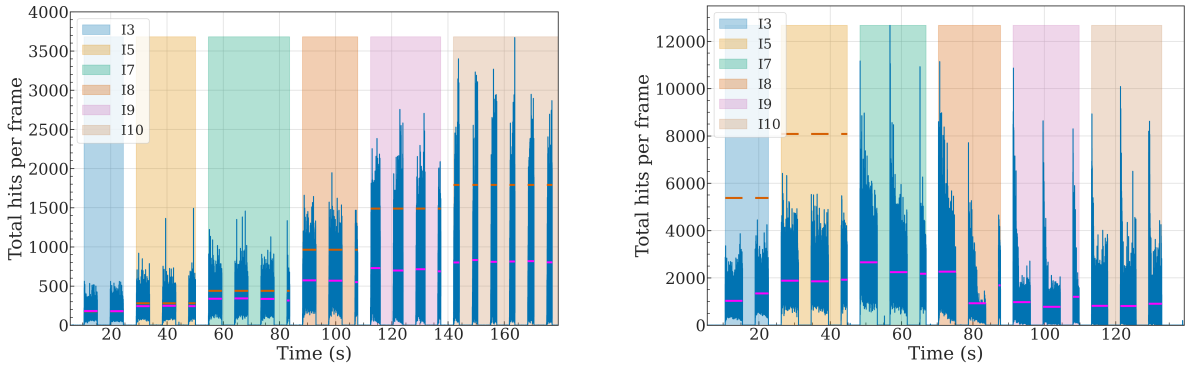


Figure 5.22.: Total number of hits per frame of carbon (left) and proton beams (right) measured using the HitPix2 sensor at different beam intensities. The orange and magenta horizontal lines represent expected and measured ⟨Total hits per frame⟩, respectively. Spills belonging to one beam intensity setting are marked with vertical color bands, as follows: I3 - blue, I5 - orange, I7 - green, I8 - red, I9 - purple, I10 - brown.

6. **Calculate average pixel hit rate** $\langle \text{Hit rate}_{ik} \rangle = \frac{1}{N_{\text{frame}}} \sum_{j=1}^{N_{\text{frame}}} \text{counts}_{ijk}$ for each pixel i and beam intensity k

7. **Simulate expected pixel hit rates in loop of 3000 frames:**
   - **Calculate the number of particles per frame** using a Poisson distribution with average number of particles equals $I_k \cdot t_{\text{frame}}$.
   - **Sample particle positions from the 2D-Gaussian distribution** counts_{ijk} with beam position and size based on $\langle \mu_{\text{x}k} \rangle$, $\langle \mu_{\text{y}k} \rangle$, $\langle \sigma_{\text{x3}} \rangle$, $\langle \sigma_{\text{y3}} \rangle$ and their random variations based on $\sigma_{\mu_{\text{x}k}}$, $\sigma_{\mu_{\text{y}k}}$ and $\sigma_{\sigma_{\text{x3}}}$, $\sigma_{\sigma_{\text{y3}}}$.

8. **Calculate average expected pixel hit rate** $\langle \text{Hit rate}_{ik} \rangle$ over 3000 simulated frames for each beam intensity setting k

For the carbon beam, the expected pixel hit rate was calculated for all intensities based on the beam size estimated at the smallest intensity I3, since the beam size should not change significantly when changing the intensity. However, in the measurement, the pixel hit rate saturation at higher intensities can lead to a beam size overestimation. Therefore, the estimated beam size at high intensities cannot be used for the expected pixel hit rate calculation. For the proton beam, the expected pixel hit rate was calculated based on the nominal beam size of 8.1 mm, because the beam does not fit into the single sensor sensitive area, leading to a beam size underestimation. An example of the measured and expected ⟨Hit rate⟩ distribution across HitPix2 pixels for the carbon beam with intensity I3 is shown in Fig. 5.23. The two distributions are well in agreement, as expected from the integral intensity plot of Fig. 5.22 for the smallest beam intensity setting.
Figure 5.24 shows the measured versus expected ⟨Hit rate⟩ for all measured carbon beam intensity settings. The measured ⟨Hit rate⟩ follows the ideal sensor behavior, represented by a black dashed line, only for the smallest beam intensity I3. Beyond this intensity, measured ⟨Hit rate⟩ saturates and its spread increases. To characterize this distribution, the combined data across all intensities was fitted with Takács' formula [Mül91] and modified Takács' formula [Die+23] given in equations 5.5 and 5.6, respectively:

$$\nu_{\text{meas}} = \frac{\nu \cdot \theta}{e^{\nu \cdot \theta \cdot \tau} + \theta - 1}, \tag{5.5}$$

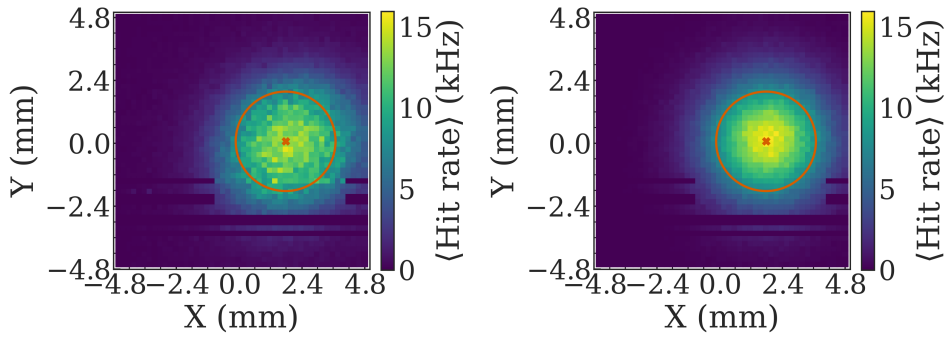


Figure 5.23.: Measured (left) and expected (right) ⟨Hit rate⟩ distribution across HitPix2 pixels for the carbon beam with intensity I3. The orange cross and ellipse represent the estimated beam position and FWHM.

$$\nu_{\text{meas}} = \frac{\epsilon \cdot \nu \cdot \theta}{e^{\epsilon \cdot \nu \cdot \theta \cdot \tau} + \theta - 1}, \tag{5.6}$$

where ν_{meas} is the measured pixel hit rate, ν is the actual pixel hit rate, τ is the pixel dead time (during this time, the pixel is insensitive to subsequent incoming particles), θ is the probability that the pixel dead time is extended by a subsequent incoming particle. A parameter θ of 0 and 1 represents non-paralyzable (dead time is not extended) and the fully paralyzable behavior, respectively. In the modified formula, an additional parameter ϵ was introduced to take into account the detection efficiency of the pixel [Pit22; Die+23]. The detection efficiency, ϵ, can be affected by factors such as misconfigured pixel electronics (a high threshold voltage `bias-DAC.Vth`, small CSA gain etc.) or radiation damage of the sensor, which reduces the measured pixel hit rate. When ϵ is set to 1, the modified equation converges to the original form.
The obtained fit parameters of carbon beam measurements for the original and modified Takács' formulas are in good agreement and are detailed in table 5.8.

Table 5.8.: Fit parameters for the original and modified Takács' formulas for the HitPix2 sensor in 430.10 MeV u^{-1} carbon beam measurements. The R^2 stands for the coefficient of determination of the fit.

Formula type	ϵ	θ	τ (µs)	R^2
Original	1	0.00 ± 0.01	17.44 ± 0.01	0.953
Modified	0.965 ± 0.003	0.00 ± 0.01	16.90 ± 0.15	0.953

The detection efficiency parameter ϵ is very close to the 1 efficiency of the original equation. This meets the expected behavior, since the carbon ions induce a high ionization signal in the pixel readout circuit, leading to a CSA output saturation (covered in subsection 5.4.2), thus the signal will be detected with a very wide range of the pixel thresholds. The large pixel dead time was unexpected, but can be explained by the long saturated CSA output signals in response to large ionization signals induced by carbon ions, as will be shown in next subsection 5.4.2. The zero value for the probability of the dead time extension is expected, due to a low expected pixel hit rate across a wide range of carbon beam intensities. A more detailed explanation is also given in the next subsection 5.4.2.

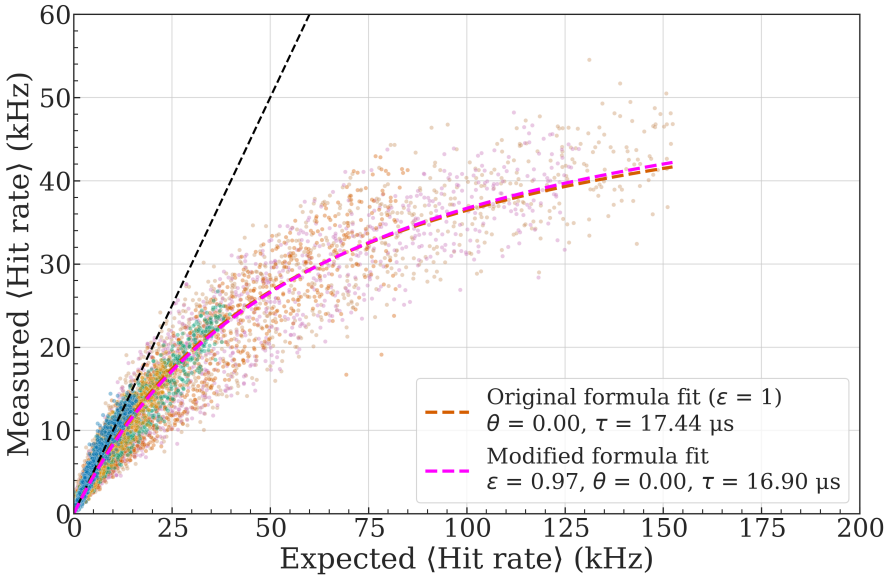


Figure 5.24.: Measured versus expected pixel ⟨Hit rate⟩ of a HitPix2 sensor at different carbon beam intensities. The black dashed line represents the ideal sensor behavior with zero dead time and 100 % detection efficiency. The orange and magenta dashed lines represent the fit curve of original and modified Takács' formula, respectively. Points are colored w.r.t. beam intensity: I3 - blue, I5 - orange, I7 - green, I8 - red, I9 - purple, I10 - brown.

The measured versus expected ⟨Hit rate⟩ for the proton beam is shown in Fig. 5.25. Data is shown only up to intensity I7 due to the high-voltage compliance issue described previously. The spread of the measured points is larger than that observed in the carbon beam results, even at intensity I3. The fit of the the original and modified Takács' formulas applied to the proton beam measurements yielded the values presented in table 5.9.

Table 5.9.: Fit parameters for the original and modified Takács' formulas for the HitPix2 sensor in 221.06 MeV u^{-1} proton beam measurements. The R^2 stands for the coefficient of determination of the fit.

Formula type	ϵ	θ	τ (µs)	R^2
Original	1	0.00 ± 0.01	22.43 ± 0.05	0.419
Modified	0.26 ± 0.01	1.00 ± 0.36	5.68 ± 0.55	0.757

The original Takács' formula provides a poorer fit to the data compared to the modified formula, due to the high threshold voltage of the sensor, which reduces the detection efficiency, ϵ to 0.26. Across all beam settings at HIT, the 221.06 MeV u^{-1} proton beam produces the smallest ionization signal, making its detection the most sensitive to threshold voltage misconfiguration. To confirm this, an additional measurement was performed using a 156.35 MeV u^{-1} proton beam, which induces larger ionization signals than 221.06 MeV u^{-1} proton beam. The results are shown in the Appendix in Fig. B.3. For this measurement, the ϵ parameter increased to 0.45 ± 0.01, confirming the initial suggestion of the threshold voltage misconfiguation. It is important to note that at a beam energy of 156.35 MeV u^{-1} the nominal beam size increases to 10.8 mm, reducing the expected ⟨Hit rate⟩.

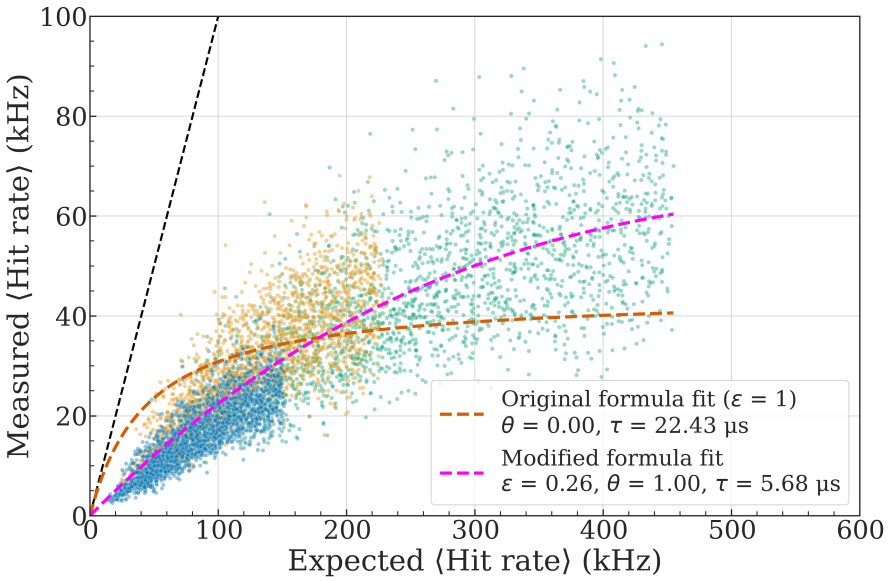


Figure 5.25.: Measured versus expected pixel ⟨Hit rate⟩ of a HitPix2 sensor at different proton beam intensities. The black dashed line represents the ideal sensor behavior with zero dead time and 100 % efficiency. The orange and magenta dashed lines represent the fit curve of original and modified Takács' formula, respectively. Points are colored w.r.t. beam intensity: I3 - blue, I5 - orange, I7 - green.

Compared to the results of the carbon beam, the dead time τ is reduced to 5.68 µs and the pixel behavior is changed from non-paralyzable to fully paralyzable. To explain these results, additional measurements were conducted and presented in subsection 5.4.2.

5.4.2. Pileup and Baseline drop effects

The normal operational mode of the in-pixel electronics during the hit counting is described in subsection 5.1.2 and shown in the left sketch of Fig. 5.26. When a charged particle hits the pixel, the induced signal amplified with CSA is compared with the threshold value `bias-DAC.Vth` $- V_{\mathrm{bl}}$, resulting in the comparator output binary signal. The comparator output transits into a logic low state only when the signal amplitude becomes lower than the threshold value. Therefore, during the time when the comparator is in a logic high state, it cannot detect consecutive signals. In the same sketch, the comparator output signal duration for the large signal is longer than for the small one. This effect explains different dead times τ measured with carbon and proton beams and presented in the previous subsection 5.4.1: the signals induced by carbon ions are larger and longer than the signals induced by protons, leading to a higher τ values.

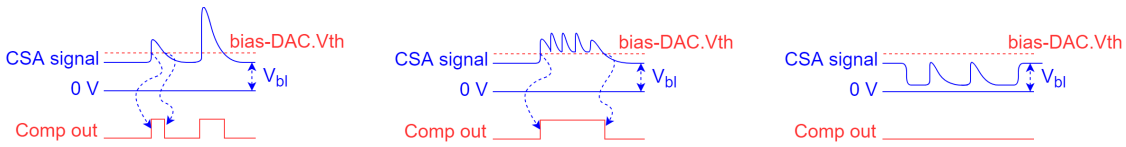


Figure 5.26.: In-pixel CSA and comparator operation. Normal mode (left), pileup (center), baseline drop (right).

The pileup effect occurs when several consecutive particles hit the pixel before the CSA output signal becomes lower than the threshold value, extending the duration of the comparator in the logic high state and reducing the number of detected particles, as shown in the central sketch of Fig. 5.26. This explains the change of the pixel behavior from non-paralyzable (carbon beam) to fully paralyzable (proton beam), since the proton beam intensity is 40 times higher than that for the carbon beam at the same setting, as shown in table 5.7. Taking into account the different beam areas at the minimal nominal focus and maximum energy settings leads to approximately seven times higher expected pixel hit rate for the proton beam at the same intensity setting.
Additional loss of detected particles may occur, if the DC baseline voltage V_{bl} drops its level and the signal amplitude is not high enough to compensate this drop, as shown in the right sketch of Fig. 5.26.
To find the origin of the observed counting limitation of the HitPix2 sensor, the direct measurements of the CSA output signals were performed using the proton and carbon beams. Output signals from the selected pixel were measured with an oscilloscope in AC mode and analyzed offline. Examples of such waveforms are shown in Fig. 5.27 and Fig. 5.28.

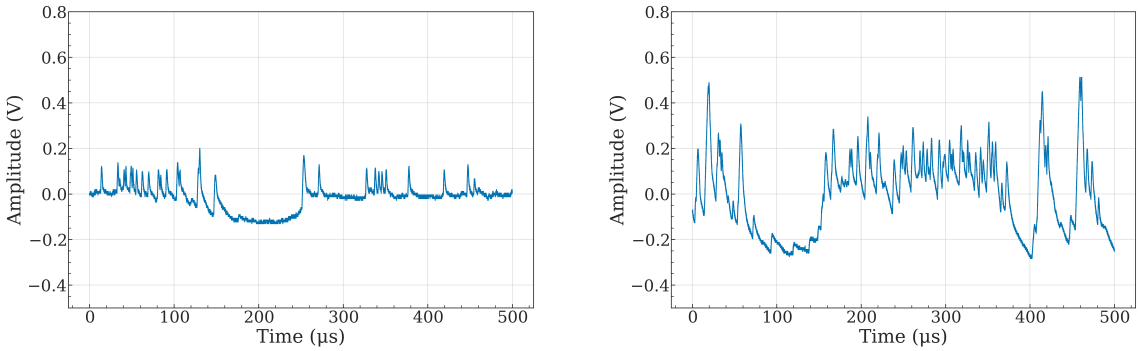


Figure 5.27.: Measured HitPix2 pixel CSA output signals using proton beams with intensities I3 (left) and I7 (right).

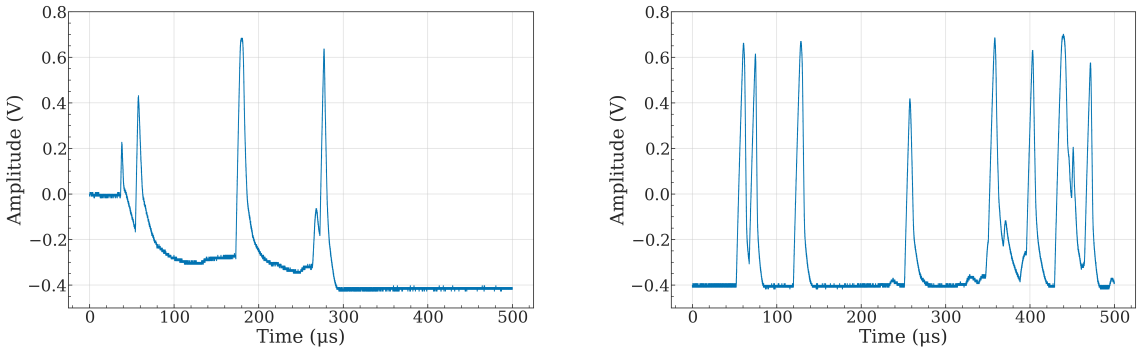


Figure 5.28.: Measured HitPix2 pixel CSA output signals using carbon beams with intensities I3 (left) and I7 (right).

A comparison of these waveforms revealed that carbon ions induce the deepest and longest baseline drops. The duration of saturated output CSA signals for carbon ions varies in the approximate range from 13 µs to 23 µs, which is well in agreement with the fitted dead time parameters for the original and modified Takács' formulas, discussed in the previous subsection. However, the large signal amplitude partially compensates for the baseline drop effect. Consequently, the measured points have less spread in Fig. 5.24 compared to Fig. 5.25.

Beyond carbon beam intensity I7 the spread of measured points and curve saturation increases with the intensity due to pileup events, when the maximum expected pixel hit rate becomes comparable with the signal duration (80 kHz or 12.5 μs^{-1} for beam intensity I8).
A typical duration of the proton signals lies in the approximate range from 3 µs to 4 µs, which is also well in agreement with the fitted dead time parameter for the modified Takács' formula. Proton-induced baseline drops have smaller magnitudes, but their influence on the measured pixel hit rate is larger due to the smaller signal amplitude. At higher intensities, the signal pileup becomes visible, confirming the change to fully paralyzable behavior. Additionally, the wide pixel threshold distribution, shown in Fig. 5.12, leads to a difference in pixel responses on the same ionization signal. This difference is negligible for the large carbon ion signals, but significant for protons. These three factors together with misconfigured threshold voltage explain the lower efficiency value ϵ and wider spread of measurement points compared to carbon beams.
Different strategies should be used to improve the sensor performance in carbon and proton beams. For the carbon beam, the dead time τ can be reduced by increasing the comparator threshold (by increasing `bias-DAC.Vth` and/or reducing V_{bl}). This also allows to partially mitigate the pileup effect, since the signal amplitude will require less reduction and time to exit the comparator logic high state. For the proton beam, the comparator threshold should be lowered to increase efficiency ϵ. The pileup effect at high beam intensities cannot be mitigated with this technique and will require changes in the pixel circuits in next HitPix3 sensor. This can include a switched reset in a CSA feedback circuit, presented in [Zha21] to shorten the CSA output signals and restore the baseline faster. Two additional questions should be investigated for the new sensor design: is the HitPix2 pixel hit rate limited to ∼80 kHz without baseline drop? And, which part of the sensor is responsible for the baseline drop effect? Dedicated measurements to address these questions are presented in subsections 5.4.3 and 5.4.4.

5.4.3. Infrared LED measurements

The baseline drop effect, previously observed in measurements with the HitPix2 CSA output, occurs when highly ionizing particles traverse the pixel. Furthermore, a larger ionization signal causes a more severe baseline alteration. To test the pixel hit rate capability without the baseline drops, photons can be used. For this purpose, a universal Infrared Light-Emitting Diode (IR LED) with wavelength of ∼940 nm and IR LED of the Karlsruhe Infrared Array (KIRA) device with a wavelength of ∼950 nm, developed by J. Braach within the scope of his master's thesis [Bra20], were used. Their light pulse frequency was controlled by an external voltage signal generator and was verified with an Optical-to-Electrical converter (two example waveforms are shown in the Appendix in Fig. B.4). During the measurements, the IR LED was positioned above a single HitPix2 sensor, without any optical fiber. The universal IR LED was used only up to light pulse frequency of 200 kHz and KIRA device was used to cover frequencies from 300 kHz to 600 kHz.
During the low frequency measurement, the sensor frame duration t_{frame} was set to 200 µs, whereas in the high frequency measurement it was reduced to 50 µs to prevent an overflow of the pixel counters. Both measurements were performed at room temperature. Noisy pixels were masked during the analysis.
Figure 5.29 shows examples of ⟨Hit rate⟩ distributions across pixels for 200 kHz light pulse frequency of the universal IR LED (left plot) and for 600 kHz light pulse frequency of KIRA IR LED (central plot).
The measured profile of the universal IR LED is homogeneous and has a round shape, since the IR LED was not collimated. In contrast, the profile of the IR LED of KIRA has a homogeneous center and truncated edges, due to the aluminum aperture frame [Bra20], which is not ideally

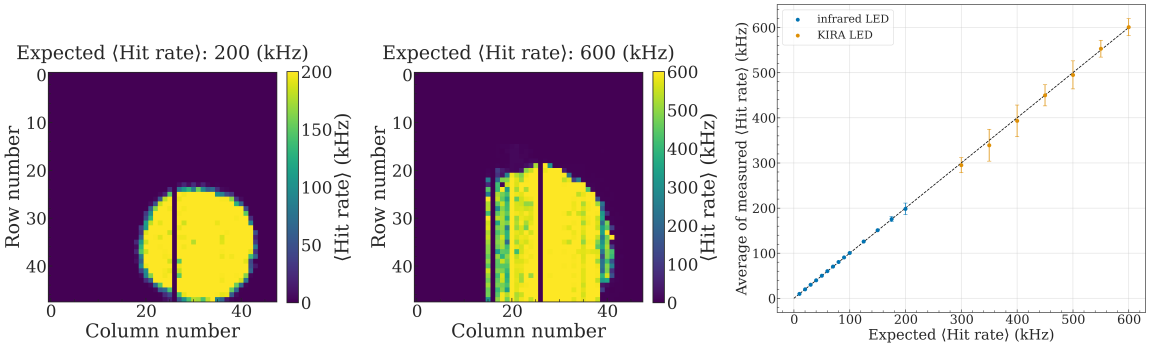


Figure 5.29.: An example of ⟨Hit rate⟩ distributions across pixels using the 200 kHz light pulses from universal IR LED (left) and 600 kHz light pulses from KIRA IR LED (center). The average of measured ⟨Hit rate⟩ is shown versus the expected ⟨Hit rate⟩ (right) using the IR LED (blue points) and the KIRA LED (orange points). The error bars represent the standard deviation of measured ⟨Hit rate⟩. The black dashed line represents the ideal sensor response.

centered w.r.t. all IR LEDs placed on the PCB carrier. The measured ⟨Hit rate⟩ of pixels in the homogeneous part of both profiles were averaged for each light pulse frequency and plotted against the expected ⟨Hit rate⟩. The results are shown in the right plot of Fig. 5.29. The measured points lie in good agreement with the ideal sensor response, shown as a black dashed line, up to measured light pulse frequency of 600 kHz. These results confirm that the HitPix2 pixels are capable to detect particles at high hit rate, if the pileups and baseline drop effect are excluded. Examples of measured CSA output signals under KIRA IR LED illumination at frequencies of 400 kHz and 600 kHz are shown in the Appendix in Fig. B.4. No baseline drop and pileups were observed during these measurements.

5.4.4. Proton microbeam test

To map the in-pixel signal response with $\mathcal{O}(\mu m^2)$ resolution and an associated signal processing circuitry responsible for the baseline drop effect, in-air proton microbeam irradiation was performed at the Ruđer Bošković Institute [Jak+16]. A photograph of the experimental setup, consisting of the single HitPix2 sensor carrier connected to the DAQ system and positioned next to the microbeam nozzle, and a schematic overview of the measurement procedure are shown in Fig. 5.30.

As described in [Top+24], a grid scan, with 50 µm steps, was performed by translating the sensor under test around the proton mircobeam with a reproducible intensity of 1400 pps, energy of 3 MeV and size of 10 µm × 10 µm. The sensor position along the Z-axis was manually adjusted to minimize the distance between sensor and beam nozzle, reducing beam scattering and energy loss in air. To find the measurement start position, shown in Fig. 5.30, the sensor was adjusted along the X- and Y-directions with the step motors of the mechanical stage and monitoring the pixel hit counts in the readout software, simultaneously.

At each beam position, the modes of the CSA output signal and baseline drop frequencies (f_{drop}) were recorded from three adjacent pixels over ten waveforms using an oscilloscope configured in AC mode [Top+24]. It measured the frequency f_{drop} of baseline drops with a magnitude larger than 100 mV.

Figure 5.31 shows an example of f_{drop} for a single HitPix2 pixel as a function of beam position (after linear interpolation). The green, magenta and yellow boxes represent the approximate locations of the sensor diode, analog and digital electronics of the pixel. The high f_{drop} region

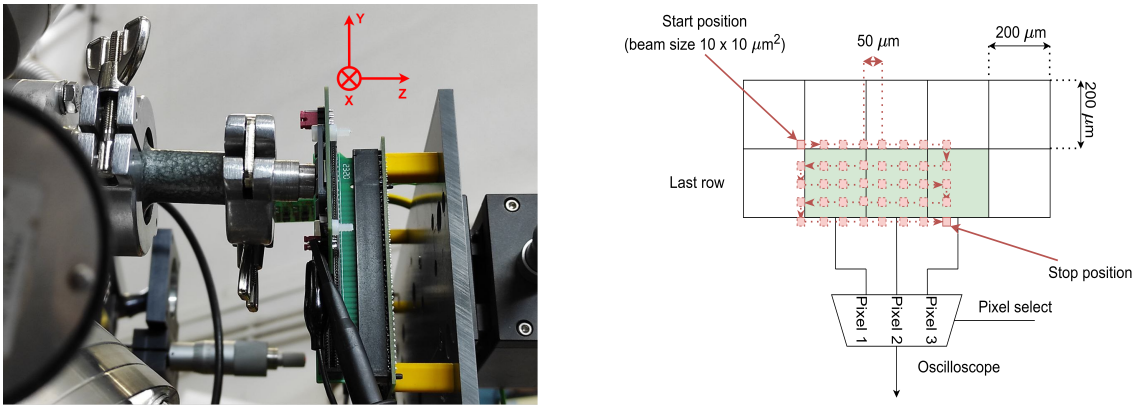


Figure 5.30.: Microbeam nozzle and HitPix2 sensor carrier (left) and pixels scanning procedure (right). From [Top+24]

is approximately rectangular, with dimensions of 200 µm × 100 µm, partially covering the sensor diode and the transition region between the diode and the in-pixel electronics [Top+24].

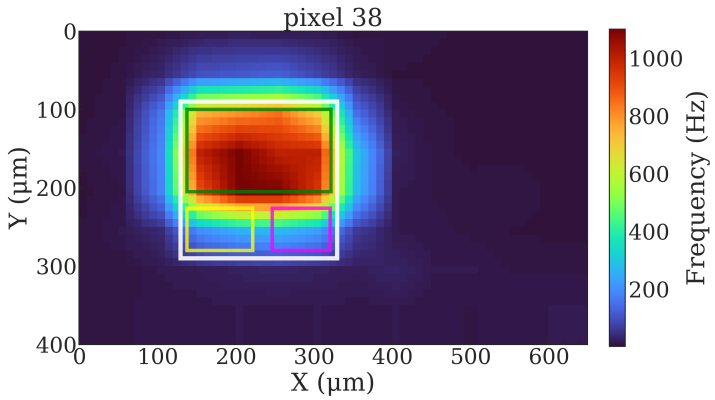


Figure 5.31.: Linearly interpolated f_{drop} map for a single HitPix2 pixel with approximate locations of sensor diode, analog and digital electronics outlined with the green, magenta and yellow boxes, respectively. Data for the plot are taken from [Top+24]

To test the different pixels topologies against the baseline drop effect, the HitPix1 and HitPix2 sensors were measured at the microbeam setup. The HitPix1 were produced in two versions: with separated n-well (STD) and isolated p-well (ISO) pixel topologies and pMOS-based CSA circuit [Web21]. As described in section 5.1, the HitPix2 pixel was designed with a separated n-well topology and nMOS-based CSA circuit [Web21].
Table 5.10 summarizes measurement results across all tested HitPix sensors. Despite the significantly lower particle hit rate compared to HIT conditions, the 3 MeV protons induced a large ionization signals. This resulted in a baseline drop occurring for almost every incident proton on a HitPix2 pixel, confirming the dependence of the baseline drop on ionization signal strength. While the measurements of HitPix1 confirmed the baseline drop location, they also demonstrated a greater tolerance to this effect, especially with the ISO pixel topology. The maximum baseline drop frequency observed for HitPix1 was significantly lower than that for HitPix2 [Top+24].
From these results, it can be concluded that the HitPix3 pixel design should be based on the ISO topology and the HitPix1 CSA design.

Table 5.10.: The f_{drop} for different HitPix versions in 3 MeV proton microbeam. Data for the table are taken from [Top+24].

Sensor	Pixel	CSA type	I_{beam} (pps)	Min. f_{drop} (kHz)	Max. f_{drop} (kHz)
HitPix2	STD	nMOS	1.4×10^3	0.90 ± 0.07	1.10 ± 0.07
HitPix1	STD	pMOS	1.4×10^3	0.10 ± 0.02	0.20 ± 0.02
HitPix1	ISO	pMOS	1.4×10^3	0.0	0.0

5.5. Radiation hardness

The final beam monitoring system will be used for direct beam parameters tracking, therefore, it will be subject to significant radiation damage with the estimated 1 MeV neutron equivalent fluence per year of $\sim 1 \times 10^{15}\,\text{cm}^{-2}$, as discussed in section 4.1. Hence, the sensors must remain operational at this fluence. As discussed in section 3.5, the silicon detector performance after radiation damage depends on the initial doping type of the substrate and its resistivity. To find the optimal substrate resistivity for the next HitPix3 sensor, HitPix2 sensors were produced on three *p*-type substrates with resistivities of 20 Ω cm, 300 Ω cm and 5000 Ω cm. Samples with these resistivities were homogeneously irradiated with a 23 MeV proton beam at Zyklotron AG (ZAG) [ZAG25] to a 1 MeV neutron equivalent fluence of approximately $1 \times 10^{15}\,\text{cm}^{-2}$. Another negative effect of radiation damage is an increase in the detector leakage current, as discussed in section 3.5. Since the leakage current is temperature dependent, it is important to determine the optimal working temperature with the minimal material budget constraints defined in section 4.1. The unirradiated and irradiated HitPix2 sensors were tested with carbon beams at different sensor temperatures during the beam test at HIT in June 2023.

5.5.1. Experimental setup

The unirradiated and irradiated HitPix2 sensors are mounted on single sensor PCB carriers. Therefore, the measurement of several sensors at different temperatures will require several cycles of cooling for each sensor. To optimize this process, a multi-carrier board was designed and produced. The PCB layout and 3D render of the board are shown in Fig. 5.32. Three single sensors can be read out by plugging them into the PCIe x8 slots on the board. Furthermore, the bias voltage is applied through the individual traces, allowing independent I-V measurements of the connected sensors. Hence, the multi-carrier board reduces the amount of required temperature cycles by a factor of three, since three sensors can be measured at the same temperature. To ensure compatibility with the existing DAQ system, the board contains a custom PCIe x16 connector compatible with the GECCO board. A photograph of the multi-carrier board populated with HitPix2 sensors is shown in Fig. 5.33 on the right.
Due to material budget constraints discussed in 4.1, the final beam monitoring system cannot use a thermoelectric cooler. Therefore, a first prototype of cooling setup for irradiated sensors was designed to test the sensor cooling via convection with a gas stream. In this setup, a cooling and thermally insulated box (designed by R. Koppenhöfer), containing the multi-carrier board, is connected to a vortex tube. The vortex tube supplies cooled gas to the box, by separating the compressed gas into hot and cold streams using a spinning vortex [Hil47]. The temperature inside the box is controlled by the flow of the compressed gas, i.e. by increasing the flow the temperature becomes lower.
The experimental setup installed at the HIT beamline is shown in Fig. 5.33 on the left. The cooling box with the populated multi-carrier board (marked as 1 in the figure) is connected to the GECCO and FPGA boards (marked as 2 in the figure). The vortex tube is connected to

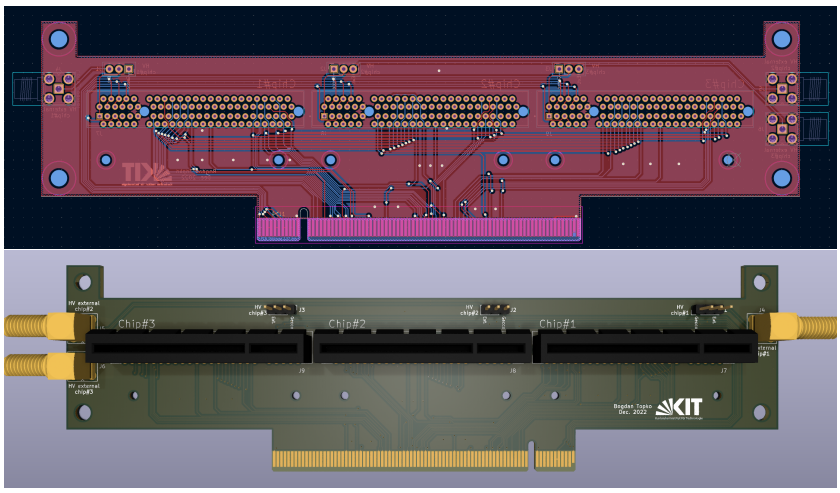


Figure 5.32.: Multi-carrier board PCB layout (top) and its 3D render (bottom).

the bottle of pressurized nitrogen gas (marked as 4 in the figure). The temperature inside the cooling box was set by manually adjusting the nitrogen flow via the valve on the gas bottle. The temperature inside the cooling box was monitored with the temperature sensor inside it. The sensor under test was remotely positioned to the beam isocenter with step motors of the mechanical stage (marked as 3 in the figure).

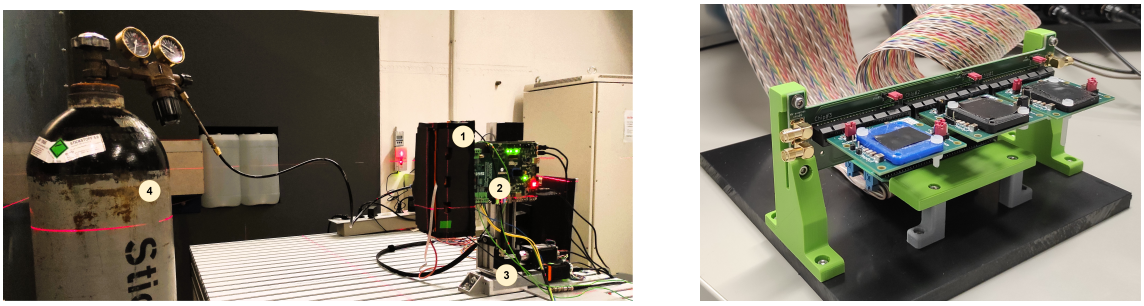


Figure 5.33.: Irradiated sensors inside the cooling box at the isocenter of HIT beamline (left). 1 - cooling box with the populated multi-carrier board, 2 - FPGA and GECCO boards, 3 - mechanical stage, 4 - bottle with pressurized nitrogen. Photograph of multi-carrier board populated with three HitPix2 sensors (right).

5.5.2. I-V measurements

During the beam test, one slot of the multi-carrier board was occupied with a sensor with mounted temperature sensor to its surface. It was used to measure the reference temperature T_{ref}. Two other slots were occupied by sensors under test. To determine their actual temperature T_{IV}, the I-V measurement of tested sensors was conducted before measurement with a carbon beam [Top+24]. The measured I-V curves of all tested samples at different temperatures are shown in Fig. 5.34.

The T_{IV} was calculated by numerically solving the equation which describes the ratio between leakage currents of a silicon detector at two different temperatures, taken and adapted from [Spi05], as given in equation 5.7:

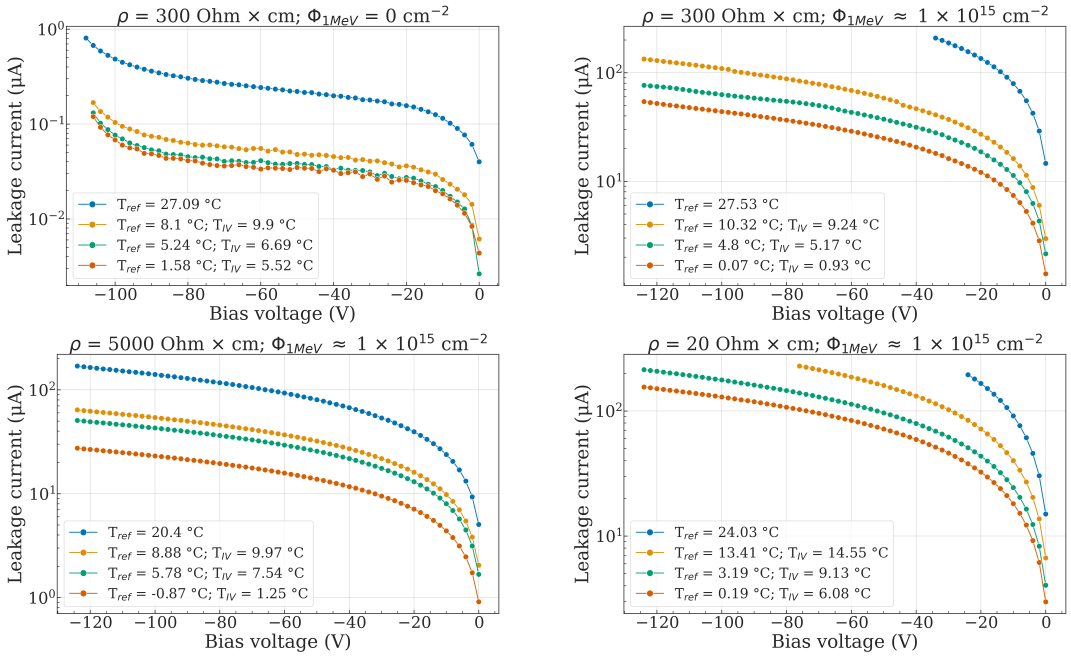


Figure 5.34.: I-V curves (leakage currents are given in absolute values) of reference unirradiated sensor with a resistivity of 300 Ω cm (top left) and irradiated sensors with the resistivities of 300 Ω cm (top right), 5000 Ω cm (bottom left), and 20 Ω cm (bottom right) at different temperatures. Data for the plot are taken from [Top+24].

$$\frac{I_{\text{leak}}(T_{\text{IV}})}{I_{\text{leak}}(T_{\text{ref0}})} = \left(\frac{T_{\text{IV}}}{T_{\text{ref0}}}\right)^2 \exp\left[-\frac{E}{2k}\left(\frac{T_{\text{ref0}} - T_{\text{IV}}}{T_{\text{ref0}} \cdot T_{\text{IV}}}\right)\right], \tag{5.7}$$

where $I_{\text{leak}}(T_{\text{IV}})$ and $I_{\text{leak}}(T_{\text{ref0}})$ are leakage currents of the silicon detector measured at temperatures T_{IV} and T_{ref0} and fixed bias voltage, respectively, T_{ref0} is the temperature of the reference sensor measured without cooling, E is the effective activation energy of 1.21 eV and k is the Boltzmann constant. The lowest achieved temperature for the tested sensors is detailed in table 5.11. The large variation across the temperature values was caused by the manual control over the gas flow.

Table 5.11.: The lowest achieved temperature for the tested unirradiated and irradiated HitPix2 sensors during the beam test at HIT.

ρ (Ω cm)	Φ_{eq} (cm^{-2})	T_{IV} (°C)
300	0	5.5
300	$\sim 1 \times 10^{15}$	0.9
5000	$\sim 1 \times 10^{15}$	1.3
20	$\sim 1 \times 10^{15}$	6.1

5.5.3. Detection efficiency

The low intensity (I3, 5×10^6 pps) carbon beam was used to estimate the changes in the sensor performance after radiation damage for different substrate resistivities, since the measurements presented in section 5.4 showed that the unirradiated HitPix2 sensor follows the ideal sensor behavior for this beam configuration. The nominal beam energy was varied in the range from 108.53 MeV u^{-1} to 423.44 MeV u^{-1}, while the beam size (FWHM) was adapted w.r.t. energy to stay within the range from 8.0 mm to 9.0 mm. The data from irradiated HitPix2 sensors measured at the lowest achieved temperatures T_{IV}, showed in the previous subsection, were compared with the data from unirradiated HitPix2 sensor measured at room temperature.

The following parameters of all sensors were fixed in all measurements: $V_{\mathrm{bias}} = -100$ V, $V_{\mathrm{dda}} = 1.85$ V, $V_{\mathrm{bl}} = 1.10$ V and $t_{\mathrm{frame}} = 350$ µs. The threshold voltage parameter was set to 168 DAC units for all sensors, except irradiated HitPix2 with a resistivity of 300 Ω cm. For this sensor the threshold voltage was set to 174 DAC units. However, due to the high ionization signal of the carbon ions on the order of hundreds of thousands of electrons, this small difference in threshold voltage will not influence the performance comparison among irradiated sensors.

The performance analysis is based on the relative comparison of ⟨Hit rate⟩ of unirradiated and irradiated sensors. To avoid the bias in the analysis caused by noisy pixels, the measurements without beam were performed to identify and exclude them from the analysis. If the pixel ⟨Hit rate⟩ was greater than 0.14 kHz (which corresponds to ∼5 % of expected ⟨Hit rate⟩ in the beam center) it was marked as noisy. It is important to note that the noisy pixels were fully functional, but required higher threshold value, becoming a limiting factor for small signal detection. The fraction of masked pixels for each irradiated sample was found to be 26.9 % (300 Ω cm), 17.3 % (5000 Ω cm), and 34.3 % (20 Ω cm) [Top+24].

Figure 5.35 shows the measured ⟨Hit rate⟩ distributions of the unirradiated reference sensor with a resistivity of 300 Ω cm and the irradiated sensor with a resistivity of 300 Ω cm using the carbon beams with different energies. For illustrative purpose, only eight out of eighteen measured beam energies are plotted. The measurement results for sensors with resistivities of 5000 Ω cm and 20 Ω cm can be found in the Appendix in Fig. B.5 and Fig. B.6, respectively.

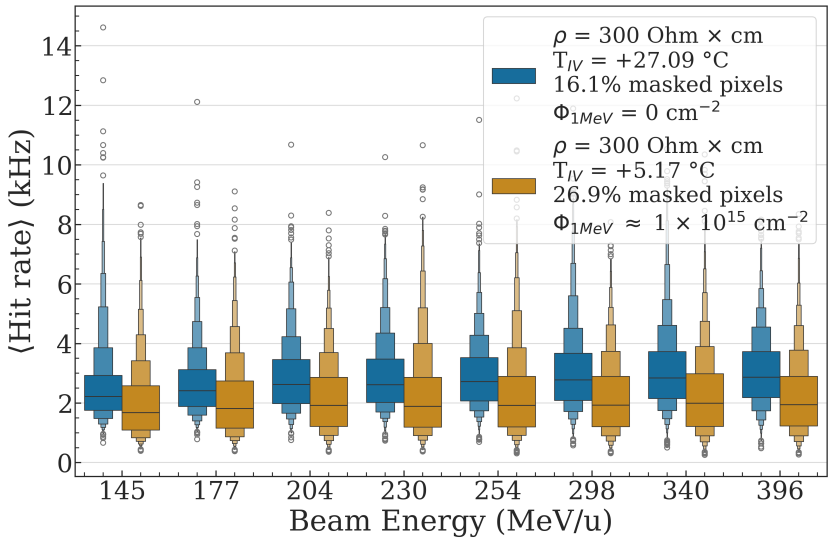


Figure 5.35.: Measured ⟨Hit rate⟩ distributions of reference unirradiated sensor with resistivity of $\rho = 300\,\Omega\,\mathrm{cm}$ (blue) and irradiated sensors with $\rho = 300\,\Omega\,\mathrm{cm}$ (orange) using the carbon beams with different energies. The beam size (FWHM) was adapted w.r.t. the beam energy to stay within the range from 8.0 mm to 9.0 mm.

The distributions of unirradiated and irradiated sensors have similar shapes with shifted median values. Therefore, these values were compared to quantify the changes in the sensor performance after irradiation, i.e. the detection efficiency of irradiated sensors were calculated with the equation 5.8 [Top+24]:

$$\text{Efficiency} = 100\% \cdot \frac{\text{median}(\{\langle \text{Hit rate} \rangle_{j,\text{irrad}} | j \not\subset \text{noisy}\})}{\text{median}(\{\langle \text{Hit rate} \rangle_{k,\text{unirrad}} | k \not\subset \text{noisy}\})} \tag{5.8}$$

The 100 % efficiency corresponds to the median value of the ⟨Hit rate⟩ distribution measured with unirradiated sensor. Figure 5.36 shows the calculated efficiencies for three irradiated samples. All three curves follow the same trend: as the beam energy increases, the efficiency decreases due to a reduction of the ionization signal at the fixed threshold voltage. The calculated efficiency of the irradiated sensor with a resistivity of 300 Ω cm is the highest across all measured samples even with its slightly higher threshold voltage compared to the other two irradiated sensors. This further confirms that the strong ionization signals from carbon ions are not affected by small variations in threshold voltage.
Based on these results, it can be concluded that the HitPix3 sensor should be produced on 300 Ω cm resistivity substrate. To address the large faction of noisy pixels, an individual pixel threshold tuning circuitry should be added to each HitPix3 pixel [Top+24].

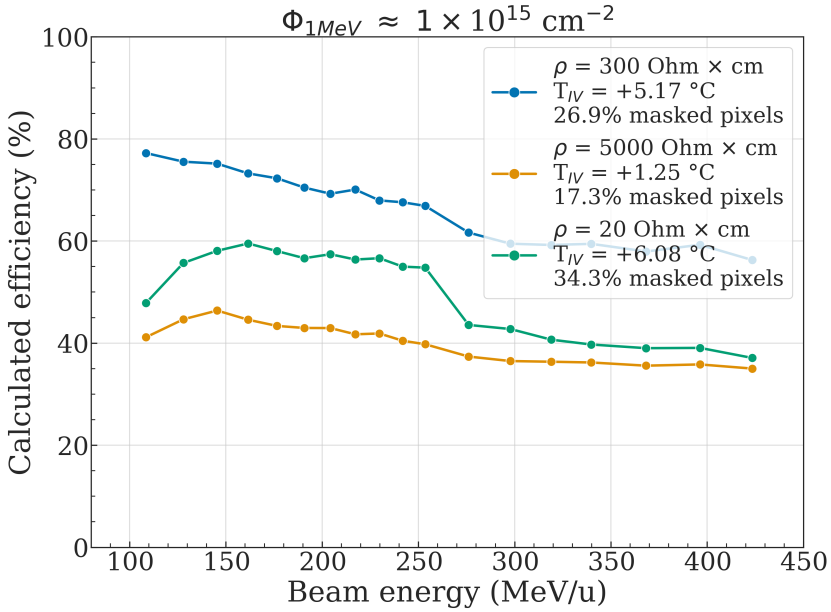


Figure 5.36.: Calculated detection efficiency of cooled irradiated samples measured using the carbon beams with different energies. The beam size (FWHM) was adapted w.r.t. the beam energy to stay within the range from 8.0 mm to 9.0 mm. Data for the plot are taken from [Top+24]

5.5.4. Estimation of the tune voltage range for the pixel threshold

Previous measurements revealed that an individual pixel threshold tuning mechanism is required in the HitPix3 design to reduce the fraction of noisy pixels, which caused by the wide threshold variations of the unirradiated sensors (section 5.2), and by the increased pixel noise after significant radiation damage (subsection 5.5.3). The pixel threshold tuning could be realized by introducing a small DAC block inside the pixel, which generates an additional DC voltage offset to be added to `bias-DAC.Vth` that is common to all pixels [Per+21].

To determine the output voltage range of this DAC block, a set of frames without radioactive source was measured with unirradiated and irradiated HitPix2 sensors with 300 Ω cm substrate resistivity at different `bias-DAC.Vth` values and temperatures. Measurements were conducted in the climatic chamber setup, shown in Fig. 5.37.

For these measurements, the following parameters were fixed for all sensors: $V_{\text{bias}} = -50\,\text{V}$, $V_{\text{dda}} = 1.85\,\text{V}$, $V_{\text{bl}} = 1.10\,\text{V}$. The frame duration t_{frame} was set to 100 µs. The temperature inside the climatic chamber varied from 10 °C to −20 °C for the measurements with the irradiated sensor. During the analysis, the comparator threshold values were converted to voltage units by equation 5.9.

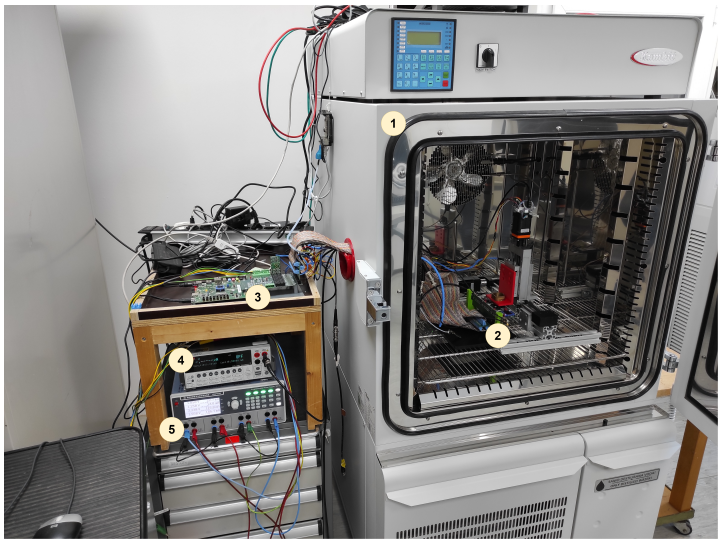


Figure 5.37.: Climatic chamber setup. 1 - climatic chamber, 2 - multi-carrier board, 3 - GECCO and FPGA boards, 4 - HV power supply, 5 - LV power supply.

$$\text{Comparator threshold} = \frac{\text{biasDAC.Vth}}{255} \cdot V_{\text{dda}} - V_{\text{bl}} \tag{5.9}$$

Dependencies of the fraction of noisy pixels (as defined in previous subsection) on the comparator threshold for unirradiated HitPix2 sensor at room temperature and irradiated HitPix2 sensor at different ambient temperatures are shown in Fig. 5.38. The fraction of noisy pixels of the irradiated sensor at the given comparator threshold decreases with lower ambient temperature, as expected. The comparator thresholds at which the fraction of noisy pixels is maximized are shown as vertical black dashed lines. The vertical colored dashed lines represent the comparator thresholds for which the fraction of noisy pixels is less than 1 % at the corresponding ambient temperature. Therefore, the tune voltage range is defined as the difference between these comparator values. The tune voltage range of the unirradiated sensor is approximately of 108 mV, while for the irradiated sensor it decreases from approximately 276 mV to 131 mV with decreasing ambient temperature from 10 °C to −20 °C.

Consequently, the output voltage range of the foreseen in-pixel DAC tune block should at least cover 300 mV to reduce the fraction of noisy pixels to less than 1 % at the foreseen working temperature range from 0 °C to 5 °C for the final beam monitoring system.

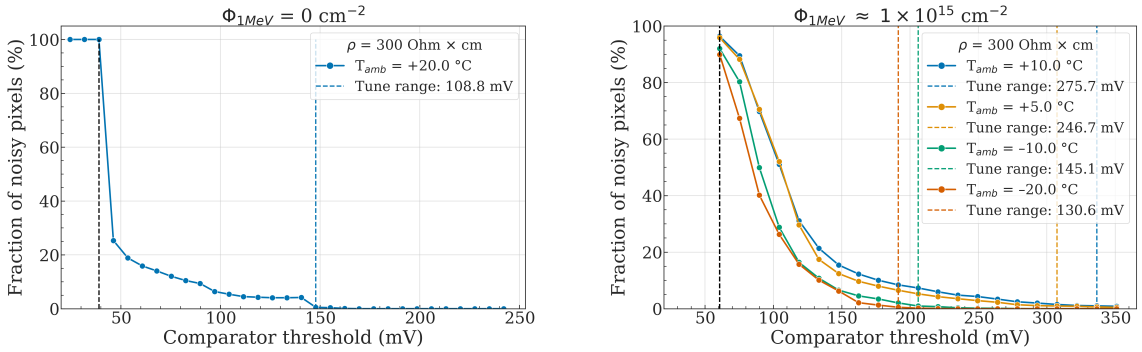


Figure 5.38.: Dependence of the fraction of noisy pixels on comparator threshold for unirradiated at room temperature (left) and irradiated (right) HitPix2 with a resistivity of 300 Ω cm sensors at different ambient temperatures: 10 °C (blue points), 5 °C (orange points), −10 °C (green points) and −20 °C (red points). The vertical black dashed lines represent the comparator threshold for which the fraction of noisy pixels is maximized. The vertical colored dashed lines represent the comparator threshold for which the fraction of noisy pixels is less than 1 % at the corresponding ambient temperature.

5.6. Summary

The studies presented in this chapter focused on characterizing the HitPix2 monolithic pixelated HV-CMOS sensor and resolving its operational issues in preparation for the next HitPix3 design.

The characterization campaign was carried out to select valid sensors for multi-sensor assemblies. The characterization process included tests of different functional parts of the sensor. The campaign revealed a production yield of 34 %. Problems with the in-pixel electronics were identified as the primary source for sensor malfunction.

A set of valid sensors which passed all tests was used to build the matrix prototype, consisting of two rows of five sensors each. The daisy chain architecture was used to read out and configure sensors within a row. Comparative measurements of beam spot profiles, measured at various focus settings using the existing ISO-MWPC detector and the prototype matrix, confirmed that the HitPix2-based matrix meets HIT requirements for beam position and size reconstruction. Furthermore, the readout speed limit of the matrix prototype demonstrated that all HitPix3 control and readout signal buffers should be redesigned according to the LVDS standard to overcome this limitation.

The previously observed limitation of the HitPix2 counting capability at high-intensity proton and carbon beams [Pit22; Die+23] were confirmed with new measurements. The pixel CSA output measurements at different ion beams attributed the origin of this limitation to pileup and baseline drop effects. Therefore, to mitigate the pileup effect, a switch-reset circuit should be introduced to the HitPix3 pixel circuitry.

Measurements with IR LEDs confirmed that the HitPix2 sensor is capable of detecting particles at high rates without saturation, if the pileup and baseline drop effects are excluded. Moreover, the scanning of single HitPix2 pixels with a proton microbeam narrowed the region responsible for the baseline drop effect to 200 µm × 100 µm size, which partially covers the sensor diode and transition area between the diode and the in-pixel electronics. Additional microbeam measurements with HitPix1 sensors revealed the highest tolerance to the baseline drop effect of HitPix1 sensors with ISO topology and pMOS-based CSA. Therefore, the HitPix3 pixel should inherit these parts of HitPix1 design.

The radiation damaged HitPix2 sensors with different substrate resistivities were uniformly irradiated to 1 MeV neutron equivalent fluence of $\sim 1 \times 10^{15}\,\mathrm{cm}^{-2}$ and used to determine the optimal substrate resistivity in terms of radiation hardness. From the carbon beam measurements, it was found that the sensor with a resistivity of $300\,\Omega\,\mathrm{cm}$ provided the highest detection efficiency across all tested samples. Therefore, the HitPix3 sensor should be produced on *p*-type substrate with this resistivity. Furthermore, these measurements also confirmed the need for air cooling in the future beam monitor to mitigate increased sensor leakage current and noise caused by radiation damage.
The HitPix3 pixel design also should have an individual in-pixel tune DAC block for pixel threshold adjustments, since a HitPix2 threshold voltage common to all pixels resulted in large fraction of pixels being masked due to increased noise after significant radiation damage. An output voltage range of 300 mV for the foreseen in-pixel tune DAC block was determined from measurements with unirradiated and irradiated samples in a climatic chamber.
All discussed features were implemented in a new HitPix3 sensor design. Several wafers containing HitPix3 sensors were produced in the second half of 2023. The detailed characterization of these sensors is covered in next chapter 6.

6 HitPix3

HitPix3 is the third iteration of the HitPix sensor family. Several improvements are implemented in this sensor based on the HitPix2 characterization results. The following chapter covers the new features of the HitPix3 sensor design compared to HitPix2, the sensor characterization process and results, and the multi-sensor assembly. The HitPix3 characterization results were used to formulate a set of design improvements for the next large scale sensor – HitPix4. They are provided at the end of the chapter.

6.1. Sensor design

HitPix3 sensors were designed and produced with a 180 nm HV-CMOS process at the TSI Semiconductors foundry. The sensor layout and photograph are shown in Fig. 6.1. The general layout of the HitPix3 sensor is inherited from the HitPix2 design. It has a total area of 9775 µm × 10 110 µm, the same active area of 9600 µm × 9600 µm formed in a matrix of 48 × 48 pixels with an individual pixel size of 200 µm × 200 µm. The peripheral electronics and connection pads occupy a similar area of 9600 µm × 420 µm at the bottom of the sensor. Based on the HitPix2 radiation hardness studies, presented in section 5.5, the HitPix3 sensor was produced on *p*-type substrate with a resistivity of 370 Ω cm.

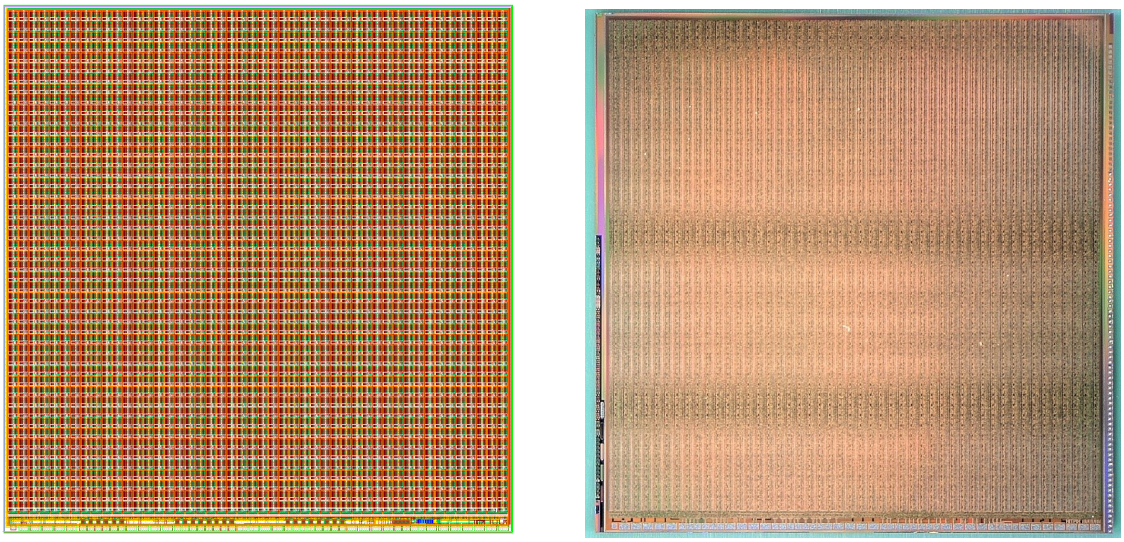


Figure 6.1.: The HitPix3 sensor layout (left) consists of a 48 × 48 pixel matrix (orange), peripheral electronics (narrow yellow-green region) and connection pads are located at the bottom of the sensor. Photograph of a HitPix3 sensor (right). Sensor layout courtesy of H. Zhang.

The significant change in the HitPix3 design is the implementation of a row-wise projection calculation compared to its predecessors HitPix1 and HitPix2, which only have a column-wise

projection calculation. A simplified concept of the two-dimensional projection calculation is shown in Fig. 6.2. As described in [ZTP26], two types of columns (A and B) are introduced in the HitPix3 pixel matrix. The pixel numeration in columns is started with zero. All counter values of even pixels in columns A (outlined in magenta color in the figure) are summed row-wise, while all counter values of odd pixels in columns B (outlined in blue color in the figure) are summed column-wise. The summation results are transmitted to the peripheral electronics of the sensor (the data path for A and B columns are shown with the magenta and blue arrows in the figure, respectively).

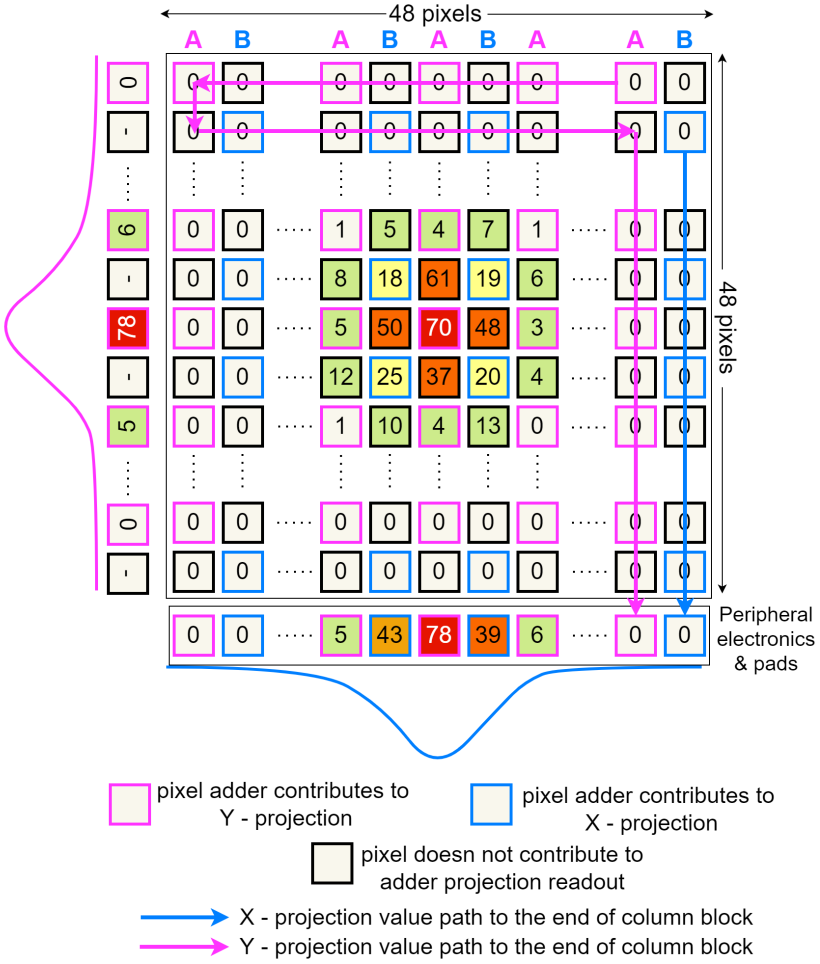


Figure 6.2.: Simplified concept of two-dimensional projection calculation.

This two-dimensional projection calculation scheme, called chess-pattern, is a result of design optimization in system complexity, power consumption, readout speed, and minimization of inactive area. In the chess-pattern, only one adder per pixel is required and the two-dimensional projection data can be read out from the shift register within one readout cycle, similar to HitPix2. However, it has a drawback: half of the pixels (outlined in black color in the figure) do not contribute to any projection calculation, increasing the effective adder pitch to 400 µm for both projections. Implementation of the full summation would require significant changes in pixel and peripheral electronics. At the pixel level, it would introduce either two adders circuits or a multiplexer, increasing the power consumption and system complexity. Data transfer would then require either two readout cycles for each projection, affecting the readout speed, or the implementation of an additional data shift register, increasing the insensitive area of the sensor, power consumption and system complexity.

It is important to note that HitPix3 with an adder chess-pattern is an intermediate step in the HitPix sensor family development. One of the primary goals is to explore the feasibility and performance in beam of such a projection calculation scheme for a next large scale sensor.

6.1.1. Pixel layout

The HitPix3 pixel cell is organized as its predecessor HitPix2 with three separate functional blocks: sensor diode, analog and digital electronics, as shown in the simplified functional diagram in Fig. 6.3 on the left. However, several improvements are introduced in the pixel layout based on the HitPix1 and HitPix2 measurement results. The HitPix3 pixel has an ISO topology (presented in section 3.4), since measurements with a HitPix1 and proton microbeam, presented in subsection 5.4.4, revealed a higher tolerance of this topology against the baseline drop effect (discussed in subsection 5.4.2) than the STD pixel topology. A simplified cross-section of the HitPix3 pixel is shown in Fig. 6.4.

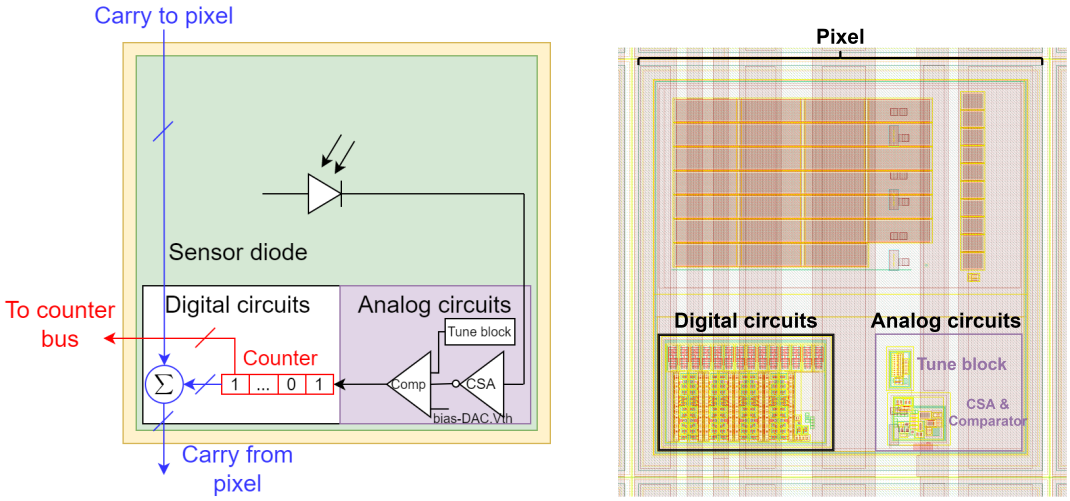


Figure 6.3.: Simplified functional diagram of the HitPix3 pixel (left) and its actual layout (right). The digital and analog circuits are outlined with black and purple boxes, respectively. Pixel layout courtesy of E. Trifonova.

The deep p-wells isolate the shallow n-wells of the analog and digital circuits, therefore the pixel electronics can be placed inside the deep n-well of the sensor diode, as shown on the functional diagram of HitPix3 pixel in Fig. 6.3 on the left and the simplified cross-section in Fig. 6.4. This topology increases the pixel fill factor to almost 100 %. In addition to the pixel topology optimization, the HitPix3 pixel design also includes new features in the pixel electronics. While the digital electronics (8 bit counter and 14 bit adder) remain unchanged, new functional blocks (tune and feedback boost blocks) are introduced to the analog circuits and are discussed in the next subsection.

6.1.2. Pixel electronics

A simplified schematic of a HitPix3 pixel electronics is shown in Fig. 6.5. The main working principles of the pixel electronics, including the Charge-Sensitive Amplifier (CSA), comparator, counter, adder and charge injection circuit remain unchanged and described in the HitPix2 pixel electronics subsection 5.1.2. The counter design flaw, previously observed for HitPix1 and HitPix2 sensors, is not corrected in the HitPix3 design, preventing the full usage of 14 bit adder range (more details in subsection 5.1.2).

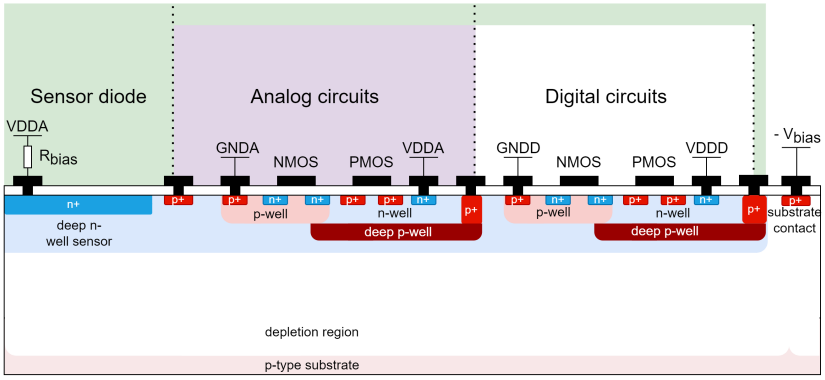


Figure 6.4.: Simplified HitPix3 pixel cross-section.

The CSA is redesigned in a pMOS-based circuit, due to its higher tolerance to the baseline drop effect compared to the nMOS-based CSA of HitPix2, as discussed in subsection 5.4.4. Additionally, a new feature, called feedback boost circuit, is introduced into the CSA to mitigate the pileup effects and to restore the baseline faster. The transistor level schematic of the CSA feedback circuit with this feature is shown in Fig. 6.6 on the left. Conceptually, it is a form of switched reset circuit, presented in [Zha21]. A large reset current source is connected in parallel to the feedback circuit of CSA via a transistor switch. The strength of the reset current source is controlled with the applied voltage `VPFBBoost`, which is connected to the `bias-DAC.infb` in parallel. The transistor switch state is controlled with a `BoostB` signal generated by the digital logic block of the pixel. Initially, the switch is in "off" state and the reset current source is disconnected from the CSA feedback circuit. Only when the in-pixel comparator transits into a logic high state after detecting a particle with the CSA output signal being higher than the comparator threshold of `bias-DAC.Vth` $- V_{\mathrm{bl}}$, the `BoostB` signal enables the reset current source, allowing to discharge the CSA feedback capacitance C_{fb} faster than a continuous reset through the resistive feedback circuit R_{fb}. When the CSA output signal becomes smaller than the comparator threshold, the `BoostB` disables the switch and disconnects the reset current source from the feedback circuit.

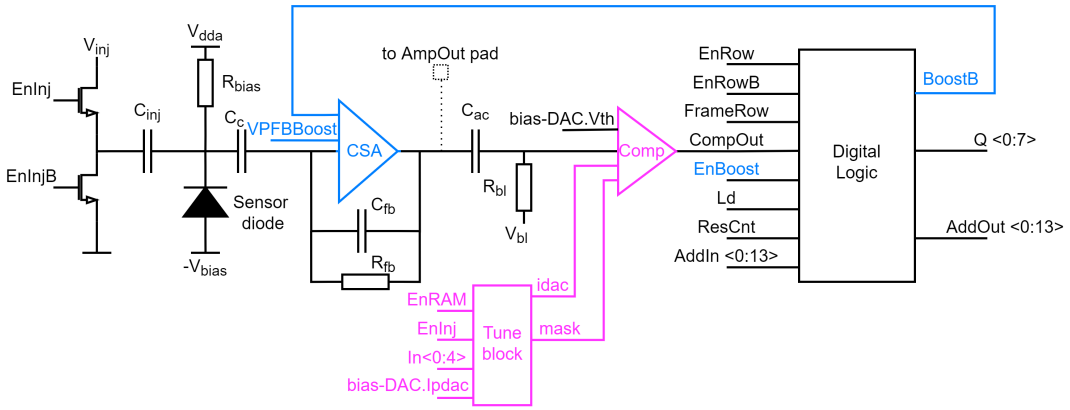


Figure 6.5.: Simplified schematic of a HitPix3 pixel electronics. Compared to the HitPix2 design, the new functional blocks are colored blue and magenta. An additional connection to the `AmpOut` pad (black dashed box) is implemented only for pixels in the row closest to the peripheral electronics. Adapted from [ZTP26].

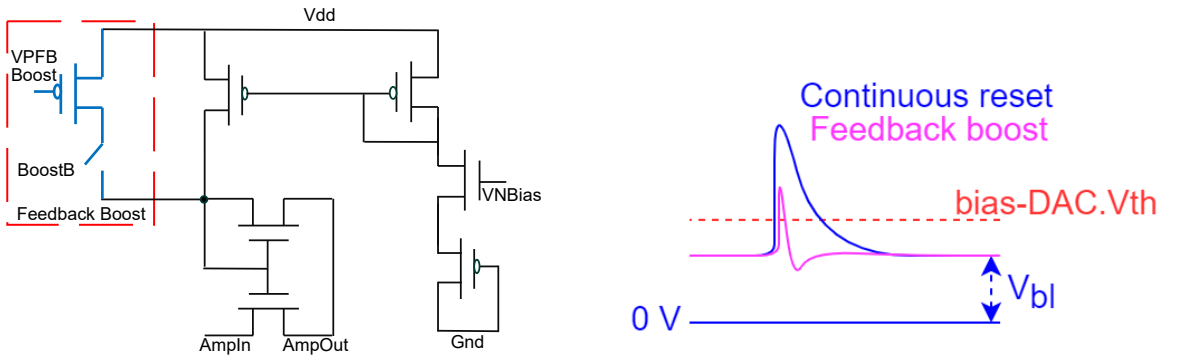


Figure 6.6.: Schematic of CSA feedback circuit with the feedback boost feature (left) and simplified examples of the CSA output signals (right) with enabled (magenta signal) and disabled (blue signal) feedback boost circuit. The schematic is taken from [ZTP26].

Simplified examples of the CSA output signals with enabled (magenta signal) and disabled (blue signal) feedback boost feature are shown in Fig. 6.6 on the right. The signal amplitude of the CSA with enabled feedback boost is reduced compared to the continuous reset configuration, since the output signal amplitude is limited by the selected comparator threshold, the transistor switching delay (time between the applied `BoostB` signal and the transistor becoming fully conductive) and the signal intrinsic rise time. If the switching delay is much shorter than the signal rise time, setting the threshold too low truncates the signal amplitude before its complete integration on the CSA. However, the amplitude truncation does not influence the number of detected particles, since the feedback boost circuit becomes active only when the comparator transits into a logic high state. The feedback boost feature can be selected for all pixels in the sensor by setting the `EnBoost` bit to a logic high state in the configuration shift register of the `bias-DAC` block (more details in subsection 6.1.3).

In the HitPix1 and HitPix2 sensors, all pixel comparators share a single global threshold voltage level, generated by the `bias-DAC` block. This common threshold leads to a wide pixel threshold distribution for unirradiated sensors and an increased fraction of noisy pixels after significant radiation damage, as discussed in subsection 5.5.4. The tune block (colored in magenta in Fig. 6.5) is introduced to the HitPix3 pixel electronics to mitigate these effects. As described in [ZTP26], it consists of a 4 bit tune DAC connected to a small 5 bit Random Access Memory (RAM) cell. Four output bits of the RAM cell set the output voltage offset of the tune DAC. The offset is added to the global threshold voltage, therefore the comparator threshold can be adjusted individually for each pixel by configuring the corresponding RAM cell value. The output voltage range of the tune DAC is controlled by the `ipdac` setting common to all pixels and generated by the `bias-DAC` block. The fifth output bit of the RAM cell, called mask bit, is directly passed to the comparator. If the mask bit is set to a logic high state, the comparator is disabled. The masking feature is important for the readout of the radiation damaged sensor in adder mode, if the pixel noise level cannot be compensated by the comparator threshold adjustment. The `EnRAM` signal of the configuration shift register of the `bias-DAC` block and `EnInj` signal control the access to the RAM cell. The RAM value can be modified only when both signals are in a logic high state to prevent an unintended modification of the RAM value caused by a Single Event Upset (SEU). More details regarding the RAM cell configuration are given in the next subsection.

6.1.3. Peripheral electronics

The HitPix3 peripheral electronics is based on HitPix2 design and consists of the same main parts: PISO shift registers, row control block and `bias-DAC` block. Their functionalities are described in subsection 5.1.3. However, several important changes are implemented to improve the HitPix3 readout speed.
The input and output buffers of HitPix2 are implemented according to the LVCMOS standard and a separate output buffer for the configuration/data shift register output is implemented according to the LVDS standard. This design limited the readout speed to 58 Mbit s^{-1} for a single HitPix2 sensor and to 36 Mbit s^{-1} for a daisy chain of five sensors, as discussed in subsections 5.2.6 and 5.3.2. Therefore, the input and output buffers of HitPix3 are redesigned according to the LVDS standard, requiring changes in the peripheral electronics architecture. The LVDS standard is based on a differential signal, i.e. one logical signal requires two separate contact pads for its non-inverted and inverted components, increasing the number of contact pads by a factor of two for the same number of control and data signals. To maintain the minimal peripheral electronics area as in HitPix2, the width of the control and data signal pads is reduced from 200 µm to 135 µm, and the distance between them is reduced from 30 µm to 15 µm. Moreover, a separate set of pads and control signals for configuration of the `bias-DAC` block shift register presented in HitPix2 (`SInDAC`, `SOutDAC`, `LdDAC`, `Clk1DAC`, `Clk2DAC`) is omitted. To compensate this, a new readout architecture based on two radiation hard demultiplexers is implemented, as shown in Fig. 6.7.

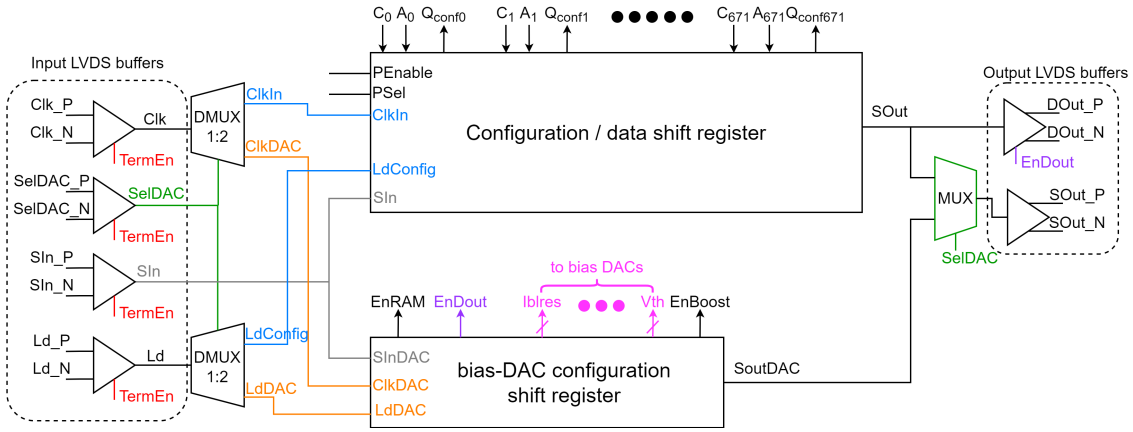


Figure 6.7.: Simplified schematic of the HitPix3 peripheral readout. The paths for the `Ld` and `Clk` signals from the demultiplexers to the configuration/data and the `bias-DAC` block shift registers, are highlighted in blue and orange, respectively. The `TermEn`, `SelDAC`, `SIn` signals are colored in red, green and gray, respectively. The output bits of the `bias-DAC` block shift register to the bias DACs and to the `DOut` buffer are colored in magenta and purple, respectively. For simplicity, the input LVDS buffers for `PEnable` and `PSel` signals are not depicted. The arrows indicate the direction of data flow to and from the shift registers.

Input LVDS control and data signals are converted into single-ended signals by passing through dedicated LVDS buffers (outlined with a dashed box on the left side of the figure). Each input buffer also has an additional `TermEn` input signal (colored red in the figure), which enables both the buffer and its internal termination resistor when the `TermEn` is in a logic high state. An exception is the `SIn` input buffer, which requires an external termination resistor. Configuration data for both the configuration/data and `bias-DAC` block shift registers can be passed through a single `SIn` buffer (colored gray in the figure). The `Clk` and `Ld` signals are

used to propagate and latch the data in the shift registers, as explained in subsection 5.1.3. Therefore, two demultiplexers were introduced to select the target shift register for data writing by using a SelDAC signal (colored green in the figure). The SelDAC enables the signal path to the configuration/data shift register (colored blue in the figure) when it is in a logic low state, and to the bias-DAC block configuration shift register otherwise (colored orange in the figure). The output data of both shift registers SOut and SOutDAC can be read out via a multiplexer connected to an SOut output LVDS buffer, which converts the single-ended signal into a differential signal. The same SelDAC signal selects which shift register will be read out. An additional output LVDS buffer is directly connected to the configuration/data shift register, designated as DOut. This buffer can be used in a multi-sensor bus architecture, discussed in subsection 5.3.1 in which DOut of all connected sensors form a common output data bus. The DOut buffer can be enabled by the EnDOut output bit (colored purple in the figure) of the bias-DAC block configuration shift register.

To simplify the HitPix3 readout process and increase its speed, the two-phase clock signal (used in HitPix2) is replaced with a single-phase clock, requiring changes in the configuration of the ScanFF, which are elementary building blocks of the configuration/data shift register (more details in subsection 5.1.3). The simplified schematic of the new single HitPix3 ScanFF is shown in Fig. 6.8. To propagate a data bit in the new ScanFF, the single-phase clock ClkIn is passed through a chain of two inverters, generating two complementary clock signals (ClkB and Clk), which are then applied to two level-sensitive D-latches. This ensures a reliable shifting process due to built-in delay between ClkB and Clk, preventing race conditions and data corruption.

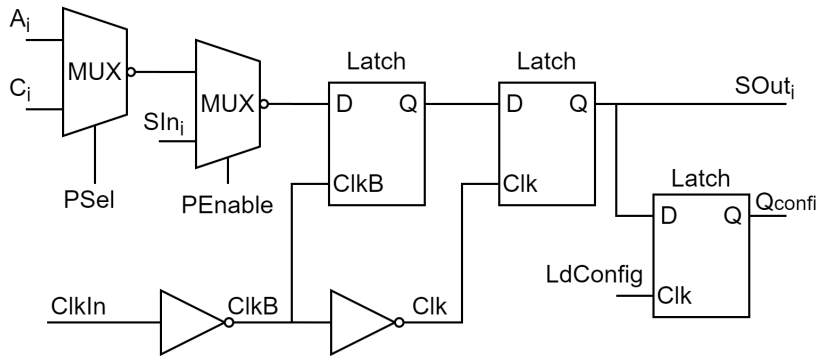


Figure 6.8.: Simplified schematic of single HitPix3 scan flip-flop. Adapted from [ZTP26].

The row control block and the bit assignment of the configuration/data shift register for address encoding, charge injection, and selection of the in-pixel amplifier test output are directly transferred from the HitPix2 design and can be found in subsection 5.1.3.

The RAM cell values of the new in-pixel tune block, described in subsection 6.1.2, can be modified for a selected row with the following sequence. First, the row configuration data is propagated through the configuration/data shift register. The configuration data includes the row address encoded in bit positions $Q_{conf}\langle 8{:}13\rangle$, the EnInj signals for selected pixels (at bit position $Q_{conf}\langle 7{::}14\rangle$, i.e. 7th bit in every column), and the 5 bit RAM cell values to be written (at bit positions from $Q_{conf}\langle 0{::}14\rangle$ to $Q_{conf}\langle 4{::}14\rangle$ in every column). Next, the EnRAM bit is set to a logic high state in the bias-DAC block shift register, followed by the assertion of the LdConfig signal for the configuration/data shift register, which writes new values into the RAM cells. Finally, the EnRAM bit is set to a logic low state.

The bias-DAC block follows the HitPix2 design with a few modifications in its configuration shift register. It was redesigned to support the single-phase clock and its size was expanded

to 76 bit to address all new features. The detailed assignment of the `bias-DAC` shift register bits is presented in the Appendix in table C.1.

6.2. HitPix3 characterization

The HitPix3 sensor layout, pixel and peripheral electronics were significantly modified compared to its predecessors HitPix1 and HitPix2, as discussed in the previous section 6.1. Hence, a verification that each new feature functions as designed is required before the design of the multi-sensor assembly. The characterization results of multiple HitPix3 sensors (before and after irradiation) in both laboratory and beam test environments are presented in this section, which extend studies previously presented in [ZTP26].

6.2.1. Single sensor carrier design

The single HitPix3 carrier PCB was designed and produced to provide all required connections for electrical power, DAQ control and data readout to a mounted sensor. The carrier layout, a 3D render and a photograph of the assembled carrier are shown in Fig. 6.9.

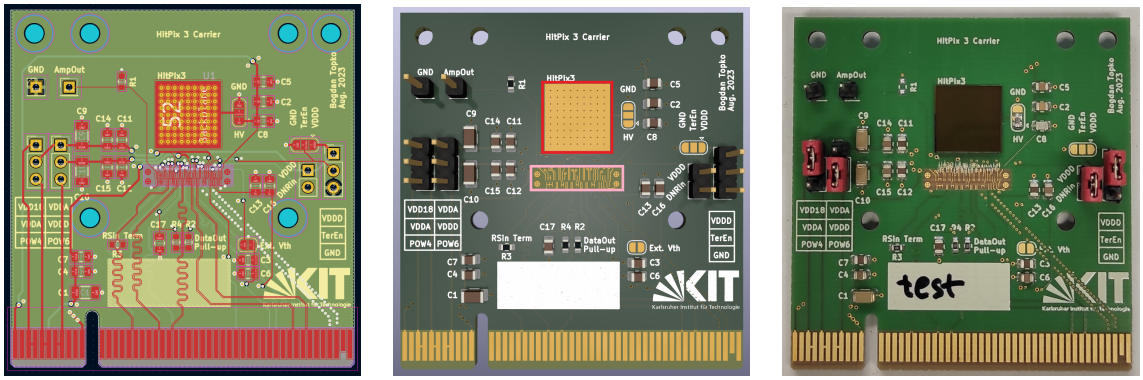


Figure 6.9.: Single sensor carrier layout (left), 3D render (center), and photograph after an assembly (right). The red and pink boxes in the 3D render outline the sensor mounting pad and wire-bonding pads, respectively. The photograph is taken from [ZTP26].

The carrier is compatible with the GECCO board, which is presented in section 4.3. A diced HitPix3 sensor is mounted onto a central exposed pad (outlined with a red box in the 3D render shown in the figure) using Araldite®2011 epoxy resin [Hun24], which has been proved as a radiation hard adhesive [GHT01]. The sensor mounting pad also serves as a heat sink. The sensor contact pads are wire-bonded to the exposed parts of the power and signal traces (outlined with a pink box in the 3D render shown in the figure).
The carrier periphery contains only passive components, including external pins, capacitors and resistors. A set of pins is used to select the power rails for analog and digital electronics of sensor, whereas a separate pair of pins is used for direct measurement of the in-pixel CSA. An individual set of decoupling capacitors is implemented for each power rail to suppress a potential high-frequency noise in the power lines. An external resistor is introduced in the carrier close to the contact pads to ensure the proper termination of the `SIn` input buffer, as discussed in subsection 6.1.3.
To ensure the high readout speed of the sensor, careful attention is given to all LVDS differential pairs. This includes: two internal continuous ground planes underneath the traces and stitching vias to ensure a proper path for high-frequency return currents, trace length tuning to minimize

intra- and inter-pair skews, increased space between each differential pair to minimize potential crosstalk, and other techniques described in [Tex18].

Several diced and unthinned HitPix3 sensors with a thickness of approximately 850 µm were assembled on the carriers to check all sensor functionality.

6.2.2. I-V test

The main advantage of the HV-CMOS sensor compared to sensors based on LVCMOS technology is its capability to operate at high bias voltages, as explained in section 3.4. Therefore, the first test of the HitPix3, which verifies its basic functionality, is an I-V test. An example of a measured I-V curve for an unirradiated HitPix3 sensor at room temperature is shown in Fig. 6.10.

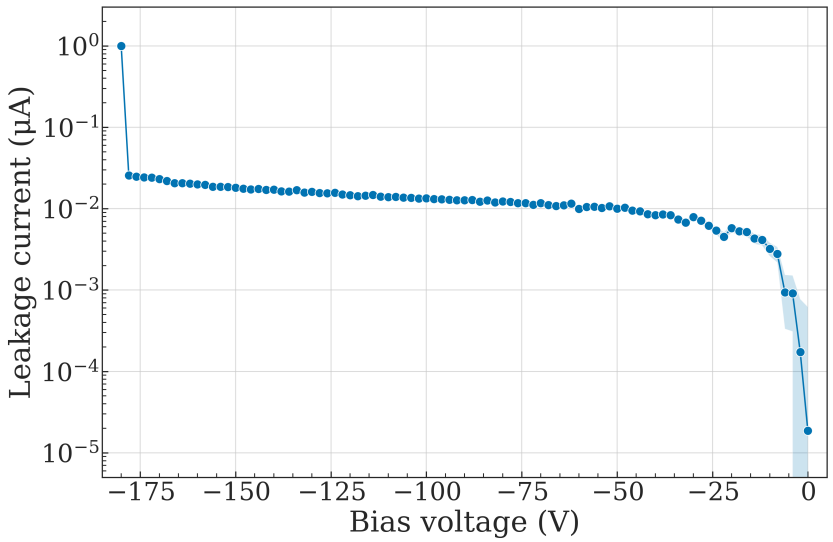


Figure 6.10.: Example of a measured I-V curve for an unirradiated HitPix3 sensor at room temperature of 23 °C. The leakage current is plotted in absolute values. The filled area corresponds to the measured current uncertainty of the Keithley 2410 power supply in the 1 µA measurement range. Data for the plot are taken from [ZTP26]

Each data point in the plot represents the average of ten current samples taken at every bias voltage. The large uncertainty in the low bias voltage range from 0 V to −10 V is determined by the HV power supply measurement uncertainty of 0.035 % + 600 pA in the 1 µA measurement range [Kei10], which becomes comparable with the measured current. The curve follows a square root dependency on the bias voltage, as expected. The measured curve confirms that an unirradiated HitPix3 sensor can withstand a high bias voltage up to −180 V without breakdown, and that its total leakage current does not exceed 20 nA.

Further I-V measurements of unirradiated sensors in a controlled temperature environment may be found in [Mor24]. The measurements were conducted by O. Moritz within the scope of his bachelor's thesis, under the author's supervision. In that work, three unirradiated sensors were measured at a temperature of 20 °C up to a bias voltage of −150 V with no breakdown and total leakage currents less than 20 nA. Therefore, the capability of the HitPix3 sensor to withstand high bias voltages was confirmed based on these measurements.

6.2.3. Latency scan measurement

To estimate the maximum readout speed of the HitPix3 sensor, a latency scan measurement was performed, as described in subsection 5.2.6. The necessary modifications of the control signal pattern were implemented to address the new single-phase clock design of the sensor peripheral electronics. The measurement result is shown in Fig. 6.11.

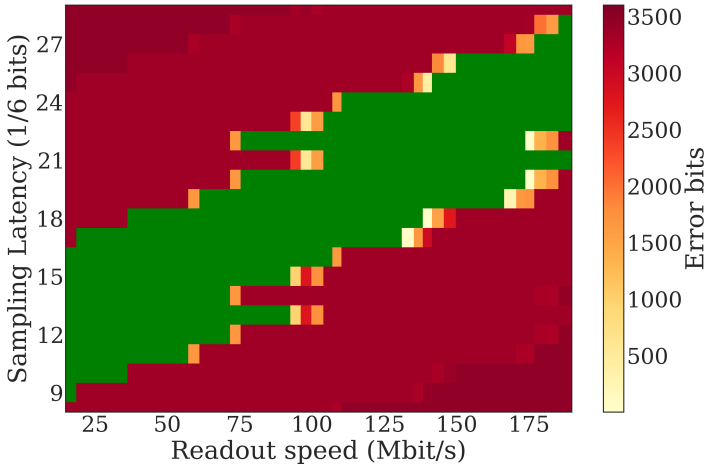


Figure 6.11.: Example of a measured latency scan for HitPix3 sensor. The green area corresponds to the readout speed and sampling latency values without an error.

The readout speed of the HitPix3 sensor is drastically increased compared to the HitPix2 results presented in subsection 5.2.6. The two main improvements in the HitPix3 peripheral electronics – the redesign of its input and output buffers according to the LVDS standard and the redesign of its shift registers to single-phase clock signal – allows the sensor to reach the maximum readout speed of 190 $\mathrm{Mbit\,s^{-1}}$ supported by the current readout firmware.

6.2.4. Experimental setups and Geant4 simulations

Once the basic functionality of the new sensor was confirmed, several tests were conducted to study the performance of the in-pixel electronics. The tests were based on the direct measurements of the CSA output signals in response to different ionizing particles and test signals generated by the charge injection circuit of the pixel. The measured output signals of the CSA and input injection signals are voltage signals. However, for a physically meaningful estimation of the important pixel parameters, such as an Equivalent Noise Charge (ENC) and a pixel threshold, it is important to express them in terms of charge, usually as a number of electrons. Therefore, a calibration of the CSA output signals and input injection signals is required. The calibration procedure is based on deriving a calibration factor that converts a measured voltage amplitude (from the amplitude spectrum) to a corresponding deposited charge within the detector from an ionizing particle or input injection signal. To estimate the deposited charge in the HitPix3 sensor, Monte-Carlo simulations of the experimental setups were performed using the Geant4 framework [Ago+03]. An important discussion regarding the limitations of the applied calibration procedure is given in subsection 6.2.7.
The simplified geometries of the experimental setups used in the Geant4 simulations are shown in Fig. 6.12. The left diagram shows the laboratory setup, which is based on a beta-radioactive Sr-90 source. The source is positioned above the HitPix3 sensor and the emitted electrons pass through the steel window with a thickness of 50 µm.

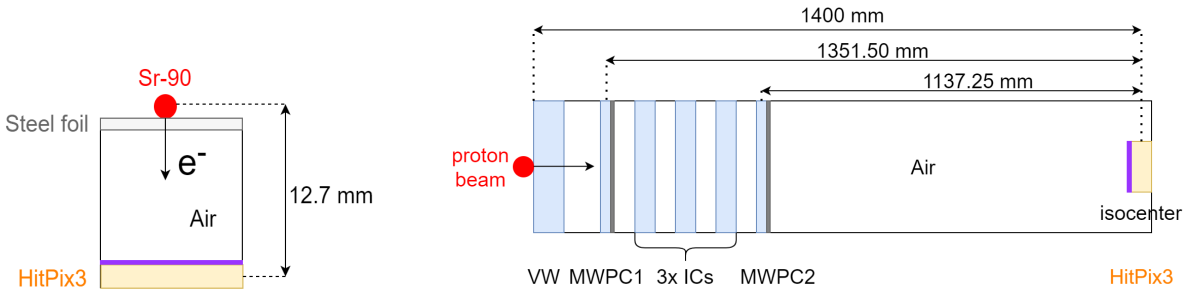


Figure 6.12.: Simplified geometries of the laboratory setup with Sr-90 source (left) and the experimental beamline at HIT (right) simulated in Geant4. The details are given in the main text.

The right diagram shows the experimental beamline at HIT. The HitPix3 sensor is positioned at the isocenter. An accelerated proton beam exits the vacuum beam pipe through the Vacuum Window (VW). After that, it passes through the installed detectors of the BAMS, which includes two MWPCs and three ICs, as described in section 4.1. To take into account the influence of these detectors and the vacuum window on the final proton energy distribution applied to the HitPix3 sensor, they are simulated as simplified water-equivalent volumes (shown as blue boxes in the figure), as explained in [Par+12]. According to [Par+12], the Water Equivalent Thickness (WET) values for the VW, MWPCs, and ICs are 360 µm, 130 µm, and 230 µm, respectively. Additionally, a thin 3 µm layer of tungsten is added into each MWPC detector volume (shown as gray boxes in the figure) to address the influence of the MWPC tungsten wires on the proton beam [Par+12].

The HitPix3 sensor geometry in the simulation consists of two main parts: a passive volume (shown as purple box in the figure) and an active volume (shown as yellow box in the figure), with the active volume placed behind the passive. The passive volume represents the non-active layers of sensor, including the aluminum metallization layers (with a total thickness of 5.33 µm) and the silicon-dioxide passivation layer (with a total thickness of 0.8 µm), which prevents mechanical damage of the sensor surface and is located on top of the metallization layer. In all simulations, the active volume of the sensor represents only its depletion region, since it is assumed that the measured signal in real experiments is primarily defined by the collected charge generated inside the depletion region since diffusion is a slower process than drift. However, this assumption will be tested against the experimental data in the following subsections.

The depletion region width depends on the applied reverse bias voltage, as explained in subsection 3.1.2. For the p-type substrate, the width of the depletion region can be calculated with equation 6.1. The original equation from [Spi05] was modified to address that the HitPix3 pixel deep n-well is connected to the positive V_{dda} power rail (more details in subsection 6.1.2).

$$w = 0.3 \cdot \sqrt{\rho \cdot (V_{\mathrm{bias}} + V_{\mathrm{bi}} + V_{\mathrm{dda}})}[\mu\mathrm{m}], \tag{6.1}$$

where w is the depletion region width in µm units, ρ is the substrate resistivity in Ω cm units, V_{bias} is the applied bias voltage, V_{bi} is built-in potential of the pn-junction. The voltages in the equation are used in absolute values.

For the HitPix3 sensor simulation, the substrate resistivity was assumed to its nominal value of 370 Ω cm, and the built-in potential was approximated by 0.6 V. In the simulation results presented below, V_{bias} and V_{dda} were set to −90 V and 1.85 V, respectively, to reflect the measurement conditions. Based on these parameters, equation 6.1 yields a depletion region width of approximately 55.5 µm or 6.5 % of the unthinned sensor total thickness (850 µm).

Both Sr-90 source and proton beam were simulated with the `G4GeneralParticleSource` class as a point-like source. The mono-energetic proton beams were individually simulated with energies 221.06 MeV u^{-1}, 156.35 MeV u^{-1}, and 94.54 MeV u^{-1} used in the measurements. In contrast to the mono-energetic proton beam, the Sr-90 source has a continuous energy spectrum of the emitted electrons. It consists of two branches corresponding to the Sr-90 decay into the Y-90 isotope with a half life time of 28.91 years and the Y-90 decay into the Zr-90 isotope with a half life time of 64.05 hours [BM20]. To accelerate the simulation process, the emission probability distribution of electrons from Sr-90 decay as a function of their energy was simulated separately with the `G4RadioactiveDecay` module. The simulated distribution with two distinct branches from Sr-90 and Y-90 decay is shown in Fig. 6.13. The simulated result is then fed into the `G4GeneralParticleSource` which emits electrons with energies sampled from the probability distribution.

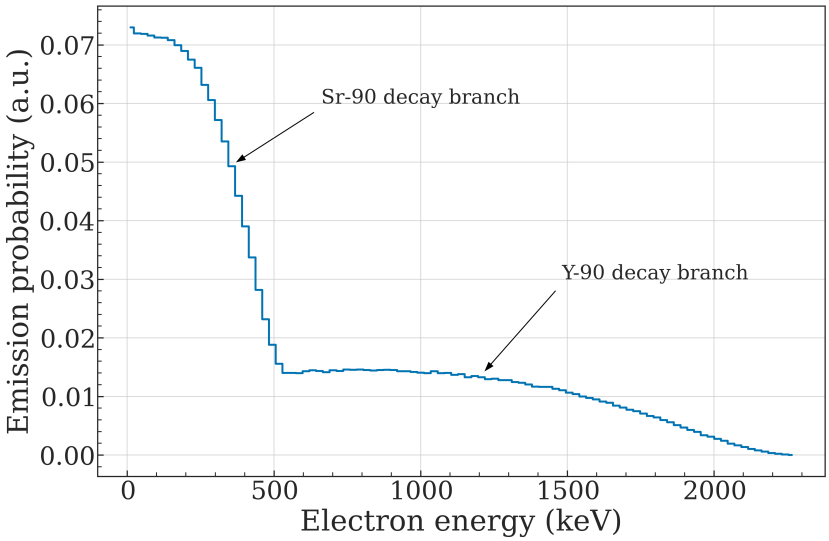


Figure 6.13.: Simulated emission probability distribution of electrons from Sr-90 decay as a function of their energy in Geant4.

Five million events were simulated for each setup. The simulated energy deposition in the HitPix3 sensor from the Sr-90 source and mono-energetic proton beams at different energies is shown in Fig. 6.14. The resulted distributions were fitted with the convolution of Landau and Gaussian functions to extract corresponding MPVs, which are indicated with vertical dashed lines in the figure. To convert the deposited energy into deposited charge, each MPV was divided by the average electron-hole pair creation energy in silicon of 3.61 eV. The simulation results are detailed in table 6.1 and used in the CSA output calibration procedure, as described in the next subsection. The presented MPVs include only fit uncertainties. A detailed discussion on the simulation accuracy is given in subsection 6.2.7.

Table 6.1.: Simulated MPVs of the deposited charge in HitPix3 depletion region using the Sr-90 source and mono-energetic proton beam at the applied bias voltage of −90 V.

Depl. width	Sr-90	p (221.06 MeV u^{-1})	p (156.35 MeV u^{-1})	p (94.54 MeV u^{-1})
55.5 µm	$4070 \pm 3\,e^-$	$8986 \pm 5\,e^-$	$11\,626 \pm 8\,e^-$	$17\,690 \pm 14\,e^-$

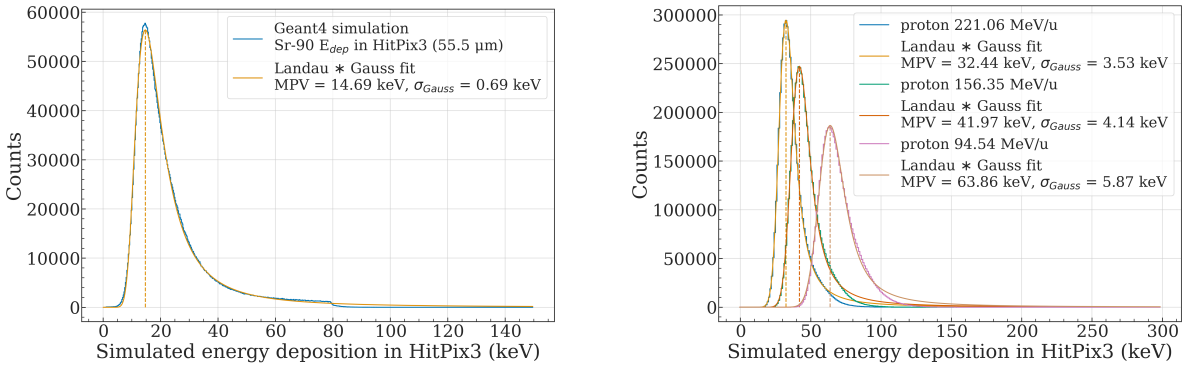


Figure 6.14.: Simulated energy deposition in a HitPix3 sensor from a Sr-90 source (left) and a mono-energetic proton beam at different energies (right). The depletion region width of HitPix3 sensor is assumed to be 55.5 µm at the applied bias voltage of −90 V. Vertical dashed lines represent the MPVs extracted from fitting the convolution of Landau and Gaussian functions.

To cross-validate the calibration results from the charged particle sources, which are based on the assumption of the negligible impact of collected charge from the undepleted region, additional measurements were also performed with a photon source. The advantage of this method is that the absorbed photons deposit all their energy within the sensor volume, leading to a distinct gaussian peak in the measured spectrum. The simplified geometry of the X-ray laboratory setup is shown in Fig. 6.15. The setup consists of an X-ray tube that irradiates a target with photons (indicated as γ_1 in the figure) in a continuous energy spectrum up to 60 keV [Gut+12]. The photons absorbed by the target material cause secondary characteristic X-ray radiation (indicated as γ_2 in the figure), which then irradiates the HitPix3 sensor. The energy of these secondary photons is unique for each chemical element, therefore, a set of targets made of different materials can be used to calibrate the CSA output with multiple energy spectra.

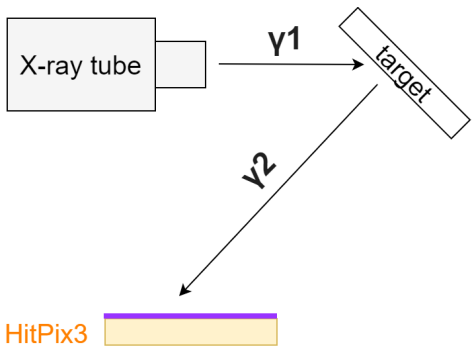


Figure 6.15.: Simplified geometry of the X-ray laboratory setup.

The main peak in each target spectrum, measured with the HitPix3 sensor, was associated with the most probable $K_{\alpha 1}$ transition energy. Since the sensor was not designed for precise spectrometry, the small difference between the measured $K_{\alpha 1}$ peak and the less probable $K_{\alpha 2}$ peak (in the order of a few hundred eV) will not be visible. Therefore, the $K_{\alpha 1}$ transition energy is referred as K_α hereafter. Table 6.2 shows the photon energies for the K_α transition in the target materials and their corresponding deposited charge in HitPix3 sensor, calculated as for the Sr-90 source and proton beams.

Table 6.2.: The photon energies for K_α transition in the target material used in the X-ray setup and their corresponding deposited charge in the HitPix3 sensor. The table data for photon energies are taken from [Des+05]

Parameter	Cu	Zn	Mo	Ag	In	Sn
Energy (eV)	8048.11	8639.10	17479.10	22162.99	24209.78	25271.34
Charge (e^-)	2229	2393	4842	6139	6706	7000

6.2.5. CSA output calibration

As explained in the previous subsection, the CSA calibration is required for a physically meaningful estimation of the pixel parameters. Similarly to the HitPix2 sensor, pixels of the HitPix3, located at the row closest to the peripheral electronics, have an additional connection to the `AmpOut` pad, which allows to directly measure the in-pixel CSA, as explained in subsection 5.1.3, and was used to calibrate the CSA output.

Two important aspects should be considered when comparing the calibration results of different partially depleted HitPix3 sensors. First, the applied bias voltage and substrate resistivity define the width of the depletion region, thus the amount of collected charge, which impacts the input signal to the CSA. Second, the `bias-DAC` block provides specific voltages to many sensor components, as explained in subsection 5.1.3. Therefore, the `bias-DAC` block settings together with the applied voltages to V_{dda} and V_{ssa} power rails control the CSA parameters, which affect the output signal height. Unless stated otherwise, the applied voltages V_{bias}, V_{dda}, V_{ssa} in all measurements presented in this and the following subsections were set to $-90\,\text{V}$, $1.85\,\text{V}$, and $1.25\,\text{V}$, respectively. The full list of the HitPix3 `bias-DAC` block settings used throughout this thesis is provided in the Appendix in table C.2 and will be referenced as "`bias-DAC` settings X, where X = A, B..." hereafter.

In the Sr-90 measurements, the sensor was configured with `bias-DAC` settings A, while a different sensor was used in proton beam and X-ray setup and was configured with `bias-DAC` settings B. The only difference between the two settings lies in the `ipfoll` and `infb` parameters. The `ipfoll` parameter controls the output impedance and speed of the CSA source follower, which has a voltage gain close to unity. The `infb` parameter controls the effective resistance of the CSA feedback loop, which determines the signal decay time (how fast the feedback capacitor discharges). In the proton beam measurements, the beam intensity was set to 2×10^8 pps to minimize possible baseline drops and pileup.

The HitPix3 design allows to measure only one pixel out of 48 in a row at the same time, by routing the output signal of the selected pixel to the `AmpOut` pad. Therefore, during the measurements, the Sr-90 source and proton beam were centered at the measured pixel, reducing the impact of particles with large angles relative to the sensor normal, which traverse a longer path through the depletion region, leading to a higher charge deposition. A large number of such events can bias the measured distribution towards higher values. In the X-ray measurements, secondary photons emitted by the target hit the HitPix3 from many different angles. However, this only affects the low-energy tail of the measured characteristic peak, which is caused by charge sharing between neighboring pixels. The main peak position, corresponding to a secondary photon absorption within the depletion region, will not be affected.

Output signals from the selected pixel were measured with an oscilloscope in AC mode and analyzed offline. Each waveform was preprocessed: its baseline was corrected based on the pedestal mean, and the waveform was smoothed with a Savitzky–Golay filter [SG64] for reliable

signal peak extraction. To prevent distortion of the signal amplitude, the filter window was kept small (11 points) compared to the total size of the signal sample (> 30000 points).
Measurements with the Sr-90 source were performed twice, with enabled and disabled feedback boost circuit (more details in subsection 6.1.2) to test its functionality. Examples of CSA output signals in both modes, after waveform preprocessing, are shown in Fig. 6.16.
The left panel of the figure shows a set of typical CSA unipolar signals with different amplitudes when the feedback boost circuit is disabled. In contrast, the right panel shows two distinct set of signals when the feedback boost circuit is enabled. The first set consists of the unipolar signals (blue, orange and green lines) with shapes similar to those observed when the feedback boost circuit is disabled. However, the second set consists of two bipolar signals (red and purple lines) with a very short positive peak followed by a long negative component. The bipolar shape reflects the feedback boost circuit behavior. When the CSA output signal reaches the comparator threshold, the comparator transits into a logic high state, triggering the digital logic block to generate the `BoostB` signal. This signal then enables a reset current source (triggered at the positive peak of the signal), which rapidly discharges the feedback capacitor, causing the fast negative component of the signal. The reset current source remains active until the comparator exits the logic high state. At this point the reset current source is disconnected from the feedback loop (the signal reaches its negative peak). The total feedback capacitance in the feedback loop then prevents instantaneous baseline restoration, leading to the observed long negative component.

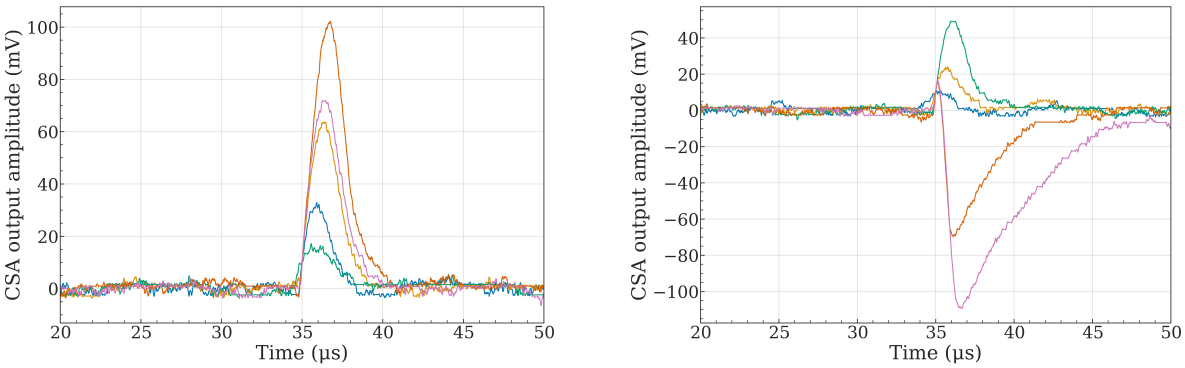


Figure 6.16.: Examples of CSA output signals using the Sr-90 source and enabled/disabled feedback boost circuit (left/right). The global threshold voltage was set to 170 DAC units in the measurement with enabled feedback boost circuit.

Figure 6.17 shows the distributions of extracted signal heights from measurements with the Sr-90 source, with the feedback boost circuit disabled and enabled, respectively. The distorted signals with a large reset component were discarded from the distribution with an enabled feedback boost circuit, since the positive peak of such signals do not reflect the actual deposited charge, as explained in subsection 6.1.2. As expected, the enabled feedback boost circuit truncates the high-energy tail of the resulting distribution. The measurements confirm the basic functionality of the feedback boost circuit. It is important to note that the shapes of the distributions are well aligned before the truncation point. This method can be used to make a rough estimation of the pixel threshold level, because its activation limits the maximum of the measured signal height (results of such a measurements are discussed in subsection 6.2.7).
Figure 6.18 shows the CSA output signal height distributions using the proton beam with nominal energies of 221.06 MeV u^{-1}, 156.35 MeV u^{-1}, and 94.54 MeV u^{-1} and disabled feedback boost circuit. All distributions were fitted with the convolution of Landau and Gaussian functions to extract corresponding MPVs. The fit results are plotted alongside the measured

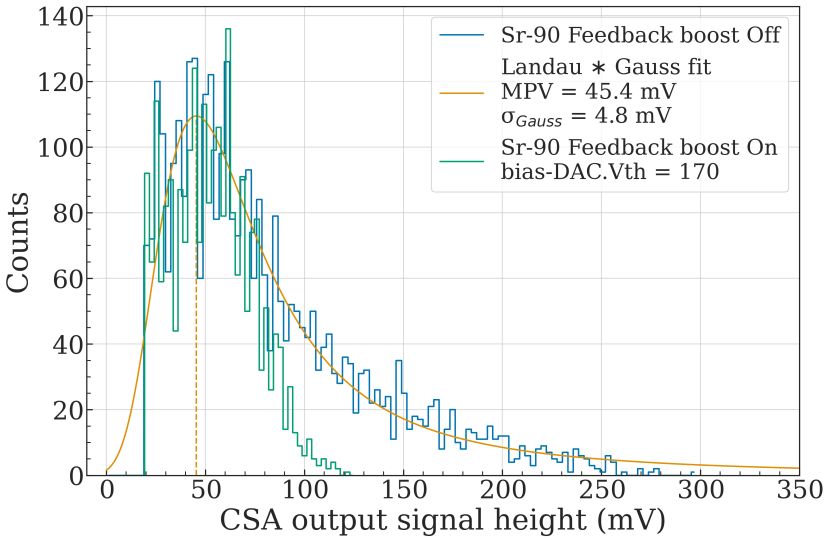


Figure 6.17.: CSA output signal height distributions using the Sr-90 source and enabled/disabled feedback boost circuit (green/blue distributions). The orange solid line represents a fit to the measurement data with disabled feedback boost circuit with a convolution of Landau and Gaussian functions. The global threshold voltage was set to 170 DAC units in the measurement with enabled feedback boost circuit.

distributions in both figures. The MPVs of the measured CSA signal heights using the Sr-90 source and proton beam are presented in table 6.3.
Based on the MPVs extracted from simulations and measurements the calibration factors can be determined for both sensors. For the sensor used in Sr-90 measurements, the calibration factor was obtained by dividing the simulated by the measured MPV, yielding a value of $89.7 \pm 4.3\,\mathrm{e^-\,mV^{-1}}$. For the sensor used in proton beam measurements, the calibration factor was derived from a linear fit of the simulated versus measured MPVs for different nominal proton beam energies. The linear fit has a slope of $64.9 \pm 1.5\,\mathrm{e^-\,mV^{-1}}$ and an intercept of $839\,\mathrm{e^-}$ (the resulting curve is shown in the Appendix, Fig. C.1). The discrepancy of the determined calibration factors can be explained by the different CSA gain. The CSA of the sensor used in the proton beam measurements has a higher gain (fewer electrons are required for a 1 mV CSA signal height), than the sensor used in Sr-90 measurements.

Table 6.3.: Measured MPVs (in mV) of the CSA output signal height distribution of HitPix3 using a Sr-90 source and proton beam at the applied bias voltage of −90 V.

Depl. width	Sr-90	p (221.06 MeV u^{-1})	p (156.35 MeV u^{-1})	p (94.54 MeV u^{-1})
55.5 µm	45.4 ± 5.1	124.3 ± 4.4	168.0 ± 2.1	259.0 ± 5.8

To confirm this, the output characteristic of both CSAs was measured. In these measurements, the GECCO injection card was used to generate a series of known injection pulses with varying amplitudes, as explained in subsection 5.2.4. The voltage pulses were then applied to the sensor `Inj` pad while recording the CSA output. More than 30 pulses were measured per injection amplitude, and their median values were used to build an output characteristics, which are shown in the Appendix in Fig. C.2. The slope of the pixel CSA used in proton

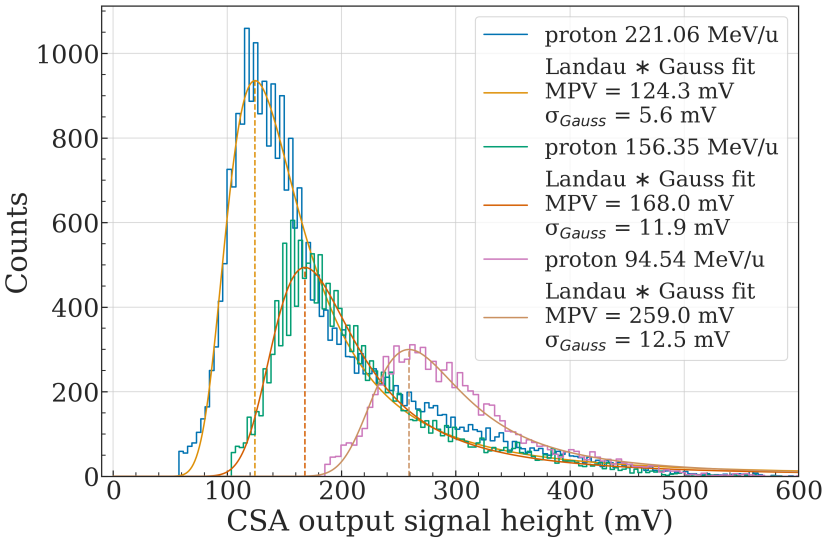


Figure 6.18.: CSA output signal height distributions using the proton beam with nominal energies of 221.06 MeV u^{-1} (blue distribution), 156.35 MeV u^{-1} (green distribution), and 94.54 MeV u^{-1} (pink distribution). The solid lines represent fits to the measurement data with a convolution of Landau and Gaussian functions.

beam measurements (142.3 ± 2.2 mV V^{-1}) is higher than that of the pixel CSA used in Sr-90 measurements (107.5 ± 1.7 mV V^{-1}) confirming the initial suggestion. The slope uncertainties were extracted from the covariance matrix of the least squares fit.
To calibrate the sensor injection circuits, the calibration parameters were applied to the measured output CSA characteristics to convert the voltage scale into an equivalent injected charge. The resulting calibration curves for the charge injection circuit based on Sr-90 source and proton beam data are shown in Fig. 6.19.

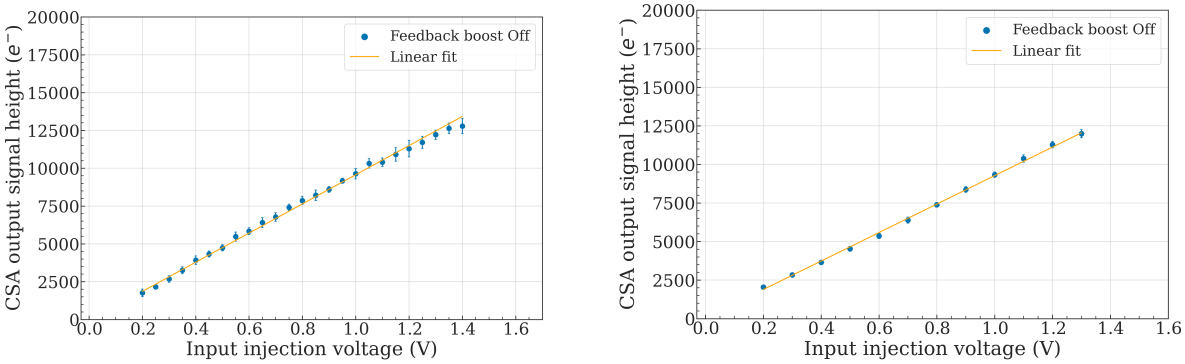


Figure 6.19.: Calibration curves for the charge injection circuit based on Sr-90 source (left) and proton beam (right) data.

Each curve was fitted with a linear function. The calibration curve based on the Sr-90 data has a slope of 9639 ± 152 e$^-$ V^{-1} and an intercept of -69 ± 112 e$^-$. For the curve based on the proton beam data these values are 9235 ± 144 e$^-$ V^{-1} and 41 ± 99 e$^-$, respectively. The calibration parameters for two different sensors and two different particle sources are in good agreement and validate the applied method for the charge injection circuit calibration. However, this method is based on the assumption of the negligible impact of the collected charge from the undepleted region, which affects the simulated MPVs and the calculated equivalent charge.

Therefore, the CSA used in proton beams and configured with the same `bias-DAC` settings B was also measured at the X-ray setup.
Figure 6.20 shows the CSA output signal height distributions measured using photons emitted from different targets irradiated by the X-ray tube. The six measured spectra have a main peak associated with the K_α transition in the target material and a low-energy tail. This tail corresponds to charge-sharing events or the events in which a photon was absorbed in the undepleted region of the sensor, leading to a smaller collected charge. The spectra of the molybdenum, silver, indium and tin targets also have the smaller peak around 12 mV, which corresponds to the zinc characteristic line because the photons emitted by the X-ray tube irradiate not only the target, but also the target holder made of steel, containing zinc in its alloy. This result is consistent with the previous measurements performed at the X-ray setup and presented in [Ehr21].

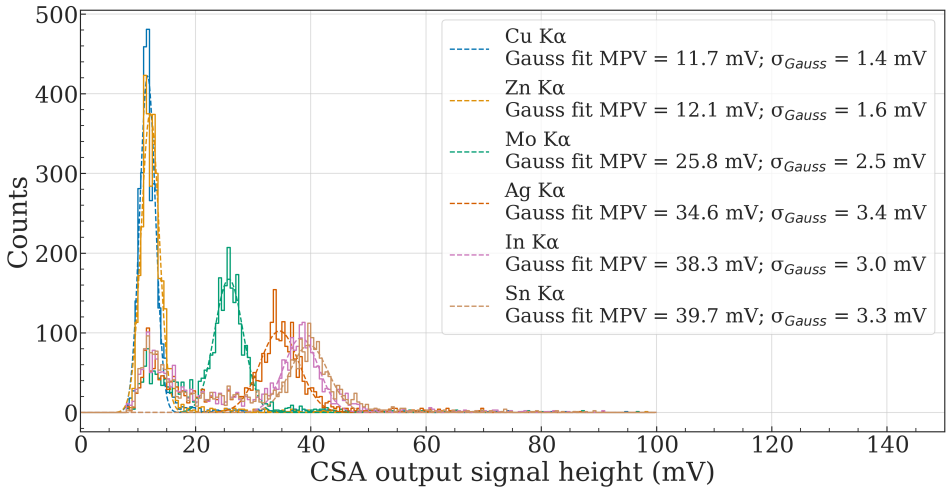


Figure 6.20.: CSA output signal height distributions measured using photons emitted from different targets irradiated by the X-ray tube. The spectrum of targets: copper, zinc, molybdenum, silver, indium, and tin is colored in blue, orange, green, red, purple and brown, respectively. The dashed lines represent fits to the characteristic peak with a Gaussian function.

The measured MPVs are detailed in table 6.4. Similar to the calibration based on the proton beams, the calibration factor was derived from a linear fit of the known deposited charge of the K_α photons versus measured MPVs for different targets. The linear fit has a slope of $167.6 \pm 3.5\,e^-\,mV^{-1}$ and an intercept of $354\,e^-$ (the curve is shown in the Appendix in Fig. C.3), indicating a smaller gain for the same pixel and `bias-DAC` setting compared to those from the proton beam calibration. After applying these calibration parameters to the experimentally measured MPVs for the Sr-90 source (with gain scaling for different pixels) and proton beam measurements, the collected charge increased by more than a factor of two compared to the Geant4 simulated results, as shown in table 6.5. The observed discrepancy between the simulated and measured MPVs can be explained by the non-negligible impact of charge generated inside the undepleted region, which can diffuse to the depletion region and be collected. Based on this calibration, the diffusion component is approximately 60 % of the total collected charge.
To confirm this, additional measurements were performed with two HitPix2 sensors. One unthinned sensor had a thickness of 850 µm, whereas the second was thinned to 50 µm. Both sensors were configured with the same `bias-DAC` settings and a bias voltage of −90 V was applied, which is sufficient to fully deplete the thinned sensor. Charge injection measurements

Table 6.4.: Measured MPVs (in mV) of the CSA output signal height distribution of HitPix3 at a bias voltage of −90 V using photons emitted from different targets irradiated by the X-ray tube.

Cu	Zn	Mo	Ag	In	Sn
11.7 ± 0.1	12.1 ± 0.1	25.8 ± 0.1	34.5 ± 0.1	38.3 ± 0.1	39.7 ± 0.1

Table 6.5.: Measured MPVs of the collected charge in HitPix3 using the Sr-90 source and proton beam based on the X-ray calibration.

Sr-90	p ($221.06\,\mathrm{MeV\,u^{-1}}$)	p ($156.35\,\mathrm{MeV\,u^{-1}}$)	p ($94.54\,\mathrm{MeV\,u^{-1}}$)
$10\,428\,\mathrm{e^-}$	$21\,188\,\mathrm{e^-}$	$28\,520\,\mathrm{e^-}$	$43\,774\,\mathrm{e^-}$

for these sensors confirmed that pixels in both sensors had similar thresholds, as shown in the Appendix in Fig. C.4, i.e. their responses to the same input charge would be similar. However, measurements with the Sr-90 source revealed that the median of the ⟨Hit rate⟩ distribution measured with the thinned sensor was reduced by more than a factor of three compared to the unthinned sample, as shown in the Appendix in Fig. C.5. This confirms that the charge generated within the undepleted region contributes significantly to the total collected charge and cannot be neglected.

Other studies performed with the different HV-CMOS active pixel sensors also support this explanation. The experimental results and TCAD simulations of the MuPix10 sensor with a substrate resistivity of 355 Ω cm showed that 25 % of the total collected charge consisted of a diffusion component, as reported in [Gon23]. Furthermore, the MPV of the 3 GeV electrons measured with the ATLASpix3 sensor was $3660\,\mathrm{e^-}$, as reported in [Per+21], while the expected MPV of these MIP-like particles for the depletion width of 32 µm [Per+21] would be approximately $1920\,\mathrm{e^-}$ based on the MPV dependency on thickness of $60\,\frac{\mathrm{e-h}}{\mu\mathrm{m}}$ [Har24] for the 50 µm thick sensor. This leads to a diffusion component of ∼47.5 % in the total collected charge for ATLASpix3. The larger contribution of the diffusion component to the total collected charge in HitPix3 compared to that for the MuPix10 and ATLASpix3 can be explained by the fact that the Sr-90 source and proton beams were not collimated during the measurements. As a result, the contribution of the particles with large angles relative to the sensor normal was not completely suppressed, shifting the measured distribution towards higher values. In subsection 6.2.7, the measurements performed with a collimated Sr-90 source confirm this explanation and reduce the diffusion component in the total collected charge to 40.2 %.

The calibration curve for the charge injection circuit based on the X-ray data is shown in Fig. 6.21. The curve has a slope and intercept of $23\,850 \pm 371\,\mathrm{e^-\,V^{-1}}$ and $-1708 \pm 256\,\mathrm{e^-}$, respectively and is plotted alongside the proton beam calibration results for comparison. As expected from the previous discussion, the large diffusion component in the total collected charge increased the slope of the calibration curve. However, for both curves, an input injection voltage of 0.96 V still corresponds to an MPV of the $221.06\,\mathrm{MeV\,u^{-1}}$ proton beam due to the linear output characteristic of the CSA.

The parameters based on the X-ray calibration were used in the following analysis of the charge injection measurements. The limitations of the calibration procedure are discussed in subsection 6.2.7.

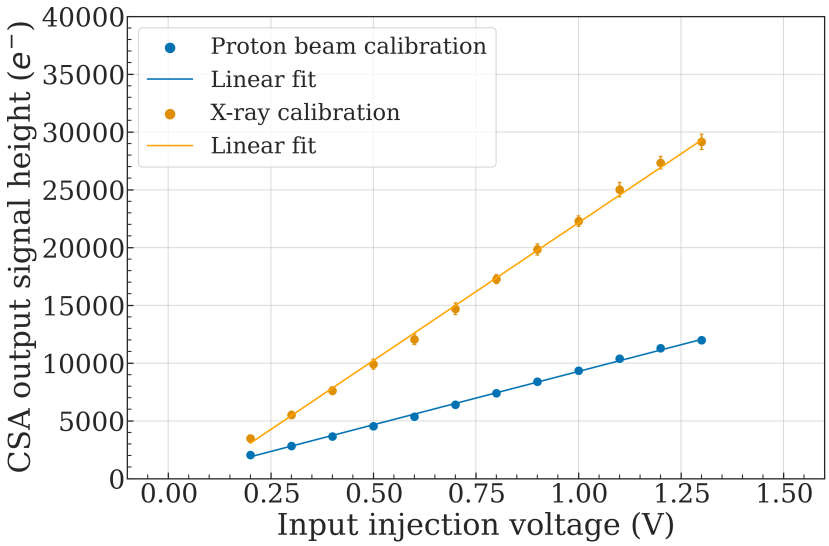


Figure 6.21.: Calibration curves for the charge injection circuit based on the proton beam (blue points) and X-ray setup (orange points) data.

6.2.6. Charge injection measurements and pixel threshold tuning

After the in-pixel CSA calibration, the pixel threshold and noise can be estimated in charge injection measurements (more details in subsection 5.2.4). Furthermore, these measurements were used to test the new HitPix3 pixel threshold tuning feature. An example of a charge injection measurement of a HitPix3 sensor pixel is shown in Fig. 6.22. The resulting distribution follows an error-function, and the important pixel parameters, threshold and noise, can be extracted from the fit.

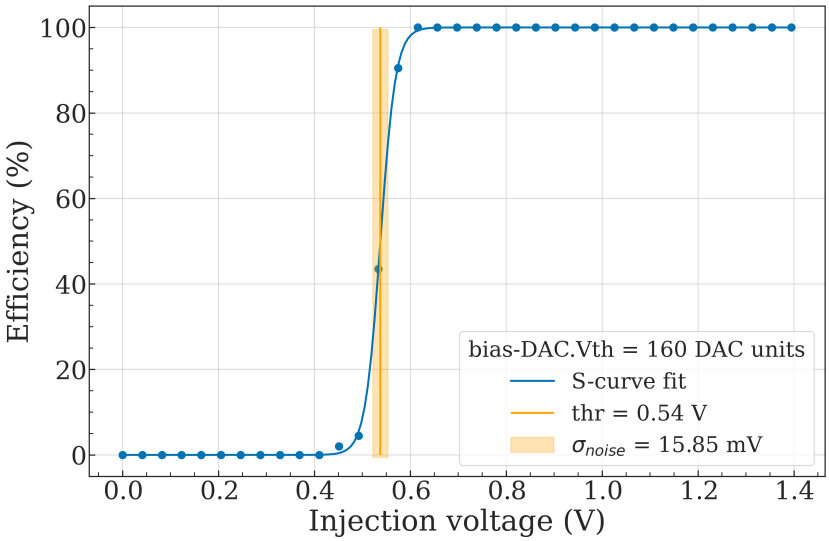


Figure 6.22.: Example of charge injection measurement of HitPix3 sensor pixel. The sensor was configured with `bias-DAC` settings B. The global threshold voltage was set to 160 DAC units. The pixel response is fitted with an error function. The vertical orange line and orange bands represent the pixel threshold and noise values, respectively.

A new pixel threshold tuning feature was introduced in the HitPix3 design to minimize the pixel threshold variations in the sensor at a given global threshold voltage, previously observed in HitPix2 sensors, as discussed in subsection 6.1.2. The pixel threshold tuning algorithm was developed by the author and was first presented in [ZTP26]. For illustrative purpose, the flowchart of the algorithm is shown in Fig. 6.23. The algorithm description is directly quoted from the article:

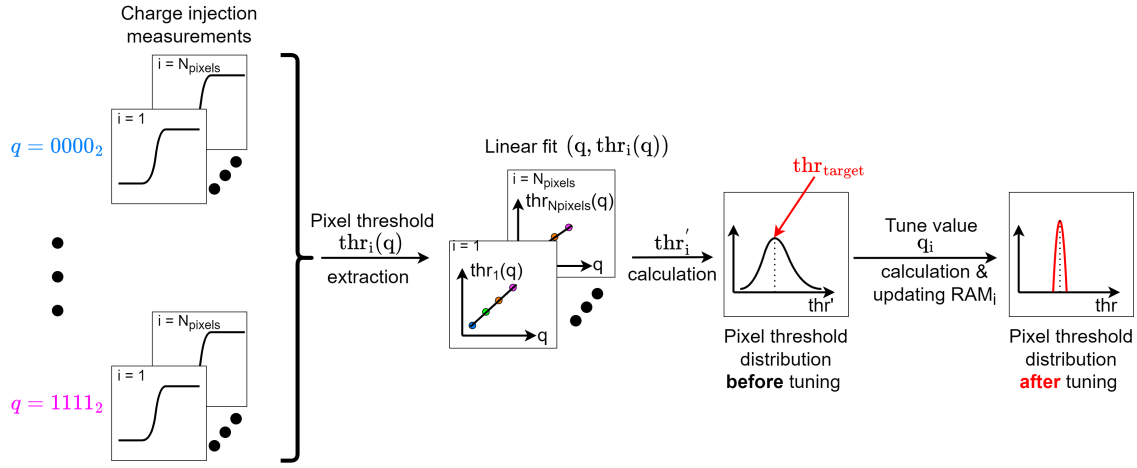


Figure 6.23.: Flowchart of the pixel threshold tuning algorithm. Details are given in the main text.

"A HitPix3 pixel has a 5 bit RAM cell which can be used for the individual threshold tuning of the pixel. Four bits of the RAM cell set the tune DAC value. The output voltage range of the tune DAC block is controlled by the `ipdac` value associated to the `bias-DAC` settings, which is common to the entire sensor. The `ipdac` parameter can take a value in the range from 0 to 63, which corresponds to the maximum output voltage range of the tune DAC block from 0 mV to 300 mV. The pixel threshold tuning procedure consists of several charge injection measurements at fixed `Vth` and `ipdac` values.

Optimal threshold values for each pixel were found with the algorithm 1, depicted hereafter. The main idea of the algorithm is to determine the linear function parameters $\mathbf{slope_i}$ and $\mathbf{inter_i}$ of each pixel with number i, which bind the pixel threshold $\mathbf{thr_i}$ and RAM values and use them to reduce the pixel-to-pixel threshold dispersion. First loop, defined in lines 1-5, iterates over q pixel RAM values from 0000_2 to 1111_2. In each iteration the q value is uploaded to each pixel $\mathbf{RAM_i}$ block (line 2), charge injection measurement is performed (line 3) and each pixel $\mathbf{thr_i}(q)$ is extracted from the pixel response curve (line 4). Next loop, defined in lines 6-9, iterates over pixel number i from 1 to N_{pixels}. In each iteration $\mathbf{slope_i}$ and $\mathbf{inter_i}$ values are determined from the linear regression on sets q and $\mathbf{thr_i}(q)$ (line 7), the pixel threshold value $\mathbf{thr_i'}$ in the middle of RAM range ($q = 0111_2$) is calculated (line 8). In the next step the target threshold $\mathbf{thr_{target}}$ value is determined as a median value of the $\mathbf{thr_i'}$ set (line 10). A typical $\mathbf{thr_i'}$ distribution has a Gaussian shape and setting the median value as a target threshold allows to effectively use half of the RAM range ($q \leq 0111_2$) to tune pixels with $\mathbf{thr_i'} \geq \mathbf{thr_{target}}$ and another half ($q > 0111_2$) to tune pixels with $\mathbf{thr_i'} < \mathbf{thr_{target}}$. Next, the optimal RAM value q_i' is calculated for each pixel based on $\mathbf{thr_{target}}$, $\mathbf{slope_i}$ and $\mathbf{inter_i}$ (line 11). The optimal value is rounded to the nearest integer number. In the last step, q_i'

is clipped to be within the RAM range from 0000_2 to 1111_2 and uploaded to each pixel (line 12)." [ZTP26]

Algorithm 1 Pixel threshold tuning. From [ZTP26].

1: **for** $q \leftarrow 0000_2$ to 1111_2 **do**
2: $\quad$ $\mathbf{RAM_i} \leftarrow q$ **for** $\mathbf{i} = 1, ..., N_{pixels}$
3: $\quad$ **Perform charge injection measurement**
4: $\quad$ **Extract pixel threshold** $\mathbf{thr_i}(q)$ **for** $\mathbf{i} = 1, ..., N_{pixels}$
5: **end for**
6: **for** $i \leftarrow 1$ to N_{pixels} **do**
7: $\quad$ $\mathbf{slope_i}, \mathbf{inter_i} \leftarrow \mathbf{linearfit}(q, \mathbf{thr_i}(q))$
8: $\quad$ $\mathbf{thr_i'} \leftarrow \mathbf{slope_i} \cdot 0111_2 + \mathbf{inter_i}$
9: **end for**
10: $\mathbf{thr_{target}} \leftarrow \mathbf{median}(\mathbf{thr_i'})$
11: $\mathbf{q_i'} \leftarrow \mathbf{ceil}(\frac{\mathbf{thr_{target}} - \mathbf{inter_i}}{\mathbf{slope_i}})$ **for** $\mathbf{i} = 1, ..., N_{pixels}$
12: $\mathbf{RAM_i} \leftarrow \mathbf{max}(0000_2, \mathbf{min}(\mathbf{q_i'}, 1111_2))$ **for** $\mathbf{i} = 1, ..., N_{pixels}$

The pixel threshold distributions were measured across a wide range of threshold voltages before and after pixel threshold tuning, as shown in Fig. 6.24. As expected, the mean of the pixel thresholds μ_{thr} are not affected by the tuning procedure and follows linear behavior w.r.t. threshold voltage. However, the pixel threshold variation is significantly reduced after tuning.

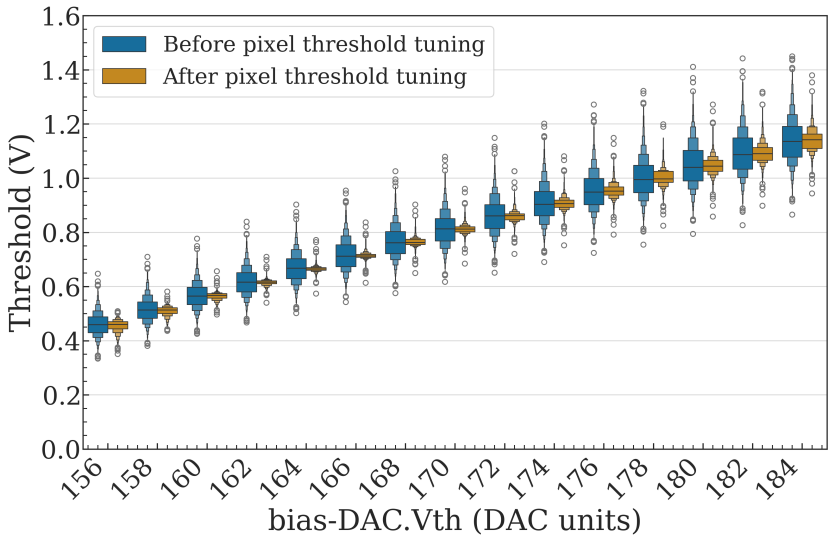


Figure 6.24.: Measured pixel threshold distribution before (blue) and after (orange) pixel threshold tuning at different threshold voltages. The sensor was configured with `bias-DAC` settings B.

To quantify the effect of the tuning procedure, each distribution was fitted with a Gaussian function to extract its standard deviation σ_{thr}. The extracted values before and after pixel threshold tuning are shown in Fig. 6.25. After the tuning, the standard deviation of the pixel thresholds is reduced by a factor of four in a range of threshold voltages from 160 DAC units to 172 DAC units. Similar results were obtained with another sensor, which was used in the Sr-90

source measurements and are shown in the Appendix in Fig. C.6 and Fig. C.7. The presented results validate the functionality of the HitPix3 pixel tune DAC.

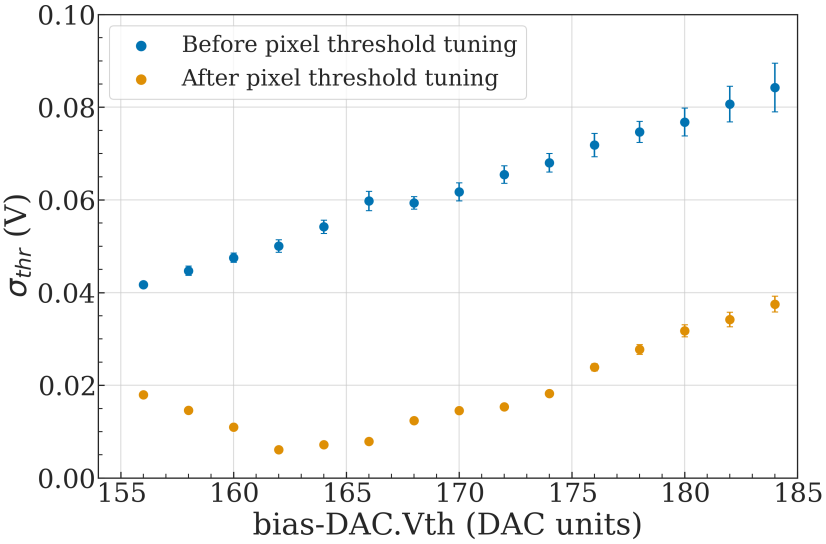


Figure 6.25.: Standard deviation of the HitPix3 pixel threshold distribution before (blue points) and after (orange points) pixel threshold tuning extracted from a Gaussian fit at different threshold voltages. The sensor was configured with `bias-DAC` settings B.

Figure 6.26 shows the pixel noise distribution of HitPix3 before and after pixel threshold tuning at different threshold voltages. The measured pixel noise distributions for the sensor configured with `bias-DAC` settings A is shown in the Appendix in Fig. C.8. As expected, the pixel noise does not depend on the threshold voltage or tuning procedure, since it depends only on the pixel electrical properties. The mean noise values for sensors configured with `bias-DAC` settings A and B are $11.8 \pm 2.2\,\mathrm{mV}$ and $13.1 \pm 2.4\,\mathrm{mV}$, respectively, and are in good agreement.
To quantify the mean noise in terms of electrons, the calibration parameters were applied to the input injection voltages, followed by an S-curve fit to the converted data, yielding corresponding mean ENC values of $293 \pm 57\,\mathrm{e}^-$ and $333 \pm 56\,\mathrm{e}^-$.
As discussed in section 4.2, a proton beam with an energy of $221.06\,\mathrm{MeV\,u^{-1}}$ provides the minimal ionization signal across all beam settings used at HIT. Therefore, it defines the minimal required pixel threshold. Based on the measured CSA signal height distribution for this beam (Fig. 6.18) and the output characteristic of the CSA, the minimal ionization signal of the low-energy tail is around 70 mV, which corresponds to the injection voltage of 0.58 V. Hence, a threshold voltage value of 160 DAC units (corresponding to $\mu_{\mathrm{thr}} = 0.57\,\mathrm{V}$ and $\sigma_{\mathrm{thr}} = 0.01\,\mathrm{V}$) is sufficient to cover over 99.9 % of the collected charge distribution from such a beam for the sensor configured with `bias-DAC` settings B. For the sensor configured with `bias-DAC` settings A, the threshold voltage of 160 DAC units is also sufficient, since it corresponds to μ_{thr} of 0.53 V and σ_{thr} of 0.02 V. Based on the X-ray calibration, these μ_{thr} and σ_{thr} values translate into ($10\,910\,\mathrm{e}^-$, $387\,\mathrm{e}^-$) and ($11\,837\,\mathrm{e}^-$, $248\,\mathrm{e}^-$), for the sensors configured with `bias-DAC` settings A and B, respectively.

6.2.7. Limitations of the calibration procedure

Some of the HitPix3 characterization results presented in the previous subsections and in [ZTP26] are based on the calibration procedure to convert the known injection voltage pulses into the

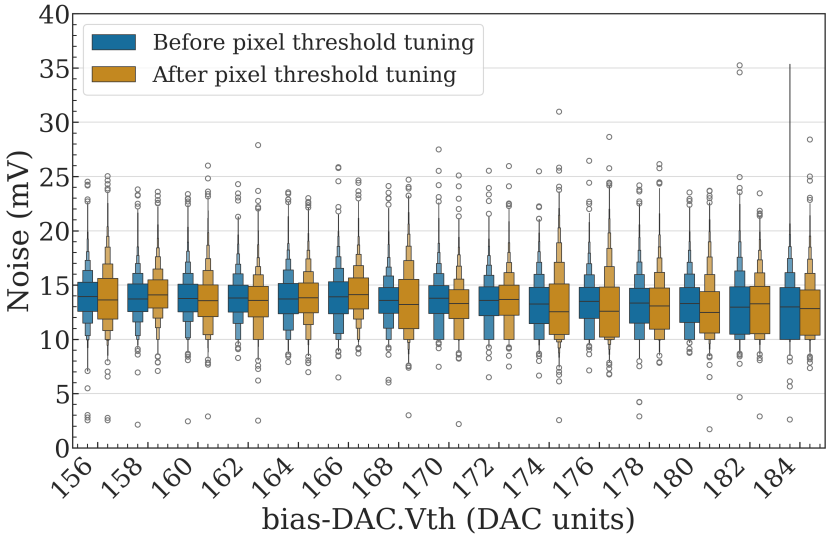


Figure 6.26.: Pixel noise distribution of HitPix3 before (blue) and after (orange) pixel threshold tuning at different threshold voltages. The sensor was configured with `bias-DAC` settings B.

equivalent injected charge. However, this method has certain limitations, which should be discussed to provide a valid interpretation of the results. The limitations arise from the accuracy of the Geant4 simulations of the experimental setups and the measurement method itself, and they can be treated separately.

The Geant4 simulation toolkit was used to estimate the MPV of the energy deposition for both the Sr-90 source and proton beams. The accuracy of the simulated MPV depends on several factors: the initial energy distribution, passive volumes that particle traverses before entering the sensor, and the active volume of the modeled sensor.

The `G4RadioactiveDecay` module of Geant4 is based on experimental nuclear data [Gea22] and was used to model an initial electron energy distribution of the Sr-90 source decay. In contrast, the proton beam was simulated as mono-energetic. This simplification is valid because the initial beam momentum spread at HIT does not exceed 0.3 % [Par+12]. Therefore, any error introduced by the initial energy distribution can be considered negligible for both particle sources.

In the Sr-90 setup, electrons emitted from the source traverse through a thin steel window of the source holder (50 µm), air (∼12 mm), and sensor passive layers, consisting of aluminum (5.33 µm) and silicon-dioxide (0.8 µm) before reaching the active volume of sensor. The passive layers can influence the energy distribution of low-energy electrons due to the energy loss in multiple scattering events.

The steel foil contributes the most to changes of initial electron energy spectrum. According to the Electron Stopping Powers and Range Tables (ESTAR) database [Ber+17], a 150 keV electron has a Continuous Slowing Down Approximation (CSDA) range in steel of ∼51 µm. In contrast, for the same electron the CSDA range in air, aluminum and silicon-dioxde is 26 cm, 136 µm, and 158 µm, respectively. Therefore, the majority of electrons with an initial energy lower than 150 keV will be stopped by the steel window and will not contribute to the energy deposition in the sensor. This low-energy cut in the initial electron energy spectrum explains the discrepancy between MPVs: 4211 e^- reported in [ZTP26] and 4070 e^- presented in subsection 6.2.4. The absence of the steel window (i.e. no low-energy cut) in the simulated setup of [ZTP26] allows low-energy electrons to reach the sensor with a thin depletion region.

The electrons with energies up to 80 keV deposit their full kinetic energy within the depletion region and contribute to the higher end of the measured spectrum relative to the MPV, thus slightly shifting (141 e^-) the MPV to higher values.
In the proton beam setup, the passive volumes of the vacuum exit window and BAMS detectors were modeled based on their exact geometrical position and properties, following the method described in [Par+12]. In this publication, various simulation setups were tested against the actual Bragg peak position measurements, resulting in satisfactory agreement between simulated and measurement results. Therefore, the simulation setup used for the HitPix3 calibration takes into account the changes induced in the initial proton beam energy spectrum by the interactions with passive volumes.
The final factor that limits the simulation result accuracy is the active volume of the modeled sensor. As described in subsection 6.2.4, the simulations took into account only charge carriers generated inside the depletion region, which is thinner than the total HitPix3 thickness of 850 µm. Hence, the estimation of the depletion region width becomes the major contributor to the overall simulation accuracy. The simulation results presented in the previous subsections rely on the nominal sensor substrate resistivity of 370 Ω cm. However, a ±10 % variation in the actual sensor resistivity would yield a change in the depletion width of approximately ±2.8 µm, resulting in a MPV shift of deposited charge from Sr-90 source of approximately ±210 e^-. Equation 6.1, used to estimate the depletion width at the given bias voltage and resistivity, was found to be in good agreement with the TCAD simulation results. The TCAD simulations were based on the exact doping concentrations in HitPix3 pixel and are presented in a master's thesis [Mar24]. However, the simulations did not take into account the significant contribution of the charge generated in the undepleted region in the total collected charge, as was shown in subsection 6.2.5, leading to a large underestimation of the collected charge by more than a factor of two. Hence, more advanced simulation techniques are required to accurately estimate the total charge collected by the partially depleted HV-CMOS sensors in response to an ionizing particle not fully absorbed in the sensor volume. These can be achieved in the future investigations with a combination of the TCAD and AllPix2 [Spa+18] simulation toolkits.
The measurement method is constrained by the number of CSAs that can be directly characterized and by the assumptions regarding their properties, such as output linearity and gain variations. Only 48 CSAs of HitPix3 pixels, located in the row closest to the peripheral electronics, can be directly measured, as explained in subsection 6.1.2. However, even if all 48 pixels were characterized and calibrated, this would still represent only 2.1 % of the total number of pixels in the sensor. Therefore, the method relies on the assumption of small variation in CSA parameters across all pixels in the sensor.
A third sensor was used to estimate the influence of the CSA parameters and their pixel-to-pixel variation on the calibration results. This sensor was used because the sensors presented in previous subsections were not available anymore for this study due to electrical damage. For the following measurements, the sensor voltages V_{bias} and V_{ssa} were set to −100 V and 1.10 V, respectively. The sensor was configured with `bias-DAC` settings C, which provides higher gain compared to settings A and B. Hence, at a fixed value of threshold voltage, more hits can be detected, since the pixel threshold decreases with the increased gain.
Figure 6.27 shows the ⟨Hit rate⟩ of HitPix3 pixels measured with the collimated Sr-90 source centered at pixel 35. As will be shown later, the `bias-DAC.ipload2` parameter controls the voltage gain of the in-pixel CSA, where a higher `ipload2` value corresponds to a smaller gain. It can be seen that the ⟨Hit rate⟩ of different pixels decreases for smaller gain values, as expected.
To further investigate the influence of the CSA configuration on the calibration results, the CSA output of pixel 35 was directly measured at `ipload2` values of 1, 10 and 30 DAC units. Due

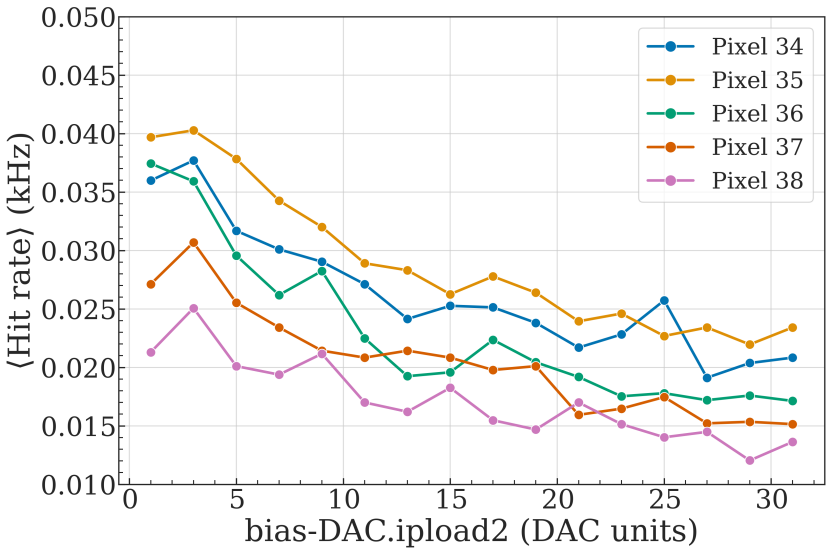


Figure 6.27.: ⟨Hit rate⟩ of HitPix3 pixels measured using a collimated Sr-90 source centered at pixel 35. Data were acquired for different `bias-DAC.ipload2` values, where higher `bias-DAC.ipload2` corresponds to a smaller CSA gain. The sensor was configured with `bias-DAC` settings C, and threshold voltage was set to 148 DAC units.

to changed bias voltage of −100 V (corresponds to a depletion width of 58.4 µm), a new Geant4 simulation was performed to estimate the MPV of the deposited charge, which yielded an MPV of 4295 e^-. It is important to note that in the following measurements, the Sr-90 source was used only to derive the calibration factors for the comparison purpose between different CSA settings or pixels and not for their absolute charge calibration because of non-negligible impact of the charge generated in the undepleted region, as previously discussed. The absolute charge calibration based on the X-ray measurements will be presented later in the text.
The measured MPVs and corresponding calibration factors of HitPix3 pixel 35, using the Sr-90 source at different `ipload2` are shown in table 6.6. The measured MPV changes from 59.3 mV to 40.4 mV with increasing `ipload2` from 1 DAC units to 30 DAC units.

Table 6.6.: Measured MPV and calibration factor of HitPix3 pixel 35 using the Sr-90 source at different CSA gain and a bias voltage of −100 V applied. The sensor was configured with `bias-DAC` settings C.

`bias-DAC.ipload2`	MPV (mV)	Calibration factor (e^- mV^{-1})
1 DAC units	59.3 ± 3.3	72.4 ± 3.2
10 DAC units	45.5 ± 3.4	94.5 ± 4.4
30 DAC units	40.4 ± 3.7	106.4 ± 5.2

The left plot of Fig. 6.28 shows the output characteristic of the in-pixel CSA, configured with different gains. Both Sr-90 source and charge injection measurements confirm the results obtained in the counter mode: a higher value of `ipload2` corresponds to a smaller CSA gain. However, after applying the calibration factor, the calibration points align only within a small injection voltage region up to 0.6 V, and diverge drastically at higher injection voltages as shown in the right plot of Fig. 6.28. These calibration results are completely different to that presented

in subsection 6.2.5, in which two different sensors measured at two different particle sources yielded calibration curves in good agreement. The divergence at higher injection voltages can be explained by the fact that `bias-DAC` settings C provides higher CSA gain at the cost of slight non-linearity of its output characteristic, while the injection charge calibration procedure relies on the linear response of CSA, i.e. the difference in the gain will be compensated by the calibration factor.

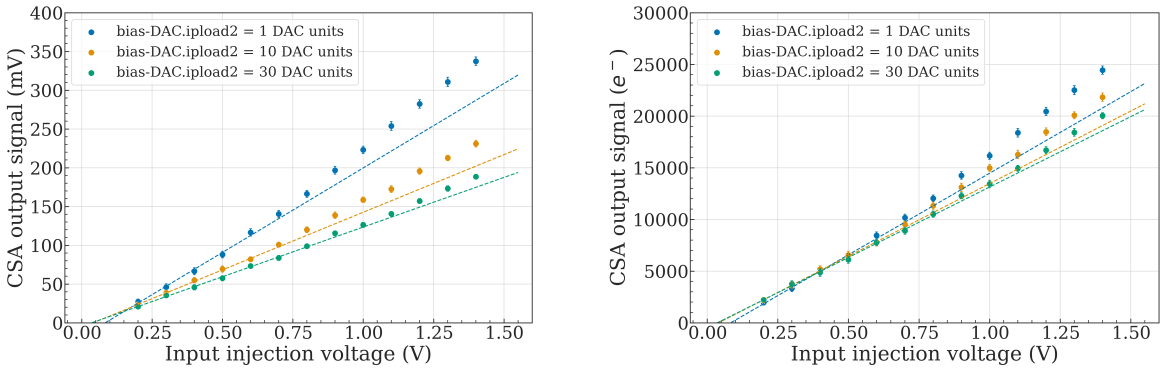


Figure 6.28.: Output characteristics of pixel CSA configured with different gains (left) and their calibration curves for the pixel charge injection circuit (right). The sensor was configured with a `bias-DAC` settings C. The `bias-DAC.ipload2` parameter was varied to 1 (blue points), 10 (orange points) and 30 DAC units (green points). For illustrative purpose, the linear fits performed on data points up to injection voltage of 0.6 V are shown as colored dashed lines. The results are based on the Sr-90 source calibration.

To confirm the non-linear behavior of the CSA at high gain, the charge injection measurement was performed for `bias-DAC` settings C. The results are shown in Fig. 6.29 in which mean pixel thresholds clearly demonstrate non-linear behavior across the applied threshold voltages compared to the linear results in Fig. 6.24.

From these results, it can be concluded that the calibration results for the high CSA gain settings should be considered valid only at small input injection voltages in which the influence of the non-linearity of CSA output characteristic is minimal. Therefore, the calibration points were fitted with a linear function only for input injection voltages from 0.2 V to 0.6 V to extract the slope ($a_{0.2-0.6}$) and intercept ($b_{0.2-0.6}$) parameters. The extracted parameters are given in table 6.7, which also includes the linear fit parameters across the full input injection voltage range for comparison ($a_{0.2-1.4}$ and $b_{0.2-1.4}$). The calculated injected charge for a 0.4 V injection voltage pulse, derived from the small injection voltage signal fits, was found to be 4994 e^-, 5039 e^- and 4956 e^- for `ipload2` of 1, 10 and 30 DAC units, respectively. These values are well in agreement, validating the applied method for the CSA configured with a high gain.

The measured Sr-90 source MPV of 59.3 mV corresponds to the input injection voltage of 0.36 V based on the CSA output characteristic. The mean pixel threshold (μ_{thr}) after tuning equals 0.29 V and 0.32 V at the threshold voltage of 145 DAC units and 146 DAC units for the sensor configured with the `bias-DAC` settings C. Therefore, these threshold voltages allow to configure the pixels with a thresholds lower than the MPV of the Sr-90 source. To validate this, the CSA of pixel 35 was measured with the feedback boost circuit enabled, while the threshold voltage was set to 145 DAC units and 146 DAC units. The measured CSA output signal height distributions using the Sr-90 source are shown in Fig. 6.30. The enabled feedback boost circuit indeed truncates the distribution (more details in subsection 6.2.5) at values smaller than MPV

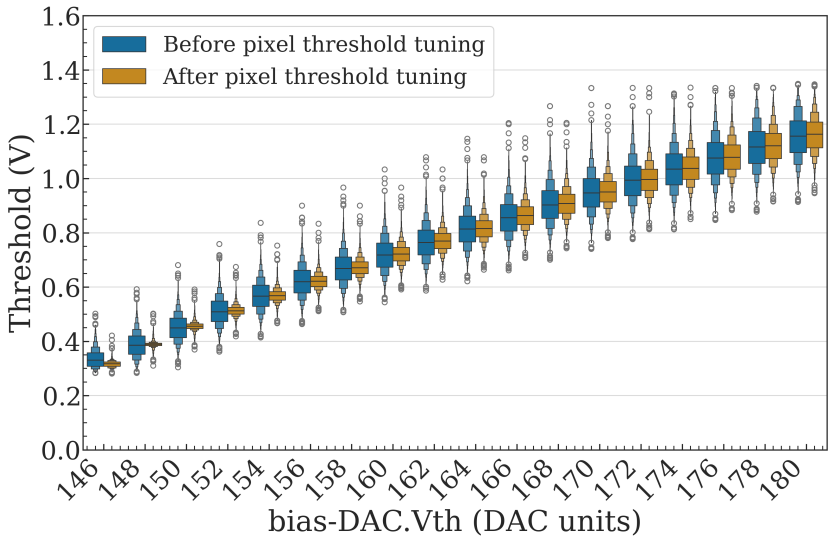


Figure 6.29.: Measured pixel threshold distribution before (blue) and after (orange) pixel threshold tuning at different threshold voltages. The sensor was configured with `bias-DAC` settings C.

Table 6.7.: Calibration curve parameters for HitPix3 pixel 35 injection circuit at different CSA gain the applied bias voltage of −100 V. The sensor was configured with `bias-DAC` settings C.

`bias-DAC.ipload2`	$a_{0.2-1.4}$ ($e^- V^{-1}$)	$b_{0.2-1.4}$ (e^-)	$a_{0.2-0.6}$ ($e^- V^{-1}$)	$b_{0.2-0.6}$ (e^-)
1 DAC units	18 860 ± 260	−2530 ± 200	15 790 ± 950	−1320 ± 380
10 DAC units	16 350 ± 240	−1456 ± 190	14 040 ± 890	−580 ± 350
30 DAC units	14 620 ± 210	−895 ± 170	13 620 ± 810	−490 ± 300

for the threshold voltages used in the test (shown as blue and orange distributions in the figure), confirming that the extracted pixel thresholds lie in the specified range.
The final factor that limits the measurement method is the pixel-to-pixel variation of the CSA parameters. The CSAs of several pixels were calibrated using the Sr-90 source. The exact values of the measured MPVs and calculated calibration factors for each pixel are given in the Appendix in table C.3. The weighted average of the measured MPVs equals 59.1 ± 1.3 mV, with a reduced χ^2_ν value of 1.30, i.e. the measured pixel MPVs are consistent with each other, considering their measurement uncertainties.
The output characteristics of the measured pixels and their calibration curves for the charge injection circuits are shown in Fig. 6.31. The output characteristics are grouped together and follow a similar behavior across the pixels. As in the measurements with different gain settings for a single pixel, the calibration points are aligned in the small input voltage range up to 0.6 V and diverge at the higher injection values, confirming the non-linearity of the sensor configured with the `bias-DAC` settings C and that the calibration procedure is valid only in the small injection voltage range.
To estimate the sensor parameters configured with the `bias-DAC` settings C, the sensor was calibrated at the X-ray setup. The measured spectra of the molybdenum, silver, indium and tin targets are shown in the Appendix in Fig. C.9. The CSA output calibration curve has a slope of 99.16 ± 1.52 $e^- mV^{-1}$ and intercept 1318 e^-, which were derived from a linear fit of

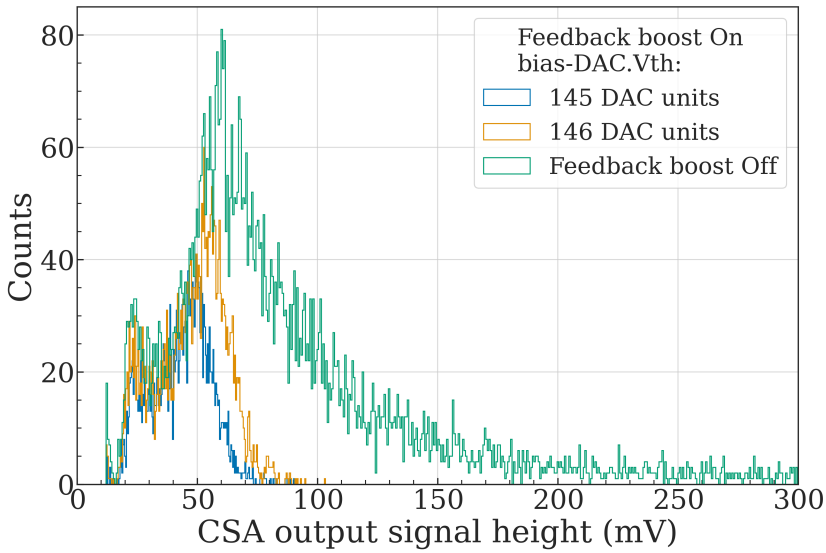


Figure 6.30.: CSA output signal height distributions using the Sr-90 source and enabled/disabled feedback boost circuit at different threshold voltages. The green distribution corresponds to the disabled feedback boost circuit. The blue and orange distributions correspond to the enabled feedback boost circuit and threshold voltages of 145 DAC units and 146 DAC units, respectively. The sensor was configured with `bias-DAC` settings C.

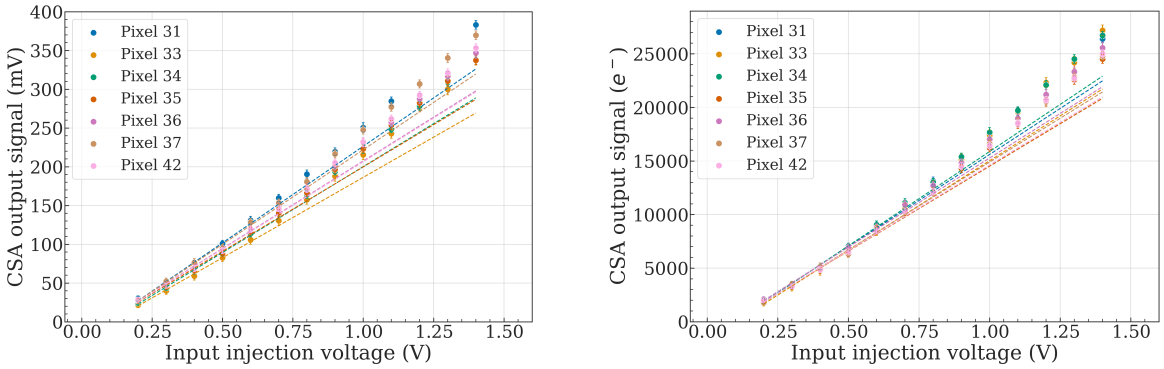


Figure 6.31.: Output characteristics of different pixel CSAs (left) and their calibration curves for the charge injection circuits (right). The sensor was configured with `bias-DAC` settings C. For illustrative purpose, the linear fits performed on data points up to injection voltage of 0.6 V are shown as colored dashed lines. The converted signals are based on the Sr-90 source calibration.

the known deposited charge of the K_α photons versus measured MPVs. After applying these parameters to the measured MPV of the Sr-90 source, the total collected charge was found to be 7188 e^-. Hence, the diffusion component in the total collected charge is 40.2 %, which is smaller than that value of ∼60 % presented in subsection 6.2.5, since the contribution of the particles with large angles relative to the sensor normal was suppressed by collimating the Sr-90 source.

The calibration parameters were applied to the CSA output characteristic in a small input injection voltage range from 0.2 V to 0.6 V, yielding the calibration slope ($a_{0.2-0.6}$) and intercept ($b_{0.2-0.6}$) parameters for the charge injection circuit of $21\,612 \pm 1296\,e^-\,V^{-1}$ and $-490 \pm 521\,e^-$,

respectively. Based on this calibration and charge injection measurements, the mean ENC of the sensor was found to be $292 \pm 40\,e^-$. The mean pixel thresholds were found to be $5438\,e^-$ and $6355\,e^-$ at the threshold voltage of 145 DAC units and 146 DAC units, respectively.
The extracted calibration slope, intercept and mean ENC are well in agreement with the corresponding values presented in subsections 6.2.5 and 6.2.6 for the different sensors configured with `bias-DAC` settings A and B. Hence, these results further validate the X-ray based calibration and the applied method for the charge injection calibration for the CSA configured with the high gain.
For the beam monitoring application, the non-linearity of the CSA output is not a critical issue, since the primary function of the HitPix3 sensor is to count incoming particles. Furthermore, the higher gain allows to achieve a small pixel threshold, which becomes essential for detecting high-energy protons with small ionization signals. Therefore, the optimal strategy for setting the threshold voltage for detecting high-energy protons is to set it as low as possible at the highest gain, while maintaining the fraction of noisy pixels below 5 %. Based on the X-ray calibration results, the minimal achievable pixel threshold of HitPix3 varies from $5438\,e^-$ to $11\,837\,e^-$, while the mean ENC varies from $292\,e^-$ to $333\,e^-$, depending on the configuration settings. These values are smaller than the expected minimal ionization signal generated by high-energy proton beam at HIT.

6.2.8. Counter and adder readout modes

After the detailed characterization of the HitPix3 pixel parameters described in subsections 6.2.5, 6.2.6 and 6.2.7, the counter and adder readout modes of the sensor, which are the most important functions for the beam monitoring application, were verified.
The counter and adder readout modes of both HitPix3 sensors, configured with `bias-DAC` settings A and B, were tested with the Sr-90 source and the proton beam with a nominal energy of $221.06\,\mathrm{MeV\,u^{-1}}$, respectively. The sensor baseline voltage and readout speed were fixed to 1.0 V and $180\,\mathrm{Mbit\,s^{-1}}$. The proton beam was delivered in spills with a duration of $\sim$5 s and intensity setting of 2×10^8 pps. The frame duration t_{frame} was set to 5 ms and 60 µs in the Sr-90 source and proton beam measurements, respectively. All measurements were performed at room temperature. The beam test at HIT was conducted in January 2024.
Figure 6.32 shows the cumulative Sr-90 source profile measured using the HitPix3 sensor in counter mode before and after pixel threshold tuning. For this measurement, the global threshold voltage was set to 160 DAC units. If a pixel ⟨Hit rate⟩ exceeded 0.01 kHz in a measurement without Sr-90 source at a given threshold voltage, it was marked as noisy and masked. The noise cutoff value corresponds to approximately 0.8 % of the smallest expected pixel ⟨Hit rate⟩ in the carbon beam center with a nominal energy of $88.83\,\mathrm{MeV\,u^{-1}}$ and intensity of 2.5×10^6 pps measured at HIT. This allows to reliably measure the particle hit rate for the smallest expected ⟨Hit rate⟩ at the HIT beamline and to estimate the fraction of noisy pixels in a laboratory environment.
Before and after pixel threshold tuning, 30 and 27 pixels were found noisy, respectively, corresponding to 1.30 % and 1.17 % of the total number of pixels. Lower threshold voltages increase the fraction of noisy pixels. At the threshold voltage of 154 DAC units the fraction of noisy pixels reaches 16 %. Examples of ⟨Hit rate⟩ measured using the HitPix3 sensor in counter mode without the Sr-90 source at the threshold voltage of 154 DAC units and 160 DAC units are shown in the Appendix in Fig. C.10.
All measured HitPix3 sensors share a similar noisy pixel location pattern: most of the noisy pixels were found at the central columns and near the sensor edges. One possible explanation of this effect is the complex routing of the pixel adders to support two-dimensional projection calculation, which could introduce digital crosstalk. However, a validation this hypothesis

would require detailed sensor simulation and falls outside the scope of this thesis. Nonetheless, this observation could provide an important insight for the design of the next HitPix4 sensor.

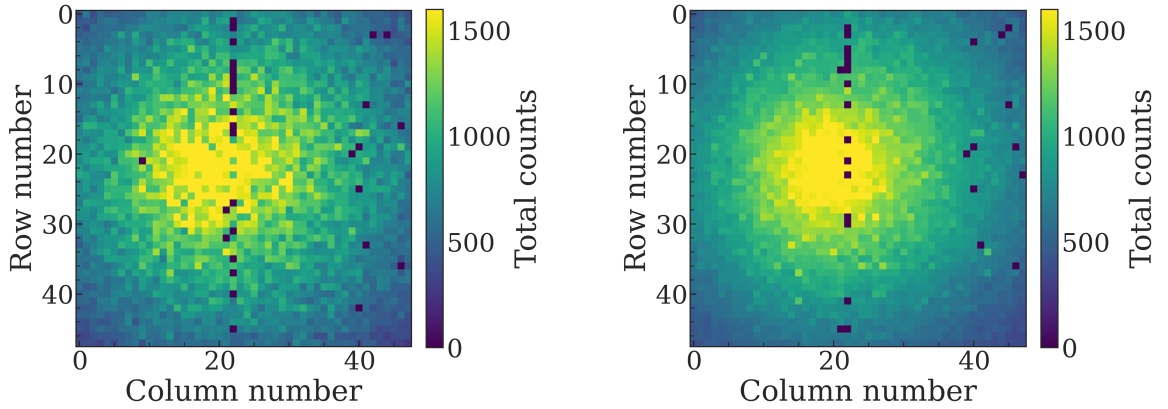


Figure 6.32.: Cumulative Sr-90 source profile measured using the HitPix3 sensor in **counter mode** before (left) and after (right) pixel threshold tuning. Frame duration: 5 ms. Number of frames: 3000. The sensor was configured with `bias-DAC` settings A.

A cumulative proton beam profile with a nominal energy of 221.06 MeV u^{-1}, obtained during one spill and measured with the HitPix3 sensor in counter mode before and after pixel threshold tuning is shown in Fig. 6.33. For these measurements, the threshold voltage was not optimal and was set to a very high value of 175 DAC units, since the accurate calibrations were performed only after the beam test. As a result, the fraction of noisy pixels was 0 %, but it came at the cost of missing 28 % of the collected charge distribution, corresponding to the small deposition energy of the Landau distribution below the MPV.

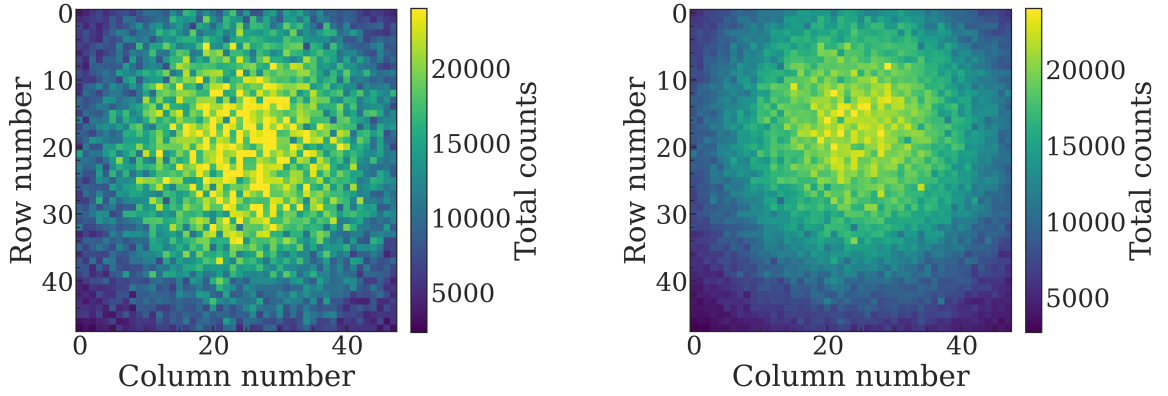


Figure 6.33.: Cumulative proton beam profile with a nominal energy of 221.06 MeV u^{-1} measured using the HitPix3 sensor in **counter mode** before (left) and after (right) pixel threshold tuning. Frame duration: 60 µs. Number of frames: 6200 (one spill). The sensor was configured with `bias-DAC` settings B.

After pixel threshold tuning, the measured spot profile shows improved regularity and smoother contours for both measurements with Sr-90 source and proton beam. This is a direct result of the reduction in pixel-to-pixel threshold variation. Therefore, the pixel threshold tuning ensures that the majority of pixels respond uniformly to incoming particles. For the proton beam measurement, the observed small changes in the beam position after the pixel threshold tuning is explained by the inherent small variations of beam position at HIT.

The same beneficial effect of the pixel threshold tuning is shown in the cumulative X- and Y-projections of the Sr-90 source and proton beams measured with the HitPix3 sensor in adder mode, which are shown in Fig. 6.34 and Fig. 6.35.

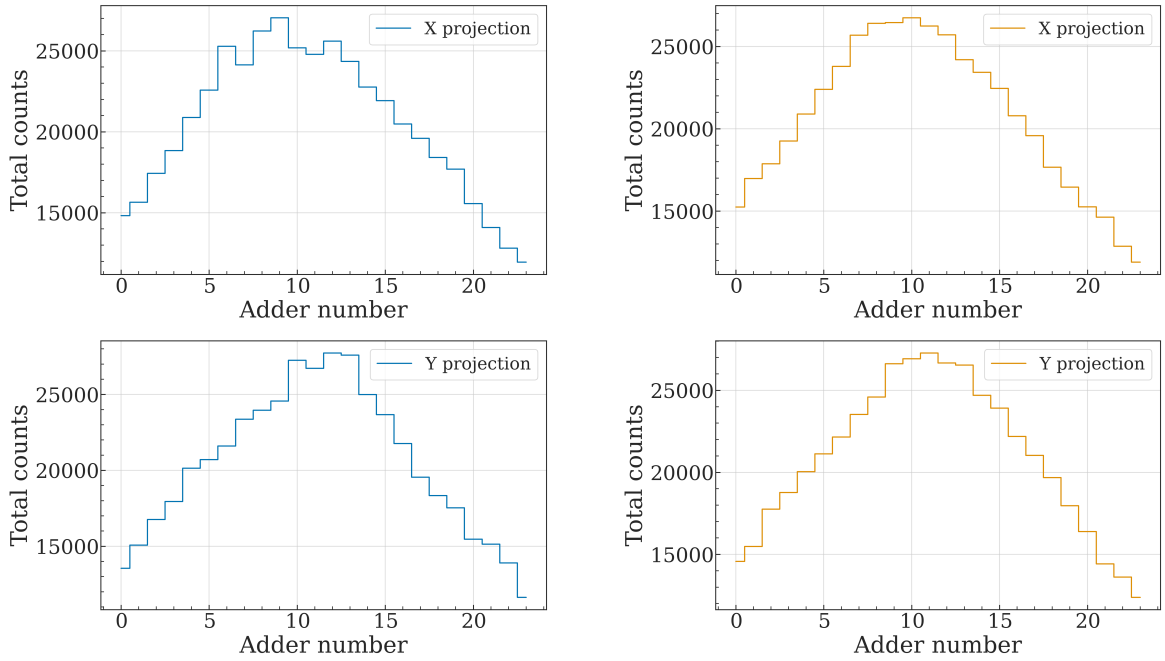


Figure 6.34.: Cumulative X- (top) and Y- (bottom) projections of the Sr-90 source profile measured using the HitPix3 sensor in **adder mode** before (blue lines) and after (orange lines) pixel threshold tuning. Frame duration: 5 ms. Number of frames: 3000. The sensor was configured with `bias-DAC` settings A.

The presented results validate the functionalities of counter and adder readout modes and demonstrate the beneficial effect of pixel threshold tuning. The pixel threshold tuning improves the detection performance for small ionization signals, such as those from the Sr-90 source and the proton beam with a nominal energy of 221.06 MeV u^{-1}, since they are close to the pixel threshold, which makes them very sensitive to its variation. In contrast, the measured carbon beam profiles yield similar results before and after tuning, as shown in the Appendix in Fig. C.11. Further optimizations for the detection of the smallest ionization signals at HIT are covered in subsections 6.2.7 and 6.2.10.

6.2.9. Pixel masking

Following the successful tests of both counter and adder readout modes, the final new feature of the HitPix3 sensor, pixel masking, was tested.

This feature was implemented in the HitPix3 design to disable selected pixel output when needed. As explained in subsection 6.1.2, it can be done by setting the fifth bit of the pixel RAM cell to a logic high state.

Figure 6.36 shows the cumulative Sr-90 source profile measured in HitPix3 counter mode with a masking pattern applied. The measurement validates the masking feature functionality, which can be used to suppress the influence of the radiation damaged pixels with a very high noise level in both readout modes.

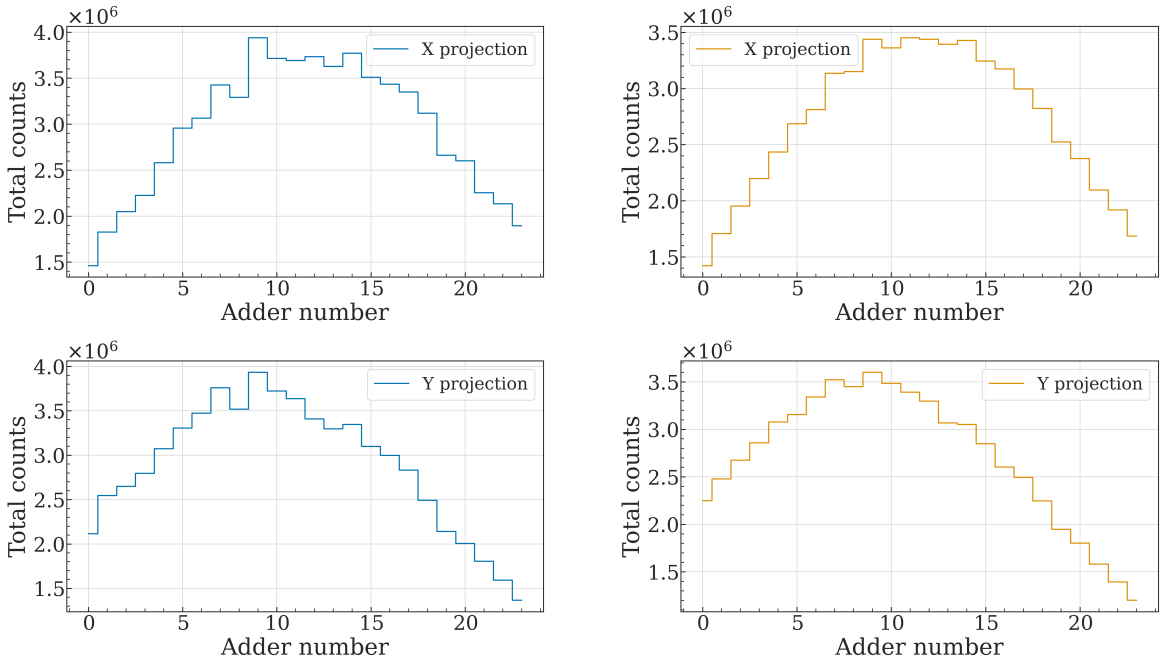


Figure 6.35.: Cumulative X- (top) and Y- (bottom) projections of the proton beam profile with a nominal energy of 221.06 MeV u^{-1} measured using the HitPix3 sensor in **adder mode** before (blue lines) and after (orange lines) pixel threshold tuning. Frame duration: 60 µs. Number of frames: 57796 (one spill). The sensor was configured with `bias-DAC` settings B.

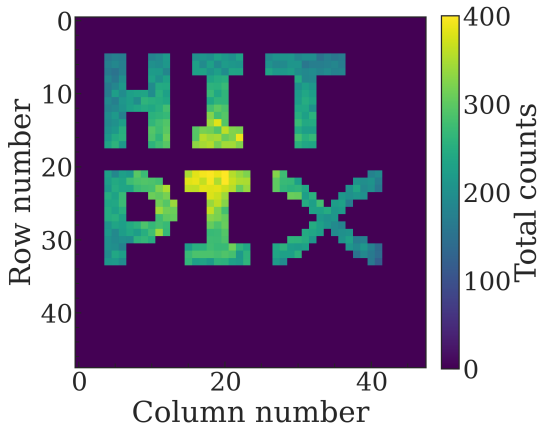


Figure 6.36.: Cumulative Sr-90 source profile measured using the HitPix3 sensor in **counter mode** with a masking pattern applied. Frame duration: 5 ms. Number of frames: 1000.

6.2.10. Performance at high particle rates

To test the HitPix3 performance at high particle rates against the HitPix2 results (subsection 5.4.1), proton and carbon beams were measured with a single HitPix3 sensor under the same nominal beam settings during the beam test at HIT in March 2025.

The HitPix3 sensor was configured with `bias-DAC` settings C. The applied voltages V_{bias}, V_{dda}, V_{ssa}, and V_{bl} were set to −100 V, 1.92 V, 1.10 V, and 1.0 V, respectively. The frame

duration t_{frame} was set to 50 µs. All measurements were performed at room temperature in counter mode after pixel threshold tuning.
The threshold voltages were set to 141 DAC units and 135 DAC units for carbon and proton beam measurements, respectively. These values are lower than those presented in the previous subsection due to increased threshold voltage scale, which depends on the V_{dda} voltage. A dedicated CSA calibration for this sensor settings was not performed during the beam test. Instead, the threshold voltage of 135 DAC units was chosen based on the strategy discussed at the end of subsection 6.2.7, i.e. this value provides the minimal achievable pixel threshold before the fraction of noisy pixels exceeds 5 %. Taking into account the calibration results for the sensor configured with `bias-DAC` settings C, the threshold voltage ensures that the pixel thresholds across the sensor were below the expected minimal ionization signal at HIT conditions. The fraction of noisy pixel was measured to be 1.4 %. The noisy pixels were masked during the proton beam measurements.
When a carbon ion hits a pixel, the CSA output signal height saturates, due to the large number of generated electron-hole pairs. Therefore, a small increase in threshold voltage is beneficial, since it reduces the fraction of noisy pixels to 0 %, while maintaining the mean pixel threshold below the expected signal level.
The total number of hits per frame of carbon and proton beams measured with HitPix3 sensor at different beam intensities are shown in Fig. 6.37. By comparing these integral characteristics with the HitPix2 results (subsection 5.4.1, Fig. 5.22), the HitPix3 demonstrates improved performance for both beam types.

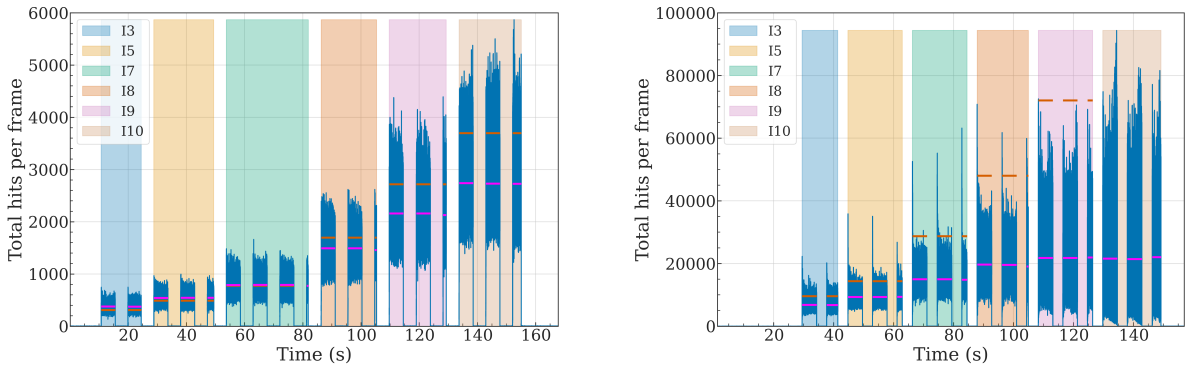


Figure 6.37.: Total number of hits per frame of carbon (left) and proton beams (right) measured using the HitPix3 sensor at different beam intensities. The orange and magenta horizontal lines represent expected and measured ⟨Total hits per frame⟩, respectively. Spills belonging to one beam intensity setting are marked with vertical color bands, as follows: I3 - blue, I5 - orange, I7 - green, I8 - red, I9 - purple, I10 - brown.

For carbon beams, the spill structures follow the expected behavior across all beam intensities: a ramp-up at the beginning of the spill and fluctuation with stable average around the mean hits per frame value. The relative difference between expected and measured ⟨Total hits per frame⟩ is around 26 % at the highest intensity I10, whereas the HitPix2 had a value of 78 %.
For the proton beams, an issue with the HV power supply (more details in subsection 5.4.1) was resolved by setting the bias current compliance to a higher value. Consequently, the measured spill structures do not degrade at beam intensity settings beyond I7, as in the HitPix2 measurements. In HitPix2 measurements, the relative difference between expected and measured ⟨Total hits per frame⟩ increases from 75 % for the smallest beam intensity I3 and

reaches 85 % for the beam intensity I7. In contrast, the HitPix3 sensor shows a value of 29 % for the beam intensity I3 and 48 % for the beam intensity I7. Starting from beam intensity I8, the ⟨Total hits per frame⟩ changes within a small range, and the fluctuation around the mean value increases with the beam intensity. This can be explained by the influence of the pileup and baseline drop effects, which were discussed in subsection 5.4.2.
To assess the HitPix3 counting capability on the pixel level, the expected pixel hit rate was estimated with the same algorithm and assumptions as for the HitPix2, which are discussed in subsection 5.4.1. An example of the measured and expected ⟨Hit rate⟩ distributions across HitPix3 pixels for the carbon beam with intensity I7 is shown in Fig. 6.38. As expected from the integral intensity plot of Fig. 6.37, these distributions are well in agreement.

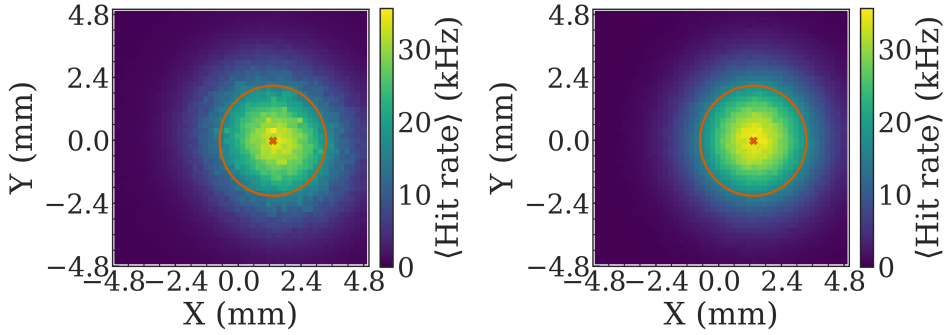


Figure 6.38.: Measured (left) and expected (right) ⟨Hit rate⟩ distribution across HitPix3 pixels for the carbon beam with intensity I7. The orange cross and ellipse represent the estimated beam position and FWHM.

Figure 6.39 shows the measured versus expected ⟨Hit rate⟩ for all carbon beam intensities in which the feedback boost circuit of the HitPix3 sensor was disabled. The measured ⟨Hit rate⟩ follows the ideal sensor behavior (black dashed line) up to intensity I7. In contrast, the measured ⟨Hit rate⟩ of HitPix2 sensor followed the ideal curve only for the smallest intensity I3 (subsection 5.4.1, Fig. 5.24). Furthermore, the HitPix3 distribution does not saturate at the high beam intensities compared to the HitPix2 results. The maximum measured pixel ⟨Hit rate⟩ for HitPix3 exceeds 100 kHz, whereas HitPix2 could only achieve 50 kHz at the highest beam setting I10.
To quantify and compare the performance between HitPix2 and HitPix3, the combined distribution across all beam settings was fitted with the original and modified Takács' formulas (equations 5.5 and 5.6, respectively). The fit results from both formulas yielded consistent parameters and are presented in table 6.8.

Table 6.8.: Fit parameters for the original and modified Takács' formulas for the HitPix3 sensor in 430.10 MeV u^{-1} carbon beam measurements. The R^2 stands for the coefficient of determination of the fit.

Formula type	ϵ	θ	τ (µs)	R^2
Original	1	0.00 ± 0.01	3.91 ± 0.01	0.981
Modified	0.933 ± 0.001	0.00 ± 0.01	3.13 ± 0.02	0.981

As expected, the θ value of 0 aligns with the HitPix2 results, since the expected pixel hit rate for the carbon beam is low compared to the proton beams (more details in subsection 5.4.2), leading to a non-paralyzable pixel dead time behavior. A slight reduction of the efficiency parameter ϵ

of 0.933 for HitPix3 results can be considered negligible, because the modified formula was introduced to address the misconfiguration of the HitPix2 sensor with a high pixel threshold, which led to a very poor fit of the original formula in proton beam measurements, which is not present in the HitPix3 results. Moreover, the HitPix3 fit results of the original formula with an efficiency of 1 and the modified formula, yielded the same coefficient of determination R^2 of 0.981, i.e. both models perfectly describe the measured distribution.

The most critical improvement compared to the HitPix2 results is the reduction of the dead time parameter by more than a factor of four, derived from both formulas. This confirms the improved performance of the HitPix3 sensor compared to HitPix2 due to new ISO pixel topology, the pMOS-based design of the CSA and the optimized `bias-DAC` settings. These results are consistent with the integral characteristic presented above.

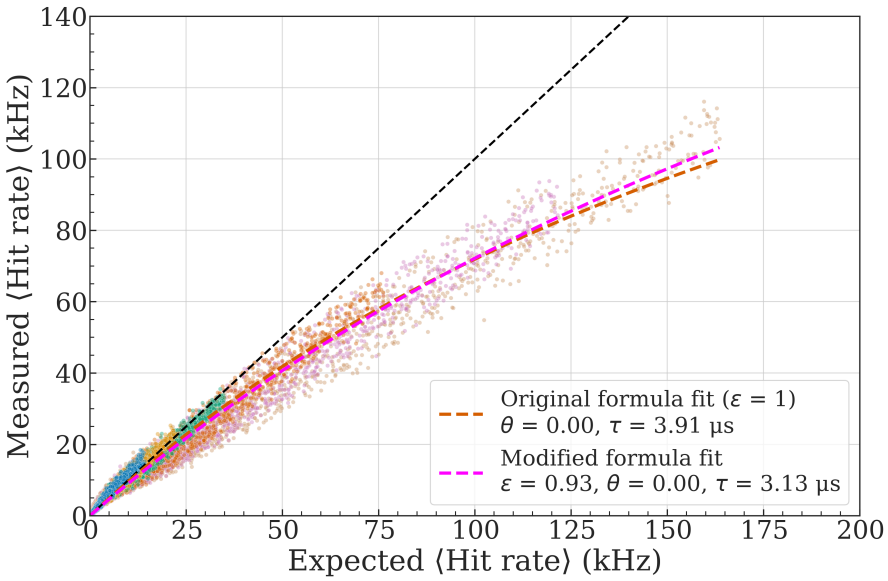


Figure 6.39.: Measured versus expected pixel ⟨Hit rate⟩ of a HitPix3 sensor at different carbon beam intensities. The feedback boost was disabled during the measurement. The black dashed line represents the ideal sensor behavior with zero dead time and 100 % detection efficiency. The orange and magenta dashed lines represent the fit curve of original and modified Takács' formula, respectively. Points are colored w.r.t. beam intensity: I3 - blue, I5 - orange, I7 - green, I8 - red, I9 - purple, I10 - brown.

The measurement results of the HitPix3 sensor for proton beams are shown in Fig. 6.40. The measured ⟨Hit rate⟩ is close to the ideal sensor behavior up to intensity I7, and starts to saturate beyond this beam intensity setting. As expected, the distribution has an increased spread of the measured ⟨Hit rate⟩ compared to carbon beam measurements, due to pileups and baseline drops. However, for the first time, the maximum ⟨Hit rate⟩ measured with proton beams exceeds the value of 350 kHz. Such a high pixel hit rate was observed in HitPix2 sensor only in measurements with an IR LED in which the pileup and baseline drop effects were excluded.

The fit of the original and modified Takács' formula applied to the proton beam measurements yielded the values presented in table 6.9.

The fit results of the original and modified formulas provide the same fit quality based on R^2 metric. In contrast, the HitPix2 fit results had R^2 of 0.757 and 0.419 for modified and original

Table 6.9.: Fit parameters for the original and modified Takács' formulas for the HitPix3 sensor in 221.06 MeV u^{-1} proton beam measurements. The R^2 stands for the coefficient of determination of the fit.

Formula type	ϵ	θ	τ (µs)	R^2
Original	1	0.31 ± 0.01	2.61 ± 0.02	0.736
Modified	0.88 ± 0.01	0.53 ± 0.02	2.21 ± 0.03	0.739

formulas, correspondingly. For both sensors, the fit qualities are lower than in carbon beam measurements, due to higher spread of the measured ⟨Hit rate⟩.

To confirm that the sensor configuration indeed provides the minimal achievable pixel thresholds across all pixels, an additional measurements was performed using a 156.35 MeV u^{-1} proton beam, which induces larger ionization signals than the 221.06 MeV u^{-1} proton beam. The measurement results are shown in the Appendix in Fig. C.12. The fit parameters of the modified Takács' formula ($\epsilon = 0.88 \pm 0.01$, $\theta = 0.51 \pm 0.04$, and $\tau = 2.21 \pm 0.03$ µs) are in good agreement with 221.06 MeV u^{-1} proton beam results. If the pixel thresholds were set higher than the minimal expected ionization signal from 221.06 MeV u^{-1} protons, the efficiency parameter would be higher for the 156.35 MeV u^{-1} protons, as was observed in HitPix2 measurements.

The probability that the pixel dead time is extended by a subsequent incoming particle (θ) is within a range from 0.3 to 0.55 and indicates that the pixel dead time behavior is changed from non-paralyzable to partially paralyzable. This is expected, due to the increased probability of pileup and baseline drops for the high-intensity proton beams. Furthermore, the θ parameter is significantly smaller than that for the HitPix2 sensor, which had a fully paralyzable behavior of the pixel dead time with a θ value of 1.

The dead time parameters (τ) are smaller than that in the carbon beam measurements because the CSA output signals in response to protons are typically shorter due to smaller ionization compared to carbon ions.

Based on the direct HitPix3 CSA output measurements, a typical pulse duration induced by 221.06 MeV u^{-1} proton varies within a range approximately from 1.2 µs to 3.4 µs, while for the 430.10 MeV u^{-1} carbon ion it varies within a range approximately from 6 µs to 10 µs, these values are aligned well with the maximum measured pixel ⟨Hit rate⟩ for both beam types. Therefore, to further increase the sensor performance at high beam intensities, the duration of the CSA output signal should be shortened to reduce the probability of pileup events.

For this purpose, additional 430.10 MeV u^{-1} carbon beam measurements were performed using the same sensor and `bias-DAC` settings C, but with enabled feedback boost circuit. The measurement results are shown in Fig. 6.41. As in the measurements with disabled feedback boost, the measured ⟨Hit rate⟩ follows the ideal sensor behavior up to intensity I7. However, beyond this beam intensity, the ⟨Hit rate⟩ degrades drastically – the distribution saturates, and the maximum measured pixel ⟨Hit rate⟩ does not exceed 80 kHz. As a result, both τ and θ are increased.

To understand this unexpected behavior, direct measurements of the CSA output were performed with enabled feedback boost circuit. The results are shown in the Appendix in Fig. C.13 in which CSA output signals with disabled feedback boost are included for comparison. As expected, the feedback boost circuit indeed shortens the CSA signals and truncates their amplitudes. However, the subsequent long baseline recovery time caused by the continuous reset circuit after the large reset current source is disconnected (more details in subsection 6.2.5),

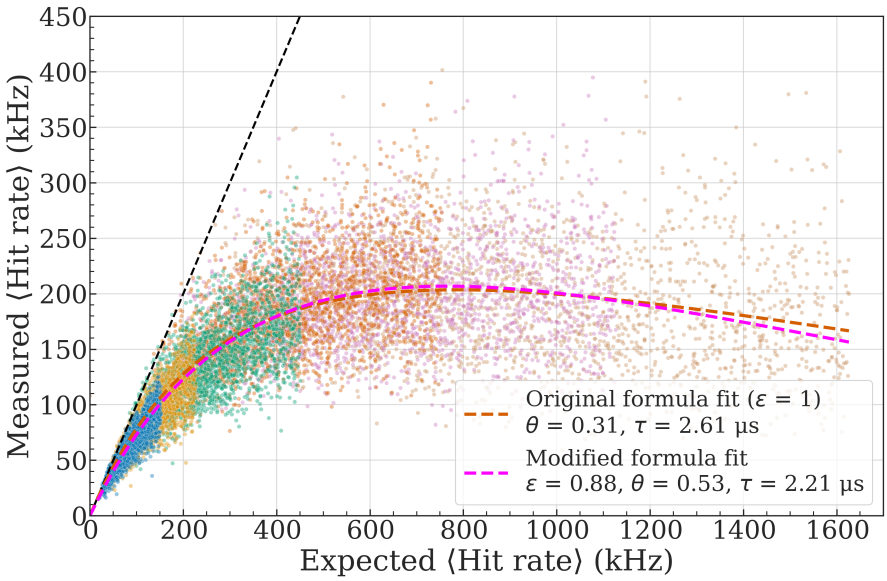


Figure 6.40.: Measured versus expected pixel ⟨Hit rate⟩ of a HitPix3 sensor at different proton beam intensities. The feedback boost was disabled during the measurement. The black dashed line represents the ideal sensor behavior with zero dead time and 100 % efficiency. The orange and magenta dashed lines represent the fit curve of original and modified Takács' formula, respectively. Points are colored w.r.t. beam intensity: I3 - blue, I5 - orange, I7 - green, I8 - red, I9 - purple, I10 - brown.

makes the baseline less stable and susceptible to baseline drop effect, thus, increasing the pixel dead time and probability of the dead time extension.
Based on HitPix3 measurement results with the carbon and proton beams and disabled feedback boost circuit, it can be concluded that the modifications introduced in HitPix3 design (ISO pixel topology and pMOS based amplifier) together with the optimal `bias-DAC` parameters settings significantly improved the high pixel hit rate capability and the sensor tolerance to the negative effects of pileup and baseline drop, when compared to its predecessor HitPix2. To further improve the sensor performance at high beam intensities, several modifications are required in the CSA design and feedback boost circuit, and, therefore, can be only introduced in a new HitPix4 design. The required modifications are discussed in section 6.5.

6.2.11. Radiation hardness

To assess the HitPix3 sensor performance after significant radiation damage, several sensors were homogeneously irradiated with 23 MeV proton beam at Zyklotron AG (ZAG) [ZAG25]. During irradiation, the sensors received a 1 MeV neutron equivalent fluence of $\sim 1 \times 10^{15}\,\mathrm{cm}^{-2}$. To compare their performance against an unirradiated HitPix3 sensor, one of the irradiated sensors was tested with 430.10 MeV u^{-1} carbon beams in the same beam intensity range from I3 to I10 during the beam test at HIT in January 2024.
In the following measurements, the irradiated sensor was configured with `bias-DAC` settings B, V_{dda} and V_{ssa} were set to 1.85 V and 1.25 V, respectively. This configuration provides low CSA gain, as discussed in subsection 6.2.7, and it was used because the beam test was conducted before the optimal `bias-DAC` settings and applied voltage levels were found. However, for carbon beams, the difference in CSA gain is not critical, due to the large ionization signals induced by the ions. The irradiated sensor had an increased leakage current due to radiation

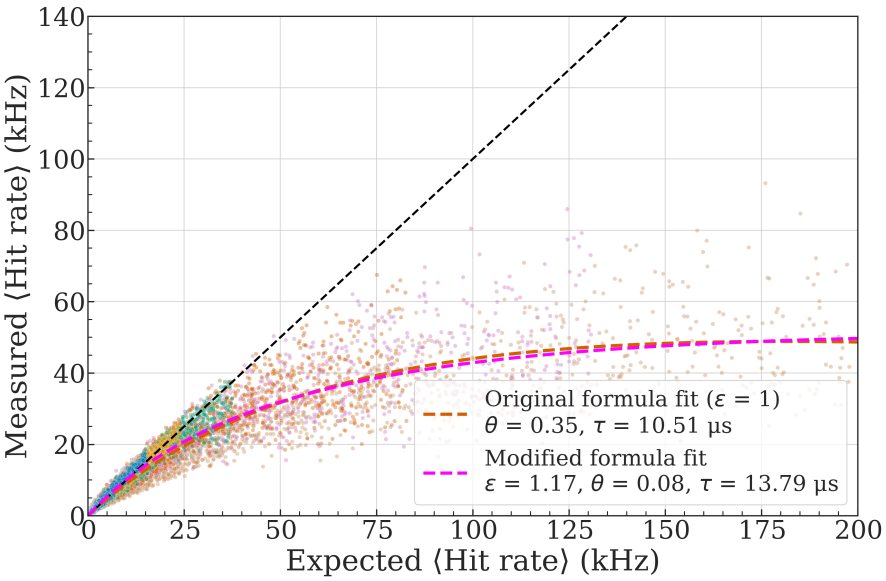


Figure 6.41.: Measured versus expected pixel ⟨Hit rate⟩ of a HitPix3 sensor at different carbon beam intensities. The feedback boost was enabled during the measurement. The black dashed line represents the ideal sensor behavior with zero dead time and 100 % detection efficiency. The orange and magenta dashed lines represent the fit curve of original and modified Takács' formula, respectively. Points are colored w.r.t. beam intensity: I3 - blue, I5 - orange, I7 - green, I8 - red, I9 - purple, I10 - brown.

damage, therefore, V_{bias} was set to -50 V to maintain the leakage current below 200 µA at room temperature. The threshold voltage was set to 155 DAC units, and the frame duration t_{frame} was set to 400 µs. The measurements were performed in counter mode after pixel threshold tuning.

The total number of hits per frame of the carbon beam measured with the irradiated HitPix3 sensor at different beam intensities are shown in Fig. 6.42. The total number of hits per frame in the figure is higher than those for the unirradiated sensor (subsection 6.2.10, Fig. 6.37) due to eight times longer frame duration. This can be confirmed by comparing the ⟨Total hits per frame⟩ at low intensity I3 in which pileup events are excluded. For the unirradiated sensor this value is approximately 377, whereas the irradiated sensor has a value of 2838, yielding a ratio of 7.53, which is close to the expected factor of eight, especially considering that the measurements were performed in two different beam tests. The spill structure does not degrade and follows the structure measured with the unirradiated sensor. Moreover, the relative difference between expected and measured ⟨Total hits per frame⟩ is around 19.5 % at beam intensity I10, which is even better than that for the unirradiated sensor.

Following the same procedure as for the unirradiated sensor, the measured versus expected pixel ⟨Hit rate⟩ distribution was calculated for the irradiated sensor and is shown in Fig. 6.43. The combined distribution across all beam intensities was fitted with the original and modified Takács' formulas. The fit parameters are given in table 6.10.

Similar to the unirradiated sensor, the measured ⟨Hit rate⟩ of the irradiated sensor follows the ideal sensor behavior (black dashed line) up to beam intensity I7. However, for higher beam intensities, the measured ⟨Hit rate⟩ of the irradiated sensor is much closer to the ideal line than that of the unirradiated sensor (subsection 6.2.10, Fig. 6.39). Consequently, the fitted dead time parameter becomes smaller than that for the unirradiated sensor. Furthermore, both

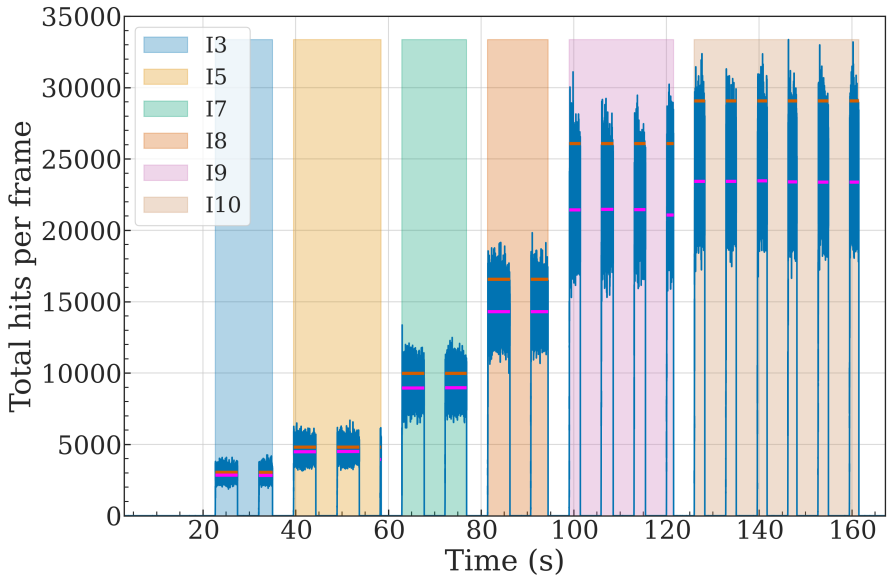


Figure 6.42.: Total number of hits per frame of carbon measured using the irradiated HitPix3 sensor at different beam intensities. Orange and magenta horizontal lines represent expected and measured ⟨Total hits per frame⟩, respectively. Spills belonging to one beam intensity setting are marked with vertical color band, as follows: I3 - blue, I5 - orange, I7 - green, I8 - red, I9 - purple, I10 - brown.

Table 6.10.: Fit parameters for the original and modified Takács' formulas for the irradiated HitPix3 sensor in 430.10 MeV u^{-1} carbon beam measurements. The R^2 stands for the coefficient of determination of the fit.

Formula type	ϵ	θ	τ (µs)	R^2
Original	1	0.00 ± 0.06	2.08 ± 0.02	0.982
Modified	0.930 ± 0.001	0.00 ± 0.01	1.52 ± 0.01	0.983

unirradiated and irradiated sensor share the same non-paralyzable dead time behavior and efficiency parameter for the modified Takács' formula.
The improved performance of the irradiated sensor can be explained by direct CSA measurements shown in the Appendix in Fig. C.14. Due to radiation damage effects and reduced bias voltage, the signals induced by the carbon ions become shorter with smaller amplitudes below CSA output saturation level compared to the signals of the unirradiated sensor. Therefore, the probability of pileup events is reduced for the irradiated sensor. These results additionally support the explanation, given in a previous subsection, that the unirradiated sensor performs worse at the high-intensity carbon beams primarily because of the pileup events of long saturated CSA signals.
Based on these measurements, it can be concluded that significant radiation damage does not degrade the HitPix3 pixel performance in carbon beams. However, measurements with proton beams are required to fully characterize the irradiated sensor performance for the beam monitoring application at HIT. During the beam test, proton beams could not be detected with the irradiated sensor, due to several factors: the proton beams provide a small ionization signal, the sensor was configured with a small gain, the reduced bias voltage narrowed the depletion region width and reduced the collected charge, and increased leakage current at room

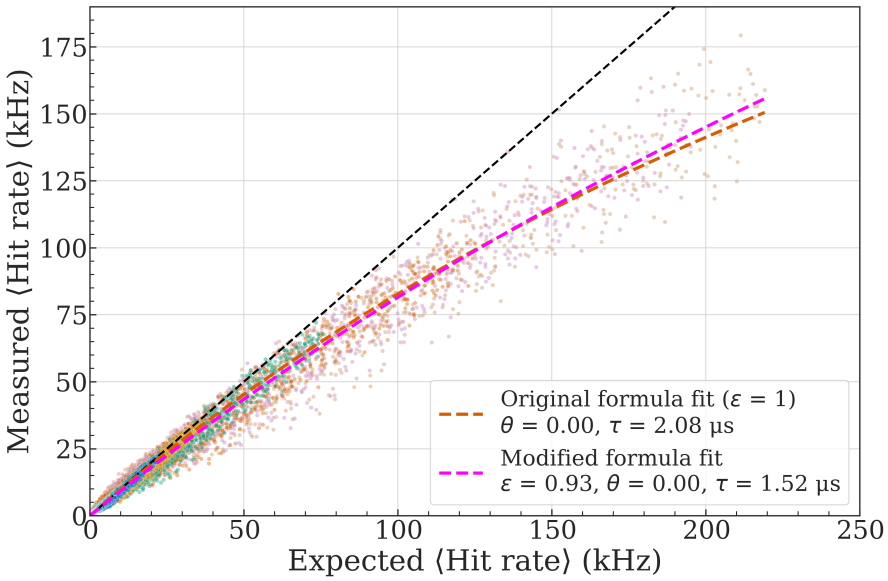


Figure 6.43.: Measured versus expected pixel ⟨Hit rate⟩ of an irradiated HitPix3 sensor at different carbon beam intensities. The feedback boost was disabled during the measurement. The black dashed line represents the ideal sensor behavior with zero dead time and 100 % detection efficiency. The orange and magenta dashed lines represent the fit curve of original and modified Takács' formula, respectively. Points are colored w.r.t. beam intensity: I3 - blue, I5 - orange, I7 - green, I8 - red, I9 - purple, I10 - brown. The sensor was configured with `bias-DAC` settings B and bias voltage of −50 V

temperature increased the pixel noise, therefore, the sensor was configured with too high pixel thresholds.

A first attempt to characterize the irradiated sensors for small ionization signals was done after the beam test within the scope of a bachelor's thesis [Mor24] under the author's supervision. During these studies, four irradiated sensors were measured with a Sr-90 source in the climatic chamber setup, covering a temperature range from −20 °C to 20 °C and a bias voltages range from −50 V to −150 V. The detection efficiency, calculated as a ratio of ⟨Hit rate⟩ of irradiated to unirradited sensors, did not exceed 30 % at a temperature of −20 °C and a bias voltage of −150 V. However, during the measurements, all tested sensors were still configured with the `bias-DAC` settings B, which provides a small CSA gain. Furthermore, the deposited charge from the Sr-90 source is approximately two times smaller than that from the 221.06 MeV u^{-1} proton beam. Therefore, a final conclusion regarding the HitPix3 sensor performance after significant radiation damage for proton beam cannot be drawn from these studies.

At the moment of writing this thesis, the second campaign has begun with the irradiated sensors configured with high CSA gain, aiming to improve their performance for detecting small signals from Sr-90 source in the temperature range from 0 °C to 20 °C. This range is foreseen as the working temperature range for the final full-scale beam monitor. Moreover, for a final performance estimation, a new cooling setup for the irradiated HitPix3 sensor should be designed and tested at HIT. Since the measurements and data analysis are not concluded at the moment of writing, the results of the campaign falls outside the scope of this thesis.

6.3. Probe station measurements

After the detailed characterization of single HitPix3 sensor assemblies, a dedicated campaign was carried out in 2024 to characterize many sensors for the assembly of 2×5 and 5×5 matrices. New details of the characterization process compared to the HitPix2 campaign and results are covered in the following section.

6.3.1. Characterization process

Similar to the HitPix2 sensors, the characterization process of HitPix3 sensors relies on the probe station measurements, presented in subsection 5.2.1. A new probe card was developed by F. Ehrler to address changes in number, assignment, pitch and size of the sensor contact pads, together with new control and data signal buffers implemented according to the LVDS standard. The photograph of a HitPix3 sensor under the needle probe card is shown in Fig. 6.44.

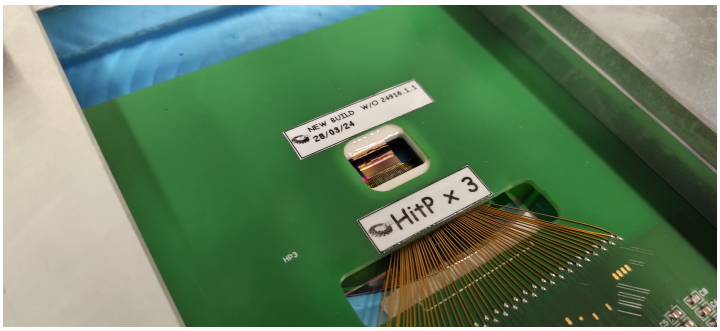


Figure 6.44.: HitPix3 sensor under the needle probe card.

The HitPix3 sensor testing procedure generally follows the same steps and tests designed for the HitPix2: sensor group positioning and fixation on the testing membrane, an alignment of the sensor pads with the probe needles, a LV compliance check, followed by a series of tests. More details can be found in subsection 5.2.1. However, several changes were introduced to address the new features of the HitPix3 sensor and to refine the quality control, based on the issues discovered in the HitPix2 testing campaign. The flowchart of the HitPix3 testing procedure is shown in Fig. 6.45.
During the HitPix2 characterization campaign, a large variation in the measured maximum readout speed of sensors was observed (more details in subsection 5.2.6). It was explained by variations of the contact quality between probe needles and sensor pads. Therefore, to ensure proper electrical contact and reliable measurements for HitPix3 sensors, the test series is modified: the latency scan test is performed, directly after the LV compliance check. If the measured maximum readout speed for a sensor under test is less than 90 MHz or not measurable, the distance between the probe needles and sensor pads is iteratively adjusted within a range from 10 µm to 200 µm. If the measured maximum readout speed does not improve to an acceptable level, the sensor is marked as malfunctional.
After ensuring proper electrical contact, the I-V test is performed to verify that the sensor breakdown voltage remains below −130 V. This is important, since the multi-sensor assemblies are foreseen to be operated at bias voltage levels up to −100 V.
In the next step, the new pixel threshold tuning feature of the HitPix3 sensor is tested, as described in subsection 6.2.6. To accelerate the sensor testing time, the number of in-pixel RAM values (q) is reduced to four. If the standard deviation of the pixel threshold distribution after tuning procedure is not reduced by at least a factor of two, a sensor under test is marked as malfunctional.

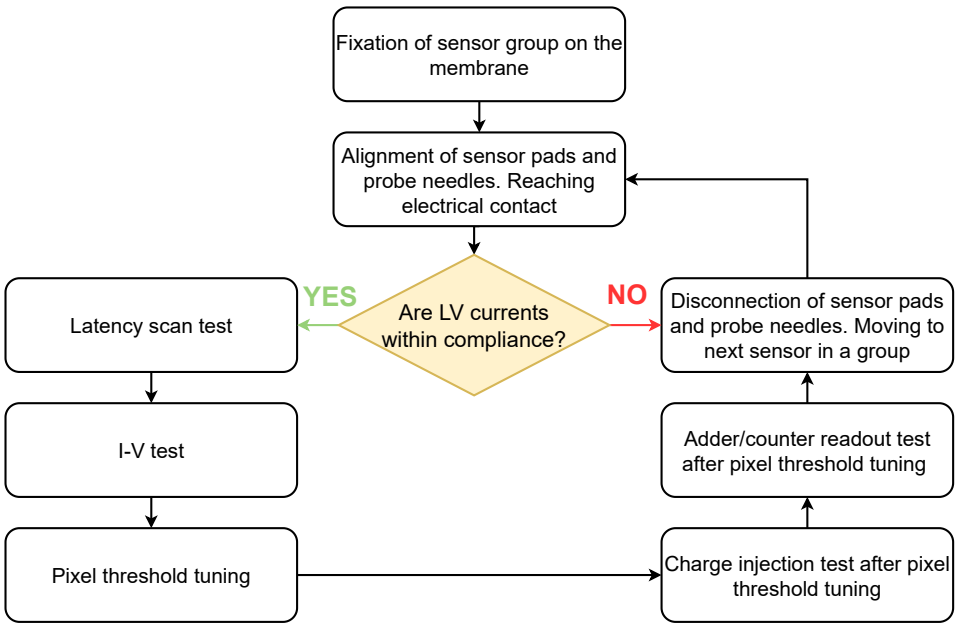


Figure 6.45.: Flowchart of the HitPix3 sensors testing procedure.

The last two testing steps include charge injection, adder and counter readout tests, and are used to verify in-pixel electronics functionality. They are performed similarly to the HitPix2 testing procedure. However, for HitPix3, pixel thresholds are tuned during the measurements to ensure that the tuning procedure does not influence either of the readout modes.

6.3.2. Wafer characterization results

Compared to the HitPix2 submission, the HitPix3 sensors occupied a larger area on the Multi-Project wafer, increasing the number of sensors per wafer. As a result, 124 HitPix3 sensors from a single Wafer 4 were characterized during the campaign. It is important to note that 14 sensors from this wafer were initially assembled on the single sensor carriers without probe station measurements. This set was used for the initial HitPix3 sensor characterization, readout and configuration debugging and radiation hardness studies. Another 16 sensors received severe mechanical damage during the sensors extraction from the wafer, including large cracks, scratches or damaged contact pads. The sensors were excluded from the final statistics, since their functionality could not be tested.
The results of the characterization campaign are detailed in table 6.11 in which the sensors mounted on the PCB carriers are included to estimate the total production yield.

Table 6.11.: Results of HitPix3 characterization campaign.

Wafer	ρ (Ω cm)	**# tested**	**# func.**	**# malfunc.**	**yield (%)**
Wafer 4	370	108	83	25	77

The number of fully functional sensors was found to be 83, leading to a total production yield of 77 %, which is significantly higher than that observed for all previously tested HitPix2 wafers. An important result of the functional sensor analysis was related to the new pixel threshold tuning step in the testing procedure. The standard deviation of the pixel threshold distribution

after tuning was reduced by a factor of 5.3 ± 1.0, averaged across all functional sensor. This result, based on a large sample of sensors, confirms the beneficial effect of the pixel threshold tuning, which was previously observed with a small subset of sensors mounted on PCB carriers. Analysis of the sensors which failed some tests revealed the following main reasons for HitPix3 sensors malfunction: LV supply issue (48 %), pixel readout failures (32 %), and failed pixel threshold tuning (12 %). The large fraction of LV supply issue and pixel failures together with the high production yield suggests that the sensor malfunctioning can be attributed to the production processing rather than to sensor design flaws.
The successful characterization campaign provided a large number of fully functional sensors, which were used in the multi-sensor assemblies. Five sensors were assembled into a single row of the 2×5 matrix, and 50 sensors formed two 5×5 beam monitor demonstrators, as presented in sections 6.4 and 7.2, respectively. Similar to the HitPix2 campaign, the malfunctional sensors were used in various mock-up assemblies to validate the assembly technology before the integration of functional sensors.

6.4. Multi-sensor readout

After successful tests of single HitPix3 sensor assemblies in both laboratory and HIT experimental environments, followed by the characterization campaign at the probe station, it is important to evaluate the simplified 2×5 multi-sensor assembly before starting the design of the 5×5 beam monitor demonstrator. This allows to verify that all required features remain functional after scaling the detector system: pixel threshold tuning and masking, counter and adder readout modes at high readout speed. The following section covers the design of such an assembly and its test results.

6.4.1. 2×5 HitPix3 matrix design

A new PCB carrier was designed to assemble a 2×5 matrix from ten validated HitPix3 sensors, similar to the 2×5 HitPix2 matrix. The carrier layout and its 3D render are shown in Fig. 6.46. As in the 2×5 HitPix2 matrix PCB design, the HitPix3 sensors are mounted onto exposed PCB sensor pads (outlined with a red box in the 3D render in the figure), and their contact pads are wire-bonded to the corresponding bonding pads (outlined with pink boxes in the 3D render in the figure). Five sensors in each row form a daisy chain, as explained in subsection 5.3.1.
In contrast to the HitPix2 sensor, the HitPix3 input and output buffers were designed according to the LVDS standard, which proved more suitable for the high-speed readout of a single sensor compared to the LVCMOS standard (subsection 6.2.3). However, this solution came with challenges, including the electrical power delivery, signal integrity, and compatibility with the existing DAQ system, which should be addressed in the PCB design to maintain the high performance of the multi-sensor assembly, while keeping the integration and debugging process simple.
The PCB was designed with a six-layer stack-up. The functional assignments of each copper layer are detailed in table 6.12. The baseline voltage V_{bl} is not presented in the table, since it is derived on the board from a voltage divider connected to V_{dda}. Additionally, a new power rail V_{dd33} was introduced for the ICs on the board.
Most copper pours for the different power rails were distributed across inner layers. This design solution allows to form a simple connection from a HitPix3 sensor power pad to its corresponding power pour through a via, optimizing power delivery and simplifying trace routing.
The first and fourth inner layers were used only for ground planes. The planes are connected to the same common potential to create a stable reference level for the signals. This design

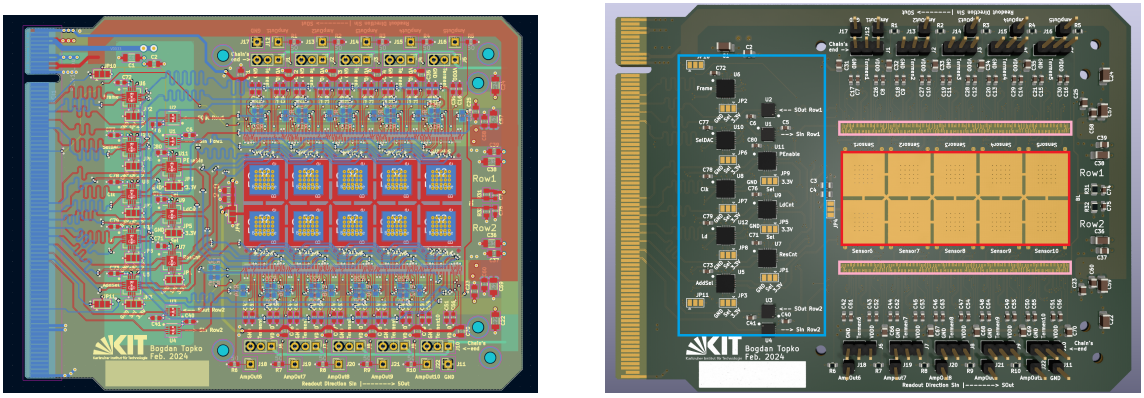
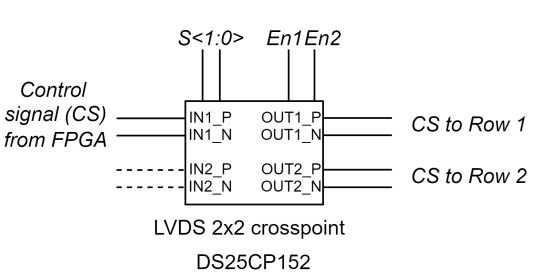


Figure 6.46.: 2×5 HitPix3 matrix PCB layout (left) and its 3D render (right). The red, pink, and blue boxes in the 3D render outline sensor mounting pads, wire-bonding pads, and signal distribution circuits, respectively.

Table 6.12.: The stack-up of the 2×5 HitPix3 matrix PCB and the functional assignments of copper layers

Layer	V_{bias}	V_{dda}	V_{ssa}	V_{dda}	V_{dd33}	GND	C&D Signals	Inj	RowEn
Top	✓	✓	✓				✓		✓
Inner 1						✓			
Inner 2	✓	✓	✓					✓	✓
Inner 3				✓	✓				
Inner 4						✓			
Bottom	✓			✓	✓		✓	✓	✓

solution is important for the signal integrity, when high-speed differential signals traverse between different layers, such as control and data signals for HitPix3 sensors (marked as C&D Signals in the table). The signals are routed only on the top and bottom layers (to prevent forming via stubs) with their trace geometry optimized to ensure the differential impedance match within $\pm 10\,\%$ tolerance of the target value of $100\,\Omega$. If a differential signal, routed on the top layer, traverses through vias to the bottom layer, its return currents switch reference plane from inner layer 1 to inner layer 4. Therefore, to form the correct path for the return currents, grounded stitching vias are placed in close proximity to vias of each differential pair.
The HitPix3 control signals must reach both rows of the matrix with minimal delay. Otherwise, the active counting period of the sensors will not be synchronized, and parallel data sampling from both rows will not be possible. To distribute and synchronize control signals for both rows of the matrix, dedicated signal distribution circuits were introduced in the PCB design (outlined by the blue box in the 3D render in Fig. 6.46). They are based on an LVDS 2×2 cross-point switch, for which the simplified block diagram is shown in Fig. 6.47. Its primary function is to repeat a single LVDS control signal for both matrix rows with a minimal delay and optimized signal integrity.
A control signal, generated by the FPGA, is fed into one of the cross-point switch inputs. The combination of two LVCMOS select signals (marked as 'S' in the figure) configures which input is connected to which output of the switch (the full configuration truth table is shown in the figure). In the PCB design, both select signals are connected together, since the purpose of the circuit is to repeat one input control signal to both outputs. The exact input can be selected



Configuration truth table

S1	S0	OUT1	OUT2
0	0	IN1	IN1
0	1	IN1	IN2
1	0	IN2	IN1
1	1	IN2	IN2

Figure 6.47.: Simplified block diagram of the LVDS 2×2 cross-point switch. The second input pair (dashed) are kept in the design as a reserve input. Adapted from [Tex13c].

via a solder jumper on the board, which connects both signals either to GND or V_{dd33}, i.e. both switch outputs are connected either to the first or second input, respectively. An additional pair of LVCMOS enable signals (En1 and En2 in the figure) controls which matrix row is read out. Activation of both enable signals allows to read out both matrix rows in parallel.

Additional techniques were used to ensure the signal integrity of the entire communication path. The data input `SIn` and output `SOut` signals are passed through an individual DS25BR150 LVDS buffers [Tex13a] to prevent signal degradation during the transmission between the sensor matrix and the FPGA board. Furthermore, as in the single HitPix3 carrier design, all trace lengths were tuned to minimize intra- and inter-pair skews between matrix rows.

Compatibility with the existing DAQ system was achieved by adding an edge connector compatible with the custom PCIe x16 socket of the GECCO board. Overall, the solutions implemented in the 2×5 HitPix3 matrix design addressed all challenges presented above.

To accelerate the development of the 5×5 beam monitor demonstrator and spare more valid sensors for its assembly, it was decided to assemble only a single row of the 2×5 matrix, which is shown in Fig. 6.48. This approach is valid, since the layout of both rows are simply mirrored. Therefore, the evaluation of a single row provides sufficient information about the performance of the daisy-chained HitPix3 sensors and the selected ICs.

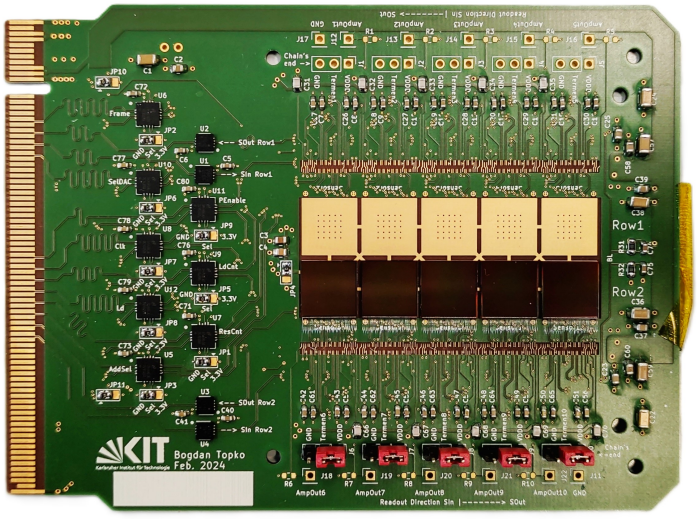


Figure 6.48.: Assembled single row of 2×5 HitPix3 matrix.

As for the 2×5 HitPix2 matrix, the HitPix3 sensor positions were measured with a microscope to create a local matrix coordinate map of each pixel center and was used in the measurements

presented in the next subsection. The pixel coordinate map of a single row of 2×5 HitPix3 matrix is shown in the Appendix in Fig. C.16.

6.4.2. Measurement results

A single row of the 2×5 HitPix3 matrix was characterized in laboratory environment to validate the matrix functionality. In the following measurements all sensors in the matrix were configured with modified `bias-DAC` settings C in which the `ipdac` parameter was set to 28 DAC units to increase the maximum output voltage range of the tune block, as explained in subsection 6.2.6. The voltages V_{bias} and V_{ssa} were set to $-100\,\text{V}$ and $1.29\,\text{V}$, respectively. To increase the strength of the `SOut` output buffers, the V_{ddd} voltage was increased to $2.35\,\text{V}$. All measurements were performed at room temperature.
First basic tests included the I-V and latency scan measurements. The matrix total leakage current did not exceed $100\,\text{nA}$ at a bias voltage of $-100\,\text{V}$. This result is expected, since a typical leakage current for a single unirradiated HitPix3 sensor does not exceed 20 nA, as shown in subsection 6.2.2 and [Mor24]. The total leakage current of the matrix is simply the sum of the individual sensor leakage currents.
The results of the latency scan measurement are shown in the Appendix in Fig. C.15, and are almost identical to that of the single HitPix3 sensor, with a maximum readout speed reaching the current firmware limitation of $190\,\text{Mbit}\,\text{s}^{-1}$ (subsection 6.2.3 Fig. 6.11). This confirms that the daisy chain readout architecture does not degrade the readout performance of the configuration/data shift register, if the input and output data are transmitted through LVDS buffers and careful attention is given to signal integrity in the PCB design.
However, during the measurements in counter and adder modes, the readout speed was reduced from standard $180\,\text{Mbit}\,\text{s}^{-1}$ to $150\,\text{Mbit}\,\text{s}^{-1}$ because one sensor in the matrix row had several corrupted data columns at readout speeds higher than $150\,\text{Mbit}\,\text{s}^{-1}$. The data corruption in these columns was insensitive to changes in the applied threshold voltage, thus excluding the noise influence of these pixels. The discrepancy between the maximum readout speed in the latency scan and counter/adder readout measurements can be explained by potential crosstalks, generated by control signals. In the latency scan measurements only one control and two data signals are used: `Clk`, `SIn`, and `SOut`, whereas in the counter/adder measurements all control signals are involved in the readout process. Overall, the maximum readout speed of a single row of the 2×5 HitPix3 matrix increased by more than a factor of five compared to that value of $36\,\text{Mbit}\,\text{s}^{-1}$ for a single row of the 2×5 HitPix2 matrix.
The charge injection test was performed to verify the pixel threshold tuning for the matrix, following the algorithm 1 from subsection 6.2.6. The measured pixel distribution for a single row of the 2×5 HitPix3 matrix before and after pixel threshold tuning are shown in Fig. 6.49. After tuning, the pixel threshold deviation is significantly reduced across all pixels in the matrix. However, a small fraction of pixels still deviates from the core distribution, indicating that the maximum output voltage range of the tune block was not sufficient to compensate the pixel offsets. Therefore, it can be potentially reduced by setting `bias-DAC.ipdac` to higher values. Both distributions before and after the tuning were fitted with a Gaussian function to extract their standard deviations. The extracted standard deviation after tuning was reduced by more than a factor of seven. The fraction of pixel thresholds lying within three fitted standard deviations from the mean value is 99.64 % and 89.51 % before and after the tuning procedure, respectively. Given that all sensors were configured with the same global threshold voltage of 140 DAC units and `bias-DAC.ipdac` of 28 DAC units, whose absolute voltage values can potentially vary from sensor to sensor, the beneficial effect of the pixel threshold tuning is clear. Therefore, the pixel threshold tuning procedure remains effective also in the multi-sensor assembly.

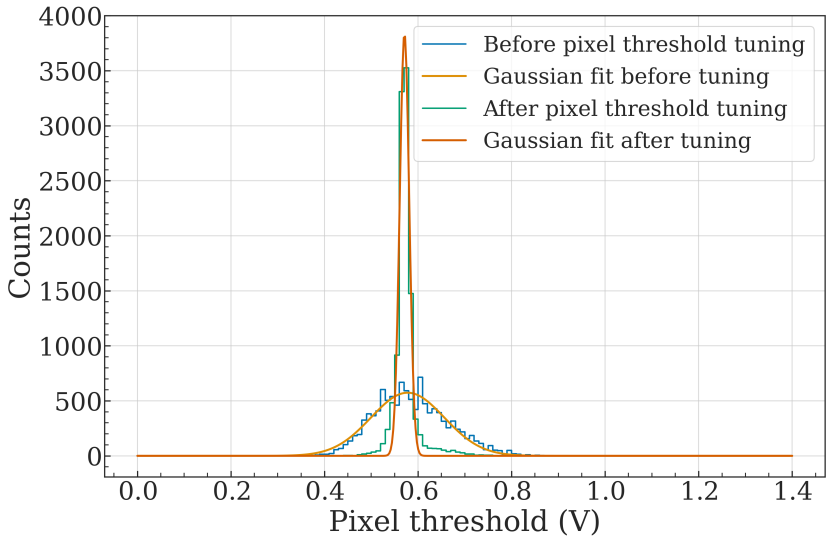


Figure 6.49.: Measured pixel threshold distribution for a single row of 2×5 HitPix3 matrix before (blue) and after (green) pixel threshold tuning. Solid lines represent Gaussian fit applied to a distribution before (orange) and after (red) tuning.

A final evaluation of the matrix performance required testing both counter and adder readout modes with a charged particle source. For all measurements, t_{frame} was set to 2 ms. Figure 6.50 shows two cumulative profiles of a Sr-90 source, measured with a single row of 2×5 HitPix3 matrix in counter mode, before and after pixel threshold tuning. The Sr-90 source was manually positioned above the central sensor in the matrix row. Noisy pixels, defined as in subsection 6.2.8, were masked, and their fraction was found to be approximately 1.1 %. Similar to the single sensor measurements, the measured spot profile showed improved regularity and smoother contours, confirming that the pixel threshold tuning unifies the pixel responses across different sensors in the matrix.

Figure 6.51 shows the cumulative Sr-90 source profile projection in the X- and Y-directions using a single row of 2×5 HitPix3 matrix in adder mode after pixel threshold tuning. The adder positions were derived with a method described in subsection 7.3.4 of the next chapter. The projections measured in adder mode (blue and orange distributions in the figure) are plotted alongside projections derived from the measurement in counter mode (black distributions in the figure) in which the counter values are summed following the HitPix3 projection calculation chess-pattern, explained in section 6.1. The resulting projections from adder and counter modes align well, validating the results obtained in the adder mode.

Furthermore, the readout dead time between two consecutive frames was 1.25 ms in counter mode, whereas in adder mode this value was 40 µs. The small dead time between frames for the matrix in adder mode ensures short latency between measured beam position and shape after scaling the detector system to 5×5 beam monitor demonstrator.

The final test verified the pixel masking feature of the HitPix3 sensor in the matrix. A pixel mask was generated to follow the HIT logo and uploaded to the pixel RAMs. The cumulative Sr-90 source profile measured using the matrix in counter mode with the applied mask is shown in Fig. 6.52. The resulting distribution exactly follows the uploaded mask, confirming the pixel masking functionality in the matrix.

Based on the presented results, it can be concluded that the HitPix3 sensors perform well even when assembled into a larger detector system. All functionalities critical for the beam monitoring application were validated.

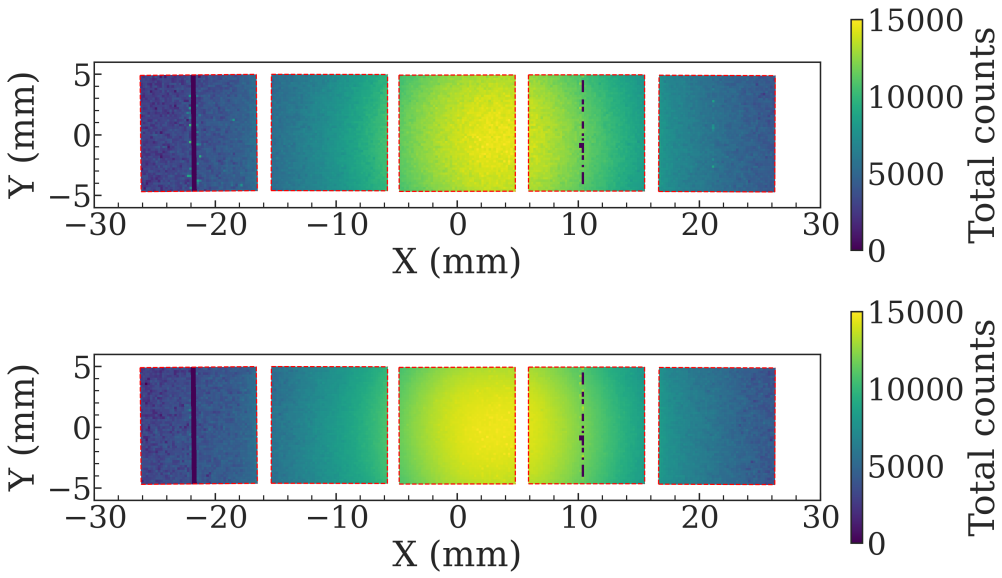


Figure 6.50.: Cumulative Sr-90 source profile measured using a single row of 2×5 HitPix3 matrix in **counter mode** before (top) and after (bottom) pixel threshold tuning. Red dashed lines enclose active areas of the sensors. Number of frames: 3000. The threshold voltage was set to 140 DAC units.

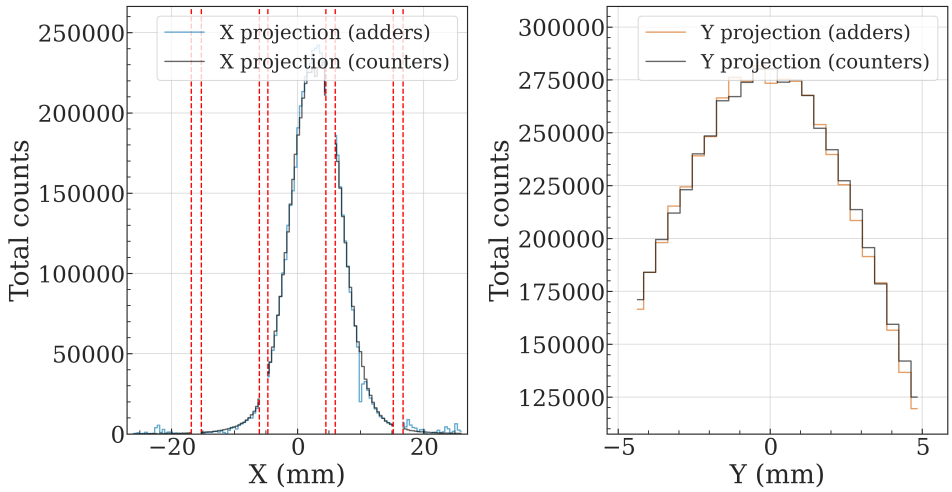


Figure 6.51.: Cumulative Sr-90 source profile projection in X- (left) and Y- (right) directions measured using a single row of 2×5 HitPix3 matrix in **adder mode** after pixel threshold tuning. The black projections are derived from the two-dimensional profile measured in counter mode. Red dashed lines outline gaps between the sensor active areas. Number of frames: 3000. The threshold voltage was set to 140 DAC units.

6.5. HitPix4 design considerations

For the full-scale beam monitor, a new sensor should be designed to fulfill the large sensitive area requirements. The findings obtained during the measurements with single HitPix3 sensors and multi-sensor assembly form a list of improvements to be addressed in the new HitPix4 sensor design.

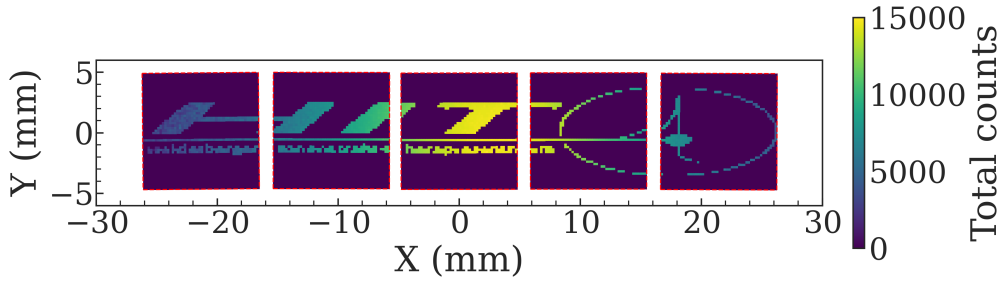


Figure 6.52.: Cumulative Sr-90 source profile measured using a single row of 2×5 matrix in **counter mode** with a masking pattern applied. Red dashed lines enclose active areas of the sensors. Number of frames: 3000. The threshold voltage was set to 140 DAC units. The generated pixel mask follows the HIT logo [Uni25b].

6.5.1. General design

Similar to the HitPix3 sensor, a HitPix4 can be produced on the same *p*-type substrate with a resistivity of 370 Ω cm, based on the radiation hardness studies preformed with HitPix2 and HitPix3 sensors.
To fulfill the large sensitive area requirements for the full-scale beam monitor, the sensor area should be increased to 2 cm × 2 cm, forming a matrix of 96 × 96 pixels with an individual pixel size of 200 µm × 200 µm.
The HitPix3 chess-pattern readout of the adder mode captures only 25 % of each projection, which can lead to challenges for the reconstruction of low-intensity beam parameters measured with short frame durations. Therefore, a full adder projection in which all pixel adders contribute in both projections, would be beneficial. However, this would require a more complex pixel matrix routing and readout scheme. Furthermore, a full adder projection would require the increase of the pixel adders range to 15 bit to address the maximal projection value of $255 \times 96 = 24480$. Therefore, the size of configuration/data shift register should be also increased to 1440 bit. The changes in the adder design should be assessed in the sensor development phase, regarding their impact on the sensor layout complexity. A final decision must be made to either adopt the chess-pattern scheme or to implement the new full adder projection calculation scheme. Moreover, significant changes in the design increase the risk of mistakes, therefore, a more careful validation is required during the HitPix4 sensor development.

6.5.2. Pixel design

The HitPix3 sensor was implemented with an ISO pixel topology and a pMOS based CSA, since the measurements with the proton microbeams, discussed in subsection 5.4.4, revealed its highest tolerance to the baseline drop effect. Measurements with a single HitPix3 sensor in the carbon and proton beams at HIT confirmed that the pixel hit rate performance was significantly improved, although direct CSA measurements showed that the baseline drop effect still occurred. This pixel design came at the cost of increased pixel capacitance and, therefore, a reduced CSA gain, which influences the minimal available pixel threshold.
Moreover, at the moment of writing this thesis, an additional set of measurements revealed that the HitPix3 sensor adders data becomes corrupted when the sensor is read out in the pipeline scheme. In this scheme, the previous frame data is read out while the pixels count particles in the current frame. The pipeline scheme reduces the readout dead time to approximately 2 µs for a single sensor with a readout speed of 180 Mbit s^{-1}. The implementation of the pipeline scheme is critical for the full-scale beam monitor to fulfill the timing requirements.

Measurements with HitPix2 (STD pixel topology) and both types of HitPix1 sensors (with STD and ISO pixel topologies) showed that sensors with STD pixel topology can be read out with the pipeline scheme without errors, while the HitPix1 with ISO pixel topology experienced the same data corruption problem as the HitPix3 sensor. These measurements were performed by T. Renkhoff within the scope of his master's thesis, under the author's supervision. The master's thesis and the results were not yet published at the moment of writing this thesis.
Based on these results, the HitPix4 pixel should be implemented with a STD topology and pMOS based CSA design. The proton microbeam results confirmed that this design is still more tolerant to the baseline drops effect than the HitPix2 pixel with STD topology and nMOS based CSA design.
Further improvements can be implemented in the CSA design to increase the pixel performance at high particle rates. To suppress the probability of pileup events, the duration of the CSA output signals must be shorter. This can be achieved by modifying both the feedback continuous reset and the feedback boost circuit. In the continuous reset circuit, a second current source could be implemented to increase the discharge speed of the feedback capacitance.
In the HitPix3 design, the feedback boost circuit activates when the in-pixel comparator transits into a logic high state. However, to detect small ionization signals from proton beams, the comparator threshold is set as small as possible. This leads to an early activation of the feedback boost circuit for the signals. A second comparator with a separate global threshold, generated at the sensor periphery, could be added to the pixel electronics to control the enable signal of the feedback boost circuit and, therefore, to control its activation time. Additionally, a DAC common to all pixels could be implemented in the sensor periphery to independently control the strength of the large reset current source. These design solution could prevent the large undershoot of the signal, which leads to a slow baseline recovery after the large reset current source is disconnected from the feedback circuit, as shown in subsection 6.2.5.
The pixel digital electronics requires only one critical modification in the counter design. In all HitPix versions, the `ResCnt` signal resets the counter value to 0, and the first detected hit then overflows it to a maximum value of 255, and consecutive hits decrement counter values by one. Despite that this flaw can be addressed in the data obtained in the counter readout mode, in the adder mode it prevents the full usage of 14 bit adder range because the number of detected hits cannot be correctly determined from the adder value, if the number of hits in the projection exceeds 255, as explained in subsection 5.1.2. Two possible modifications could be implemented in the counter design to avoid adder value ambiguity: `ResCnt` signal resets counter value to 255 instead of 0, with all consecutive hits decrementing the counter value, or the `ResCnt` signal resets counter value to 0, but all consecutive hits increment the counter value from 0 to 255.
The presented modifications of the pixel analog and digital electronics require careful simulations before the HitPix4 sensor can be submitted to the production. For the analog electronics, the pixel response should be simulated in a wide range of the input ionization charge expected at the HIT conditions, while for the digital electronics, it is important to simulate the behavior of the counter and adder circuits.

6.5.3. Peripheral electronics design

Redesigning all input and output buffers according to the LVDS standard and using a single-phase clock for the data propagation proved to be an efficient solution for high-speed readout of both single HitPix3 sensor and multi-sensor assemblies. Therefore, this solution should be transferred to the new HitPix4 design.
The following improvements for the peripheral electronics design aim to simplify the sensor integration into the multi-sensor assembly.

The DOut output buffer requires external pull-up resistors, while the SIn input buffer requires external termination resistor in the HitPix3 design. The resistors ideally should be placed as close as possible to the buffers, increasing the complexity of the multi-sensor assembly, especially if the sensors are interconnected with thin aluminum-polyimide cables. Therefore, to reduce the number of external passive components in the multi-sensor assembly the resistors could be implemented in the internal circuitry of the buffers.
The HitPix3 sensor requires five power rails for correct operation: V_{bias}, V_{dda}, V_{ssa}, V_{ddd}, and V_{bl}. To simplify the power delivery in the multi-sensor assembly, the baseline voltage could be generated internally by an additional DAC implemented in the sensor periphery.
The pixel threshold tuning procedure in HitPix3 relies on charge injection measurements. However, the injection pulses can only be generated with an external GECCO injection card or other voltage pulse sources. To further simplify the number of external circuitry the injection amplitudes can be also generated by an additional DAC in the sensor periphery, as was implemented in the ATLASpix3 design [Per+21].

6.6. Summary

The studies presented in this chapter focused on the initial characterization of the HitPix3 sensor, the third iteration of HitPix sensor family. A set of new features was introduced in the sensor design to address the limitations of HitPix2 sensor performance previously observed in ion beams. The set includes: the ISO pixel topology and a modified CSA, pixel threshold tuning and masking, and two-dimensional projection calculation
Various measurements were performed with single HitPix3 assemblies in a laboratory environment and during beam tests at HIT. The results confirmed the full functionality of all new design features. Furthermore, the improved performance compared to HitPix2 results, was demonstrated for an unirradiated HitPix3 sensor in carbon and proton beams at different intensities. Additionally, the beam test with an irradiated HitPix3 sensor revealed no degradation in pixel performance in carbon beams.
A characterization campaign was carried out to select valid sensors for multi-sensor assemblies. The campaign results demonstrated that the HitPix3 production yield increased to 77 % compared to the HitPix2 results of 34 %. Low-voltage supply issue and pixel readout failures were identified as the primary sources of the sensor malfunction.
A new multi-sensor assembly, a 2×5 HitPix3 matrix, was designed to evaluate sensors performance after scaling the detector system. A single row containing five sensors, tested at the probe station, was assembled in a daisy chain architecture and tested in a laboratory environment. The HitPix3 sensors performed well when integrated into the multi-sensor assembly, and all new sensor functionalities were successfully validated. The knowledge gained from the 2×5 matrix PCB design and measurements was applied to the design of the 5×5 beam monitor demonstrator, which is covered in next chapter 7.
Based on the HitPix3 characterization results, a list of improvements was formulated to be addressed in a new HitPix4 design, which is foreseen to be an elementary building block of a full-scale beam monitor with an active area of 26 cm $\times$ 26 cm.

7
Beam monitor demonstrator

After the successful performance evaluation of single and small multi-sensor HitPix assemblies, the next step towards the final full-scale beam monitor is to design a detector system capable of covering all available beam sizes at HIT. This intermediate step is required to evaluate the performance of this detector system in beam parameter reconstruction for both counter and adder readout modes, and to explore possible integration technologies for HitPix sensors into a large detector system.
The following chapter covers the exploration of an assembly technology for the beam monitor demonstrator based on HitPix2 sensors, the design and assembly process of the demonstrator based on HitPix3 sensors, and the results from its beam tests. The findings from these studies were used to formulate the design considerations for the full-scale beam monitor, which are provided at the end of the chapter.

7.1. Exploration of an assembly technology

The primary goal of the HitPix beam monitor demonstrator is to reliably reconstruct the beam position and size across a wide range of ion beam settings available at HIT. The demonstrator also allows to identify potential issues that may arise during the design and assembly of the final full-scale beam monitor. Therefore, not all requirements for the clinical application, discussed in section 4.1, were applied to the demonstrator design, allowing to simplify it from the perspective of assembling, readout and thermal management.
The nominal ion beam size (FWHM) at HIT varies in a wide range, depending on the ion type, beam energy and focus, from 3.4 mm (430.10 MeV u^{-1} carbon ions) to 32.9 mm (48.12 MeV u^{-1} protons). Therefore, the beam monitor demonstrator should be designed to cover at least an area of approximately 50 mm × 50 mm. This ensures that parameters of the largest expected beams (assuming the beam is centered on the detector) can be reliably reconstructed by capturing approximately 92 % of their particle distribution (proton beams with a size of 32.9 mm), while maintaining a relatively simple beam demonstrator design. This can be achieved by assembling a matrix of 5 × 5 HitPix sensors with an individual sensor active area of 9.6 mm × 9.6 mm.
Furthermore, the sensors can be mounted onto a rigid PCB, which simplifies the assembly procedure at the cost of increased material budget and is acceptable for evaluation purposes. The PCB provides all necessary connections for sensor control, data signals, and power supplies. The sensors interconnection in the matrix can be achieved either with bump- or wire-bonding. The following section describes the steps towards first prototypes based on HitPix2 sensors assembled with these technologies.

7.1.1. Optical characterization of HitPix2 sensors

HitPix2 sensors were selected for the 5 × 5 matrix assembly, based on the characterization campaign results discussed in subsection 5.2.7. All sensors were diced from the wafer with a diamond saw, leading to an outer dimension variation from the nominal values of 9800 µm × 10 100 µm across the sensors. If some of the sensors have an outer dimension significantly larger

than the nominal values, there is a risk that the 5×5 matrix cannot be assembled. To address this, a safe distance between the sensors within the rows and columns of the matrix must be introduced in the PCB design. Simultaneously, the distance should be minimized to reduce gaps between sensors in the matrix, since they create insensitive areas that can affect the beam parameter reconstruction.
A dedicated optical characterization of each sensor was conducted using a 1 µm resolution microscope to estimate the variation of sensor outer dimensions. The measurements were performed by L. Hahn within the scope of her bachelor's thesis under the author's supervision. The measurement results are detailed in table 7.1. More details regarding the measurement procedure may be found in [Hah23].

Table 7.1.: Measured outer dimensions of the HitPix2 sensors selected for the 5×5 matrix assembly. Units: µm. The data are taken from [Hah23].

Parameter	Nominal	Mean	Std. deviation	Min	Max
Width	9800.0	9828.9	13	9782.0	9859.6
Height	10 100.0	10 193.6	73	10 157.0	10 487.2

The measured sensor height has a standard deviation of 73 µm, which is significantly larger than the width deviation of 13 µm and can be attributed to uneven dicing. For the PCB design, it was decided to use the maximum values of measured width and height as the reference values.

7.1.2. HitPix2 matrix design based on bump-bonding

The small 2×5 HitPix2 and HitPix3 matrices were designed for assembly with wire-bonding interconnection between sensors of each matrix row. The sensor pads were wire-bonded to the PCB bonding pads placed away from the sensor edges to simplify the bonding process. In this design, two matrix rows can be assembled with minimal gaps between them only if both rows are mirrored, as shown in subsections 5.3.2 and 6.4.1.
However, this approach cannot be scaled to the 5×5 matrix assembly because gaps between pairs of matrix rows will be significant and require a complex PCB design. Therefore, a first attempt in design and assembly of the 5×5 HitPix2 matrix was based on the bump-bonding interconnection technology, which allows to assembly the matrix with small gaps between sensors and minimal parasitic capacitance and inductance compared to wire bonds.
Figure 7.1 shows a 3D render of the HitPix2 5×5 bump-bonding PCB, which was designed by F. Ehrler. Its layout is shown in Appendix Fig. D.1. The HitPix2 sensors are bump-bonded onto dedicated mounting area with exposed traces and bonding pads (outlined with the solid red box in the figure). The matrix rows on the PCB are designated alphabetically (e.g. A, B, etc.) starting with A from the top, while the sensor positions within the row are designated numerically (e.g. 1, 2, 3, etc.) starting with 1 from the left. Based on the sensor optical characterization results, the safe distance between sensors within the matrix row (i.e. sensors at positions A1, A2, A3 etc.) was set to ∼400 µm, while the safe distance between the matrix rows (i.e. sensors at positions A1, B1, C1 etc.) was set to ∼220 µm. This translates into corresponding distances of ∼1000 µm and ∼450 µm between sensor active areas, which are acceptable for the required accuracy of the reconstructed beam parameters. The influence of the gap size between sensor active areas in the matrix was simulated by P. Marchesi within the scope of his master's thesis [Mar24] under the author's supervision. The simulation results revealed that the beam parameters can be reconstructed within the required accuracy if the gap between active areas does not exceed 1200 µm.

Each matrix row connects five sensors in a daisy chain architecture. The control signals are delivered to the matrix rows via a shared bus, while the row input and output data are transmitted through an individual pair of corresponding lines, allowing for the parallel readout of the entire matrix.
Control and input data LVDS signals, generated by the FPGA, are fed into LVDS-LVCMOS signal converters ICs to convert them into LVCMOS signals suitable for the HitPix2 input buffers. Output data from each row is transmitted via the LVCMOS `SOut` output buffer of the last sensor in the chain, which are then fed into LVCMOS-LVDS converters to transmit them to the FPGA. The signal converter ICs are outlined with the solid blue box in Fig. 7.1.
To minimize signal latency between the matrix and the FPGA, the PCB was designed for direct connection to the FPGA board (without the GECCO board) via an LPC-FMC connector, which is soldered on the bottom layer. All necessary low and high voltages for the matrix and signal converters operation are delivered via external power connectors (outlined with the solid magenta boxes in Fig. 7.1).

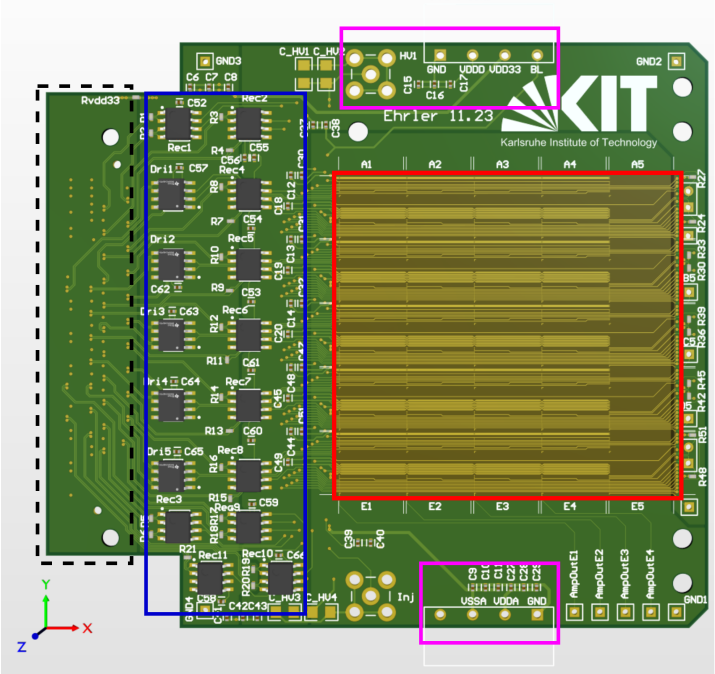


Figure 7.1.: 3D render of the HitPix2 5×5 bump-bonding PCB. The red, magenta, and blue solid boxes outline the sensor mounting area, power connectors mounting areas, and signal converter ICs, respectively. The black dashed box outlines the location of the LPC-FMC connector, which is placed at the PCB bottom layer. The PCB was designed by F. Ehrler.

A simplified view of the bump-bonding assembly for the 5×5 HitPix2 matrix is shown in Fig. 7.2. The assembly method is based on the Stud Bump Bonding (SBB) technology. As described in [Cas+16], a ball-wedge bonder forms a gold stud on each sensor contact pad in a few steps. Initially, the machine melts the tip of a gold wire to form a free-air ball, which is then brought into contact with the sensor pad and thermosonically bonded. After that, the wire is cut above the stud, creating a bump with a consistent height of approximately 40 µm. Figure 7.3 shows a photograph of the HitPix2 pads with applied gold studs and their measured heights.
After the formation of gold studs on the sensor pads, an anisotropic conductive glue is dispensed onto the PCB bonding pads to ensure proper electrical contact. Next, the sensor is flipped

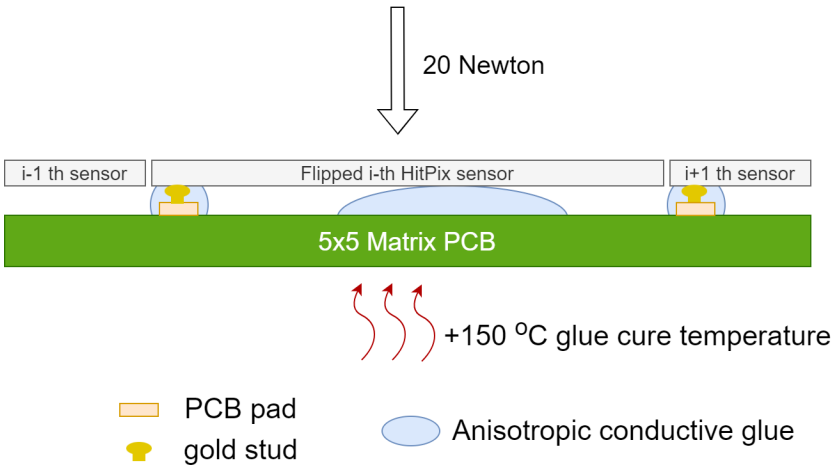


Figure 7.2.: Simplified view of the bump-bonding assembly for the 5 × 5 HitPix2 matrix.

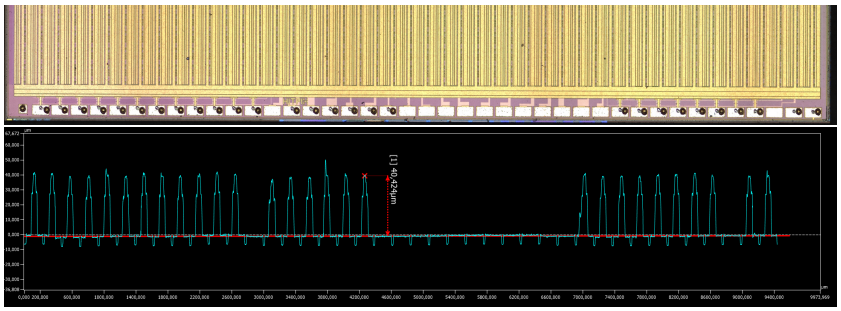


Figure 7.3.: The HitPix2 pads with applied gold studs (top) and their measured heights (bottom). Photo courtesy of M. Caselle.

with an automated flip-chip machine, followed by an accurate alignment between the gold studs and PCB bonding pads. After the alignment, the flip-chip machine apply a force of approximately 20 N at the glue cure temperature of 150 °C to establish the electrical and mechanical connection.

Compared to hybrid detector systems in which the detector and readout ASIC have the contact pads evenly distributed across their areas, the HitPix contact pads are located only at its bottom edge to minimize the insensitive area. Therefore, an additional mechanical support must be created to avoid a potential crack of the sensor caused by applying force to the sensor, which has a different heights of edges with and without gold studs. This mechanical support is created with a thin glue layer under the sensor geometrical center.

Before the matrix assembly, several single sensor carriers, designed by F. Ehrler, were assembled and successfully tested to validate the SBB assembly method. Despite the test results of the single sensor carriers, the assembly of the matrix mock-up based on the sensors, which failed characterization tests, revealed a severe problem of this method when it is scaled to the matrix integration. Figure 7.4 shows a photograph of four HitPix2 sensors assembled onto the 5 × 5 bump-bonding PCB.

During the assembly, only one sensor can be mounted at its corresponding position on the PCB, which includes a complete thermal cycle from 20 °C to 150 °C. Therefore, the first mounted sensor will experience 25 temperature cycles at the end of the matrix assembly, which could lead to degradation of the glue support layer. It was observed that after the assembly of several sensors in the mock-up, some of them detached from the mounting area. Several attempts were

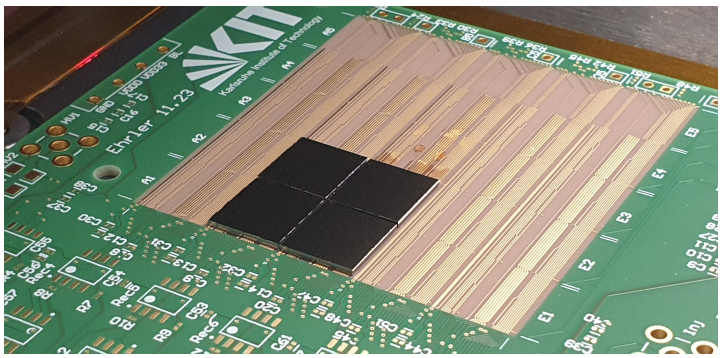


Figure 7.4.: Four HitPix2 sensors assembled on the 5×5 bump-bonding PCB. Photo courtesy of M. Caselle.

made to mitigate the problem, including testing different temperature profiles and types of glue. However, an optimal solution for a reliable matrix assembly with the SBB method was not found. Therefore, it was decided to adapt the PCB design for the wire-bonding assembly method.

7.1.3. HitPix2 matrix design based on wire-bonding

Initially, a SBB technology was selected for the 5×5 HitPix2 matrix assembly, which allows to design a relatively simple PCB with straightforward interconnections between sensors in the matrix. However, as discussed in the previous subsection, the sensor detachment during the assembly of the mock-up matrix led to the design of a more complex PCB adapted for the wire-bonding technology, which requires special assembly techniques to maintain small gaps between the sensors. A simplified view of the wire-bonding assembly for the 5×5 HitPix2 matrix is shown in Fig. 7.5.

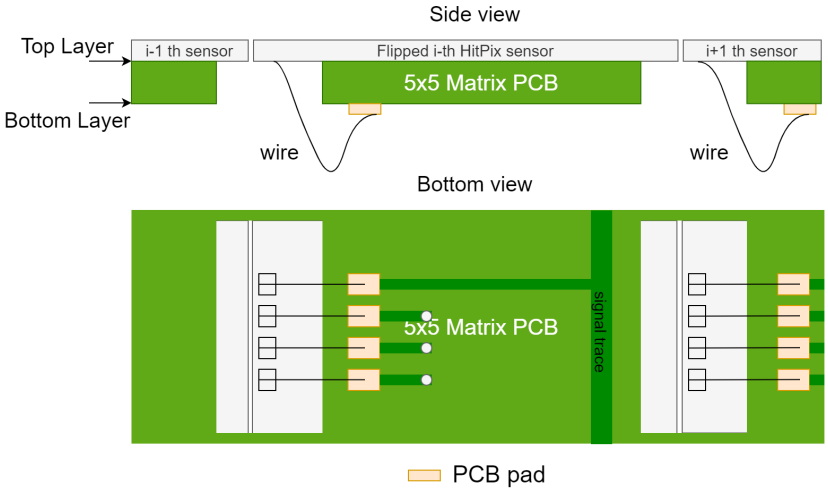


Figure 7.5.: Simplified view of the wire-bonding assembly for the 5×5 HitPix2 matrix.

Flipped HitPix2 sensors are positioned and mounted on the top layer of the PCB, i.e. their active side with contact pads is glued to the PCB, as shown in the side view of the figure. When all sensors are mounted, the entire assembly is flipped over and secured on the assembly jig, which prevents assembly movements during the bonding. To provide access to the sensor

pads, which are now facing upwards, mechanical cutouts are introduced on the PCB, allowing to wire-bond the sensor pads to corresponding bonding pads located on the PCB bottom layer. The HitPix2 5 × 5 matrix bump-bonding PCB was redesigned by the author and F. Ehrler to address the new assembly method. Figure 7.6 shows the top and bottom 3D render views of the new PCB. The PCB layout is shown in the Appendix in Fig. D.2.

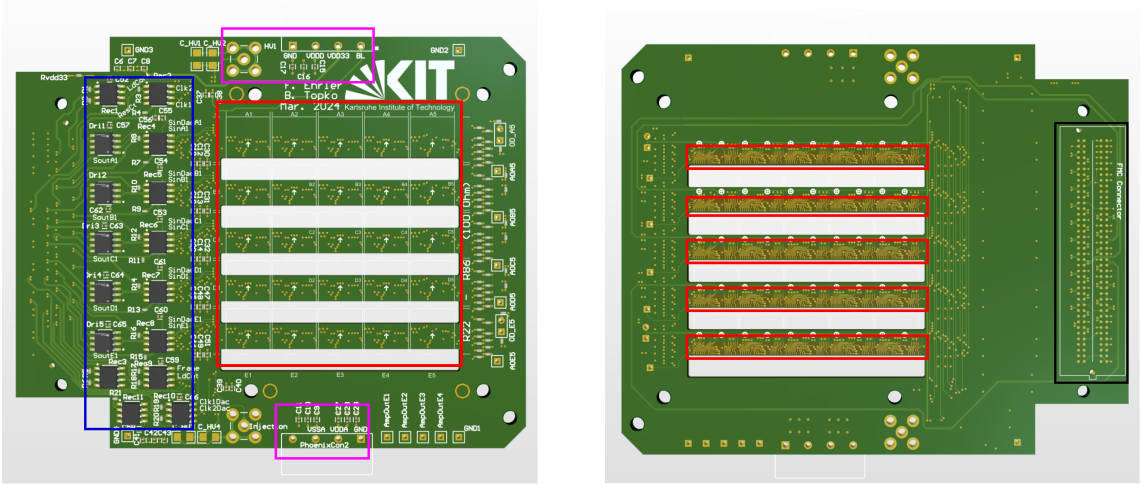


Figure 7.6.: Top (left) and bottom (right) 3D render views of the HitPix2 5 × 5 matrix wire-bonding PCB. The red, magenta, and blue solid boxes in the top view outline the sensor mounting area, power connectors mounting areas, and signal converter ICs, respectively. The black and red solid boxes in the bottom view outline the location of the LPC-FMC connector and wire-bonding pads, respectively. The PCB was designed by the author and F. Ehrler.

The PCB periphery, consisting of the signal converters, power supply connectors, and LPC-FMC connector remained unchanged and were transferred from the bump-bonding PCB design. The main difference between the two boards lies in the sensor mounting area. As for the bump-bonding PCB, five sensors in each matrix row form a daisy chain. However, in the bump-bonding PCB, the sensors in a row were positioned such that the contact pads of one sensor were parallel to those of the other, allowing for straightforward connection between sensors in a row on a single PCB layer. In contrast, for the wire-bonding PCB, sensors in a matrix row are positioned such that their contact pads are aligned along a straight line for access through the mechanical cutouts in the mounting area. The new sensor orientation in the matrix and implemented mechanical cutouts led to an increased safe distance between sensors compared to the bump-bonding PCB. The distance between sensors within the matrix row (i.e. sensors at positions A1, A2, A3 etc.) was increased from ∼400 µm to ∼480 µm, while the safe distance between the matrix rows (i.e. sensors at positions A1, B1, C1 etc.) was increased from ∼220 µm to ∼500 µm. This translates into corresponding distances of ∼700 µm and ∼1100 µm between sensor active areas, which are still within the acceptable range discussed in the previous subsection.

The minimal size of the mechanical cutouts is constrained by the capability of the wire-bonding machine, whose bonding head requires space to bond a wire from the PCB bonding pad (outlined with the red boxes in the bottom 3D render view in the figure) to the sensor contact pad. Hence, the width of the mechanical cutout was set to 5 mm. This design solution narrows the available PCB routing space to ∼5.5 mm for matrix rows located between cutouts, as can be seen in the figure. Together with the different sensor orientation compared to the bump-bonding PCB, this led to an increased routing complexity and increased number of layers in the board

stack-up from four to eight. The increased routing complexity becomes clear by comparing the two layouts in Fig. D.1 and Fig. D.2 in the Appendix.
The 25 HitPix2 sensors validated during the characterization campaign, were assembled into the 5×5 matrix. A photograph of the final assembly is shown in Fig. 7.7.

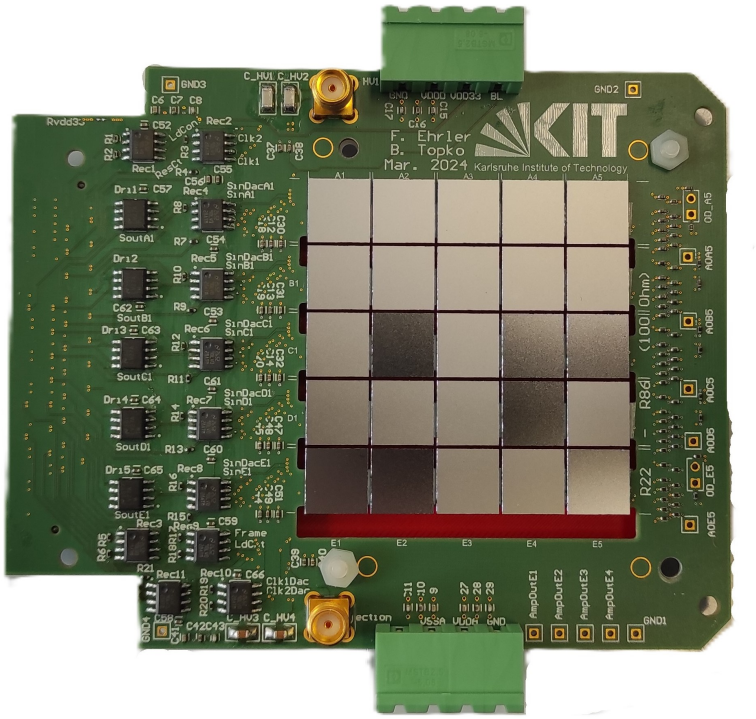


Figure 7.7.: Assembled 5×5 HitPix2 matrix.

After an initial power-up of the system, the power consumption in the low- and high-voltage power channels matched the expected values based on the sensor characterization results, confirming that all sensors in the matrix had a reliable electrical contact with the power rails. However, the matrix could not be read out. An oscilloscope measurement of individual control and data signals in the matrix confirmed that the signals were delivered to the sensors. Moreover, the row data was propagated through each daisy chain as expected, but the output voltage level of the sensor LVCMOS `SOut` output buffer was much smaller than the expected input signal range of the LVCMOS-LVDS converter.
To correct this issue, the new PCB design would require a level shift IC right after the HitPix2 `SOut` output buffer to adjust the output level of the signal, or a redesign of each matrix row to use the LVDS `SOut` HitPix2 output buffer. Since only one set of valid HitPix2 sensors was available for the assembly due to low production yield, it was decided to stop further development of the 5×5 matrix based on the HitPix2 sensors. Nonetheless, the knowledge and experience gained from the design, development and assembly of both HitPix2 5×5 matrices was applied to the beam monitor demonstrator design based on HitPix3 sensors, presented in the next section.

7.2. HitPix3 beam monitor demonstrator design

The 5×5 HitPix2 matrices for bump- and wire-bonding assembly technologies were designed such that all 25 tested sensors are mounted on a single PCB carrier, which provides all necessary connections for sensor power supplies, control and data signals, allowing to assemble a very

compact detector system. However, after the analysis of the 5×5 HitPix2 matrices assembly results, discussed in the previous section, the following list of risks and challenges were identified for such a system:

- Since all sensors are assembled onto a single PCB carrier (monolithic design), a 5×5 matrix assembly requires 25 individual positioning, mounting and bonding operations, increasing the risk of losing the matrix if even a single sensor is damaged, mispositioned, or improperly connected during the integration phase. For the beam monitor demonstrator designed for HIT, the failure of even one sensor is not acceptable.

- If a sensor is damaged or not fully integrated within the matrix, it is difficult to replace it without the risk of causing further damage to the matrix or the PCB carrier.

- For both assembly technologies, certain electrical components (power connectors, ICs) can only be soldered after the entire sensor matrix is mounted to the PCB carrier, due to constraints of the wire-bonding and flip-chip machines. Therefore, the assembly sequence increases the risk of damaging sensors during the placement of these components. Furthermore, the components can only be assembled manually without a reflow oven, because the high reflow temperature could degrade the adhesiveness of the glue used to mount sensors on the board, further increasing the complexity of the assembly process.

- Reworking flaws in the peripheral electronics, which may happen during the PCB design or production, is almost impossible once the sensors are integrated, leading to the loss of all functional sensors. Moreover, a possible sensor de-integration from such a failed PCB for reuse on a corrected one involves severe risk of sensor damage.

To address these challenges, the beam monitor demonstrator, based on HitPix3 sensors, was designed with a modular architecture. The 3D render of the detector system is shown in Fig. 7.8. The 5×5 matrix was segmented into five 1×5 HitPix3 strips, which are connected to a separate PCB, called motherboard. The motherboard is responsible for the control and data signal distribution and power delivery to the matrix.
The motherboard can be directly connected to the FPGA board (Digilent Nexys Video [Dig20]), which controls the data flows between the demonstrator and the control PC, as explained in section 4.3. Alternatively, the connection between the motherboard and the FPGA can be established via a cable, which is important for system tests inside magnetic fields, since it allows the FPGA board, which has components sensitive to such fields as reported in [Pit22], to be positioned away from them.
The modular design of the beam monitor demonstrator provides several important benefits compared to the monolithic design, which are listed as follows:

- The sensor assembly process is significantly simplified. Instead of handling 25 sensors in a single assembly process, only five sensors per 1×5 strip are positioned, mounted and bonded.

- Each 1×5 strip can be individually tested after every assembly phase, which enables greater control throughout the assembly process and ensures that only valid 1×5 strips are integrated into the demonstrator.

- If sensors in a 1×5 strip are damaged during final integration or due to radiation degradation, that strip can be replaced independently without disturbing the entire assembly.

- All peripheral electronics are assembled separately on the motherboard, allowing all components to be soldered in the reflow oven, simplifying the entire process. Furthermore, the motherboard can be reworked or upgraded independently.

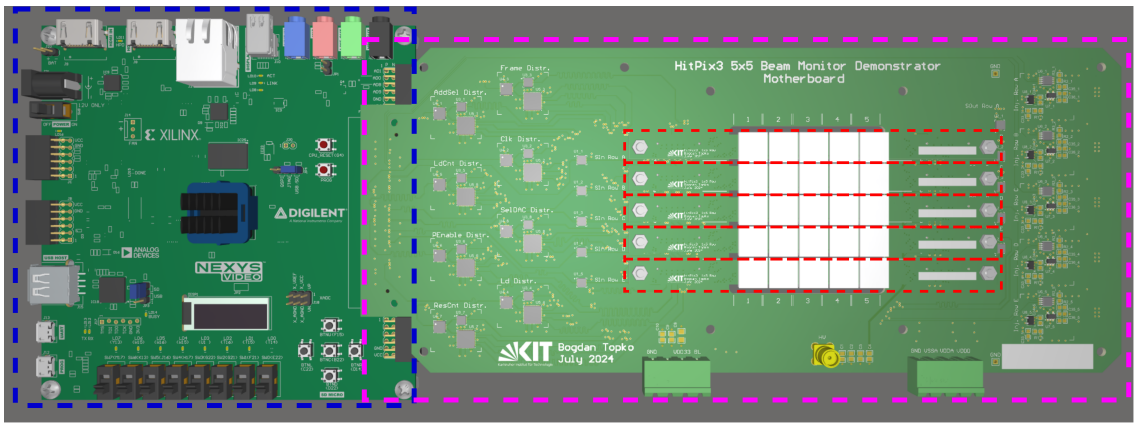


Figure 7.8.: 3D render of the assembled beam monitor demonstrator. The blue, magenta and red dashed boxes outline the FPGA board, the beam monitor demonstrator motherboard, and the five 1×5 HitPix3 strips, respectively.

The following subsections provide more details regarding the design of each component of the HitPix3 beam monitor demonstrator.

7.2.1. HitPix3 sensor optical characterization

Similar to the 5×5 HitPix2 matrix assembly, the HitPix3 sensors selected for the beam monitor demonstrators must be optically characterized to estimate their outer dimension variation w.r.t. the nominal values of 9775 µm × 10 110 µm to define the safe distances between sensors within the rows and columns of the matrix in the 1×5 strip and motherboard designs.
Fifty selected sensors were measured with a microscope, following the same procedure as for the HitPix2 sensors. The measurement results are detailed in table 7.2.

Table 7.2.: Measured outer dimensions of the HitPix3 sensors selected for two 5×5 matrix assemblies. Units: µm.

Parameter	Nominal	Mean	Std. deviation	Min	Max
Width	9775	10 126.5	4	10 118.7	10 135.5
Height	10 110	10 173.0	4	10 156.6	10 180.7

The measurement revealed significant improvements in the dicing procedure, since both standard deviations of sensor width and height yielded the same value of 4 µm. These values are much smaller than the corresponding values of 13 µm and 73 µm observed for HitPix2 sensors.
The measured mean sensor width is larger than the nominal value, due to ∼176 µm of extra insensitive wafer material accidentally introduced at both sensor sides during dicing. However, the improved consistency in outer dimensions is more critical than the slight increase in insensitive area, since it allows to define smaller safe distances between sensors in the matrix. The maximum measured values for width and height were used as reference for the PCB design.

7.2.2. 1 × 5 strip

The modular design of the HitPix3 beam monitor demonstrator is based on the 5 × 5 matrix segmented into five 1 × 5 strips. The 1 × 5 strip consists of five HitPix3 sensors and the PCB carrier. A 3D render of the assembled 1 × 5 strip in isometric view is shown in Fig. 7.9. The designed distance between sensor edges within the strip is 140 µm, corresponding to a 680 µm distance between sensor active areas, which is well within the acceptable range discussed in subsection 7.1.2.

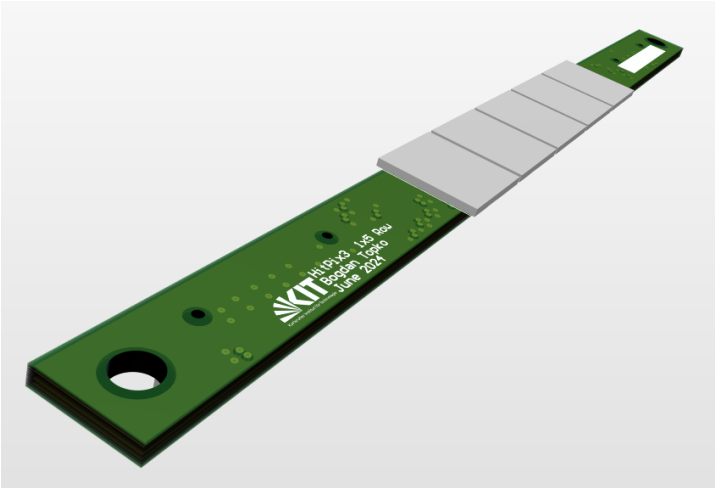


Figure 7.9.: 3D render of the assembled 1 × 5 strip in isometric view. The gray boxes represent the HitPix3 sensors.

Following the assembly technique developed for the 5 × 5 HitPix2 wire-bonding PCB (more details in subsection 7.1.3), the sensors are flipped and glued to the PCB carrier top layer with an epoxy resin. The PCB carrier height of 8.3 mm is designed narrower than the maximum sensor height of 10.181 mm, allowing to wire bond the sensor pads and the exposed bonding pads on the PCB bottom layer, which are shown in bottom view of the 1 × 5 strip 3D render in Fig. 7.10.

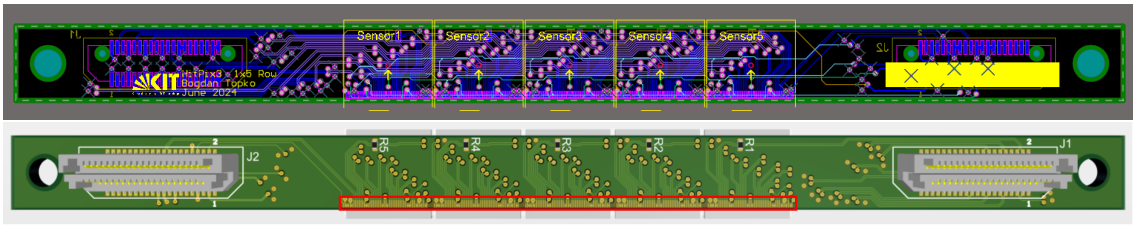


Figure 7.10.: 1 × 5 strip PCB layout (top) and 3D render of the bottom view (bottom). The red box outlines the PCB bonding pads in the 3D render.

Fine-pitch Samtec Razor Beam High-Speed Hermaphroditic connectors [Sam25] are positioned at both ends of the PCB carrier to establish connections with the motherboard. Careful attention was given to the alignment of the connectors on the PCB carrier. Their parallel placement (without any rotation and offset) is important, since the connector misalignment would prevent the integration of the 1 × 5 strip into the demonstrator. The connectors transmit ten LVDS control and data signals, one single-ended charge injection signal, four LV and one HV power supply voltages to the daisy-chained sensors.

The PCB was designed with a ten layer stack-up due to the main mechanical constraint defined by the sensor height. This allows to route all signal and power traces, while maintaining the signal integrity. However, some design requirements were relaxed due to limited space. All control and data signals were routed only at the bottom and 7th inner PCB layers. In this configuration, the signals share the same reference GND plane, placed at the 8th inner layer, consequently, no stitching vias are required when differential signals traverse these layers. However, it came at the cost of increased tolerance of $\pm 19\,\%$ to the target value of $100\,\Omega$ for the differential impedance of traces placed on the inner layer, due to constraints on trace geometry within the narrow PCB space of approximately $10\,\text{mm} \times 8.3\,\text{mm}$ per sensor. While the tolerance is considerable, the relatively low maximum readout speed of $150\,\text{Mbit}\,\text{s}^{-1}$ for the LVDS signals, measured for the 2×5 HitPix3 matrix in counter and adder readout modes, ensures that the 1×5 strip can be reliably read out.

7.2.3. Motherboard

In the modular design of the beam monitor demonstrator, the motherboard PCB has several functions: it hosts the 5×5 HitPix3 matrix and provides mechanical support, delivers electrical power to the HitPix3 sensors and peripheral electronics, establishes connection with an FPGA board, and distributes the control and data signals to and from the HitPix3 sensors. The motherboard PCB layout, based on eight layers stack-up, and its 3D render are shown in Fig. 7.11.

Five assembled 1×5 strips are connected to the motherboard PCB to form a 5×5 HitPix3 matrix. The designed edge-to-edge distance between neighboring matrix rows is 450 µm, corresponding to a 1015 µm distance between sensor active areas, which is well within the acceptable range for the matrix performance requirements. A large mechanical cutout is implemented under the 5×5 matrix area to minimize the beam scattering in the passive PCB material.

During the matrix assembly, the 1×5 strips are connected to corresponding pairs of the Samtec connectors, which have a fine pitch and interlocking mechanism. Maintaining proper linear and angular alignment during mating and unmating of the connectors is important to prevent their damage [Sam19]. To ensure the safe installation and extraction of the strips, Samtec Micro Jack Screw standoffs [Sam19] are positioned close to the connectors. Additionally, screws with rubber caps can be inserted into alignment holes near the connectors to prevent strip bending during the strip extraction.

All required LV power rails for the HitPix3 sensors (V_{dda}, V_{ssa}, V_{ddd}, and V_{bl}) and for the motherboard peripheral electronics (V_{dd33}) are delivered, already regulated by external laboratory power supplies, through two 4-pin connectors, located at the motherboard bottom edge. The power rails for the sensors are routed with wide traces and are connected to the 1×5 strips in parallel. For the peripheral electronics, the V_{dd33} rail is routed as a copper pour for most ICs, which are located close to the motherboard left edge. In contrast, for the charge injection circuits and output LVDS buffers, which are located at the PCB right edge, the V_{dd33} rail is routed with wide traces. The HitPix3 HV bias voltage (V_{bias}) is delivered through a single SMA connector and wide traces connected to all strips in parallel.

A connection to the FPGA Nexys Video board, which generates control and input data signals for the HitPix3 sensors and acquires matrix output data, is established using an LPC-FMC connector located at the bottom PCB layer. The connector serves as a standard high-speed interface, which allows to route up to 34 differential pairs. Furthermore, it is compatible with a wide range of FPGAs boards, therefore, the system can be upgraded without redesign of the motherboard, if the system will require higher readout speed than the current limit of $190\,\text{Mbit}\,\text{s}^{-1}$.

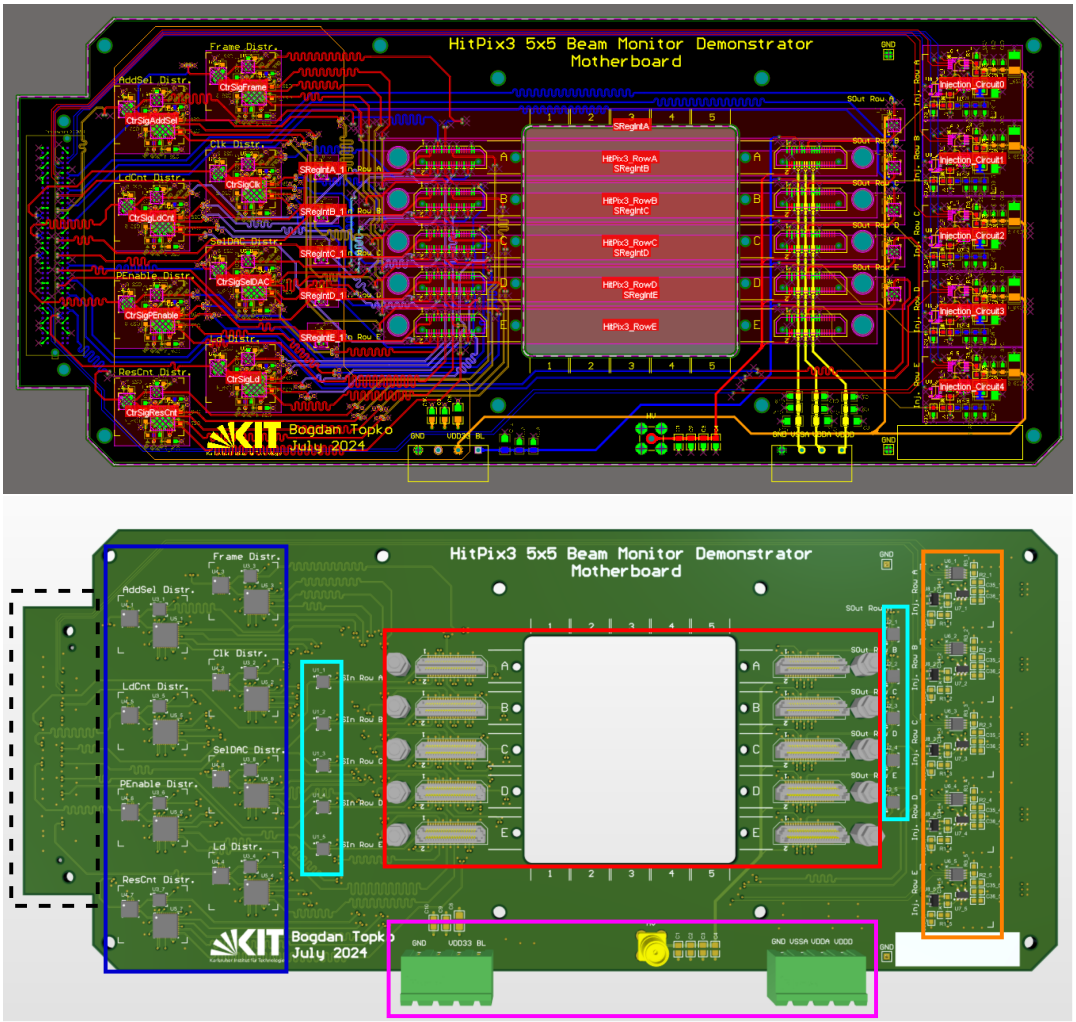


Figure 7.11.: Motherboard PCB layout (top) and its 3D render (bottom). The red, magenta, blue, light blue and orange solid boxes in the 3D render outline the 1×5 strips mounting area, power connectors, LVDS repeater circuits, LVDS input and output buffers, and charge injection circuits, respectively. The black dashed box in the 3D render outlines the location of the LPC-FMC connector, which is placed at the PCB bottom layer.

One of the motherboard primary functions is to transmit HitPix3 control signals (`Clk`, `ResCnt`, `PEnable` etc.) and input configuration data, generated by the FPGA, to each 1×5 strip, and to transmit their output data back to the FPGA with minimal time jitter between the control signals for different strips. Simple individual trace routing from the LPC-FMC to the 1×5 strip connectors would require $5 \times (8\ \text{[control]} + 1\ \text{[input data]} + 1\ \text{[output data]}) = 50$ differential pairs only for communication between FPGA and the matrix (excluding configuration and control signals for the charge injection circuits). Therefore, to simplify the communication and PCB design, an LVDS repeater circuit is implemented for each control signal.

A simplified schematic of the LVDS repeater is shown in Fig. 7.12. The repeater fans out the control signal, generated by the FPGA, to five matrix rows. The matrix rows on the motherboard are designated alphabetically (e.g. Row A, Row B, etc.) starting with A from the top, and will be referred to as such hereafter. The sensor positions within the row are designated numerically (e.g. 1, 2, 3, etc.) starting with 1 from the left.

The control signal is fed into the first stage of the repeater, which is based on an LVDS 2×2 cross-point DS25CP152 [Tex13c], and is repeated by its two LVDS output buffers. One output is transmitted to Row A through an LVDS buffer DS25BR150 [Tex13a], and the second output is repeated for Row B, C, D and E with an LVDS 4×4 cross-point DS25CP104A [Tex13b]. This allows to fan-out one control signal with a 1:5 ratio by using commercially available ICs. Consequently, the number of required differential pairs routed from the LPC-FMC is reduced to 8 [control] + 5 × (1 [input data] + 1 [output data]) = 18.

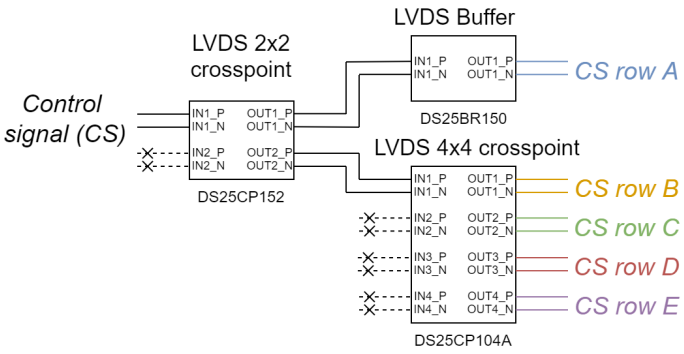


Figure 7.12.: Simplified schematic of the LVDS repeater. The ICs inputs indicated with dashed lines are not connected on the motherboard.

To ensure data signal integrity, the input and output data are transmitted through individual pairs of LVDS buffers DS25BR150. To support the `Sout` HitPix3 output buffers, the DS25BR150 are placed close to the 1×5 strip connectors on the PCB right side. This design solution is essential when the communication between the FPGA and beam monitor demonstrator is established via a long cable, which can cause signal loss. Furthermore, the LVDS repeaters and the input data signal buffers drive the 1×5 strips, which are connected to the motherboard via connectors, thus preventing signals degradation.
As for the 2×5 HitPix3 matrix (section 6.4), all signal trace lengths are tuned to minimize the inter- and intra-pair skews, which are required for the parallel readout of the matrix rows. The traces geometry is optimized to ensure a differential impedance match within a $\pm 7\,\%$ tolerance of the target value of $100\,\Omega$.
The charge injection circuits are implemented on the motherboard to perform individual pixel threshold tuning of sensors within each matrix row, following the procedure described in subsection 6.2.6. The circuits are based on the design of GECCO charge injection card [Ehr21], and are implemented for each matrix row. The voltage DAC of each circuit generates an amplitude level for the injection pulse. The DAC output is then buffered by a voltage follower, whose output is connected to an analog switch. When an enable pulse is applied to the switch, it shortly connects the follower output to ground, generating a short injection pulse with a controllable amplitude, which is then transmitted to the corresponding matrix row and subsequently to all HitPix3 sensors on that row. The configuration data and control signals for the charge injection circuits are generated by the FPGA and delivered to the circuits in parallel.

7.2.4. Parallel readout of the 5 × 5 matrix

A parallel readout architecture is implemented in the beam monitor demonstrator design to maintain a short readout dead time between frames. It is achieved by creating separate input and output data paths for each matrix row, while the control signals are distributed to all rows

in parallel via the LVDS repeaters. Furthermore, the minimized inter- and intra-pair skews for differential pairs ensures the parallel data transmission at high readout speeds.

The first version of the parallel readout scheme is based on the bit slicing of the matrix row output data, as shown in Fig. 7.13. The HitPix3 sensors in each 1×5 strip are daisy-chained, therefore, their configuration/data shift registers form a single shift register with a size of $5 \times 672 = 3360$ bit. The `Clk` signal delivered to all matrix rows in parallel via corresponding LVDS repeater simultaneously shifts out the last bit of each row shift register. These five bits form a bit slice. The bit slice is acquired by the FPGA in parallel after a controllable latency. Subsequently, the FPGA packs the slice into a 32 bit data packet. The size of the data packet allows to pack up to six bit slices. After the data packet is formed, it is processed by the existing data pipeline in the firmware to transmit the packet to the control PC. The existing data pipeline uses the Consistent Overhead Byte Stuffing (COBS) encoding algorithm for reliable data transmission, as explained in [Pit22].

In parallel with the matrix output data readout, the same `Clk` signal is used to simultaneously shift input HitPix3 configuration data (more details in subsection 6.1.3) into each matrix row shift register. The configuration data is similarly packed in bit slices, which are deserialized and directed to the corresponding matrix row shift register by the FPGA in parallel.

This readout scheme allows to organize the parallel readout of the matrix with minimal changes in the existing firmware. Most beam test results presented in this chapter are acquired with a firmware which implements this readout scheme, unless mentioned otherwise. However, the scheme has a drawback: the real-time decoding of the output data packets requires significant computational power for the control PC, due to a large number of bit operations including masking and shifts.

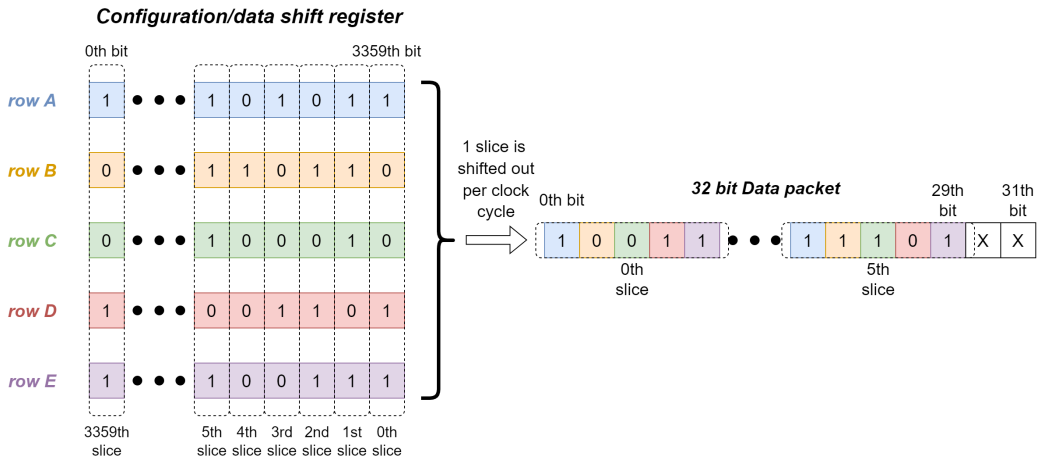


Figure 7.13.: Simplified scheme of the 5×5 HitPix3 matrix parallel readout.

The second version of the parallel readout was developed and successfully tested with the beam monitor demonstrator. In this version, five 6 bit buffers are filled with the matrix output data in parallel. When the buffers are completely filled or when it is the last bit slice, the buffered data is packed into the data packet in a block-wise manner starting from Row A, i.e. the first 6 bit of the data packet belongs to Row A, the next 6 bit belongs to Row B, etc. In this scheme, data decoding is simplified, since it includes only five bit shift operations per data packet. The readout performance measured using the beam monitor demonstrator and the FPGA configured with both firmware versions are provided in subsection 7.4.1.

7.2.5. Strip testing module

As discussed at the beginning of the section, in addition to the simplified matrix assembly process, the modular design enables greater control over the matrix and its components. While the motherboard PCB hosts the 5×5 HitPix3 matrix segmented into five 1×5 strips and ensures its operation, a specialized PCB called strip testing module was designed to test each strip throughout the beam monitor demonstrator production process. The module allows to identify possible strip issues with sensors connectivity, configuration or readout before its integration into the demonstrator, thus it ensures that all integrated strips meet the desired quality. The testing module PCB layout, based on four layers stack-up, and its 3D render are shown in Fig. 7.14.

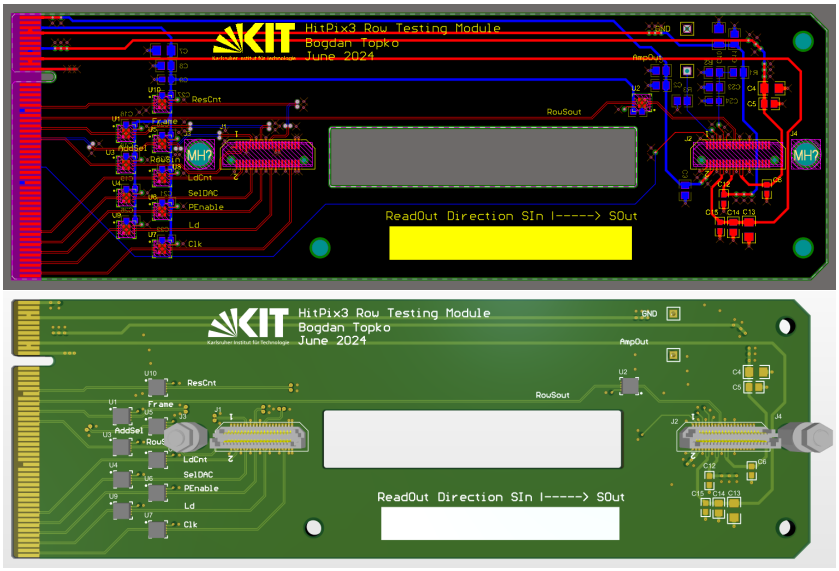


Figure 7.14.: Strip testing module PCB layout (top) and its 3D render (bottom).

As for the motherboard PCB, an assembled 1×5 strip is connected to corresponding pairs of the Samtec connectors, allowing to test the assembled strip compatibility with the motherboard connectors. A pair of the Samtec Micro Jack Screw standoffs is implemented on the module to additionally test the safe mating and unmating process of the 1×5 strip connectors. A mechanical cutout is introduced under the strip area with HitPix3 sensors. The cutout allows to optically inspect the wire bonds between sensor pads and PCB bonding pads and also provides a direct access to the PCB traces which can be probed with an oscilloscope during the debugging process.
To simplify the PCB design in terms of power delivery and connection to the FPGA board, a PCIe x8 edge connector compatible with the GECCO board socket is implemented on the strip testing module. This design solution allows to use the existing DAQ system for the testing procedure, presented in section 4.3, and to deliver all required LV and HV power rails, control, data and charge injection signals to the connected strip via a single interface. Additionally, each power rail of the testing module is equipped with an individual set of decoupling capacitors to suppress possible high-frequency noise.
Since the testing module is designed for testing a single 1×5 strip, no complex LVDS repeaters are required. However, to ensure the signal integrity, all control and data signals are buffered through individual LVDS buffers DS25BR150, which allows to effectively drive the HitPix3 sensors via connectors. As for the motherboard PCB, to support the HitPix3 `SOut` output buffer, the DS25BR150 is placed close to the connector. The trace geometry is optimized to

ensure the differential impedance match within a ±5 % tolerance of the target value of 100 Ω. Their lengths are also tuned to minimize the inter- and intra-pair skews.
Additionally, a separate pair of pins can be used for the direct measurement of the in-pixel CSA.

7.3. Beam monitor production workflow

The beam monitor demonstrator is a more complex detector system compared to the single sensor and small multi-sensor assemblies discussed in the previous chapters. To achieve the required system performance, each system component must be assembled and tested individually in a controlled environment. The demonstrator modular design allows to establish a streamlined production and quality control workflow, as shown in Fig. 7.15.

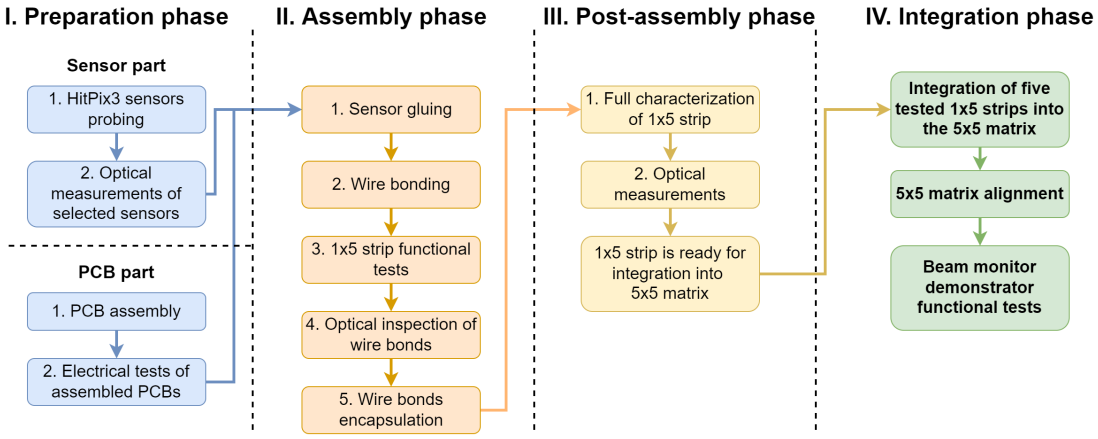


Figure 7.15.: Block diagram of production and quality control workflow of the beam monitor demonstrator.

The workflow consists of four phases. In the initial preparation phase, the production and quality control are performed in parallel for the HitPix3 sensors and PCBs. The former includes probe station testing and optical measurements of selected sensors, while the latter includes assembling and electrical testing of all PCBs: 1×5 carriers, the motherboard and the strip testing module. The assembly and post-assembly phases focus on the assembly of the 1×5 strips and their full characterization before integration into the 5×5 matrix. In the final integration phase, the 1×5 strips that successfully passed all characterization tests are integrated into the 5×5 matrix, followed by the sensor alignment procedure and the functional tests of the beam monitor demonstrator. Each workflow phase is described in detail in the following subsections.

7.3.1. Preparation phase

During the preparation phase, the HitPix3 sensors are characterized at the probe station and selected for the beam monitor demonstrator assembly. The testing procedure and characterization campaign results are discussed in section 6.3. The fifty valid sensors selected for the assembly of two beam monitor demonstrators are optically characterized to measure their outer dimensions, which define the safe distances between sensors within the rows and columns of the matrix. The optical characterization results are discussed in subsection 7.2.1.
In parallel to the sensor validation process, the produced 1×5 carriers, the motherboard and the strip testing module PCBs follow their own assembling and testing processes. This ensures

that only fully functional PCBs are used for assembling with the validated sensors. A general assembly and testing process can be briefly summarized as follows:

- Each PCB is optically inspected for possible production defects. Careful attention is given to the exposed bonding pads of the 1×5 carriers.
- All traces for the HitPix3 sensor control and data signals, and power rails are electrically tested with a multimeter for possible shorts or missing connections.
- Electrical components of the PCBs are soldered using a reflow oven and applying a validated temperature profile, provided by the soldering paste manufacturer.
- To remove possible residuals of the soldering paste, each PCB is cleaned with isopropanol.
- The assembled PCBs are optically and electrically re-tested to ensure that bonding pads were not corrupted during the assembly process and that no shorts were introduced during component soldering.

The strip testing module was assembled and tested first because later it was used for additional electrical tests of the 1×5 carriers. In these tests, the HitPix3 control and data signals are measured with an oscilloscope on the 1×5 carriers. Additionally, each LV and HV voltage level is measured with a multimeter. The testing procedure ensures that the assembled 1×5 carriers will provide all necessary connections to the HitPix3 sensors.
The motherboard PCB is tested independently after its assembly. Similar to the 1×5 carriers, the tests include multimeter measurements of each LV and HV voltage level, and oscilloscope measurements of all control and input data signals from the LVDS repeaters to confirm their functionality. Furthermore, the time jitter between the control signals repeated for the pair of the most distant matrix rows, Row A and Row E, is measured to check the motherboard capability for the parallel readout, as explained in subsection 7.2.4. The measured time jitter between the signals did not exceed 100 ps, which is more than sufficient for the anticipated system readout speed below $150\,\mathrm{Mbit\,s^{-1}}$. This also validates the design approach and allows to potentially upgrade the system readout speed to a few $\mathrm{Gbit\,s^{-1}}$ for a more powerful FPGA board and new firmware.
After the sensor and the PCB part of the preparation phase are completed, the main system components are validated for the next assembly phase.

7.3.2. Assembly phase

During the assembly phase, the validated HitPix3 sensors and 1×5 carriers are assembled together to form the 1×5 strips of the beam monitor demonstrator. A diagram of the 1×5 assembly flow is shown in Fig. 7.16.
In the first assembly step, the assembly jig (designed by S. Maier) is cleaned with isopropanol to prevent contamination of the PCB bonding pads. The jig is used to secure the carrier during the assembly process. The mechanical cutouts are implemented on the jig for the carrier connectors and termination resistors, which are located on the bottom and top PCB layers, respectively. The cutouts ensure the carrier planarity during the assembly process.
After the jig preparation, the 1×5 carrier is positioned onto it with the sensor mounting area, located on the top PCB layer, facing upwards. A special aluminum sensor stencil (designed by S. Maier) is then positioned and aligned on top of the carrier. The sensor stencil is designed to match the carrier geometry with a mechanical cutout under the carrier sensor mounting area. The stencil prevents sensor movement relative to the carrier and ensures the sensor vertical alignment within the matrix row. Otherwise, a 1×5 strip with a significant vertical offset of

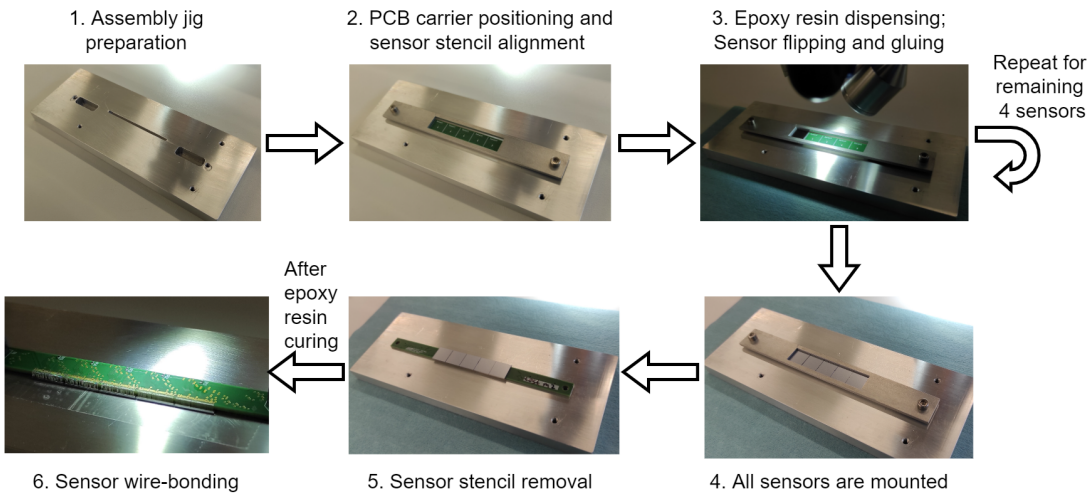


Figure 7.16.: Diagram of the 1×5 strip assembly flow.

the sensor position w.r.t. the carrier could not be integrated into the 5×5 matrix, since edges of sensors in that strip would overlap with sensors from a neighboring strip. After the stencil alignment, both the carrier and the sensor stencil are secured with screws on the assembly jig.

In the next step, Araldite®2011 epoxy resin [Hun24] is dispensed on the carrier mounting area. The flipped HitPix3 sensor is then glued to the corresponding position on the carrier. The horizontal alignment of the sensors is performed manually by using the silkscreen-printed alignment lines on the carrier surface. This step is repeated for the remaining four sensors. After all sensors are mounted on the carrier, the sensor stencil is carefully removed to avoid disturbing the glued sensors. Afterwards, the carrier with glued sensors is placed into a special box and left there for 24 hours to cure the epoxy resin at room temperature.

In the last step, the carrier with the mounted sensors is positioned and secured on the assembly jig with the PCB bonding pads, located on the bottom PCB layer, facing upwards, to wire bond the sensor to the PCB bonding pads.

After wire-bonding, the 1×5 strip is connected to the strip testing module, as shown in Fig. 7.17, to perform a series of functional tests. These tests verify that all electrical connections between the HitPix3 sensors and the PCB carrier are established before the wire bonds are encapsulated, since it allows to rework missing or corrupted wire bonds.

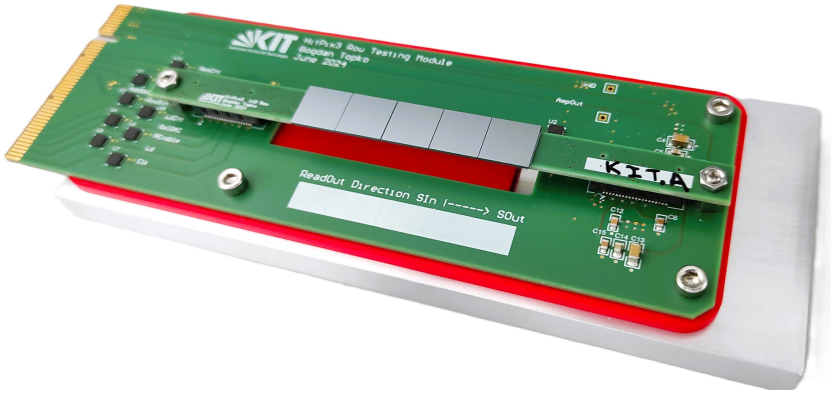


Figure 7.17.: An assembled 1×5 strip connected to the strip testing module.

The testing sequence and results of the 1×5 strips are only presented for the post-assembly phase in the next subsection 7.3.3, since the full characterization tests include all functional tests and the assembled 1×5 strips demonstrated no significant deviation between the functional test and full characterization results.
If a 1×5 strip successfully passed all functional tests, it is disconnected from the strip testing module and optically inspected under a microscope to verify that wire bonds were not damaged during the PCB probing or disconnection from the module. After the optical inspection, the wire feet bonded to the PCB are encapsulated with Sylgard 186 silicone elastomer [The17]. The encapsulation is performed only on this side of the wire bond because encapsulating the second foot, which is located in the narrow ∼1.1 mm region between the PCB and sensor edges, has a severe risk of forming an elastomer blob at the sensor edge. Such a blob could prevent the strip integration into the 5×5 matrix. Photographs of wire bonds before and after encapsulation are shown in Fig. 7.18.

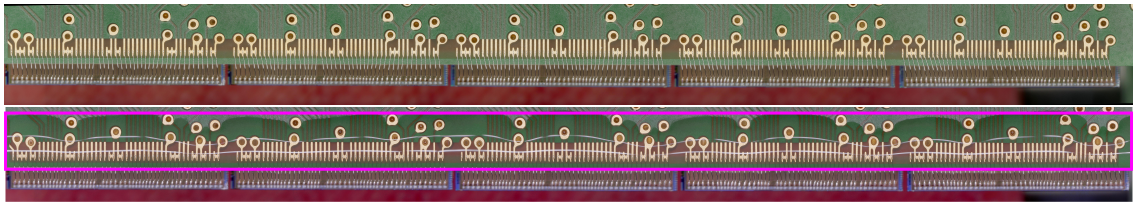


Figure 7.18.: Wire bonds before (top) and after (bottom) encapsulation. The dispensed encapsulant is outlined with the magenta box.

After the encapsulation, the 1×5 strip is left in a box for 24 hours to cure the silicone elastomer at room temperature. When the encapsulant is cured, the assembled 1×5 strip is ready for the full characterization in the post-assembly phase.

7.3.3. Post-assembly phase

During the post-assembly phase, the assembled 1×5 strips are connected to the strip testing module and are validated in a series of tests, as shown in Fig. 7.19. The test series is based on the 2×5 HitPix3 matrix characterization measurements (more details in subsection 6.4.2) and includes the latency scan and I-V tests, the pixel threshold tuning procedure, followed by the charge injection test. For the final characterization, the cumulative profile of a Sr-90 source, positioned above each sensor in the strip, is measured in both counter and adder readout modes. The results presented in this and the following subsections were obtained for the 1×5 strips of the beam monitor demonstrator used in the beam tests at HIT.

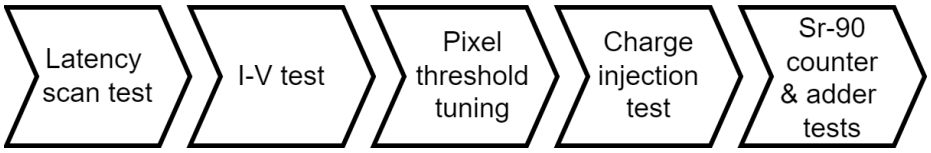


Figure 7.19.: Block diagram of the testing flow of assembled 1×5 strip.

In the following tests all sensors in the matrix were configured with `bias-DAC` settings D. The voltages V_{dda}, V_{ssa} and V_{bl} were set to 1.90 V, 1.16 V and 1.0 V, respectively. To increase the strength of the `SOut` output buffers, the V_{ddd} voltage was increased to 2.25 V. For the pixel threshold tuning, charge injection and Sr-90 source tests, the bias voltage V_{bias} was set to −90 V. All measurements were performed at room temperature.

To estimate the maximum readout speed of each strip, a latency scan was performed. The measured latency scans are shown in the Appendix in Fig. D.3. As for the 2×5 HitPix3 matrix, the latency scan tests demonstrated that all strips can reach the readout speed limit of 190 Mbit s^{-1} for the current firmware. However, for the measurements in counter and adder readout modes, the readout speed of the 1×5 strip was reduced to 95 Mbit s^{-1} and 140 Mbit s^{-1}, respectively. This decision was made due to corrupted data effects observed at higher readout speeds, similar to those observed for the 2×5 HitPix3 matrix. The 1×5 strips have a lower maximum readout speed compared to the 2×5 HitPix3 matrix value of 150 Mbit s^{-1} because of their design compromises discussed in subsection 7.2.2, which can make them more susceptible to possible crosstalk.

Next, the I-V test verifies that all sensors in the strips can withstand a high bias voltage up to −130 V. Figure 7.20 shows the individual I-V curves of the assembled 1×5 strips. As expected, all curves follow a square root function of bias voltage and do not have early breakdown voltages below −130 V. The total leakage current (shown as the brown points in the figure) was calculated as the sum of individual strip leakage currents. The total leakage current of 25 HitPix3 sensors does not exceed 750 nA at bias voltage of −100 V and lies well within the expectations.

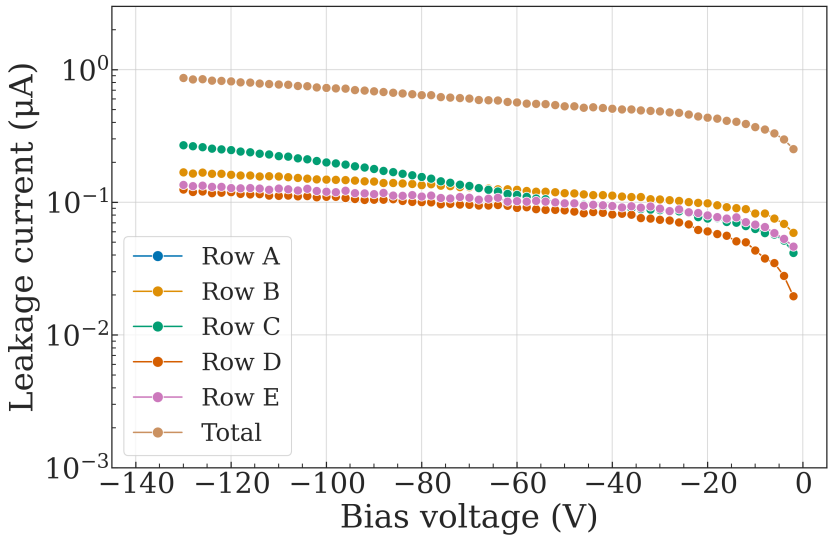


Figure 7.20.: I-V tests of each 1×5 strip. The brown points represents the sum of individual 1×5 strip leakage currents.

After testing the basic functionality of the 1×5 strips, a charge injection test was performed to verify the pixel threshold tuning functionality, following algorithm 1 from subsection 6.2.6. For this test, the threshold voltage was set to 138 DAC units for all strips, except the strip for matrix Row D, which was configured with a slightly higher value of 140 DAC units to achieve the same pixel threshold level.

The measured pixel threshold distributions for each 1×5 strip before and after pixel threshold tuning are shown in Fig. 7.21. After the tuning, the pixel threshold deviation was reduced by a factor of two across all strips. This could be further improved by increasing the `bias-DAC.ipdac` to higher values, since similar measurements for the 2×5 HitPix3 matrix yielded a reduction factor of seven at the `bias-DAC.ipdac` setting of 28 DAC units, whereas the strips were measured with the `bias-DAC.ipdac` setting of 14 DAC units. Nonetheless, the tests confirmed the pixel threshold tuning functionality for all sensors in the strips.

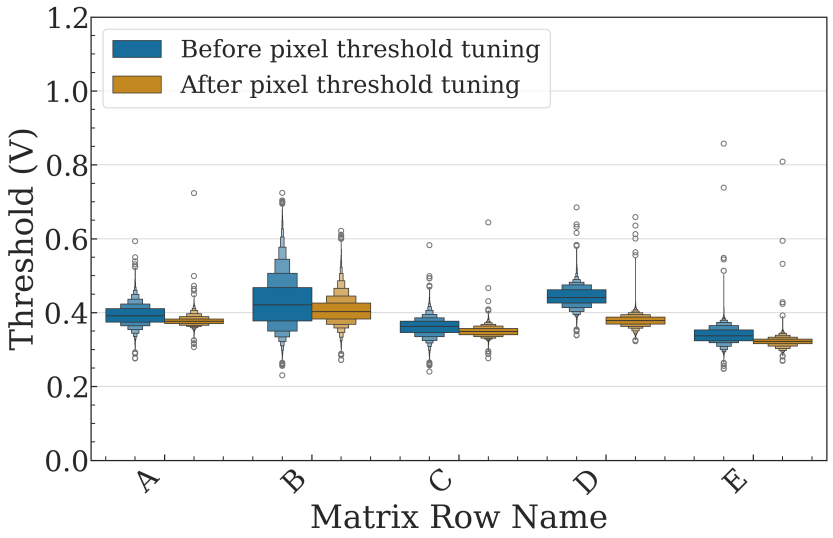


Figure 7.21.: Measured pixel threshold distribution for each 1×5 strip before (blue) and after (orange) pixel threshold tuning. The threshold voltage was set to 138 DAC units for all strips, except the strip for matrix Row D, which was configured with a threshold voltage of 140 DAC units.

The pixel thresholds of the strip for the matrix Row B have a larger deviation before and after pixel threshold tuning compared to other strips. This can be explained by individual offsets in the common threshold voltage of some sensors in that strip. A higher threshold voltage for these sensors can shift their pixel threshold mean to higher values, consequently increasing the distribution width, even when the individual pixel offsets are compensated.

During the final test, a Sr-90 source was positioned above each sensor in the strip and measurements were performed in both counter and adder modes after the pixel threshold tuning. In these measurements, the frame duration and the threshold voltage were set to 5 ms and 150 DAC units, respectively. Each Sr-90 source position was measured in 2000 frames. The noisy pixels, defined as in subsection 6.2.8, were masked, and their fraction was found to be ∼0.44 % of all pixels combined for all strips.

Figure 7.22 shows the combined cumulative Sr-90 source profiles measured using each sensor of every 1×5 strip in counter mode. As expected, after the pixel threshold tuning, each spot profile has improved regularity and smoothed contours. The same effect is observed in the Sr-90 profiles measured in adder mode, which are shown in the Appendix in Fig. D.4.

However, two sensors (2 and 3) in Row B, one sensor (3) in Row C, and one sensor (1) in Row A have smaller total counts at the center of their measured profiles. This can be explained by offsets in their threshold voltage, which were previously observed in the charge injection measurements. Therefore, for the optimal matrix operation, a new pixel threshold tuning algorithm should be implemented, which would include additional steps to adjust individual threshold voltage for each sensor within the matrix. This can be done only after the integration of all strips into the 5×5 matrix to address all possible voltage offsets introduced by the motherboard interconnections and peripherals.

The distinct pattern of the masked pixels at the edges of the sensor 1 in Rows C, D and E was attributed to the corrupted data effect discussed at the beginning of this subsection. These pixels were found fully functional at a lower readout speed of 85 Mbit s^{-1}.

After the full characterization, each 1×5 strip is individually measured with a microscope to ensure that sensors are well-positioned within the strips (Y-direction) and will not overlap with

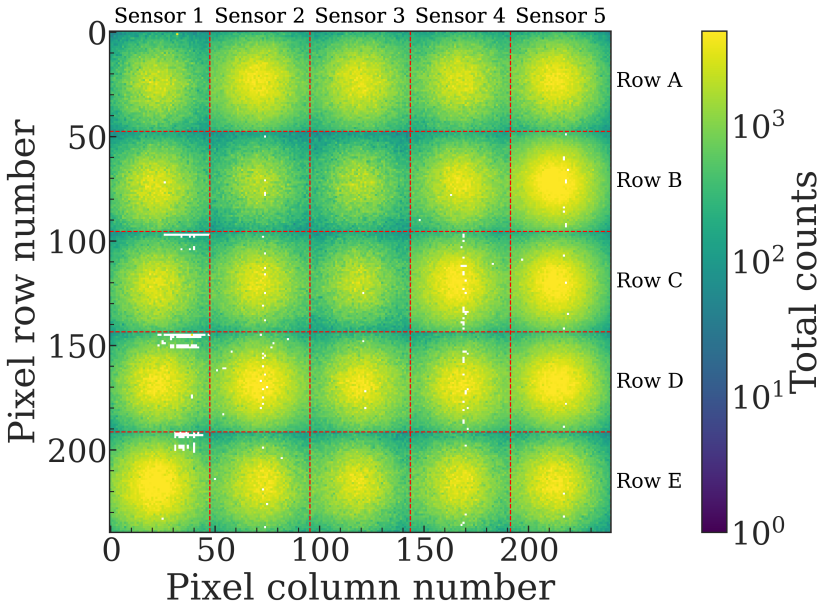


Figure 7.22.: Cumulative Sr-90 source profiles measured using each sensor of every 1×5 strip after pixel threshold tuning in counter mode. Red dashed lines outline individual pixel matrix for each sensor. Number of frames per source position: 2000. The threshold voltage was set to 150 DAC units.

sensors from the neighboring rows in the 5×5 matrix. The measured difference between the actual and designed sensor positions within each assembled 1×5 strip (Y-direction) is detailed in table 7.3.

Table 7.3.: Measured difference between the actual and designed sensor positions within the 1×5 strip (Y-direction). Units: µm.

Matrix Row Name	Mean	Std. deviation	Min	Max
A	34.0	20.5	2.8	75.2
B	135.8	19.0	100.0	172.7
C	68.9	17.8	41.7	115.6
D	142.2	19.0	116.7	179.7
E	196.6	10.0	173.0	233.4

The mean measured difference between the actual and designed sensor positions is biased towards positive values for all strips and can be explained by non-ideal alignment of the sensor stencil and the 1×5 PCB carrier during the assembly phase. However, the designed safe distance of 450 µm for the neighboring matrix rows is sufficient to cover these differences. Therefore, the assembled and tested 1×5 strips are ready for final integration into the 5×5 matrix of the HitPix3 beam monitor demonstrator.

7.3.4. Integration phase

During the integration phase, the assembled and fully characterized 1×5 strips are integrated into the 5×5 matrix on the assembled and tested motherboard. A photograph of the assembled

HitPix3 beam monitor demonstrator directly connected to the FPGA board is shown in Fig. 7.23.

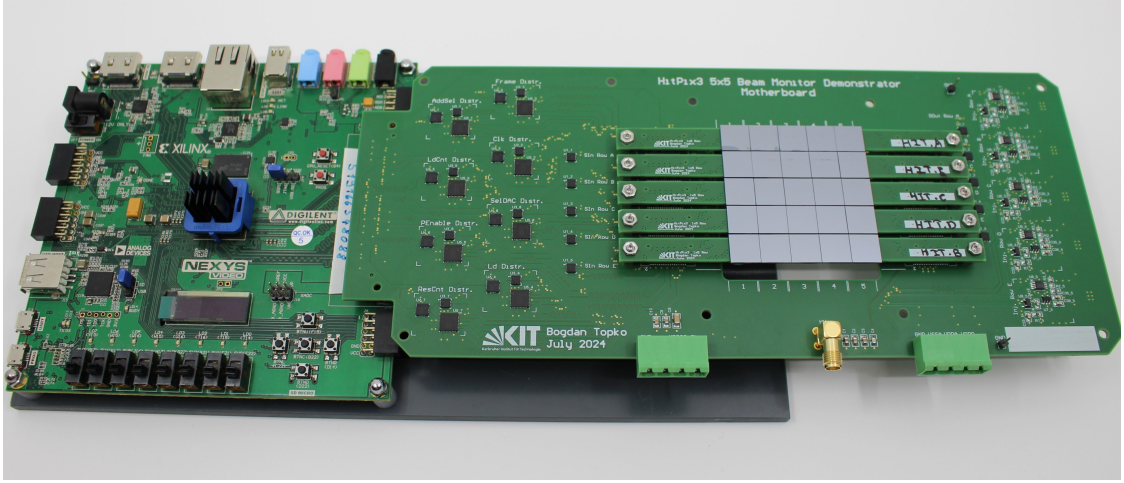


Figure 7.23.: Assembled HitPix3 beam monitor demonstrator connected to the FPGA board.

As for the small HitPix2 and HitPix3 multi-sensor assemblies, individual sensor offsets and local rotations, introduced during the assembly, can bias the reconstructed beam position and size without alignment. Therefore, to compensate this, all sensors in the matrix were measured with a microscope to create a local pixel coordinate map, which is shown in Fig. 7.24. Its local coordinate origin (0,0) is located at the matrix geometrical center, calculated as a half of the average horizontal and vertical distance from the matrix edges. The map X- and Y-axes are aligned with the axes of the existing beam monitoring system at HIT, with the Z-axis pointing downstream the beam path.

The local pixel coordinate map allows to assess the matrix assembly quality in terms of local sensor rotations and offsets. The local rotation angle distribution of the HitPix3 sensors in the beam monitor demonstrator is shown in the Appendix in Fig. D.5. The average local rotation angle was found to be 0.00° with a standard deviation of 0.10° and a maximum value of 0.23°, confirming that local sensor rotations are almost negligible.

To estimate the individual sensors offsets, the distances between active areas of neighboring sensors were calculated and compared to the designed values, as shown in the zoomed pixel coordinate map of four neighboring sensors of Fig. 7.25.

To collect a large dataset, the estimation was performed on the pixel level: distances in the X- and Y-directions were measured between edge pixels of neighboring sensors within the matrix rows and columns and are detailed in table 7.4.

Table 7.4.: Measured distances in the X- and Y-directions between edge pixels of neighboring sensors within the matrix rows and columns. Units: µm.

Parameter	Designed value	Mean	Std. deviation	Min	Max
ΔX_{col}	680.0	675.8	39.5	582.5	753.5
ΔY_{col}	0.0	−3.1	18.7	−41.3	31.7
ΔX_{row}	0.0	24.5	68.8	−112.4	132.6
ΔY_{row}	1015.0	1024.6	41.9	932.4	1093.2

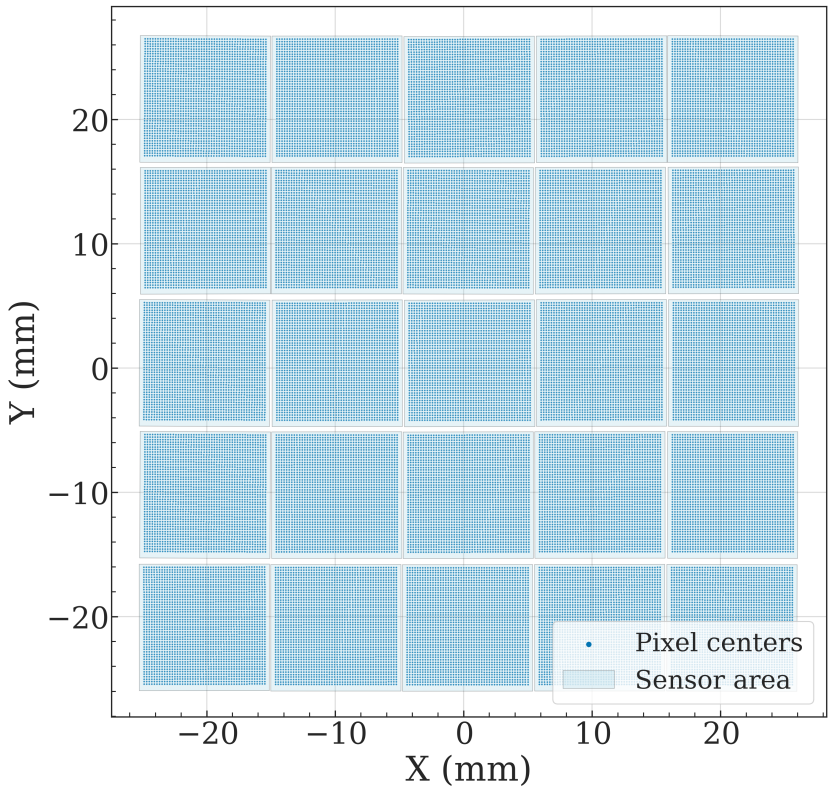


Figure 7.24.: Pixel coordinate map of the HitPix3 beam monitor demonstrator.

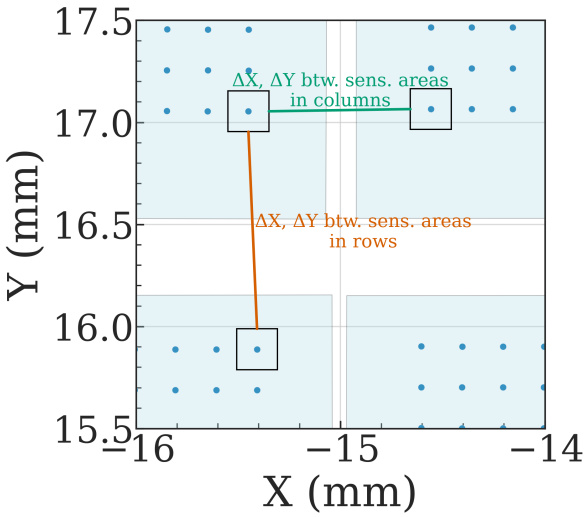


Figure 7.25.: Zoomed pixel coordinate map of four neighboring sensors in the matrix. Black boxes and blue points represent the pixel area and its center, respectively.

The mean distances are well in agreement with the designed values. Moreover, the minimum and maximum distances do not deviate from the designed value by more than 132.6 µm, which is less than the single pixel size of 200 µm. Given that the sensors in the matrix were assembled without an automated machine, the presented results confirm a good assembly quality of the beam monitor demonstrator.

The beam monitor demonstrator will operate in both counter and adder readout modes. The counter mode will be used as a beam diagnostic tool, providing a detailed two-dimensional image of the beam. In contrast, the adder mode is foreseen to be the main operational mode, which provides already calculated beam projections in the X- and Y-directions for the fast beam parameters reconstruction. Therefore, it is important to correctly derive the adder coordinates from the pixel coordinate map.
Figure 7.26 shows the coordinate assignment strategies for adders of HitPix3 sensors without and with local sensor rotation. If a sensor does not have any local rotation, as shown on the left panel of the figure, then the adder coordinate (X_{add1} or Y_{add1} in the figure) is simply equal to the X or Y coordinate of all pixels contributing to the summation along the corresponding sensor row (Y_1, Y_2, Y_3 in the figure) or column (X_1, X_2, X_3 in the figure), since all pixels share the same coordinate projected onto the X- or Y-axes.

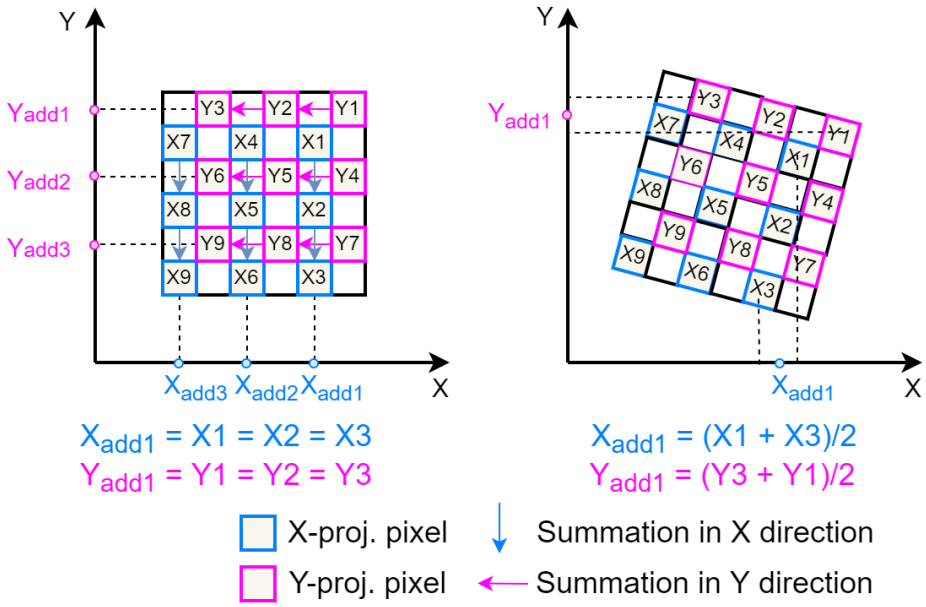


Figure 7.26.: Coordinate assignment for adders of HitPix3 sensor without (left) and with (right) local sensor rotation.

However, if a sensor is rotated, as shown on the right panel of the figure, then the pixels that contribute to the summation will have different projected coordinates onto the X- and Y-axes, leading to an uncertainty of the measured coordinate for a particle that traversed through one of the pixels. Therefore, to minimize this uncertainty, the adder coordinate is assigned as the arithmetic mean of the two most distant projected coordinates in the sensor row or column. This leads to a symmetric uncertainty distribution, which does not exceed $\pm 20\,\mu m$ across all adders in the assembled matrix and is almost negligible compared to the effective adders pitch of $400\,\mu m$.
Figure 7.27 shows the resulting adder coordinate map of the HitPix3 beam monitor demonstrator for projections in the X- and Y-directions for each 5×5 matrix row. In this map, every 24 adders belong to a sensor in the corresponding matrix row.
The total measured projections of the matrix are combined from the five adders in the corresponding row or column of the matrix. To calculate a single projection point, the five corresponding adder values must be summed, and the projection coordinate must be assigned based on the adder coordinates. The projection coordinate assignment depends on the adder alignment, as shown in Fig. 7.28 for the projection in the X-direction.

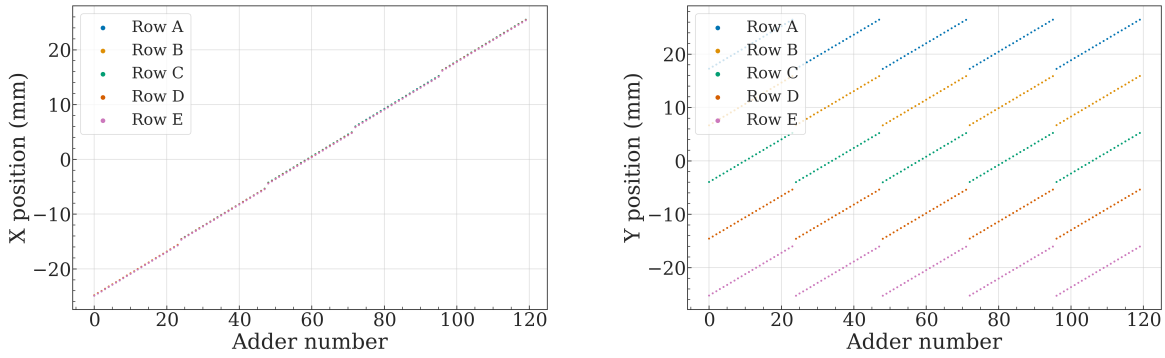


Figure 7.27.: Adder coordinate map of HitPix3 beam monitor demonstrator for projections in the X- (left) and Y- (right) directions. The adder coordinate maps for the projections in the X-direction are almost identical due to the good sensor alignment.

If the five adders in the matrix rows are ideally aligned (marked as "Ideal case" in the figure), a difference between their coordinates is negligible, and the projection coordinate is simply equal to the adder coordinates. However, based on the adder coordinate map, the mean difference between corresponding adders in the matrix equals $-43.5 \pm 62.5\,\mu m$ and $-1.0 \pm 21.8\,\mu m$ in the X- and Y-directions, respectively. To minimize their influence on the reconstructed beam parameters, the projection coordinate for every measured frame is calculated as a weighted mean of the five adder coordinates (marked as "Real case" in the figure) in which the coordinate weight is the ratio of the corresponding adder count to the total projection value.

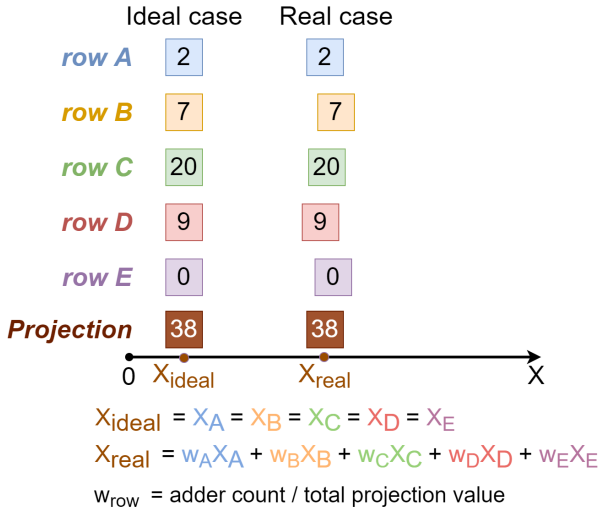


Figure 7.28.: Projection coordinate assignment for the 5×5 matrix in the X-direction for an ideal (left) and a real (right) case.

After the pixel and adders alignment, the beam monitor demonstrator passed through a series of tests, similar to those used in the post-assembly phase. While most of the test results were well within the expectations from the 1×5 strips characterization results, two important exceptions should be discussed.
During the latency scan test, the beam monitor demonstrator maximum readout speed was limited to $145\,Mbit\,s^{-1}$, which is lower compared to the individual 1×5 strip results from the post-assembly phase. One possible explanation is that the LVDS buffers supporting the HitPix3

SOut buffers are placed at a larger distance from the connectors in the demonstrator compared to this distance in the strip testing module, due to space limitations in the motherboard mounting area. The longer traces can lead to signal integrity issues at high readout speeds, especially if the SOut driving current is small.
The charge injections could not be reliably performed due to an error in the charge injection circuits, introduced during transferring their design to the motherboard. Hence, the pixel threshold tuning procedure could not be performed on the matrix level, since it relies on the charge injections measurements. To address this issue, a new revised motherboard needs to be designed and produced. Instead, for the first beam tests with the beam monitor demonstrator, presented in this thesis, a combined map of pixel tune values was created from the individual 1×5 strip measurements obtained during the post-assembly phase. This approach is valid because the offsets corrected by the tuning procedure are not expected to change significantly after the 1×5 strips integration, and the sensors were not radiation damaged.

7.4. Beam test results

The HitPix3 beam monitor demonstrator was installed and tested at the HIT beamline in August 2024 to evaluate the demonstrator performance for beam parameter reconstruction. Photographs of the experimental setup are shown in Fig. 7.29. The beam monitor demonstrator was mounted on the mechanical stage and positioned at the beamline isocenter using the laser-based alignment system (pink lines in the photographs).

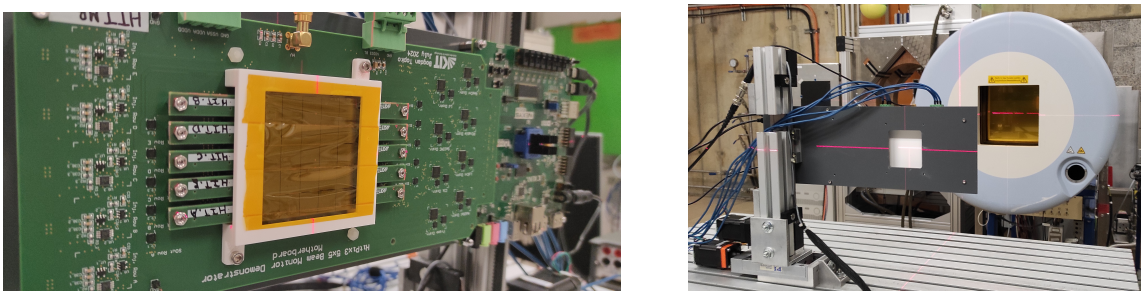


Figure 7.29.: The HitPix3 beam monitor demonstrator installed at the isocenter of the HIT beamline. The photographs of the system are shown in views downstream (left) and upstream (right) the beam. The pink lines represent the laser-based alignment system.

In the beam test with the small 2×5 HitPix2 matrix, the ISO-MWPC detector was used as a reference system, as described in subsection 5.3.3. However, during the beam test of the demonstrator, the ISO-MWPC was not available. Therefore, to estimate the accuracy of the reconstructed beam position, beam positions measured with the MWPC located at the beam nozzle were projected onto the isocenter and used as the reference values. To calculate the projected values, the measured beam position in the X- and Y-directions (in mm units) from the MWPC was multiplied by the corresponding scaling factors of 1.2126 and 1.1885, respectively, which were provided by HIT. The MWPC was configured with 125 µs integration time for all measurements.

7.4.1. Spot measurements

Proton and carbon beams were measured with the HitPix3 beam monitor demonstrator in a wide range of energy and intensity settings at a fixed beam focus setting. All beams were

configured to irradiate a single central spot at the coordinate origin of the beamline isocenter (0, 0). The beams were delivered in three spills with an approximate duration of 5 s per spill. In a beam measurement plan, the planned dose is configured as the number of particles per beam position. Hence, if the number of planned particles was not delivered in three spills, a fourth, shorter spill might be delivered to fulfill the plan. The nominal beam parameters used in the measurements are detailed in table 7.5. It is important to note that at the HIT accelerator facility, the dynamic intensity controller [Sch+15] reduces the beam intensity by a factor of two for a beam energy setting less than E18, which is reflected in the table for beams configured with the lowest E1 setting.

Table 7.5.: Nominal beam parameters for the measurements with the HitPix3 beam monitor demonstrator. The table data are taken from the actual List of Ion Beam Characteristics (LIBC) of HIT. All beams were configured with the beam focus setting F1.

Ion	Setting	Energy (MeV u^{-1})	Intensity (pps)	FWHM (mm)
carbon	E1, I7	88.83	1.0×10^7	9.8
carbon	E1, I10	88.83	4.0×10^7	9.8
carbon	E18, I7	124.25	2.0×10^7	7.7
carbon	E18, I10	124.25	8.0×10^7	7.7
carbon	E255, I7	430.10	2.0×10^7	3.4
carbon	E255, I10	430.10	8.0×10^7	3.4
proton	E1, I2	48.12	0.6×10^8	32.4
proton	E1, I7	48.12	4.0×10^8	32.4
proton	E18, I2	67.10	1.2×10^8	23.8
proton	E18, I7	67.10	8.0×10^8	23.8
proton	E255, I2	221.06	1.2×10^8	8.1
proton	E255, I7	221.06	8.0×10^8	8.1

The following operational parameters of the beam monitor demonstrator were fixed for all measurements: $V_{\text{bias}} = -90\,\text{V}$, $V_{\text{dda}} = 1.85\,\text{V}$, $V_{\text{ssa}} = 1.34\,\text{V}$, $V_{\text{ddd}} = 2.40\,\text{V}$ and $V_{\text{bl}} = 0.99\,\text{V}$. All sensors in the demonstrator were configured with the `bias-DAC` settings E, and their pixel thresholds were tuned. The threshold voltage and frame duration were set to 164 DAC units and 500 µs, respectively. The applied threshold voltage ensured that the fraction of noisy pixels was ∼0 % across all sensors. All measurements were performed at room temperature.

The demonstrator performance was evaluated in both counter and adder mode. The FPGA was configured with a first version of the firmware (based on the bit slicing), as discussed in subsection 7.2.4. Hence, for the adder mode, the readout speed was set to 85 Mbit s^{-1}, while for the counter mode, the readout speed was reduced to 25 Mbit s^{-1} due to the limited computational power of the control PC, which could not decode the large amount of counter data from the demonstrator in real time. This configuration led to a dead time between two consecutive frames of 68 µs and 8759 µs for adder and counter modes, respectively. An optimized firmware (more details in subsection 7.2.4) was tested after this beam test and allowed the demonstrator to be read out in both modes at a readout speed of 90 Mbit s^{-1}, reducing the corresponding dead time to 61 µs and 2689 µs.

To test the demonstrator capability to track changes in delivered beam spills, the total number of carbon ions measured in every frame by adders was checked against the BAMS IC data. Since only half of the pixels contribute to the adder readout of HitPix3 sensor (more details

in subsection 6.1), the beam intensity measured with the demonstrator and IC data was normalized to their median values for a fair comparison. Furthermore, every ten 50 µs frames measured by the IC were averaged to match the demonstrator frame duration of 500 µs. An example of such a comparison for the carbon beam configured with the (E18, I10) setting is shown in Fig. 7.30.
The left panel of the figure shows all four spills delivered during the measurement. The first spill measured with the demonstrator shows a missing ramp-up due to a slightly delayed manual start of the measurement. Except that, all data points are very well aligned. The zoomed structure of the second spill, shown on the right panel of the figure, confirms that the beam monitor demonstrator tracks every change in the spill structure.

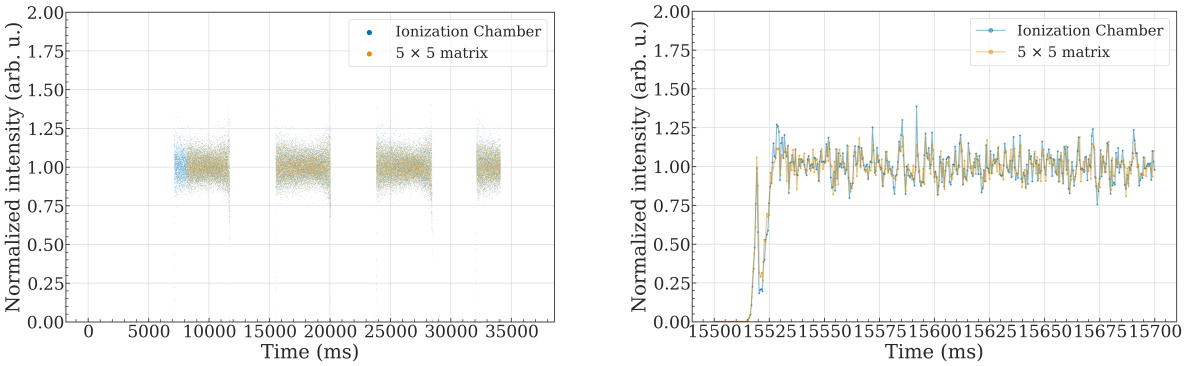


Figure 7.30.: Normalized intensity of four spills (left) and the zoomed structure of the second spill (right) for the carbon beam (E18, I10) measured using the reference IC (blue points) and beam monitor demonstrator in **adder mode** (orange points).

The same good agreement between normalized beam intensities measured using the demonstrator and the IC was observed for all carbon beam settings. However, anomalies were discovered in two measurements with (E1, I10) and (E255, I7) settings, which are important for the subsequent analysis.
Figure 7.31 shows the normalized beam intensity measured for the carbon beam configured with the (E1, I10) setting. In a short period after the initial ramp-up, the first spill measured with the demonstrator has a normalized beam intensity lower than the remaining part of this spill, while the IC does not show such behavior. The other three spills measured with both detectors are in good agreement.

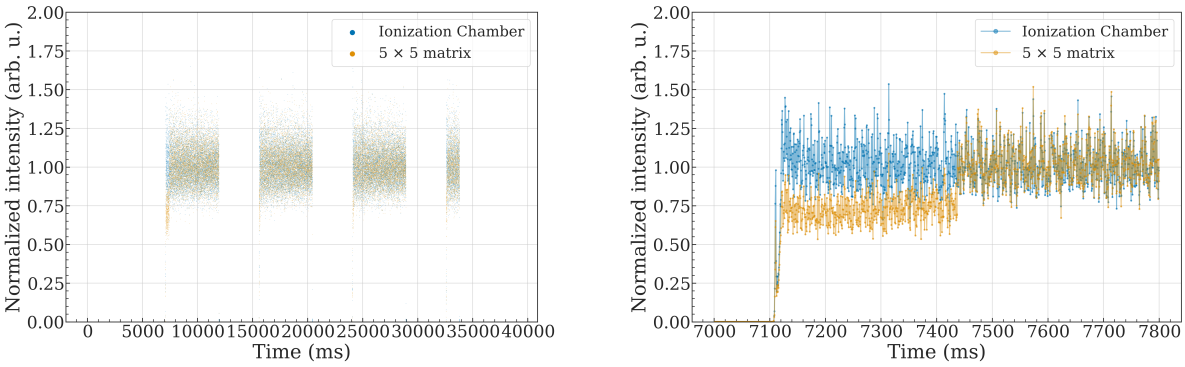


Figure 7.31.: Normalized intensity of four spills (left) and the zoomed structure of the first spill (right) for the carbon beam (E1, I10) measured using the reference IC (blue points) and beam monitor demonstrator in **adder mode** (orange points).

The beam profiles measured in this low-intensity region indeed had fewer counts and a flatter peak compared to other frames, which leads to a beam size overestimation for the projections measured in this region. Therefore, it was decided to exclude these frames from the subsequent analysis because they do not reflect the actual beam size due to a temporary instability in the sensors operation, which will be discussed later. The fraction of such excluded frames was found to be 2 % and 24 % for the beam settings (E1, I10) and (E255, I7), respectively.

The exact origin of these anomalies was not determined at the moment of writing this thesis. However, several important insights were drawn from a detailed analysis of the demonstrator data. The anomalies cannot be attributed to the high-voltage compliance issue discussed in subsection 5.4.1, because in such events, the measured intensity does not return to the normal level since the bias current would always be higher than the compliance setting during the spill. The anomalies also cannot be attributed to a single event upset in the `bias-DAC` configuration register, in which bits could be flipped, changing the threshold voltage or in-pixel CSA settings, since the flipped bits would not be restored after their change (the sensor DACs are configured only once at the start of the measurement). Moreover, a probable single event upset would appear at any moment during the irradiation, whereas the observed low-intensity frames appear only at the beginning of the spill. The most probable explanation of these anomalies is temporal voltage offsets in some of the power supply channels V_{dda}, V_{ssa}, or V_{bl}, which could temporarily increase pixel thresholds or change CSA settings. These voltage spikes might appear due to increased in-pixel electronics activity when the beam hits the matrix, which instantly increases its power consumption. The increased fraction of low-intensity frames for the beam configured with the highest energy E255 partially supports this hypothesis, since at this setting the beam is more focused, increasing the pixel ⟨Hit rate⟩. However, the absence of low-intensity frames for the beam setting (E255, I10) contradicts the hypothesis because at this setting, the in-pixel electronics activity is even higher than that at I7. Therefore, a final conclusion cannot be drawn from the analysis of the matrix data and requires a dedicated beam test with implemented LV current monitoring with high time resolution.

Overall, the beam monitor demonstrator showed very good performance in tracking changes in delivered spills across a wide range of carbon beam settings. Future investigations of the short low-intensity anomalies will result in a revised system design, which will further improve the demonstrator performance.

To validate the accuracy and precision of the demonstrator against the system requirements, the beam position and size reconstructed by the demonstrator in counter and adder modes were compared with the reference data.

The data comparison, the beam parameter reconstruction and the calculation of the beam profile cutoff value methods follow the procedures described in subsection 5.3.5 for measurements performed in counter mode. For the measurements performed in adder mode, each non-empty frame of the beam monitor demonstrator was fitted with a 1D-Gaussian function to extract the beam position and size from both projections. The cutoff values were calculated for every frame as 10 % of the Gaussian amplitude fitted for the projection without cutoff applied.

Since the ISO-MWPC was not available during this beam test, the direct estimation of the beam size reconstruction accuracy of the demonstrator was not possible. Instead, the reconstructed beam size with and without cutoff applied was compared against the tolerance range from −15 % to 25 % for the beam size deviation from the nominal value given in table 7.5.

Figure 7.32 shows an example of a carbon beam profile configured with (E18, I10) settings and measured using the beam monitor demonstrator in counter mode in the local coordinate system. The color palette for the counts is in logarithmic scale to visualize the contribution of particles with large scattering angles in the measured profiles. As for the measurements with the 2×5 HitPix2 matrix (more details in subsection 5.3.6), the effect of the applied cutoff,

which suppresses the contribution of the large-angle scattered particles in the estimated beam size, is clearly visible.

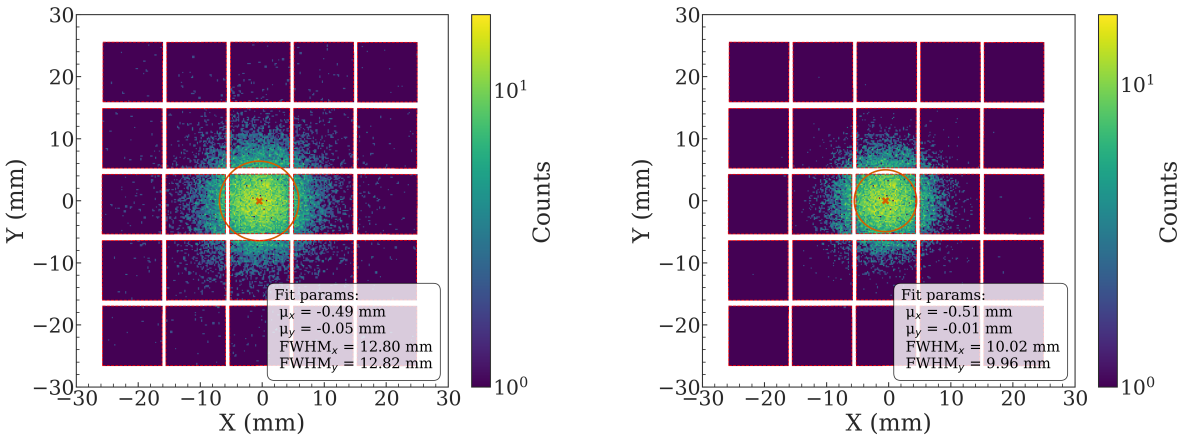


Figure 7.32.: Carbon beam profile (E18, I10) measured using the beam monitor demonstrator in one 500 µs frame **(counter mode)** without (left) and with (right) beam profile cutoff applied in the local coordinate system. Red dashed lines enclose the active areas of the sensors. The orange cross and ellipse represent the estimated beam position and size from a 2D-Gaussian fit.

An example of projections in the X- and Y-direction of a carbon beam is shown in Fig. 7.33. The beam was configured with the same settings and measured using the demonstrator in adder mode. The reconstructed beam parameters align well for both readout modes. Since the adder readout mode is considered the main operational mode of the beam monitor demonstrator (due to its small dead time between frames), most of the analysis results are presented for this mode. The relevant measurement results for the counter mode can be found in the Appendix in section D.3.

Measurements performed in adder mode without cutoff applied for a carbon beam configured with settings (E18, I10), were used to align the beam monitor demonstrator and BAMS MWPC local coordinate systems to mitigate a systematic offset of each local detector coordinate system position w.r.t. the isocenter. As for the 2×5 HitPix2 matrix measurements, the systematic offsets x_{align} and y_{align} were calculated during the analysis as a difference between the corresponding mean positions measured with the beam monitor demonstrator and the MWPC and were added to all pixel and adder coordinates for all measurements.

Measured distributions of carbon beam size FWHM_x and FWHM_y using the demonstrator without and with cutoff applied for different beam settings are shown in Fig. 7.34. As expected, all distributions follow the same trend: the beam size decreases for higher beam energies. Furthermore, the applied cutoff significantly reduces the estimated beam size due to the suppressed contribution of particles with large scattering angles.

To quantify the demonstrator performance in beam size reconstruction, the mean carbon beam size in the X- and Y-directions and their standard deviations were estimated on the measured distributions using the method described in subsection 5.3.5. The results for the measurements with and without cutoff applied are detailed in table 7.6 and the Appendix in table D.1, respectively. The last two columns $\Delta_{\text{FWHM}_\text{xcut}}$ and $\Delta_{\text{FWHM}_\text{ycut}}$ in the table show the relative difference of the estimated mean beam size measured with the demonstrator ($\langle\text{FWHM}_\text{xcut}\rangle$, $\langle\text{FWHM}_\text{ycut}\rangle$) and the nominal value from the LIBC of HIT, which are given in table 7.5.

Across all measured carbon beam settings, the beam size is reconstructed with a precision ($\sigma_{\text{FWHM}_\text{xcut}}$, $\sigma_{\text{FWHM}_\text{ycut}}$) better than the 0.4 mm required for the final beam monitoring system

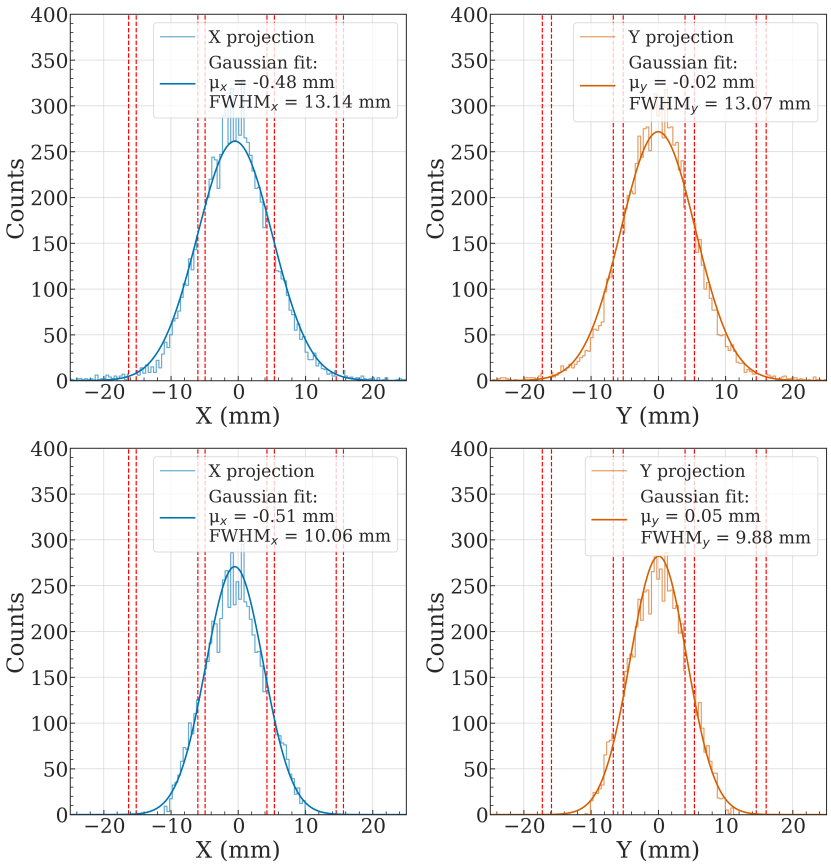


Figure 7.33.: Projections in the X- (left) and Y- (right) directions of carbon beam profile (E18, I10) measured using the beam monitor demonstrator in one 500 µs frame **(adder mode)** without (top) and with (bottom) beam profile cutoff applied in the local coordinate system. Solid lines represent fits to the measurement data with a 1D-Gaussian function. Red dashed lines outline gaps between the matrix rows and columns.

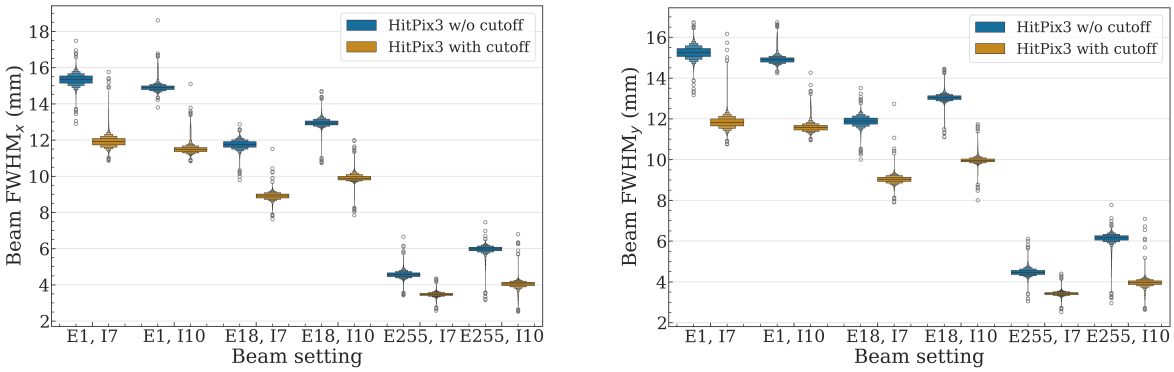


Figure 7.34.: Measured distributions of carbon beam size $FWHM_x$ (left) and $FWHM_y$ (right) using the beam monitor demonstrator in **adder mode** without (blue color) and with (orange color) beam profile cutoff applied for different beam settings.

defined in section 4.1. The relative difference of the beam size with cutoff applied is well within the defined tolerance of −15 % to 25 % from the nominal values, with a slight increase for the

Table 7.6.: The ⟨FWHM⟩ of the measured carbon beam size in the X- and Y-directions using the beam monitor demonstrator in **adder mode with cutoff** applied for different beam settings. The $\sigma_{\mathrm{FWHM_{xcut}}}$ and $\sigma_{\mathrm{FWHM_{ycut}}}$ (used in main text) represent the standard deviation of the estimated beam size. The $\Delta_{\mathrm{FWHM_{xcut}}}$ and $\Delta_{\mathrm{FWHM_{ycut}}}$ represent the relative difference of the estimated mean beam size measured with the demonstrator and the nominal value from the LIBC of HIT.

Setting	$\langle \mathrm{FWHM_{xcut}} \rangle$ (mm)	$\langle \mathrm{FWHM_{ycut}} \rangle$ (mm)	$\Delta_{\mathrm{FWHM_{xcut}}}$ (%)	$\Delta_{\mathrm{FWHM_{ycut}}}$ (%)
E1, I7	11.91 ± 0.26	11.82 ± 0.26	21.5	20.6
E1, I10	11.47 ± 0.17	11.56 ± 0.16	17.1	18.0
E18, I7	8.91 ± 0.16	9.03 ± 0.16	15.8	17.3
E18, I10	9.88 ± 0.14	9.96 ± 0.11	28.3	29.4
E255, I7	3.48 ± 0.09	3.43 ± 0.08	2.3	0.8
E255, I10	4.06 ± 0.14	3.96 ± 0.14	19.4	16.6

beam settings (E18, I10). However, for the beam sizes estimated without cutoff applied (more details in the Appendix in table D.1), the relative difference exceeds this tolerance range across all measured beam settings. This can be explained by the fact that all measurement plans for carbon beams included a plexiglass ripple filter, which can be optionally installed after the last BAMS MWPC at the beam nozzle, whereas the nominal values from the LIBC are provided for the setup without an installed ripple filter. As explained in [Par+12] and [Par+10], the ripple filter is used for carbon beams to broaden their narrow Bragg peaks and reduce the number of required energy layers in the treatment plan. As shown in [Par+12], the ripple filter significantly increases the lateral beam size of the carbon beam.

To validate the influence of the ripple filter on the reconstructed beam size measured using the beam monitor demonstrator, the demonstrator results with cutoff applied were compared against measurements performed in a separate beam test in March 2025. During this beam test, the ISO-MWPC detector was installed at the isocenter and measured at the same beam settings. The ISO-MWPC beam size measurement results are shown in the Appendix in Fig. D.6 and detailed in table 7.7. The same effect of the increased lateral beam size caused by the ripple filter is observed for these measurements.

Table 7.7.: The ⟨FWHM⟩ of the measured carbon beam size in the X- and Y-directions using the ISO-MWPC **during a separate beam test in March 2025**. The $\Delta_{\mathrm{FWHM_{xISO}}}$ and $\Delta_{\mathrm{FWHM_{xISO}}}$ represent the relative difference of the estimated mean beam size measured with the ISO-MWPC and the nominal value from the LIBC of HIT.

Setting	$\langle \mathrm{FWHM_{xISO}} \rangle$ (mm)	$\langle \mathrm{FWHM_{yISO}} \rangle$ (mm)	$\Delta_{\mathrm{FWHM_{xISO}}}$ (%)	$\Delta_{\mathrm{FWHM_{yISO}}}$ (%)
E1, I7	12.00 ± 0.21	11.74 ± 0.19	22.5	19.8
E1, I10	12.47 ± 0.16	12.19 ± 0.16	27.2	24.4
E18, I7	8.64 ± 0.11	8.52 ± 0.11	12.2	10.7
E18, I10	9.38 ± 0.14	9.24 ± 0.15	21.8	20.0
E255, I7	3.47 ± 0.07	3.23 ± 0.08	2.1	−5.0
E255, I10	4.01 ± 0.12	3.94 ± 0.11	17.9	15.9

Furthermore, the relative difference between the estimated mean size using the ISO-MWPC and the demonstrator does not exceed 8 % for any carbon beam settings. Given that these measurements were performed in two beam tests separated by seven months, the ISO-MWPC and the demonstrator values are very well in agreement, confirming the demonstrator capability to reconstruct the carbon beam sizes with the required level of accuracy for the final beam monitoring system.

Measured distributions of carbon beam position μ_x and μ_y using the projected values from the MWPC and the demonstrator without and with cutoff applied for different beam settings are shown in Fig. 7.35. As expected, the measured beam positions with the demonstrator without and with cutoff applied are well in agreement.

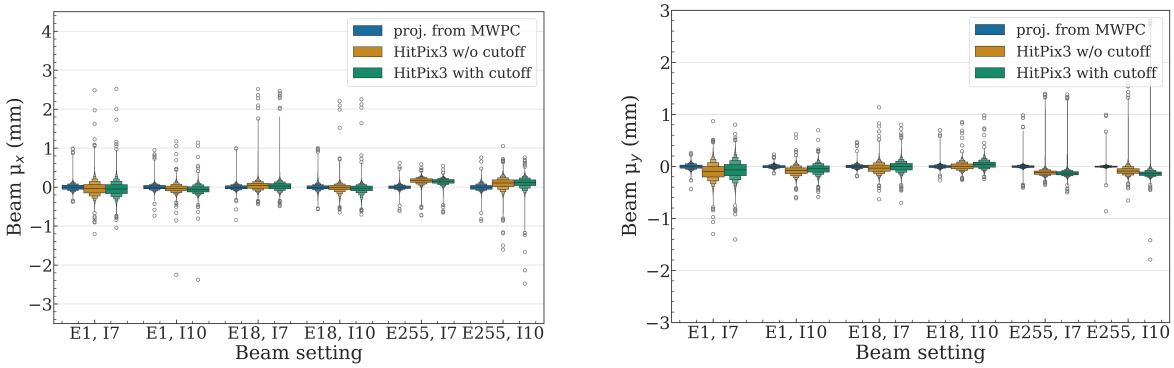


Figure 7.35.: Measured distributions of carbon beam position μ_x (left) and μ_y (right) using the projected MWPC values (blue color) and the beam monitor demonstrator without (orange color) and with (green color) beam profile cutoff applied for different beam settings.

Following a similar procedure as for the mean beam size, the mean carbon beam position in the X- and Y-directions and their standard deviations were estimated on the measured distributions with the MWPC and the demonstrator with cutoff applied. The resulting values are presented in table 7.8. The last two columns in the table show the difference between mean projected positions measured with the MWPC ($\langle\mu_{xref}\rangle$, $\langle\mu_{yref}\rangle$) and the beam monitor demonstrator ($\langle\mu_{xcut}\rangle$, $\langle\mu_{ycut}\rangle$). Across all measured carbon beam settings, the beam position is reconstructed by the demonstrator with an accuracy ($\Delta\mu_{xcut}$, $\Delta\mu_{ycut}$) and precision ($\sigma_{\mu_{xcut}}$, $\sigma_{\mu_{ycut}}$) better than 0.2 mm required for the final beam monitoring system.

The same performance in the reconstructed carbon beam position and size was observed for the beam monitor demonstrator in counter mode. The detailed tables and plots can be found in the Appendix in section D.3.

The beam monitor demonstrator was also tested in proton beams. Figure 7.36 shows the comparison between the proton spill structures measured using the BAMS IC and the demonstrator in adder mode for the beam configured with the E1, I7 setting. As for the carbon beams, the results confirm the demonstrator capability to track every change in the proton spill structure.

For the beam settings (E1, I2), (E18, I7) and (E255, I7), the measurements performed in adder mode were corrupted due to the high-voltage compliance issue discussed in subsection 5.4.1. Therefore, they were excluded form the analysis. As shown in the Appendix in Fig. D.9, the spill structure measured using the demonstrator degrades after an initial ramp-up. This behavior was similar to the one observed for the single HitPix2 sensor measurements, as discussed in subsection 5.4.1, and was first realized during this beam test and fixed for the latter beam test with a single HitPix3 sensor, as discussed in subsection 6.2.10.

Table 7.8.: The $\langle\mu\rangle$ of the measured carbon beam position in the X- and Y-directions using the beam monitor demonstrator in **adder mode with cutoff** applied for different beam settings. The $\sigma_{\mu_{xcut}}$ and $\sigma_{\mu_{ycut}}$ (used in main text) represent the standard deviation of the estimated beam position. The $\Delta\mu_{xcut}$ and $\Delta\mu_{ycut}$ represent the difference of the estimated mean beam position measured with the MWPC and the demonstrator. Units: mm

Setting	$\langle\mu_{xref}\rangle$	$\langle\mu_{yref}\rangle$	$\langle\mu_{xcut}\rangle$	$\langle\mu_{ycut}\rangle$	$\Delta\mu_{xcut}$	$\Delta\mu_{ycut}$
E1, I7	0.00 ± 0.07	0.00 ± 0.04	-0.05 ± 0.17	-0.07 ± 0.16	0.05	0.07
E1, I10	0.00 ± 0.06	0.00 ± 0.03	-0.06 ± 0.10	-0.05 ± 0.09	0.06	0.05
E18, I7	0.00 ± 0.06	0.00 ± 0.03	0.02 ± 0.10	0.00 ± 0.09	-0.02	0.00
E18, I10	0.00 ± 0.06	0.00 ± 0.03	-0.02 ± 0.09	0.03 ± 0.07	0.02	-0.03
E255, I7	0.00 ± 0.05	0.00 ± 0.02	0.16 ± 0.07	-0.13 ± 0.05	-0.16	0.13
E255, I10	-0.01 ± 0.07	0.00 ± 0.02	0.12 ± 0.11	-0.14 ± 0.06	-0.13	0.14

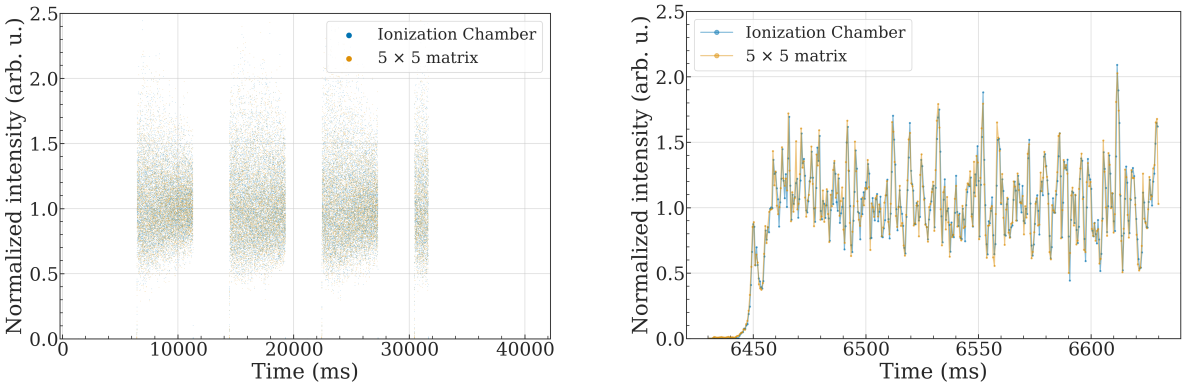


Figure 7.36.: Normalized intensity of four spills (left) and the zoomed structure of the first spill (right) for the proton beam (E1, I7) measured using the reference IC (blue points) and beam monitor demonstrator in **adder mode** (orange points).

Figures 7.37 and 7.38 show examples of a proton beam profile configured with (E1, I7) setting and measured using the beam monitor demonstrator in counter and adder modes, respectively, without and with cutoff applied in the local coordinate system. As expected, such a wide beam irradiates the entire demonstrator active area (more details in section 7.1) and no inhomogeneities in the profiles were observed for both readout modes.

Measured distributions of proton beam size $\mathrm{FWHM_x}$ and $\mathrm{FWHM_y}$ using the demonstrator without and with cutoff applied for different beam settings are shown in the Appendix in Fig. D.10. As for the carbon beam measurements, the beam size decreases for higher beam energies and the applied cutoff reduces the estimated beam size. Table 7.9 and the Appendix in table D.4 present the mean beam size in the X- and Y-directions using the beam monitor demonstrator in adder mode with and without cutoff applied, respectively.

Across all measured proton beam settings, the beam size is reconstructed with a precision ($\sigma_{\mathrm{FWHM_{xcut}}}$, $\sigma_{\mathrm{FWHM_{ycut}}}$) better than the 0.4 mm required for the final beam monitoring system defined in section 4.1. Compared to the carbon beam measurements, the ripple filter was removed for the proton beam measurements. Therefore, the relative difference of the beam size with and without cutoff applied is well within the defined tolerance of $-15\,\%$ to $25\,\%$ compared to the nominal values from LIBC.

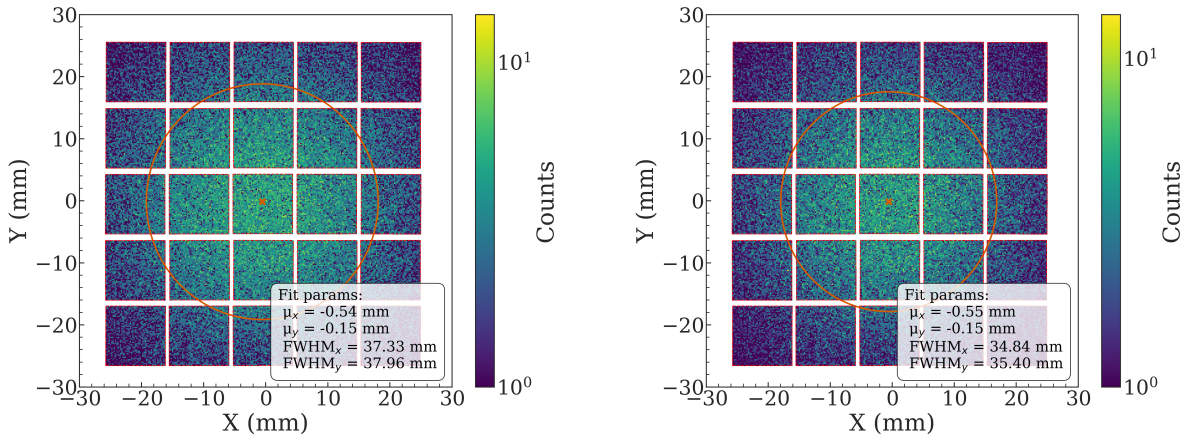


Figure 7.37.: Proton beam profile with nominal parameters E1 and I7 measured using the beam monitor demonstrator in one 500 µs frame **(counter mode)** without (left) and with (right) beam profile cutoff applied in the local coordinate system. Red dashed lines enclose the active areas of the sensors. The orange cross and ellipse represent the estimated beam position and size from a 2D-Gaussian fit, respectively.

Table 7.9.: The ⟨FWHM⟩ of the measured proton beam size in the X- and Y-directions using the beam monitor demonstrator in **adder mode with cutoff** applied for different beam settings. The $\sigma_{\mathrm{FWHM_{xcut}}}$ and $\sigma_{\mathrm{FWHM_{ycut}}}$ (used in main text) represent the standard deviation of the estimated beam size. The $\Delta_{\mathrm{FWHM_{xcut}}}$ and $\Delta_{\mathrm{FWHM_{ycut}}}$ represent the relative difference of the estimated mean beam size measured with the demonstrator and the nominal value from the LIBC of HIT.

Setting	$\langle \mathrm{FWHM_{xcut}} \rangle$ (mm)	$\langle \mathrm{FWHM_{ycut}} \rangle$ (mm)	$\Delta_{\mathrm{FWHM_{xcut}}}$ (%)	$\Delta_{\mathrm{FWHM_{ycut}}}$ (%)
E1, I7	32.86 ± 0.39	33.76 ± 0.38	1.4	4.2
E18, I2	22.66 ± 0.33	22.50 ± 0.32	−4.8	−5.5
E255, I2	7.22 ± 0.25	6.91 ± 0.23	−10.8	−14.6

The measured distribution of proton beam position in the X- and Y-directions are shown in the Appendix in Fig. D.11. The mean and standard deviations of these distributions measured with the MWPC ($\langle \mu_{\mathrm{xref}} \rangle$, $\langle \mu_{\mathrm{yref}} \rangle$) and demonstrator with cutoff applied ($\langle \mu_{\mathrm{xcut}} \rangle$, $\langle \mu_{\mathrm{ycut}} \rangle$) are detailed in table 7.10. The beam position is reconstructed by the demonstrator in adder mode with an accuracy ($\Delta\mu_{\mathrm{xcut}}$, $\Delta\mu_{\mathrm{ycut}}$) and precision ($\sigma_{\mu_{\mathrm{xcut}}}$, $\sigma_{\mu_{\mathrm{ycut}}}$) better than 0.2 mm required for the final beam monitoring system, except for the beam settings (E1, I7). A slightly worse accuracy in the X-direction for the (E1, I7) setting can be explained by the fact that this wide proton beam does not entirely fit into the demonstrator active area, which can affect the fitting results.
A similar performance in the reconstructed proton beam position and size was observed for the beam monitor demonstrator in counter mode. The detailed tables and plots can be found in the Appendix in section D.3.
Overall, from the beam spot measurement results it can be concluded that the HitPix3 beam monitor demonstrator matches the HIT beam monitoring system requirements for beam position and size reconstruction accuracy and precision across a wide range of beam settings. Furthermore, the analysis of the normalized carbon and proton beam intensities measured using

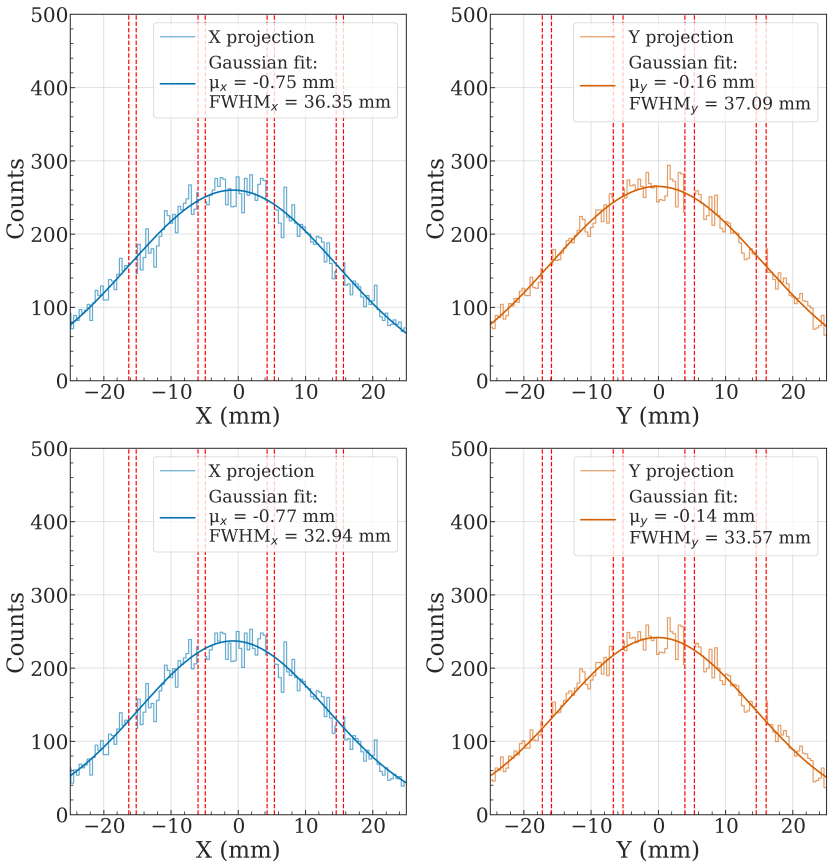


Figure 7.38.: Proton beam (E1, I7) profile projection in the X- (left) and Y- (right) directions measured using the beam monitor demonstrator in one 500 µs frame **(adder mode)** without (top) and with (bottom) beam profile cutoff applied in the local coordinate system. Solid lines represent fits to the measurement data with a 1D-Gaussian function. Red dashed lines outline gaps between the matrix rows and columns.

Table 7.10.: The $\langle\mu\rangle$ of the measured proton beam position in the X- and Y-directions using the beam monitor demonstrator in **adder mode with cutoff** applied for different beam settings. The $\sigma_{\mu_{\mathrm{xcut}}}$ and $\sigma_{\mu_{\mathrm{ycut}}}$ (used in main text) represent the standard deviation of the estimated beam position. The $\Delta\mu_{\mathrm{xcut}}$ and $\Delta\mu_{\mathrm{ycut}}$ represent the difference of the estimated mean beam position measured with the MWPC and the demonstrator. Units: mm

Setting	$\langle\mu_{\mathrm{xref}}\rangle$	$\langle\mu_{\mathrm{yref}}\rangle$	$\langle\mu_{\mathrm{xcut}}\rangle$	$\langle\mu_{\mathrm{ycut}}\rangle$	$\Delta\mu_{\mathrm{xcut}}$	$\Delta\mu_{\mathrm{ycut}}$
E1, I7	-0.01 ± 0.15	0.00 ± 0.06	-0.36 ± 0.18	0.04 ± 0.14	0.35	-0.04
E18, I2	-0.01 ± 0.14	-0.01 ± 0.03	-0.16 ± 0.19	-0.07 ± 0.14	0.15	0.06
E255, I2	-0.03 ± 0.17	0.00 ± 0.03	-0.01 ± 0.17	-0.11 ± 0.13	-0.02	0.11

the reference IC and the demonstrator confirms that the demonstrator is capable of tracking the changes in the beam spill structure.

7.4.2. Raster scan measurements

In the measurements discussed in the previous subsection, the beam position was fixed at the coordinate origin of the isocenter for all delivered spills. However, in a real treatment plan, the beam is deflected by a magnetic raster-scanning system to create a grid of beam positions (raster points) for each beam energy layer, as explained in sections 2.1 and 4.1.
To further assess the beam monitor demonstrator performance for beam parameter reconstruction under conditions close to a real treatment, raster scan measurements were performed for carbon and proton beams configured with the (E255, I7) and (E255, I3) settings, respectively. This scan, for both ion types, was configured to cover the entire active area of the beam monitor demonstrator with a two-dimensional grid with a step size of 3 mm, resulting in 17×17 raster points. The raster scan path was formed in a serpentine manner: starting from a fixed X coordinate of approximately -25 mm, the raster points were scanned in the Y-direction in the range approximately from 25 mm to -25 mm with a 3 mm step size. After that, the raster position was shifted in the X-direction with a 3 mm step towards positive X values, and the raster points were scanned again in the backward Y-direction from -25 mm to 25 mm. This process was repeated until the last scan at the X coordinate of approximately 25 mm. The beam was delivered in spills with an approximate duration of 5 s. Within the spill, the raster point was changed every time when the number of particles detected by the BAMS IC reached a value defined in the treatment plan.
The operational parameters of the beam monitor demonstrator were the same as for the spot measurements (more details in the previous subsection). It was read out in adder mode to minimize the dead time between frames and to track changes in the beam position and size. Additionally, the beam positions measured using the demonstrator were compared against the projected values from the BAMS MWPC (every four MWPC frames were averaged to match the frame duration of the demonstrator). The beam size data was analyzed without cutoff applied, since the ISO-MWPC was not available during this beam test.
Figure 7.39 shows the carbon beam positions in the X- and Y-directions measured during the raster scan using the beam monitor demonstrator in adder mode and the projected values from the MWPC. The beam positions measured with both detectors accurately reconstruct the raster points path with clearly visible pauses between delivered spills.
Furthermore, the beam monitor demonstrator and projected values from the MWPC are well in agreement during the entire raster scan, with the exception of raster points located at the edges of the beam monitor demonstrator (close to an approximate position of ± 25 mm in the X- and Y-directions). This is expected, since only part of the beam is detected by the demonstrator at these positions, leading to poorer fit results compared to the raster points in which the beam is entirely captured by the demonstrator.
Figure 7.40 shows the carbon beam size in the X- and Y-directions measured during the raster scan using the beam monitor demonstrator. As expected, the measured beam size fluctuates with a stable average around the mean value for most of the raster scan. Moreover, the beam size is lower at the beginning of each spill in the X- and Y-directions because of the smaller number of particle during the initial ramp-up of the spill. The remaining outliers in the beam size distributions correspond to the raster points located at the edges of the beam monitor demonstrator, leading to poorer fit results, as with the reconstructed beam positions.
The measured beam positions with both detectors allow to reconstruct the measured grid of the carbon beam raster scan by combining them onto the X-Y plane, as shown in Fig. 7.41. As expected, the two grids measured with the beam monitor demonstrator and the MWPC are in good agreement.
Furthermore, most of the measured data points are grouped together in clusters corresponding to a certain raster point in the grid. However, a small fraction of data points lie outside the

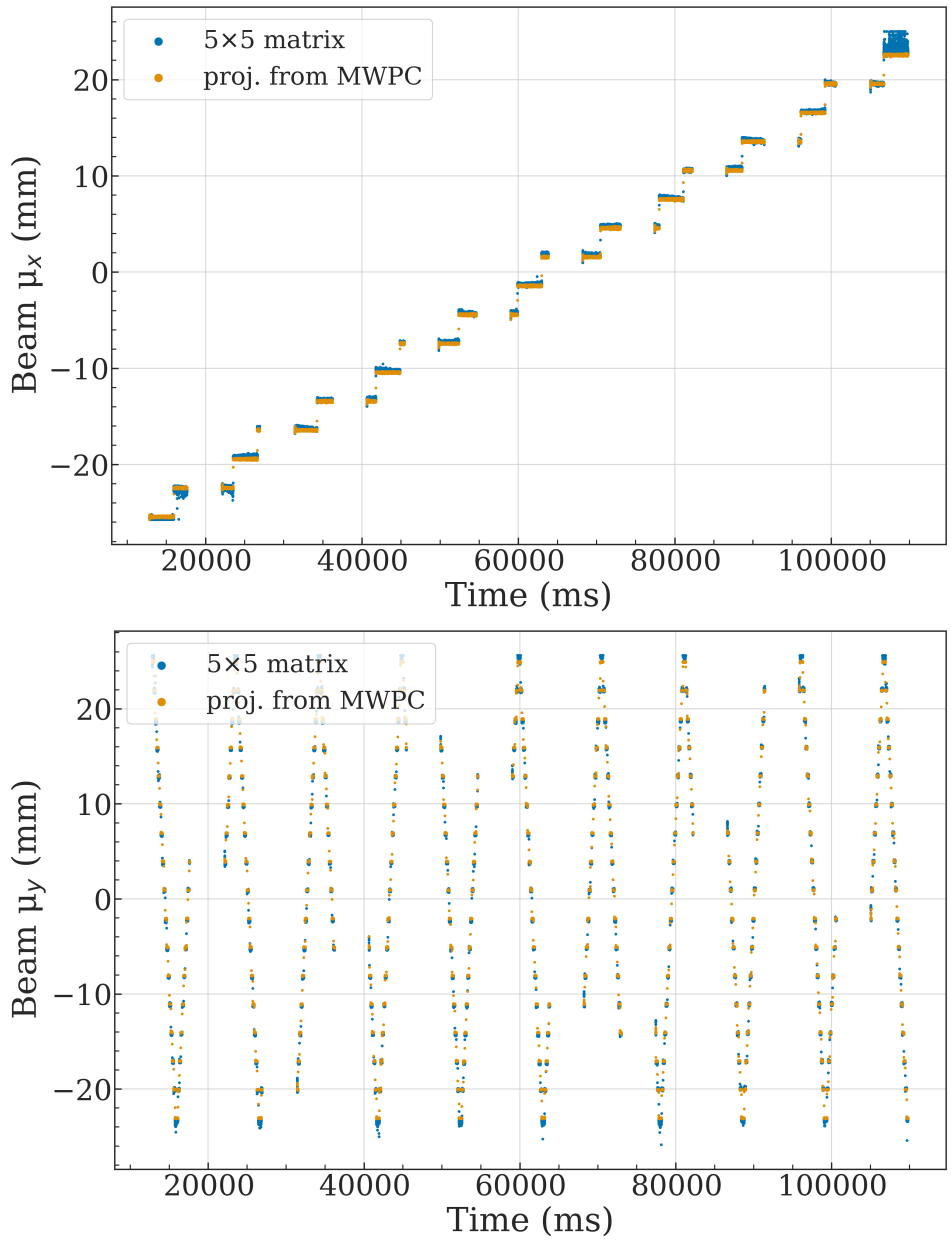


Figure 7.39.: Carbon beam (E255, I7) positions in the X- (top) and Y- (bottom) directions versus time measured during a raster scan with a 3 mm grid step size using the beam monitor demonstrator in **adder mode without cutoff applied** (blue points) and the projected values from the MWPC (orange points).

clusters. Based on the measured beam position versus time in Fig. 7.39, it can be seen that these points correspond either to the beginning of the spill or to the intermediate positions between changed raster points. In these regions, the number of particles is smaller, leading to shifts in the measured beam positions.

The reconstruction bias at the demonstrator edges is clearly visible and expected. In the final beam monitoring system, the active area will cover the entire treatment field, therefore, the edge effects will not be present and are not relevant for the demonstrator evaluation. In contrast, the gaps between the sensors are unavoidable in the final system and relevant for the evaluation. However, the measurement results confirm that the beam position reconstruction

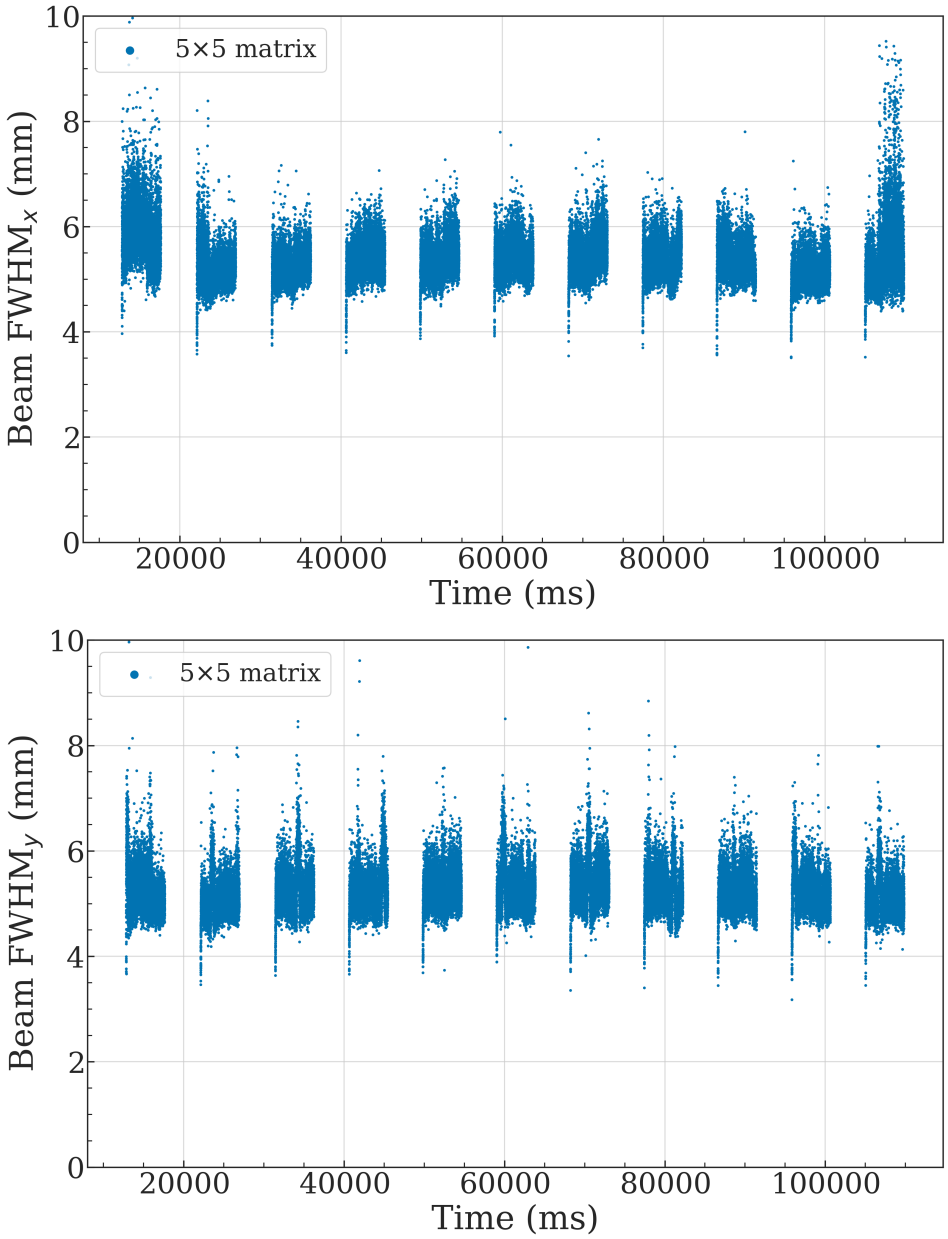


Figure 7.40.: Carbon beam (E255, I7) size in the X- (top) and Y- (bottom) directions versus time measured during a raster scan with a 3 mm grid step size using the beam monitor demonstrator in **adder mode without cutoff applied**.

does not degrade for the raster points located in the gaps between sensitive areas, such as for the raster points with an X-coordinate of ∼5 mm or with a Y coordinate of ∼16 mm. Hence, the designed gaps between sensitive areas in the demonstrator, which were based on the simulation results (more details in section 7.2) do not bias the reconstruction and define the maximum allowed gaps between the sensors in the final system.

Similar results were obtained for the proton beam. The measured beam positions and sizes versus time can be found in the the Appendix in Fig. D.14 and D.15, respectively. The measured grid of the proton beam raster scan is shown in Fig. 7.42.

Since the proton beam has a nominal beam size more than twice as large as for the carbon beam, the edge effects are more pronounced for the proton beam. Nonetheless, the raster points

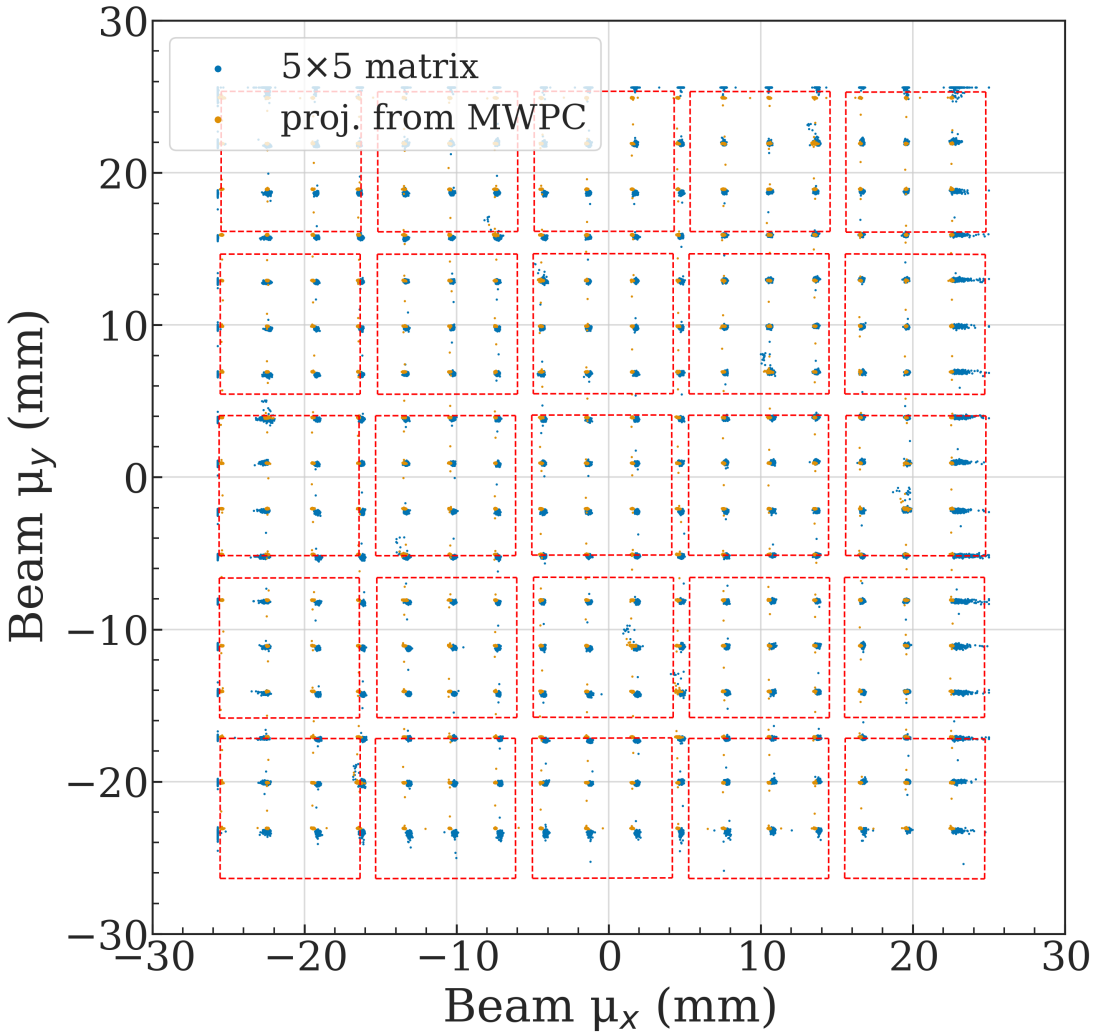


Figure 7.41.: Grid of the carbon beam (E255, I7) raster scan measured using the beam monitor demonstrator in **adder mode without cutoff applied** (blue points) and the projected values from the MWPC (orange points). Red dashed lines enclose the active areas of the sensors.

are well reconstructed in the gaps between the sensitive areas, and the grid points measured with the beam monitor demonstrator and the MWPC are very well aligned.
To quantify the beam monitor demonstrator performance, several parameters were extracted from these measurements for the X- and Y-directions and compared against the system requirements. These parameters are listed as follows:

- The accuracy, $\langle \Delta\mu \rangle$, is defined as the mean difference between the centers of clusters measured with the MWPC and the beam monitor demonstrator for the corresponding raster point.
- The grid step size is defined as the mean distance between the centers of neighboring clusters measured with the beam monitor demonstrator.
- The size of the measured clusters, $\langle \sigma_\mu \rangle$, is defined as a mean standard deviation of the beam positions within the cluster measured with the beam monitor demonstrator.

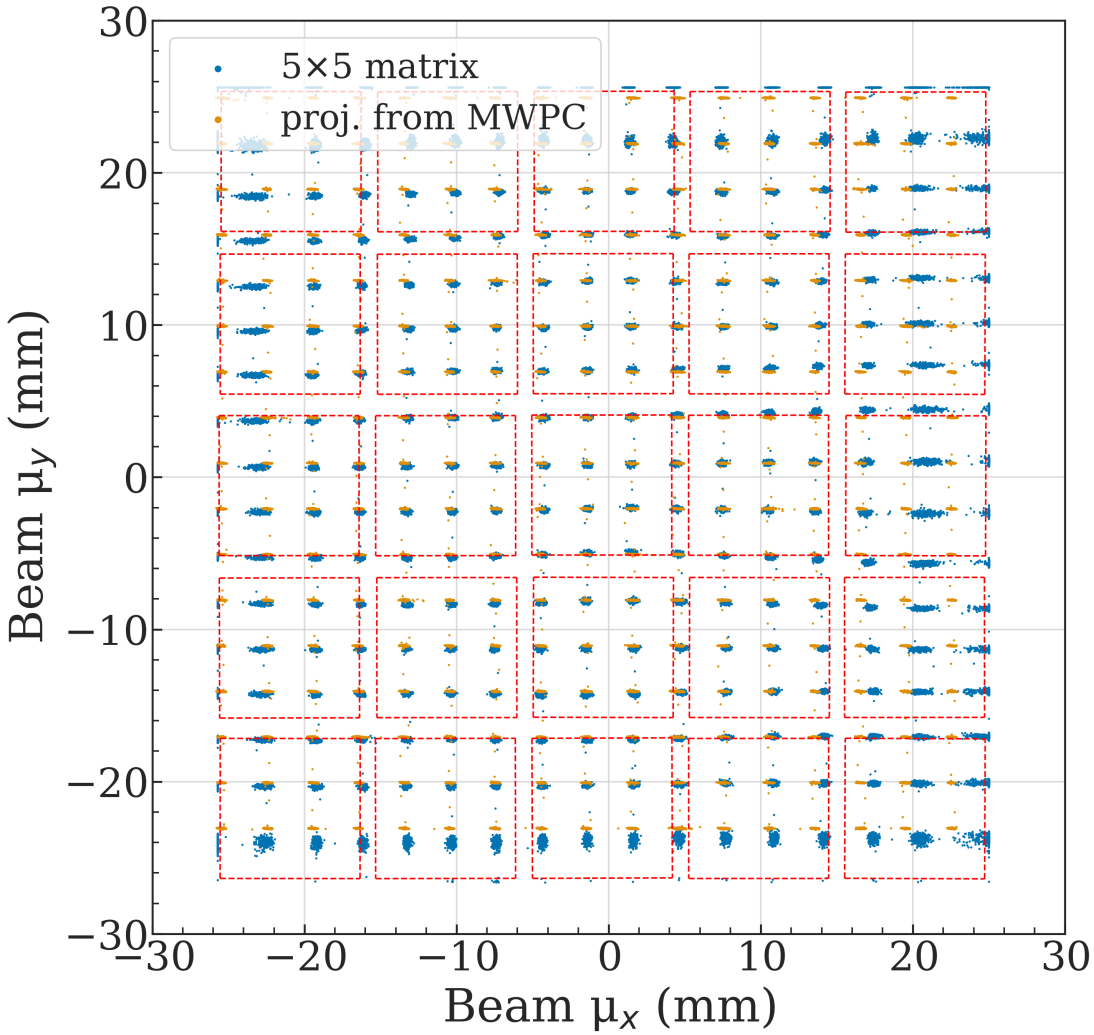


Figure 7.42.: Grid of the proton beam (E255, I3) raster scan measured using the beam monitor demonstrator in **adder mode without cutoff applied** (blue points) and the projected values from the MWPC (orange points). Red dashed lines enclose the active areas of the sensors.

- The mean beam size, ⟨FWHM⟩ is defined as for the spot measurements, subsection 7.4.1.

The raster scan parameters extracted from the measurements are detailed in table 7.11. It is important to note that the data points measured near the demonstrator edges were excluded from the analysis, since they are not relevant for the performance estimation, as discussed above. For both carbon and proton beams, the beam positions were reconstructed by the demonstrator with an accuracy and precision better than 0.2 mm required for the final system and the reconstructed grid step size is in good agreement with the nominal value of 3 mm. Furthermore, the size of the measured clusters and its precision are also well within 0.2 mm. Finally, the precision of the reconstructed carbon beam size is well within 0.4 mm of the final system requirement, while the beam size of the proton beam slightly exceeds this value in the Y-direction.
Based on these results, it can be concluded that the HitPix3 beam monitor demonstrator meets the HIT beam monitoring system requirements for beam position and size reconstruction for carbon and proton beams in the raster scans.

Table 7.11.: The raster scan parameters extracted from measurements with the beam monitor demonstrator in **adder mode without cutoff** applied for carbon and proton beams. Units: mm

Ion	Direction	$\langle \Delta\mu \rangle$	Grid step size	$\langle \sigma_\mu \rangle$	$\langle$FWHM$\rangle$
carbon	X	-0.18 ± 0.10	2.97 ± 0.14	0.067 ± 0.006	5.29 ± 0.31
carbon	Y	0.10 ± 0.10	2.98 ± 0.07	0.058 ± 0.007	5.15 ± 0.29
proton	X	-0.12 ± 0.14	3.06 ± 0.22	0.136 ± 0.013	9.98 ± 0.39
proton	Y	0.13 ± 0.14	2.99 ± 0.09	0.078 ± 0.007	9.46 ± 0.45

7.5. MRI test results

The final full-scale beam monitoring system must be tolerant to the static and changing magnetic fields for the MRI-guided ion beam therapy application. Therefore, the beam monitor demonstrator was tested at the MRI setup at HIT in March 2025. As described in [Pau+24], the setup consist of a compact MRI scanner (Esaote, Italy) based on a C-shape permanent magnet with a vertical static field of 0.25 T and a gradient system with a maximum gradient strength of $20\,\mathrm{mT\,m^{-1}}$ and a maximum slew rate of $56\,\mathrm{mT\,m^{-1}\,ms^{-1}}$. The MRI scanner is positioned inside an RF-shielded cabin, which can be transported to the beamline isocenter by a rail system. Photographs inside the cabin of the MRI setup with the beam monitor demonstrator positioned at the isocenter are shown in Fig. 7.43. The cabin wall closest to the beam nozzle has a square window made of copper foil, which allows an ion beam to enter the shielding cabin and traverse the MRI setup (indicated with a red arrow in the figure).



Figure 7.43.: General (left) and zoomed (right) views of the HitPix3 beam monitor demonstrator installed at the isocenter of the MRI setup at HIT. The red and magenta arrows in the general view represent the direction of the beam and static magnetic field, respectively. The orange arrows in the general view represent the axes of the demonstrator local coordinate system.

The beam monitor demonstrator was connected to the FPGA board via a ∼1 m cable to suppress the influence of the magnetic fields on the FPGA board components. Due to the cable length limitation, the demonstrator was positioned at the isocenter only in the Z- (beam path) and Y- (vertical) directions, whereas the local coordinate system of the demonstrator was significantly shifted relative to the isocenter horizontal position towards negative X coordinates (in the local coordinate system, X-axis points into the page). However, this shift was partially compensated by the deflection of the positively charged ions inside the static magnetic field of the MRI scanner (indicated with the magenta arrow in the figure).

A first test was performed inside the static field of the MRI scanner without active MRI-scanning. Carbon and proton beams configured with the (E255, I7) and (E1, I7) settings, respectively, were measured using the beam monitor demonstrator in counter mode.
The sensors were configured with the `bias-DAC` settings C with a modified `vncomp` value of 10 DAC units and 28 DAC units for the measurements with carbon and proton beams, respectively. For both measurements, the frame duration was set to 50 µs, while the threshold voltages were set to 160 DAC units and 140 DAC units for the carbon and proton beams, respectively. These changes in the settings were applied to address the different pairs of applied voltages V_{ssa} and V_{bl} of 1.26 V, 1.02 V (carbon beam) and 1.51 V, 0.57 V (proton beam). The V_{bias} and V_{dda} were fixed to −100 V and 2.01 V, respectively. An optimized firmware (more details in subsection 7.2.4) was used during this beam test, allowing the demonstrator to be read out at a readout speed of 90 Mbit s^{-1}. All measurements were performed at room temperature.
Figure 7.44 shows two cumulative profiles of the carbon and proton beams measured using the beam monitor demonstrator inside the static magnetic field of the MRI setup. The non-optimal sensor configuration led to an increased fraction of noisy pixels of 3.61 %, which were masked during the measurements. As expected, the low-energy proton beam was more deflected inside the static magnetic field compared to the carbon beam configured with the highest energy setting. To verify the reconstruction performance of the demonstrator inside the magnetic field, it was decided to compare the measured deflection of both ion beams against the measurements independently performed at HIT. Since the exact position of the beam monitor demonstrator w.r.t. the isocenter was not measured, the relative deflections of carbon and proton beams were used as a performance metric. To calculate this value, both cumulative profiles were fitted with a 2D-Gaussian function to extract the deflected beam positions. The measured carbon beam position was then subtracted from the measured proton beam position, yielding a value of 33.52 ± 0.21 mm, which is well in a agreement with a value of 33.5 ± 1.4 mm provided by HIT. This measurement confirms the beam monitor demonstrator tolerance to static magnetic fields.

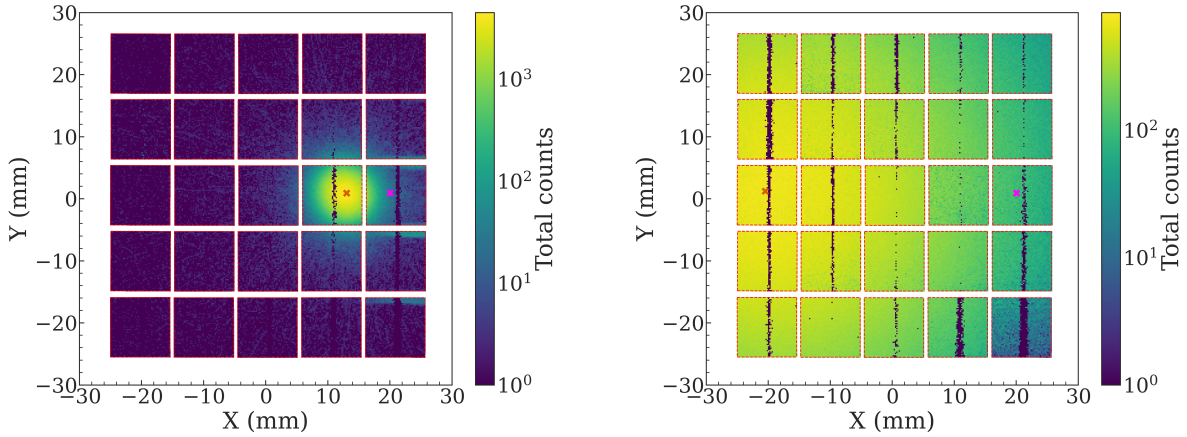


Figure 7.44.: Cumulative profiles of the carbon (left) and proton (right) beams measured using the beam monitor demonstrator inside the static magnetic field of the MRI setup. The carbon and proton beams were configured with (E255, I7) and (E1, I7), respectively. The orange crosses represent the estimated beam positions with a 2D-Gaussian fit. The magenta crosses represent the approximate location of the beam isocenter without the magnetic field. Number of measured non-empty frames: 2950.

Two additional tests were performed with an active MRI-scanning, but without an ion beam. In the first test, the beam monitor demonstrator was positioned at the beamline isocenter, as

in the measurements with the static magnetic field. During this test, the beam monitor did not provide any valid data. In the second test, the beam monitor demonstrator was moved closer to the copper foil window of the setup, to reduce the influence of the gradient fields. The demonstrator was successfully read out, but some portion of the data was still corrupted. This behavior can be attributed either to the influence of the changing magnetic fields on the FPGA board components or to the influence of parasitic currents induced to the connection cable between the FPGA board and the demonstrator. To find the exact origin of the demonstrator readout issue during active MRI-scanning, a new cable must be designed and produced. To suppress the influence of the gradient fields, the cable design can be based on a set of twisted pairs and ground shielding. Additionally, the cable must be long enough to position the FPGA board outside the RF-shielded cabin. The design of such a cable and the additional tests of the demonstrator during the active MRI-scanning fall outside the scope of this thesis.

7.6. Full-scale beam monitor design considerations

After the successful evaluation of the HitPix3 beam monitor demonstrator, several design considerations can be formulated for the future full-scale beam monitor, which will be based on the HitPix4 sensors with a large sensitive area of 2 cm × 2 cm.

On a system level, the modular architecture with segmented 1×5 strips of the demonstrator proved to be an optimal solution for building a large detector system from many sensors, enabling greater control over the production workflow. Therefore, it should be transferred to the final beam monitor design.

The safe distance between sensors within the 5×5 matrix row and columns was set conservatively large due to the manual assembly workflow, leading to relatively large insensitive regions between the active areas. To reduce the insensitive regions, a new assembly workflow must be designed to include an automated sensor placement with an accuracy of a few µm.

The 1×5 strips of the beam monitor demonstrator were assembled on a rigid PCB carrier with a ten layer stack-up to implement the complex routing for the sensors interconnection within the matrix row. This, together with mounted unthinned HitPix3 sensors with a thickness of ∼850 µm, led to a large material budget, which did not meet the corresponding system requirement. Therefore, the HitPix4 sensors must be thinned to approximately 100 µm thickness, and the interconnection between the sensors can be implemented with a thin polyimide cable with aluminum traces.

An initial idea for the sensors interconnection via this cable was based on the single-point Tape Automated Bonding (spTAB) method [Nov+24], as shown on the left panel of Fig. 7.45. The sensors of the beam monitor strip are mounted on a thin carbon plate, which serves as mechanical support. Then, openings in the cable and the aluminum traces are aligned with the sensor pads. In the last step, a bonding tip applies pressure to bend the trace to the contact pad, followed by ultrasonic bonding. However, this method has the risk of trace breakage (outlined with the red dashed ellipse in the figure) when scaled for multiple sensor interconnections, since each trace must be bend and bonded several times.

A more conservative approach for sensor interconnection can be implemented with a wire-bonding method, as shown on the right panel of the figure. In the cable, each signal trace is segmented by bonding openings. After alignment of the cable and sensor pads, the pads are wire-bonded twice to connect both trace segments. When all connections are established, the wire bonds must be encapsulated to prevent their damage. An additional advantage of this method is the more relaxed alignment requirement between the sensor pads and the cable compared to the spTAB, since the wire bond positions can be individually adjusted.

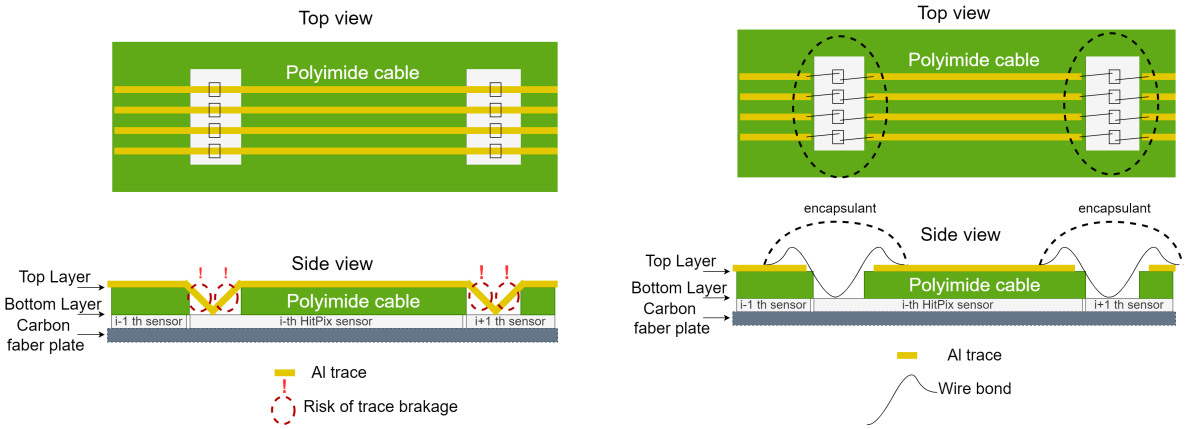


Figure 7.45.: Simplified views of the sensor interconnection cable design based on spTAB (left) and wire-bonding (right) methods

In both interconnection methods, the sensor pads within the matrix row are aligned in parallel, similar to the 5×5 HitPix2 matrix based on bump-bonding. This simplifies the cable design and enables greater control over the differential impedance of the signal traces compared to the complex routing in the 1×5 PCB carrier, which led to compromises in the design and reduced maximum readout speed of the demonstrator, as discussed in subsections 7.3.3 and 7.3.4.

Another important design consideration, which should be addressed in the future beam monitor is the cooling system. As discussed in section 5.5 and subsection 6.2.11, the final system should operate at a temperature of 0 °C or lower to mitigate the negative effects of radiation damage to HitPix sensors, such as increased leakage currents and noise, and reduced detection efficiency. During beam tests at HIT, the beam monitor demonstrator used a simple air fan, which maintained the temperature of the unirradiated sensors in an approximate range from 25 °C to 30 °C. However, this method does not allow to reach the target value of 0 °C for the final system and is not MRI-compatible. Therefore, a careful design of a cooling system, supported by detailed thermal simulations and tests, is required for the full-scale beam monitor.

7.7. Summary

The studies presented in this chapter focused on the development and validation of the beam monitor demonstrator, which consists of 25 sensors integrated into the 5×5 matrix.

To select a reliable assembly technology for the demonstrator, prototypes of the 5×5 matrix based on HitPix2 sensors were designed, produced and tested using both Stud Bump Bonding (SBB) and wire-bonding technologies. The tests revealed a significant problem with sensor detachment after several thermal cycles for the initially selected SBB technology. This led to a new prototype design suitable for the wire-bonding technology. However, the monolithic architecture of the prototypes in which all 25 sensors were mounted onto a single PCB carrier, resulted in the loss of a single set of valid HitPix2 sensors, due to a design flaw in the peripheral electronics of the carrier.

To address the assembly challenges identified during the assembly technology exploration phase, the beam monitor demonstrator, based on HitPix3 sensors, was designed with a modular architecture. The 5×5 matrix was segmented into five 1×5 strips, which were connected to a separate motherboard PCB. This design solution allowed to develop and establish a reliable production workflow with greater control over the assembly and testing of individual

demonstrator components before their final integration. As a result, two functional HitPix3 beam monitor demonstrators were produced.
One of the demonstrators was tested with ion beams at HIT to verify its performance in the reconstruction of beam position and size in both counter and adder readout modes. The spot measurements confirmed that the demonstrator meets the final system requirements across a wide range of carbon and proton beam settings. Furthermore, the comparison of the normalized beam intensity measured with the reference Ionization Chamber of the Beam Application and Monitoring System and the demonstrator, confirmed the demonstrator capability to track changes in delivered spills of carbon and proton beams. Moreover, the analysis of the carbon and proton beam raster scans measured with the demonstrator validated its accuracy and precision for the reconstructed beam positions better than 0.2 mm under the beam conditions close to a real treatment plan.
The demonstrator was also tested inside the MRI setup at HIT. The measurements with proton and carbon beams without active MRI-scanning confirmed the demonstrator tolerance to static magnetic fields. However, during the active MRI-scanning, the negative influence of the changing magnetic fields on the FPGA board sensitive components and the long, unshielded $\sim$1 m connection cable between the demonstrator and FPGA board prevented the demonstrator validation under these magnetic field conditions. Future tests will require a new cable design based on a set of twisted pairs and ground shielding. The cable also must be long enough to position the FPGA board outside the MRI setup.
After the successful beam tests, the HitPix3 beam monitor demonstrator was delivered to HIT for further evaluation regarding its potential integration into a beam quality control procedure. The knowledge and experience gained from these studies allowed to formulate design considerations for the final full-scale beam monitor, which will be based on the HitPix4 sensors with a large sensitive area of 2 cm $\times$ 2 cm.

Part III.

Summary and Outlook

8

Summary and Outlook

Adaptive RadioThErapy with MR-guided Ion beamS (ARTEMIS) is a research project focused on the development and clinical implementation of an MRI-guided ion beam therapy system at the Heidelberg Ion Beam Therapy Center (HIT). This future system aims to overcome current limitations of ion beam therapy for clinical cases in which dose distribution can be significantly affected by the motion of the tumor or healthy organs, or by changes in the tumor volume. This can be achieved by utilizing real-time MRI tracking of the tumor changes to guide the beam delivery system, maximizing the conformity of the dose distribution and minimizing the negative radiation effects on healthy tissue.

To ensure accurate and safe dose delivery, this system requires a beam monitoring system for the fast estimation of the main beam parameters, such as position, size and intensity. These parameters must be controlled in real time to precisely follow the treatment plan. The existing beam monitoring system, based on Multi-Wire Proportional Chambers (MWPCs), is limited by the relatively slow ions drift time in the chamber and in case of an MRI-guided application by deteriorated performance due to the acoustic noise of the MRI scanner. Therefore, the Institute of Experimental Particle Physics (ETP) and Institute for Data Processing and Electronics (IPE) of Karlsruhe Institute of Technology (KIT) jointly proposed a new beam monitoring system design based on HV-CMOS Monolithic Active Pixel Sensors, which have an advantage over the existing MWPC detectors because of their fast charge collection time and insensitivity to magnetic fields and acoustic noise. In this proposed design, 169 sensors with an area of $2\,\text{cm} \times 2\,\text{cm}$ are integrated into a 13×13 matrix to cover a treatment field of $20\,\text{cm} \times 20\,\text{cm}$ with an adjustable beam size in the range of 3 mm to 33 mm available at HIT.

The HitPix R&D project began in 2019 as a part of "Adaptation of the beam application system and the monitoring system (BAMS)" sub-project of ARTEMIS, aiming to develop a new sensor with an architecture tailored for ion beam monitoring. At the moment of writing this thesis, three HitPix sensor iterations (HitPix1, HitPix2 and HitPix3) were developed, produced and evaluated. All three iterations were designed by the ASIC and Detector Laboratory (ADL) at the IPE, KIT, and share common architecture features developed for ion beam monitoring: frame-based readout, hit-counting pixels, on-sensor beam projection calculation (adder mode) and radiation tolerant design.

The scope of this thesis within the project timeline begins with the characterization campaign of the HitPix2 sensors carried out to select valid sensors for several multi-sensor assemblies. A testing workflow was developed and implemented at the ADL probe station to verify every functional part of each sensor. This campaign revealed a low total production yield of 34 %, based on the characterization of 153 sensors from five wafers. The low yield was attributed to the malfunctioning of in-pixel electronics.

Ten validated HitPix2 sensors were selected for the multi-sensor prototype and integrated into a 2×5 matrix. The five sensors in each matrix row were daisy-chained for configuration and readout. The assembled matrix was tested at HIT with proton and carbon ion beams configured with different beam sizes. The beam position and size reconstructed using the 2×5 HitPix2 matrix were compared against the data from the existing reference ISO-MWPC detector. It

was confirmed that the 2×5 HitPix2 matrix meets the final system requirements in accuracy and precision of 0.2 mm (0.4 mm) for the reconstructed beam position (size). These results were an important proof of concept for the reconstruction capability of a multi-sensor assembly based on HitPix sensors.

In parallel with the evaluation of the 2×5 HitPix2 matrix, studies of individual HitPix2 sensors were conducted to formulate a set of new requirements for the next HitPix3 sensor design to improve its performance.

The previously observed limitation of the HitPix2 counting capability at high-intensity proton and carbon beams [Pit22; Die+23] was confirmed with new measurements, which yielded pixel dead time values of $\sim$17 µs and $\sim$6 µs for 430.10 MeV u^{-1} carbon and 221.06 MeV u^{-1} proton beams, respectively. Direct measurements of the in-pixel Charge-Sensitive Amplifier output at different ion beams allowed to attribute this limitation to pileup and baseline drop effects. To further investigate the influence of these effects on the sensor performance, measurements with infrared LEDs were preformed. The results confirmed that the HitPix2 sensor is capable of detecting particles at high rates without saturation, if the pileup and baseline drop effects are excluded. Furthermore, the scanning of a single HitPix2 pixel with a proton microbeam narrowed the region responsible for the baseline drop effect to a 200 µm $\times$ 100 µm area, which partially covers the sensor diode and the transition area between the diode and the in-pixel electronics. Additionally, proton microbeam tests of HitPix1 sensors with different pixel topologies revealed that a pixel designed with the ISO topology and a pMOS based CSA had the highest tolerance to the baseline drop effect. Therefore, the following features were proposed for the new HitPix3 sensor design: a switch-reset circuit in the CSA to suppress pileup and to restore the baseline faster, ISO pixel topology and pMOS based CSA design.

To define the optimal *p*-type substrate resistivity in terms of radiation hardness, the HitPix2 sensors, produced on different substrates with resistivities of 20 Ω cm, 300 Ω cm and 5000 Ω cm, were uniformly irradiated with a 23 MeV proton beam to 1 MeV neutron equivalent fluence of $\sim 1 \times 10^{15}$ cm^{-2}. These sensors were then tested with carbon beams at different working temperatures. The measurements showed that the sensor based on 300 Ω cm had the highest efficiency after significant radiation damage. Therefore, this resistivity was chosen for the HitPix3 sensor. Moreover, these tests confirmed that the final beam monitor must include a cooling system to mitigate the increased sensor leakage current and noise after radiation damage.

It was also observed that the HitPix2 design with a single comparator threshold common to all pixels resulted in a wide pixel threshold distribution due to production variations in pixels. This led to a non-uniform response to particles with signals close to the threshold value. Furthermore, after significant radiation damage, this design solution led to a large fraction of pixels being masked during the analysis due to increased noise. Therefore, based on the measurements with unirradiated and irradiated HitPix2 sensors, an individual in-pixel DAC block for pixel threshold adjustments with an output voltage range of 300 mV and a pixel output masking feature were proposed for the HitPix3 pixel design.

Additionally, the HitPix2 sensor maximum readout speed, which defines the dead time between frames, was found to be 55 Mbit s^{-1} and 36 Mbit s^{-1} for a single sensor and a daisy chain of five sensors, respectively. To overcome this, it was proposed to redesign the HitPix3 control and data input/output buffers according to the LVDS standard and to redesign the shift registers in the peripheral electronics for a single phase clock.

The on-sensor beam projection calculation (adder mode) was implemented in HitPix2 sensor only column-wise. However, for the final beam monitor system, the beam parameters must be estimated in both X- and Y-directions. Therefore, it was proposed to implement an additional row-wise projection calculation in the HitPix3 design.

All discussed features were implemented in the HitPix3 sensor design, followed by its production in the second half of 2023. Several HitPix3 sensors were characterized in detail in the laboratory environment and during beam tests at HIT. The results confirmed the full functionality of all new design features and the improved performance of the HitPix3 sensor compared to its predecessor HitPix2. The most important results were: the HitPix3 could be read out at the maximum readout speed supported by the current firmware of 190 Mbit s^{-1}, the developed pixel threshold tuning procedure allowed to reduce the pixel threshold deviation by a factor of four, leading to a more uniform pixel response for small-signal particles, and the pixel dead time was significantly reduced to ∼3 µs and ∼2 µs for 430.10 MeV u^{-1} carbon and 221.06 MeV u^{-1} proton beams, respectively. Furthermore, a beam test of an irradiated HitPix3 sensor with a 1 MeV neutron equivalent fluence of $\sim 1 \times 10^{15}$ cm^{-2} revealed no degradation in pixel performance in carbon beams at room temperature. The proton beams could not be detected with this sensor at room temperature due to high pixel thresholds, which were set to compensate the high pixel noise after irradiation without cooling. Therefore, a final conclusion regarding the HitPix3 sensor performance after significant radiation damage for proton beam detection could not be drawn from these studies. For a final performance estimation, a new cooling setup for the irradiated HitPix3 sensor should be designed and tested at HIT.

A new characterization campaign with an updated testing workflow was carried out to select valid HitPix3 sensors for a small multi-sensor assembly and the beam monitor demonstrator. Compared to the HitPix2 results, the production yield significantly increased to 77 %, demonstrating an improved manufacturing process.

A small 1×5 HitPix3 multi-sensor assembly was designed, produced and tested in a laboratory environment. Additionally, the assembly technology for 5×5 HitPix2 matrix prototypes was explored, after which the beam monitor demonstrator, based on HitPix3 sensors, was designed with a modular architecture. In this design, 25 HitPix3 sensors formed a 5×5 matrix segmented into five 1×5 strips, which were connected to a separate motherboard PCB. This design solution allowed to develop and establish a reliable production workflow with greater control over the assembly and testing of individual demonstrator components before their final integration compared to initial monolithic design of the 5×5 HitPix2 matrices. As a result, two functional HitPix3 beam monitor demonstrators were produced.

One of the demonstrators was successfully tested at HIT with proton and carbon beams configured in a wide range of beam settings. Spot and raster scan measurements confirmed the demonstrator capability to track changes in the delivered spills and to reconstruct the beam position and size within the required accuracy and precision in beam conditions close to a real treatment plan. The demonstrator was also tested inside the MRI setup at HIT. The measurements with proton and carbon beams without active MRI-scanning confirmed the demonstrator tolerance to static magnetic fields. However, during active MRI-scanning, the negative influence of the changing magnetic fields on the FPGA board sensitive components and the long, unshielded ∼1 m connection cable between the demonstrator and FPGA board prevented the demonstrator validation in these magnetic field conditions. Future tests will require a new cable design based on a set of twisted pairs and ground shielding. The cable must be also long enough to position the FPGA board outside the MRI setup.

After the successful beam tests, the HitPix3 beam monitor demonstrator was delivered to HIT for further evaluation regarding its potential integration into a beam quality control procedure. This concludes the scope and results of this thesis within the project timeline.

However, the project will continue by the design of the new HitPix4 sensor with a large sensitive area of 2 cm × 2 cm and a final full-scale beam monitor demonstrator. The knowledge and experience gained during this thesis allowed to formulate a list of design considerations for the HitPix4 sensor and the full-scale beam monitor.

In summary, the beam monitor demonstrator based on HV-CMOS HitPix3 sensors showed very good performance during ion beam tests at HIT, confirming that a detector system based on HV-CMOS HitPix sensors is a promising candidate for the beam monitoring of therapeutic ion beams.

Part IV.

Appendix

A

Monolithic Active Pixel Sensor

Table A.1 details the input and output voltage levels for the LVCMOS and the LVDS standards used within the scope of this thesis.

Table A.1.: Input and output voltage ranges of LVCMOS18 and LVDS logic standards. From [Adv].

Standard	**Signal Type**	**Logic State**	**Voltage Level (V)**
LVCMOS18	Input (V_{IL})	Low	-0.3 to 0.63
LVCMOS18	Input (V_{IH})	High	1.2 to 2.1
LVCMOS18	Output (V_{OL})	Low	0 to 0.45
LVCMOS18	Output (V_{OH})	High	1.4 to 1.8
LVDS	Input (V_{ID})	Diff. Low	-0.6 to -0.1
LVDS	Input (V_{ID})	Diff. High	0.1 to 0.6
LVDS	Output (V_{OD})	Diff. Low	≈ -0.35
LVDS	Output (V_{OD})	Diff. High	≈ 0.35
LVDS	Common Mode Voltage (V_{CM})	-	≈ 1.2

B HitPix2

B.1. HitPix2 sensor design

Table B.1 shows the `bias-DAC` block shift register bits assignment of the HitPix2 sensor.

Table B.1.: The `bias-DAC` block shift register bits assignment of the HitPix2 sensor. After [Pit22]

Name	Size (bit)	Default value	Function
Vth	8	170	Comparator threshold voltage
ipfoll	6	1	Source follower setting
vncomp	6	1	Comparator setting
ipload2	6	3	CSA amplifier setting
infb2	6	4	Deep n-well bias resistance
vn2	6	0	CSA amplifier setting
vndell	6	8	CSA amplifier setting
vnfoll	6	1	Source follower setting
infb	6	63	CSA feedback strength
vn1	6	30	CSA amplifier setting
iblres	6	63	Baseline resistance
unlock	3	5	Turn on bias-DAC
reserved	1	0	reserved
out_lvds	1	1	Enable LVDS output
out_cmos	1	1	Enable LVCMOS output

B.2. Multi-sensor readout

The cumulative carbon beam profile measured using the 2×5 HitPix2 matrix (**counter mode**) without cutoff applied at focus settings F2, F3, and F4 is shown in Fig. B.1.

B.3. Performance at high particle rates

Zoomed spill structure of low-intensity carbon and proton beams measured using the HitPix2 sensor is shown in Fig. B.2.
Measured versus expected ⟨Hit rate⟩ of HitPix2 sensor at different proton beam intensities with energy of 156.35 MeV u^{-1} is shown in Fig. B.3.
Examples of measured signal of KIRA IR LED after optical-to-electrical conversion and corresponding CSA output signal of HitPix2 pixel at 400 kHz and 600 kHz light pulse frequency are shown in Fig. B.4.

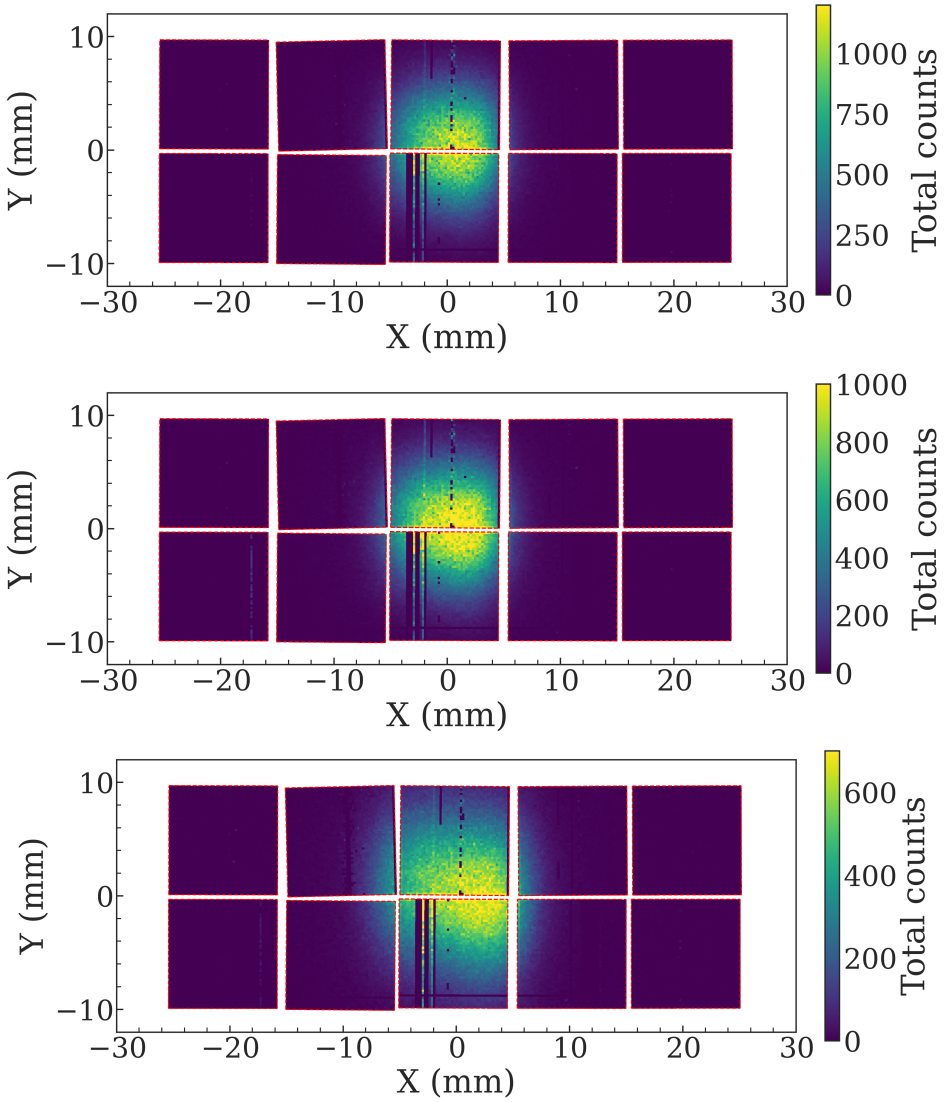


Figure B.1.: Cumulative 430.10 MeV u^{-1} carbon beam profile measured using the 2 × 5 HitPix2 matrix (**counter mode**) without cutoff applied at focus settings F2 (top, nominal FWHM of 5.5 mm), F3 (center, nominal FWHM of 7.8 mm) and F4 (bottom, nominal FWHM of 9.8 mm). Red dashed lines enclose the active areas of the sensors. Number of frames: 880. Frame duration: 350 µs

B.4. Radiation hardness

Measured ⟨Hit rate⟩ distributions of reference unirradiated sensor with resistivity (ρ) of 300 Ω cm and irradiated sensors with $\rho = 5000\,\Omega\,\text{cm}$ and $\rho = 20\,\Omega\,\text{cm}$ are shown in Fig. B.5 and Fig. B.6, respectively.

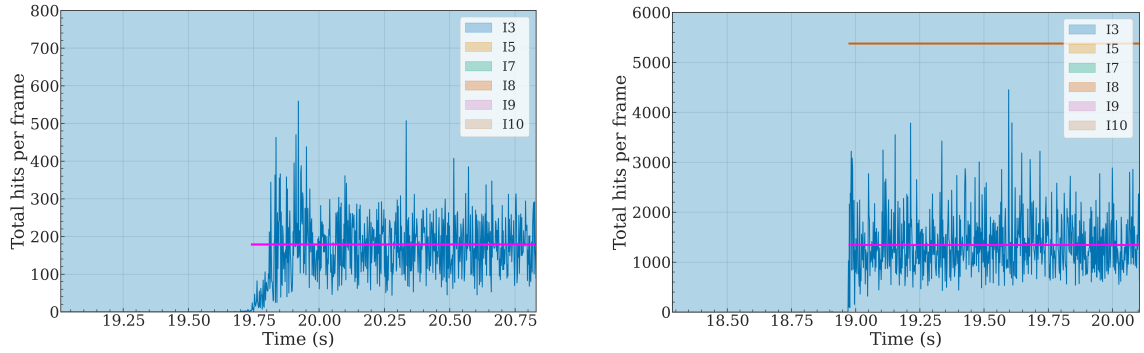


Figure B.2.: Zoomed spill structure of low-intensity carbon (left) and proton beams (right) measured using the HitPix2 sensor. The orange and magenta horizontal lines represent expected and measured ⟨Total hits per frame⟩, respectively.

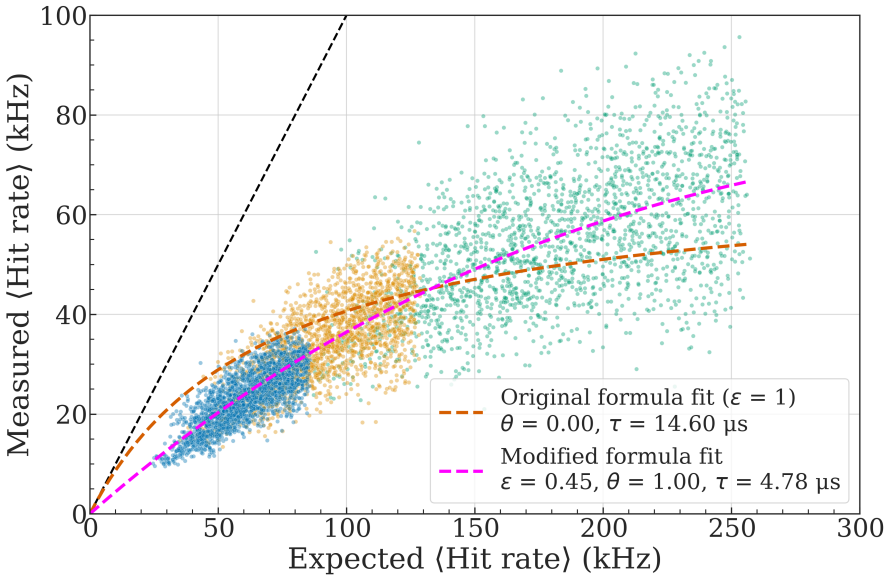


Figure B.3.: Measured versus expected pixel ⟨Hit rate⟩ of a HitPix2 sensor at different proton beam intensities with energy 156.35 MeV u^{-1}. The black dashed line represents the ideal sensor behavior with zero dead time and 100 % efficiency. The orange and magenta dashed lines represent the fit curve of original and modified Takacs' formula, respectively. Points are colored w.r.t. beam intensity: I3 - blue, I5 - orange, I7 - green.

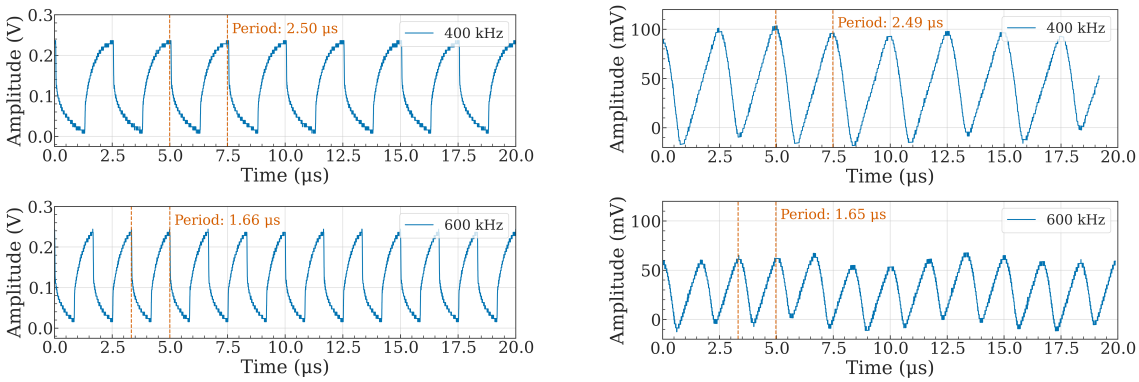


Figure B.4.: Measured signal of KIRA IR LED after optical-to-electrical conversion (left) and corresponding CSA output signal of HitPix2 pixel (right) at 400 kHz (top) and 600 kHz (bottom) light pulse frequency.

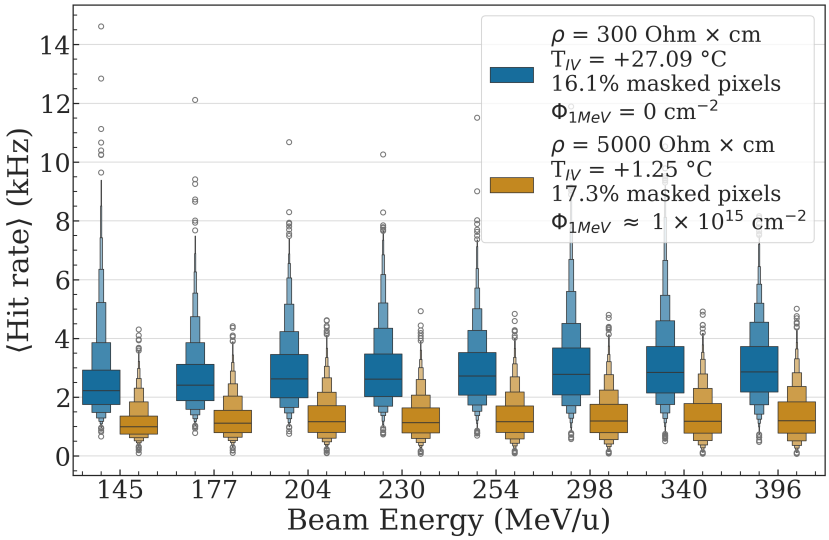


Figure B.5.: Measured ⟨Hit rate⟩ distributions of reference unirradiated sensor with resistivity of $\rho = 300\,\Omega\,\mathrm{cm}$ (blue) and irradiated sensors with $\rho = 5000\,\Omega\,\mathrm{cm}$ (orange) using the carbon beams with different energies. The beam size (FWHM) was adapted w.r.t. the beam energy to stay within 8.0 - 9.0 mm.

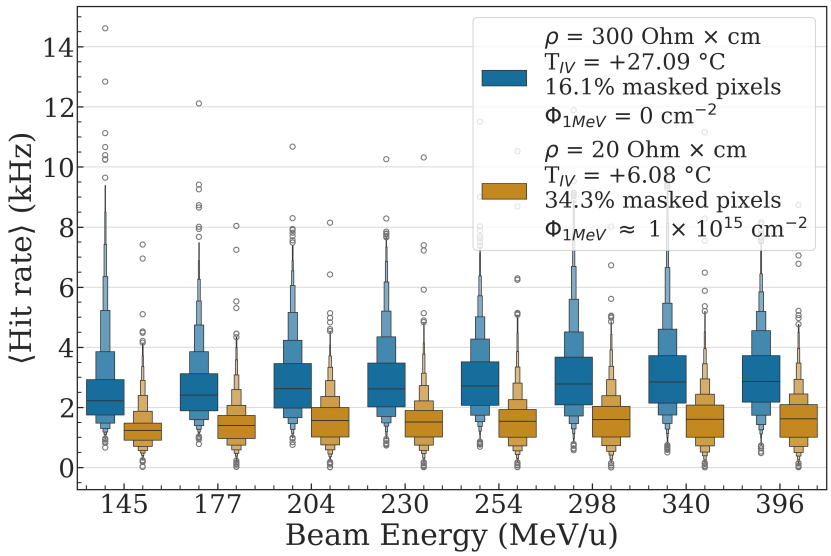


Figure B.6.: Measured ⟨Hit rate⟩ distributions of reference unirradiated sensor with resistivity of $\rho = 300\,\Omega\,\mathrm{cm}$ (blue) and irradiated sensors with $\rho = 20\,\Omega\,\mathrm{cm}$ (orange) using the carbon beams with different energies. The beam size (FWHM) was adapted w.r.t. the beam energy to stay within 8.0 - 9.0 mm.

C HitPix3

Table C.1 shows the bias-DAC block shift register bits assignment of the HitPix3 sensor.

C.1. HitPix3 sensor design

Table C.1.: The bias-DAC block shift register bits assignment of the HitPix3 sensor.

Name	Size (bit)	Default value	Function
EnBoost	1	0	Enable feedback boost feature
reserved	1	0	reserved
Vth	8	160	Comparator threshold voltage
ipfoll	6	1	Source follower setting
vncomp	6	14	Comparator setting
ipload2	6	1	CSA amplifier setting
infb2	6	4	Deep n-well bias resistance
vn2	6	52	CSA amplifier setting
ipdac	6	15	Output voltage range of pixel tune DAC
vnfoll	6	1	Source follower setting
infb	6	34	CSA feedback strength
vn1	6	52	CSA amplifier setting
iblres	6	31	Baseline resistance
unlock	3	5	Turn on bias-DAC
reserved	1	0	reserved
EnDOut	1	0	Enable DOut LVDS buffer
EnRAM	1	0	Enable pixel RAM writing

C.2. HitPix3 characterization

The full list of HitPix3 bias-DAC block settings used throughout this thesis is detailed in table C.2.
The CSA output calibration curve based on the simulated versus measured MPVs for the proton beam with nominal energies of 221.06 MeV, 156.35 MeV, and 94.54 MeV is shown in Fig. C.1.
The CSA output characteristics of the HitPix3 sensors configured with the bias-DAC settings A and B are shown in Fig. C.2. The fitted parameters are presented in the figure caption.
The CSA output calibration curve based on the the known deposited charge of the K_α photons versus measured MPVs for different targets is shown in Fig. C.3.
The measured pixel threshold and ⟨Hit rate⟩ distributions for the thinned (50 µm) and unthinned (850 µm) HitPix2 sensors at different threshold voltages are shown in Fig. C.4 and Fig. C.5, respectively.

Table C.2.: The `bias-DAC` settings used in measurements.

Name	Settings A	Settings B	Settings C	Settings D	Settings E
ipfoll	1	12	14	12	12
vncomp	14	14	50	45	52
ipload2	1	1	1	1	1
infb2	4	4	63	63	63
vn2	52	52	38	53	46
ipdac	15	15	14	14	14
vnfoll	1	1	1	1	1
infb	34	63	63	25	63
vn1	52	52	38	10	31
iblres	31	31	63	9	63

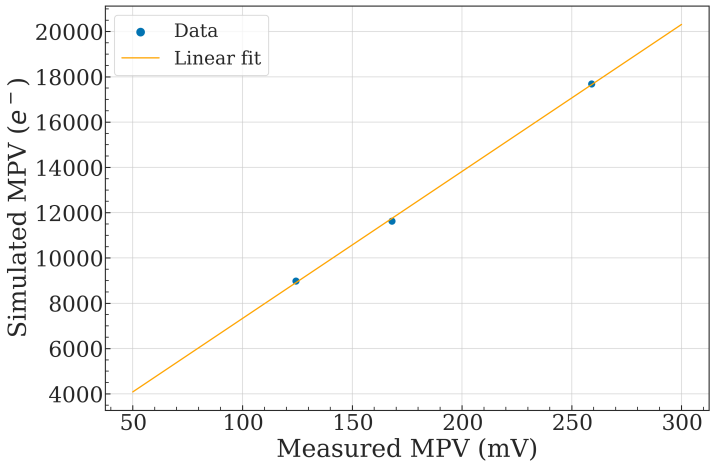


Figure C.1.: CSA output calibration curve based on simulated and measured MPVs of proton beam with nominal energies of 221.06 MeV, 156.35 MeV, and 94.54 MeV.

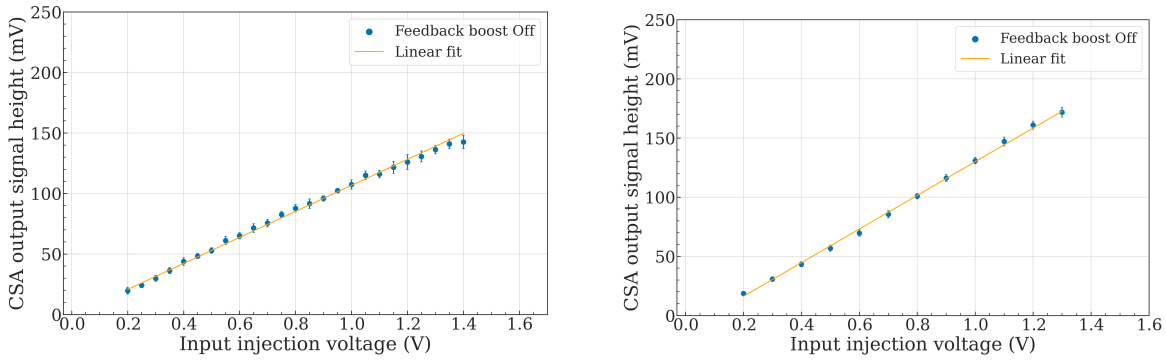


Figure C.2.: Output characteristic of the pixel CSA, fitted with a linear function for the `bias-DAC` settings A (left) and B (right). The fitted slopes and intercepts for the `bias-DAC` settings A and B are $(107.5 \pm 1.7\,\mathrm{mV\,V^{-1}};\ -0.8 \pm 1.3\,\mathrm{mV})$ and $(142.3 \pm 2.2\,\mathrm{mV\,V^{-1}};\ -12.3 \pm 1.5\,\mathrm{mV})$, respectively.

The measured pixel threshold, its standard deviation and pixel noise distributions for the HitPix3 sensor configured with `bias-DAC` settings A are shown in Fig. C.6, C.7 and C.8, respectively.

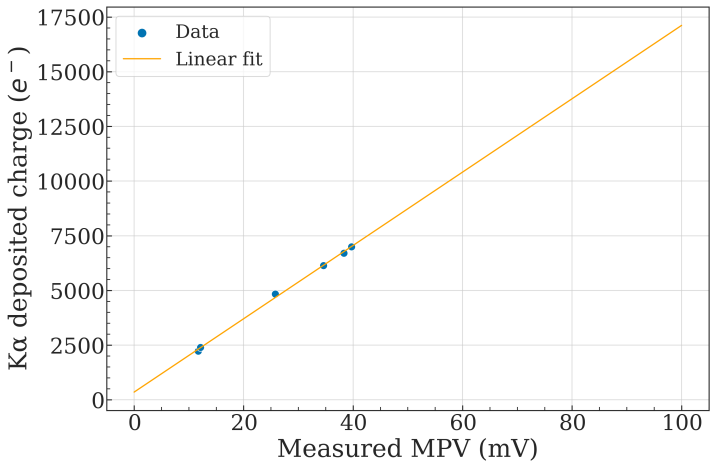


Figure C.3.: CSA output calibration curve based on tabulated data of K_α emission lines for different target materials irradiated by the X-ray tube.

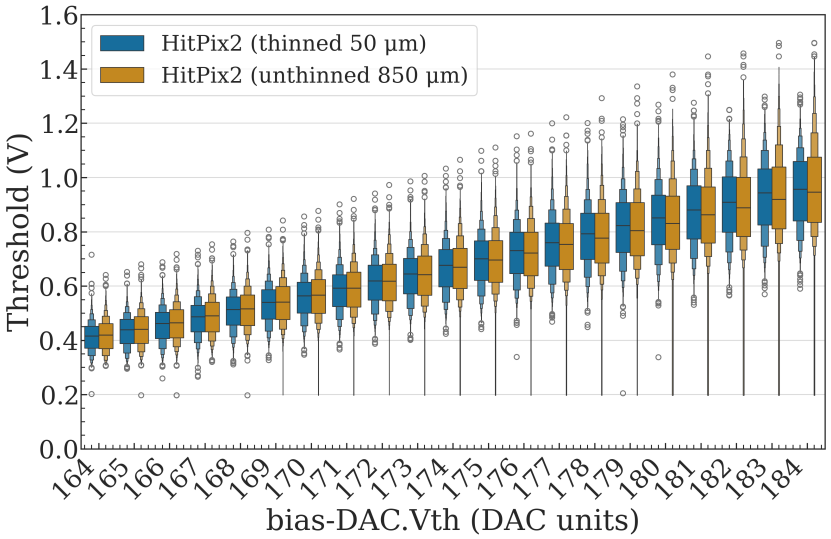


Figure C.4.: Measured pixel threshold distribution for the thinned (blue) and unthinned (orange) HitPix2 sensors at different threshold voltage values.

Tables C.3 and C.4 detail the measured MPV and calibration factor, and calibration curve parameters for injection circuits, respectively, for different HitPix3 pixels.
The CSA output signal height distributions measured using photons emitted from different targets irradiated by the X-ray tube for HitPix3 sensor configured with `bias-DAC` settings C is shown in Fig. C.9.
Figure C.10 shows the average pixel hit rate measured in HitPix3 counter mode without the Sr-90 source at threshold voltage of 154 DAC units and 160 DAC units before pixel threshold tuning.
Figure C.11 shows the cumulative carbon beam profile with a nominal energy of 430.10 MeV measured in HitPix3 counter mode before and after pixel threshold tuning.
The measured versus expected pixel ⟨Hit rate⟩ of HitPix3 sensor at different proton beam intensities with energy 156.35 MeV u^{-1} is shown in Fig. C.12. The CSA output measured using the unirradiated and irradiated HitPix3 sensors in carbon beam are shown in Fig. C.13 and Fig. C.14.

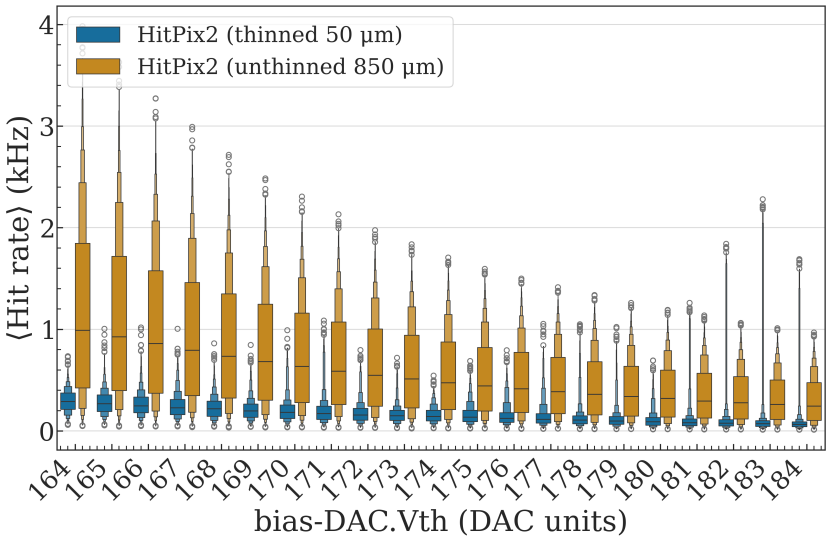


Figure C.5.: Measured ⟨Hit rate⟩ distribution for the thinned (blue) and unthinned (orange) HitPix2 sensors at different threshold voltage values using the Sr-90 source.

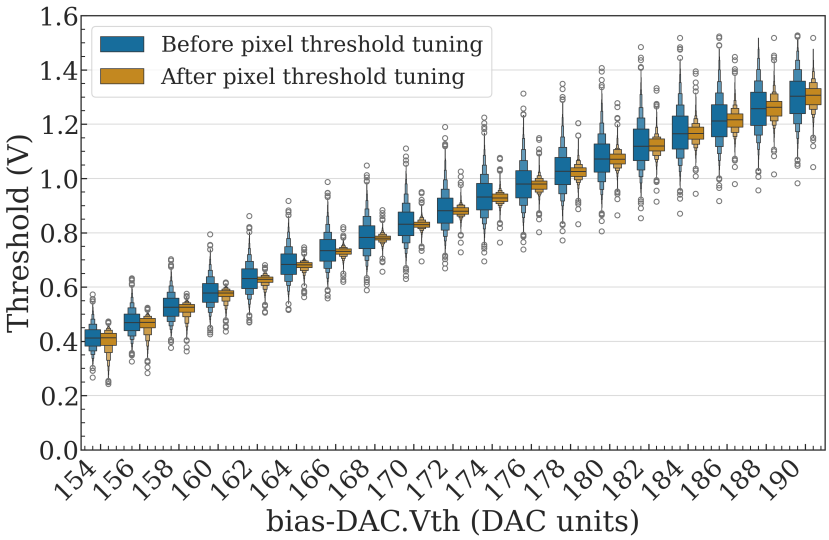


Figure C.6.: Measured pixel threshold distribution before (blue) and after (orange) pixel threshold tuning at different threshold voltage values. The sensor was configured with `bias-DAC` settings A.

C.3. Multi-sensor readout

An example of measured latency scan and the pixel coordinate map for a single row of 2×5 HitPix3 matrix are shown in Fig. C.15 and C.16, respectively.

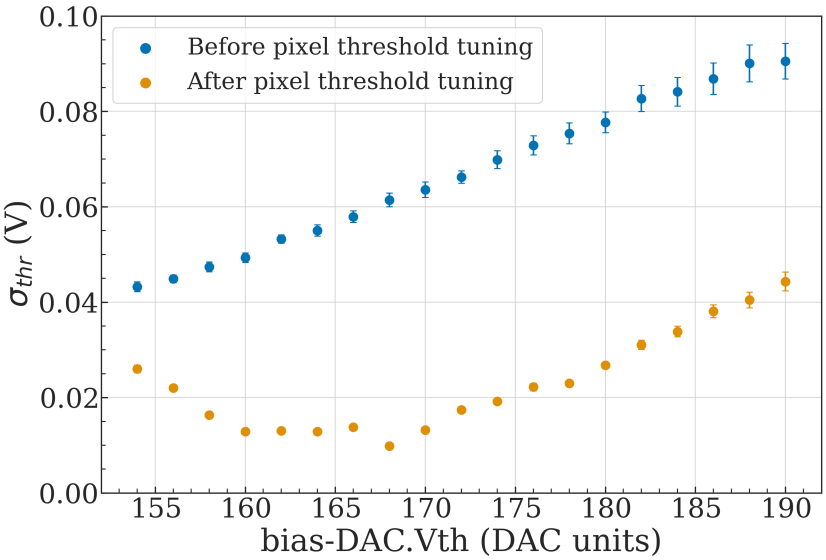


Figure C.7.: Standard deviation of the HitPix3 pixel threshold distribution before (blue points) and after (orange points) pixel threshold tuning extracted from a Gaussian fit at different threshold voltages. The sensor was configured with `bias-DAC` settings A.

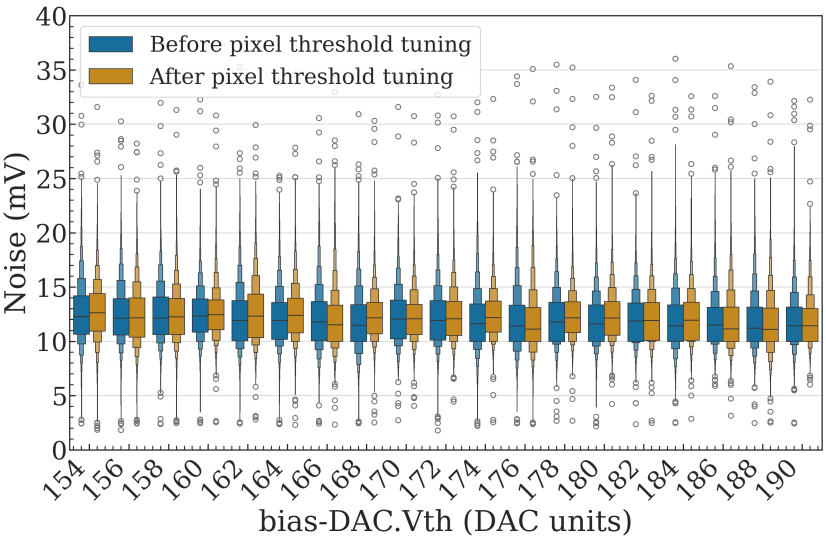


Figure C.8.: Pixel noise distribution of HitPix3 before (blue) and after (orange) pixel threshold tuning at different threshold voltage values. The sensor was configured with `bias-DAC` settings A.

Table C.3.: Measured MPV and calibration factor of HitPix3 pixels using the Sr-90 source at a bias voltage of −100 V. The sensor was configured with `bias-DAC` settings C.

Pixel number	MPV (mV)	Calibration factor ($e^- mV^{-1}$)
31	62.3 ± 3.3	68.9 ± 2.6
33	53.3 ± 4.0	80.7 ± 3.3
34	54.1 ± 3.3	79.4 ± 3.4
35	59.1 ± 3.3	72.7 ± 3.0
36	58.3 ± 3.9	73.7 ± 3.1
37	64.0 ± 3.3	67.1 ± 2.4
42	60.7 ± 3.3	70.8 ± 2.7

Table C.4.: Calibration curve parameters for HitPix3 pixel injection circuits at the applied bias voltage of −100 V. The sensor was configured with `bias-DAC` settings C.

Pixel number	$a_{0.2-1.4}$ ($e^- V^{-1}$)	$b_{0.2-1.4}$ (e^-)	$a_{0.2-0.6}$ ($e^- V^{-1}$)	$b_{0.2-0.6}$ (e^-)
31	$20\,090 \pm 280$	-2650 ± 200	$17\,180 \pm 930$	-1570 ± 360
33	$20\,820 \pm 300$	-3170 ± 230	$16\,730 \pm 1140$	-1700 ± 430
34	$20\,580 \pm 230$	-2810 ± 180	$17\,590 \pm 900$	-1710 ± 340
35	$18\,920 \pm 260$	-2540 ± 210	$15\,840 \pm 950$	-1330 ± 380
36	$19\,400 \pm 270$	-2370 ± 210	$16\,630 \pm 950$	-1360 ± 370
37	$19\,080 \pm 230$	-2460 ± 180	$16\,370 \pm 870$	-1480 ± 330
42	$19\,090 \pm 220$	-2520 ± 170	$15\,960 \pm 790$	-1340 ± 310

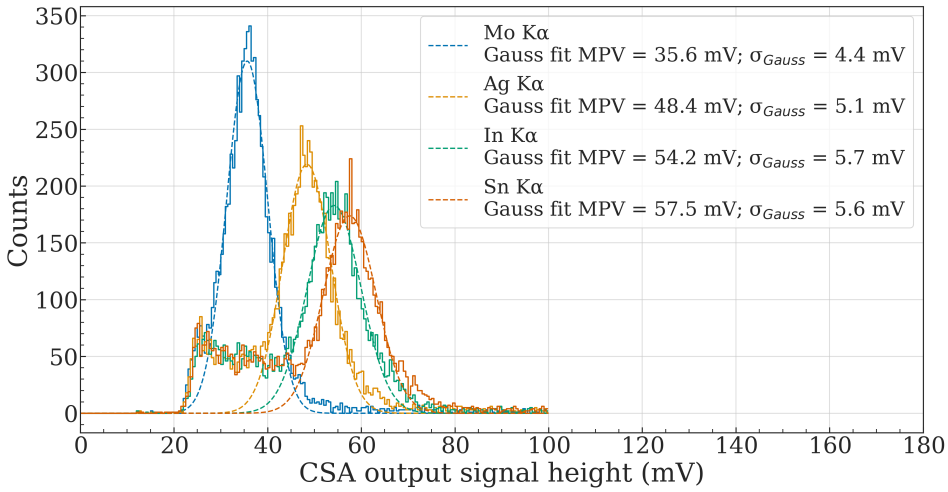


Figure C.9.: CSA output signal height distributions measured using photons emitted from different targets irradiated by the X-ray tube. The spectrum of targets: molybdenum, silver, indium, and tin is colored in blue, orange, green, and red, respectively. The dashed lines represent fits to the characteristic peak with a Gaussian function. The sensor was configured with `bias-DAC` settings C.

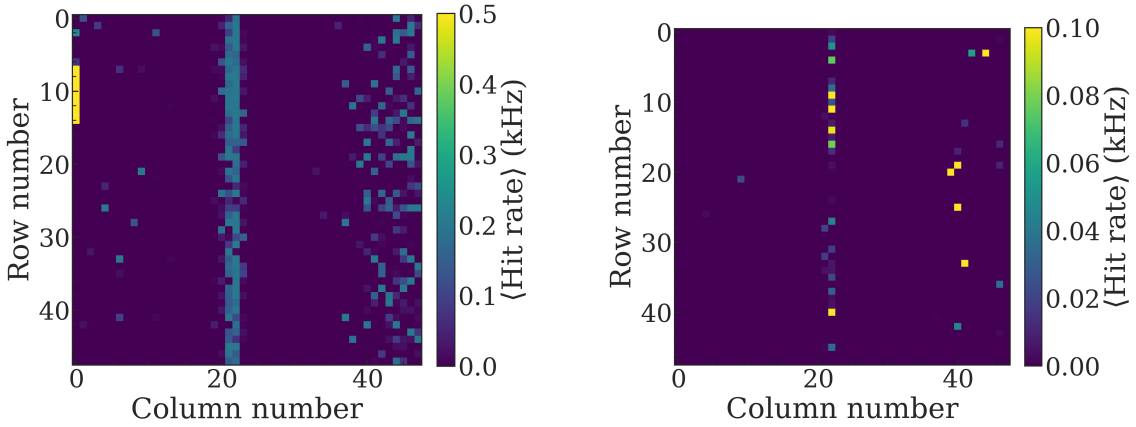


Figure C.10.: Average pixel hit rate measured using the HitPix3 sensor in **counter mode** without the Sr-90 source at threshold voltage of 154 DAC units (left) and 160 DAC units (right) before pixel threshold tuning. Frame duration: 5 ms. The sensor was configured with `bias-DAC` settings A.

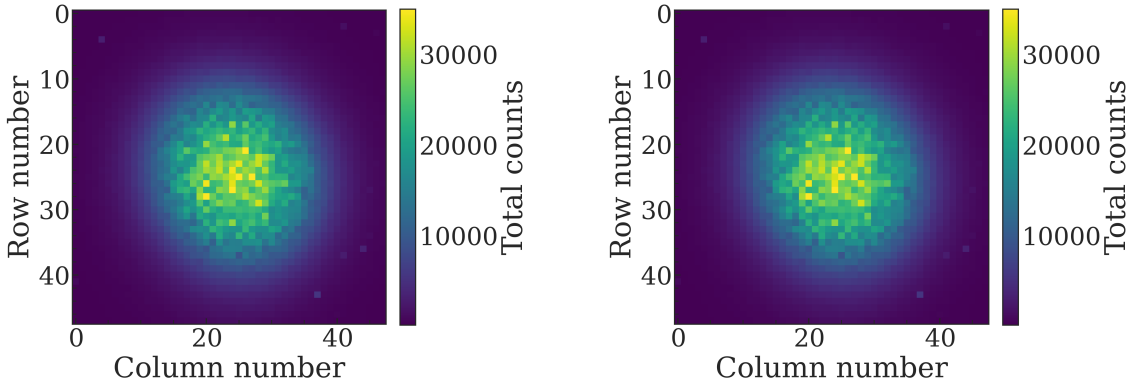


Figure C.11.: Cumulative carbon beam profile with a nominal energy of 430.10 MeV u^{-1} measured using the HitPix3 sensor in **counter mode** before (left) and after (right) pixel threshold tuning. Frame duration: 400 µs. Number of frames: 4288 (one spill). Threshold voltage = 175 DAC units. The sensor was configured with `bias-DAC` settings B.

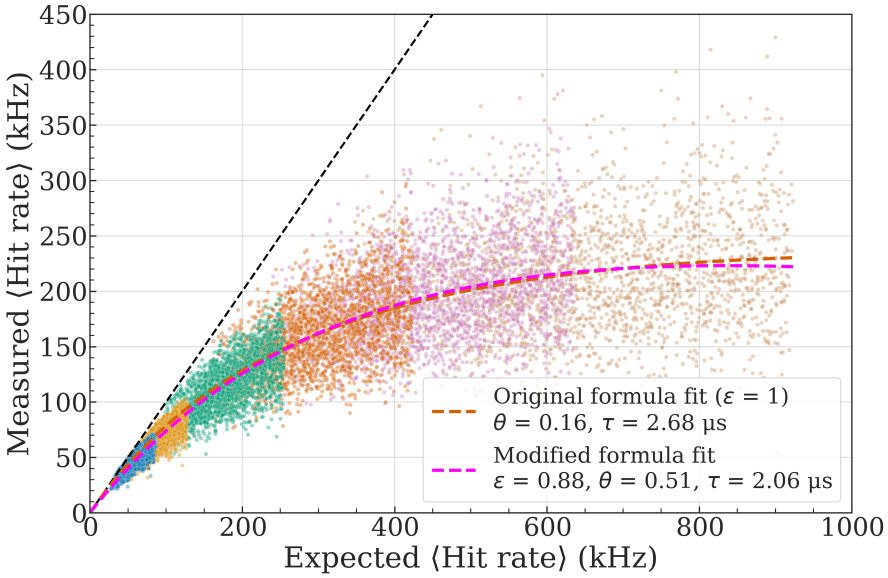


Figure C.12.: Measured versus expected pixel ⟨Hit rate⟩ of a HitPix3 sensor at different proton beam intensities with energy 156.35 MeV u^{-1}. The feedback boost was disabled during the measurement. The black dashed line represents the ideal sensor behavior with zero dead time and 100 % efficiency. The orange and magenta dashed lines represent the fit curve of original and modified Takacs' formula, respectively. Points are colored w.r.t. beam intensity: I3 - blue, I5 - orange, I7 - green, I8 - red, I9 - purple, I10 - brown.

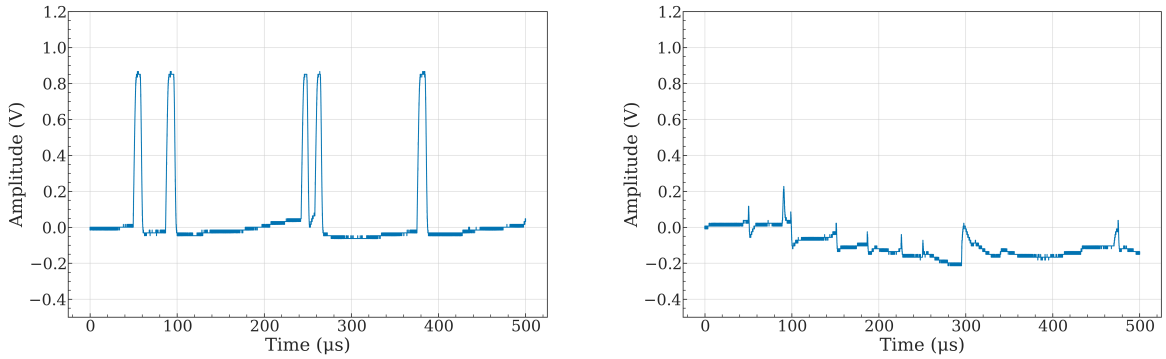


Figure C.13.: Measured HitPix3 pixel CSA output of 430.10 MeV u^{-1} carbon beams with intensity I2 (left) and I3 (right) and disabled/enabled feedback boost circuit (left/right). The threshold voltage was set to 155 DAC units. The sensor was configured with `bias-DAC` settings C.

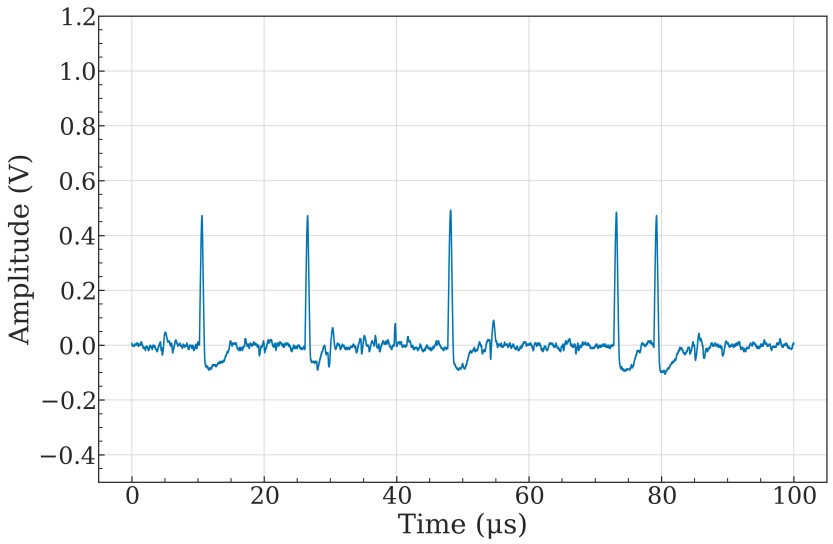


Figure C.14.: Pixel CSA output of the irradiated HitPix3 sensor in response to 430.10 MeV u^{-1} carbon beams with intensity I3. The sensor was irradiated with equivalent neutron fluence of $\sim 1 \times 10^{15}\,cm^{-2}$. The sensor was configured with `biasDAC` settings B. The bias voltage was set to $-50\,V$.

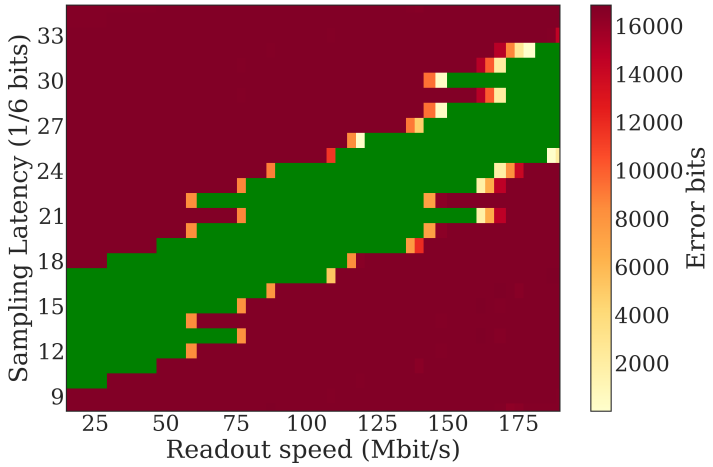


Figure C.15.: Example of a measured latency scan for a single row of 2×5 HitPix3 matrix. The green area corresponds to the readout speed and sampling latency values without an error.

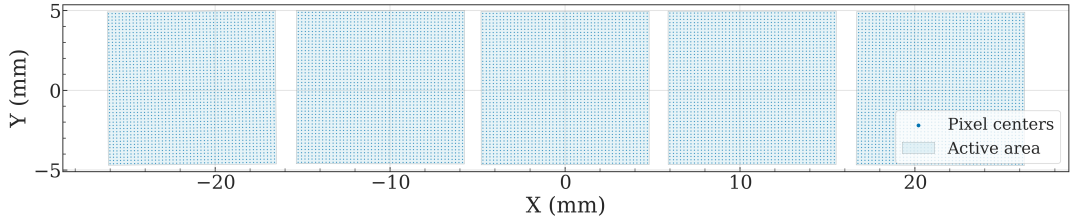


Figure C.16.: Pixel coordinate map of a single row of 2×5 HitPix3 matrix. The coordinate origin (0,0) is located at the matrix geometrical center.

D

Beam monitor demonstrator

D.1. Assembly technology exploration

The layouts of the 5 × 5 HitPix2 bump-bonding and wire-bonding PCBs are shown in Fig. D.1 and D.2, respectively.

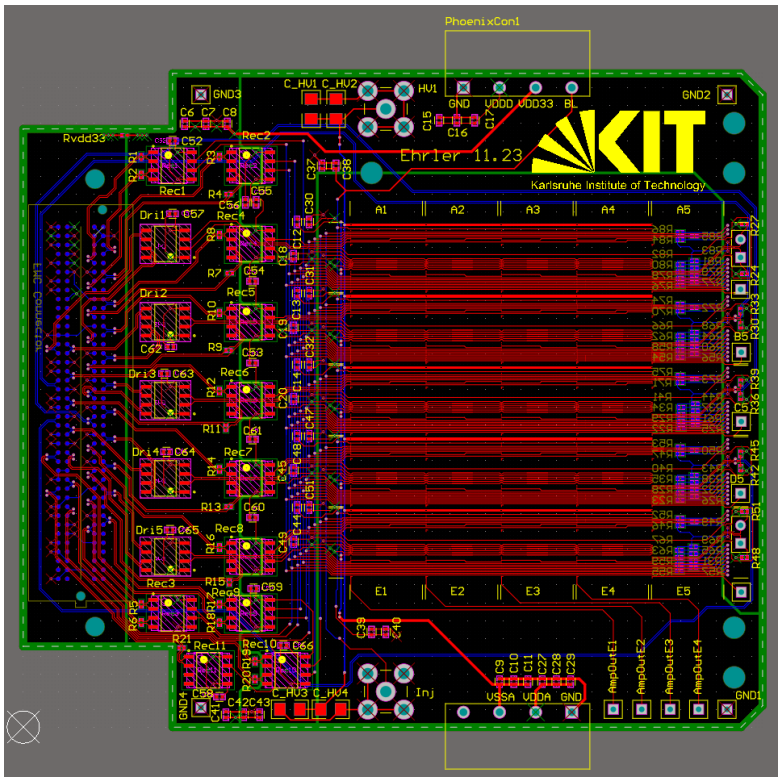


Figure D.1.: Layout of the 5 × 5 HitPix2 bump-bonding PCB. The PCB was designed by F. Ehrler.

D.2. Beam monitor production workflow

The measured latency scan and adder test with the Sr-90 source for each 1 × 5 strip performed during the post assembly phase are shown in Fig. D.3 and D.4, respectively.

The local rotation angle distribution of the HitPix3 sensors in the beam monitor demonstrator is shown in Fig. D.5.

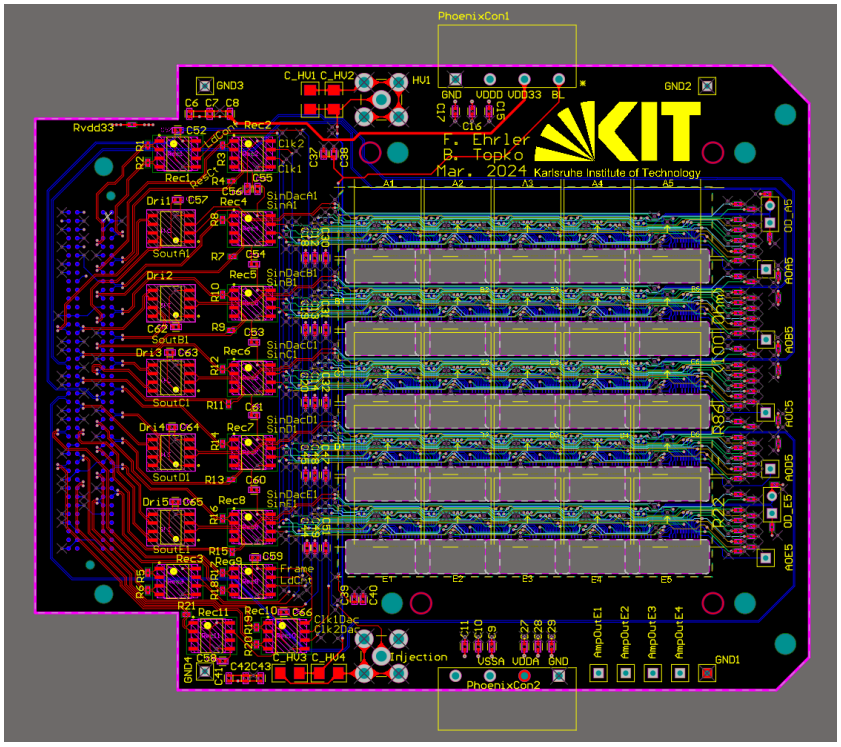


Figure D.2.: Layout of the 5 × 5 HitPix2 wire-bonding PCB. The PCB was designed by the author and F. Ehrler.

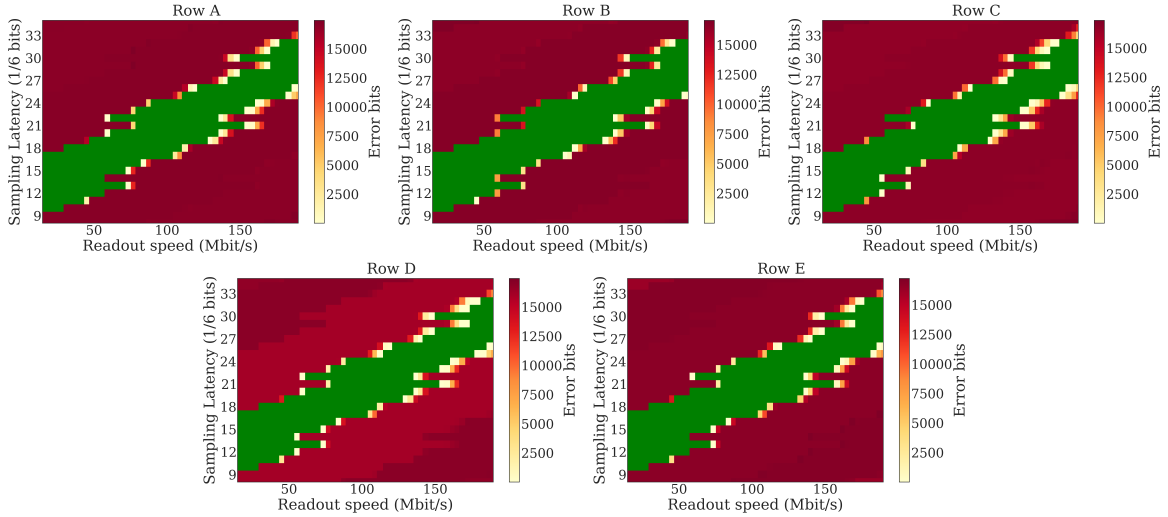


Figure D.3.: Measured latency scan for each 1 × 5 strip. The green area corresponds to the readout speed and sampling latency values without an error.

D.3. Beam test results

The ⟨FWHM⟩ of the measured carbon beam size in the X- and Y-directions using the beam monitor demonstrator in **adder mode without cutoff** applied is detailed in table D.1.

The measured distributions of carbon beam size $FWHM_x$ and $FWHM_y$ using the existing ISO-MWPC detector for different beam settings are shown in Fig. D.6. The measurements were conducted during a separate beam test in March 2025.

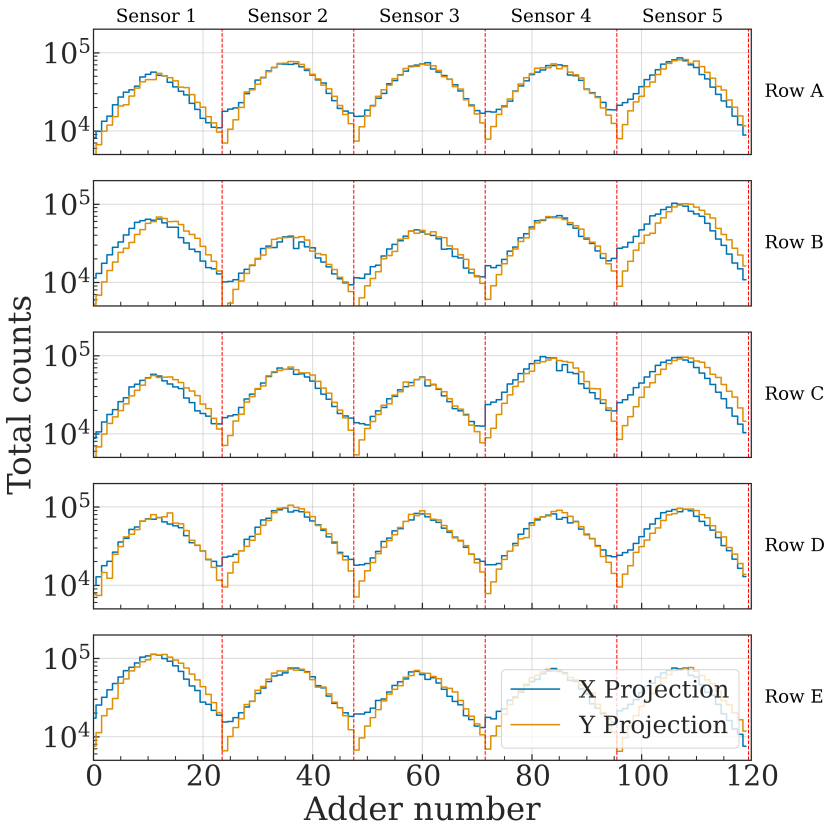


Figure D.4.: Cumulative Sr-90 source profile projection in the X- (blue) and Y- (orange) directions measured using each sensor of every 1×5 strip after pixel threshold tuning in adder mode. Red dashed lines outline individual set of adders for each sensor. Number of frames per source position: 2000. The threshold voltage was set to 150 DAC units.

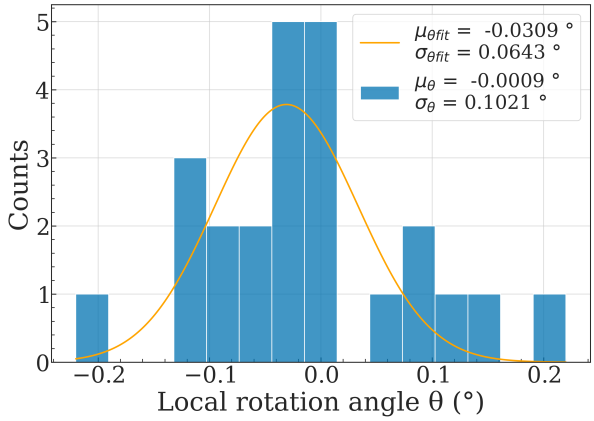


Figure D.5.: Local rotation angle distribution of the HitPix3 sensors in the beam monitor demonstrator. The orange solid line represents a fit to the measurement data with a Gaussian function.

The measured distributions of carbon beam size and position using the beam monitor demonstrator in **counter mode** without and with cutoff applied for different beam settings are shown

Table D.1.: The ⟨FWHM⟩ of the measured carbon beam size in the X- and Y-directions using the beam monitor demonstrator in **adder mode without cutoff** applied for different beam settings. The $\Delta_{\mathrm{FWHM_x}}$ and $\Delta_{\mathrm{FWHM_y}}$ represent the relative difference of the estimated mean beam size measured with the demonstrator and the nominal value from the LIBC of HIT.

Setting	$\langle \mathrm{FWHM_x} \rangle$ (mm)	$\langle \mathrm{FWHM_y} \rangle$ (mm)	$\Delta_{\mathrm{FWHM_x}}$ (%)	$\Delta_{\mathrm{FWHM_y}}$ (%)
E1, I7	15.34 ± 0.29	15.26 ± 0.29	56.6	55.7
E1, I10	14.89 ± 0.15	14.89 ± 0.15	52.0	52.0
E18, I7	11.76 ± 0.23	11.89 ± 0.22	52.7	54.4
E18, I10	12.94 ± 0.16	13.04 ± 0.14	68.0	69.3
E255, I7	4.56 ± 0.15	4.46 ± 0.14	34.2	31.2
E255, I10	5.99 ± 0.14	6.16 ± 0.16	76.1	81.3

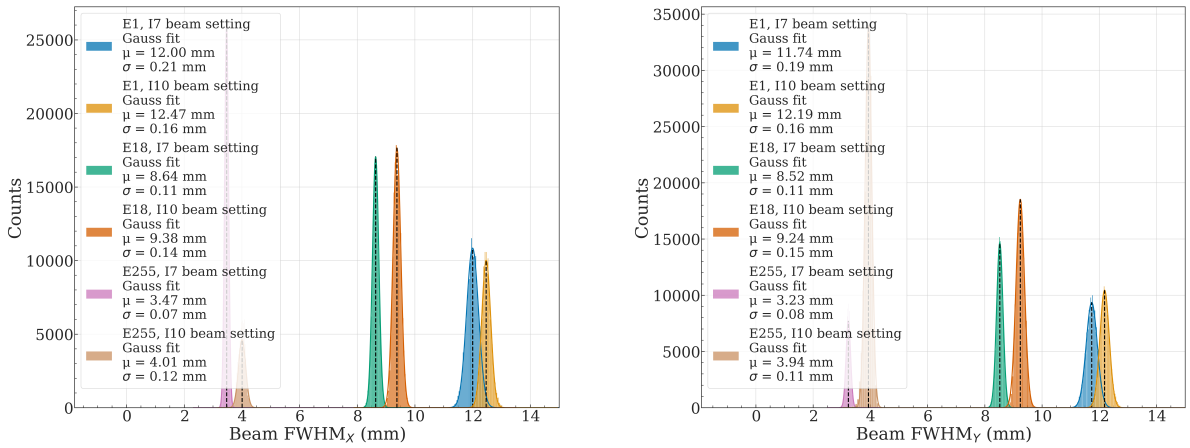


Figure D.6.: Measured distributions of carbon beam size $\mathrm{FWHM_x}$ (left) and $\mathrm{FWHM_y}$ (right) using the existing ISO-MWPC detector for different beam settings. Solid lines represent fits to the measurement data with a 1D-Gaussian function. The measurements were conducted during a separate beam test in March 2025.

in Fig. D.7 and D.8, respectively. For these measurements, the mean of the reconstructed beam parameters are detailed in tables D.2 and D.3.

Figure D.9 shows the normalized intensity of four spills for the proton beam (E18, I7) measured using the reference IC and the beam monitor demonstrator in **adder mode**.

The measured distributions of proton beam size and position using the beam monitor demonstrator in **adder mode** without and with cutoff applied for different beam settings are shown in Fig. D.10 and D.11, respectively. The mean of the reconstructed beam size is detailed in table D.4.

The measured distributions of proton beam size and position using the beam monitor demonstrator in **counter mode** without and with cutoff applied for different beam settings are shown in Fig. D.12 and D.13, respectively. For these measurements, the mean of the reconstructed beam parameters are detailed in tables D.5 and D.6.

The proton beam (E255, I3) position and size in the X- and Y-directions versus time measured during the raster scan with a 3 mm grid size using the beam monitor demonstrator in adder

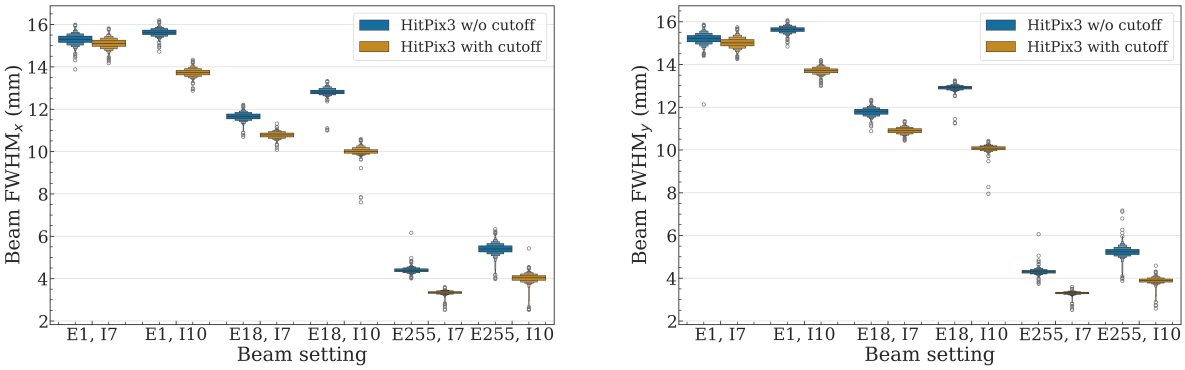


Figure D.7.: Measured distributions of carbon beam size $FWHM_x$ (left) and $FWHM_y$ (right) using the beam monitor demonstrator in **counter mode** without (blue color) and with (orange color) cutoff applied for different beam settings.

Table D.2.: The $\langle FWHM \rangle$ of the measured carbon beam size in the X- and Y-directions using the beam monitor demonstrator in **counter mode without cutoff** applied for different beam settings. The Δ_{FWHM_x} and Δ_{FWHM_y} represent the relative difference of the estimated mean beam size measured with the demonstrator and the nominal value from the LIBC of HIT.

Setting	$\langle FWHM_x \rangle$ (mm)	$\langle FWHM_y \rangle$ (mm)	Δ_{FWHM_x} (%)	Δ_{FWHM_y} (%)
E1, I7	15.31 ± 0.22	15.20 ± 0.22	56.2	55.2
E1, I10	15.63 ± 0.16	15.63 ± 0.14	59.5	59.5
E18, I7	11.67 ± 0.17	11.78 ± 0.18	51.5	53.0
E18, I10	12.80 ± 0.13	12.92 ± 0.10	66.2	67.8
E255, I7	4.40 ± 0.10	4.30 ± 0.09	29.3	26.4
E255, I10	5.40 ± 0.21	5.22 ± 0.18	58.9	53.5

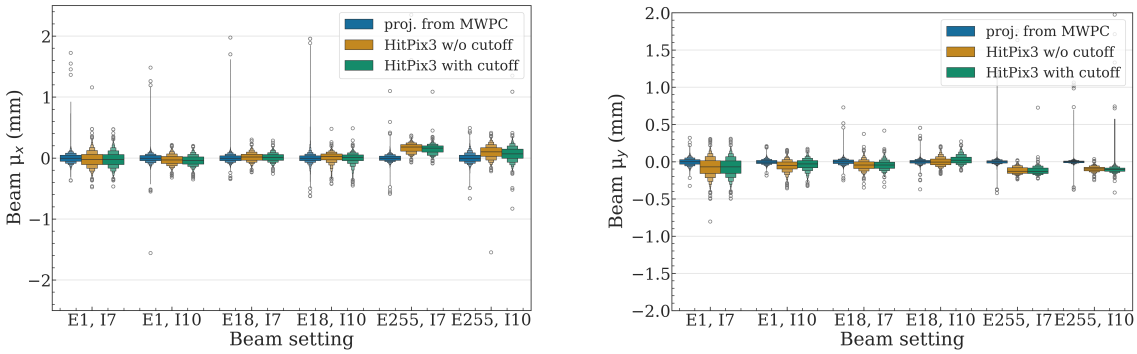


Figure D.8.: Measured distributions of carbon beam position μ_x (left) and μ_y (right) using the projected MWPC values (blue color) and the beam monitor demonstrator in **counter mode** without (orange color) and with (green color) cutoff applied for different beam settings.

mode without cutoff applied and the projected values from the MWPC are shown in Fig. D.14 and D.15, respectively.

Table D.3.: The $\langle\mu\rangle$ of the measured carbon beam position in the X- and Y-directions using the beam monitor demonstrator in **counter mode without cutoff** applied for different beam settings. The $\Delta\mu_x$ and $\Delta\mu_y$ represent the difference of the estimated mean beam position measured with the MWPC and the demonstrator. Units: mm

Setting	$\langle\mu_{xref}\rangle$	$\langle\mu_{yref}\rangle$	$\langle\mu_x\rangle$	$\langle\mu_y\rangle$	$\Delta\mu_x$	$\Delta\mu_y$
E1, I7	0.00 ± 0.07	0.00 ± 0.04	-0.02 ± 0.12	-0.07 ± 0.12	0.02	0.07
E1, I10	0.00 ± 0.06	0.00 ± 0.03	-0.03 ± 0.09	-0.05 ± 0.07	0.03	0.05
E18, I7	0.00 ± 0.06	0.00 ± 0.03	0.01 ± 0.07	-0.05 ± 0.07	-0.01	0.05
E18, I10	0.00 ± 0.06	0.00 ± 0.03	0.03 ± 0.07	-0.01 ± 0.06	-0.03	0.01
E255, I7	0.00 ± 0.05	0.00 ± 0.02	0.18 ± 0.07	-0.13 ± 0.05	-0.18	0.13
E255, I10	-0.01 ± 0.07	0.00 ± 0.02	0.10 ± 0.11	-0.10 ± 0.03	-0.11	0.10

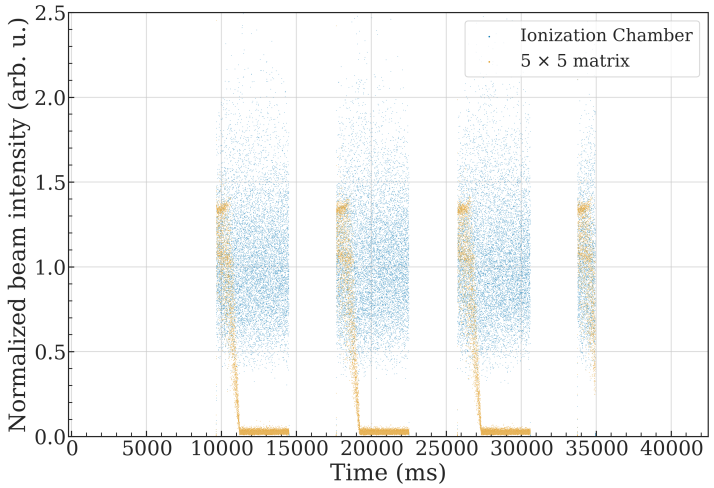


Figure D.9.: Normalized intensity of four spills for the proton beam (E18, I7) measured using the reference IC (blue points) and beam monitor demonstrator in **adder mode** (orange points). The measurement was affected by the high-voltage compliance issue (more details in subsection 5.4.1), leading to the degradation of the spill structure measured using the demonstrator after an initial ramp-up.

Table D.4.: The $\langle$FWHM$\rangle$ of the measured proton beam size in the X- and Y-directions using the beam monitor demonstrator in **adder mode without cutoff** applied for different beam settings. The Δ_{FWHM_x} and Δ_{FWHM_y} represent the relative difference of the estimated mean beam size measured with the demonstrator and the nominal value from the LIBC of HIT.

Setting	$\langle FWHM_x\rangle$ (mm)	$\langle FWHM_y\rangle$ (mm)	Δ_{FWHM_x} (%)	Δ_{FWHM_y} (%)
E1, I7	36.27 ± 0.39	37.28 ± 0.37	12.0	15.1
E18, I2	26.80 ± 0.28	26.87 ± 0.28	12.6	12.9
E255, I2	10.01 ± 0.34	9.70 ± 0.32	23.6	19.8

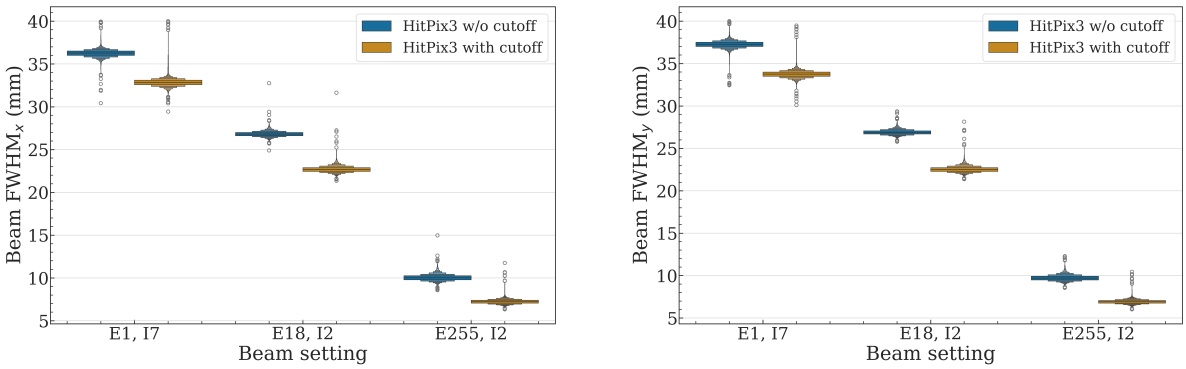


Figure D.10.: Measured distributions of proton beam size $FWHM_x$ (left) and $FWHM_y$ (right) using the beam monitor demonstrator in **adder mode** without (blue color) and with (orange color) cutoff applied for different beam settings.

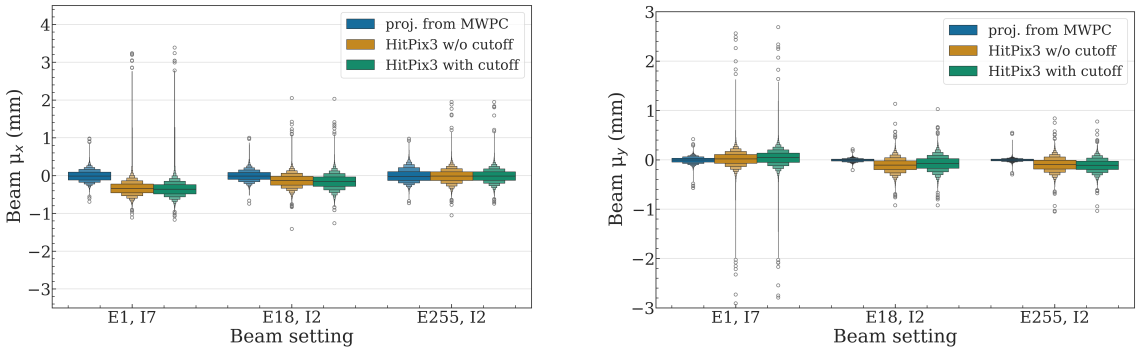


Figure D.11.: Measured distributions of proton beam position μ_x (left) and μ_y (right) using the projected MWPC values (blue color) and the beam monitor demonstrator in **adder mode** without (orange color) and with (green color) cutoff applied for different beam settings.

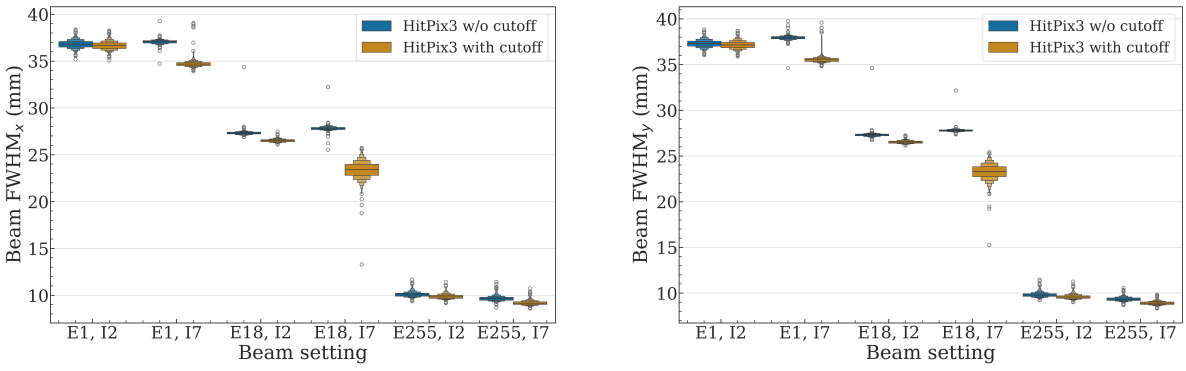


Figure D.12.: Measured distributions of proton beam size $FWHM_x$ (left) and $FWHM_y$ (right) using the beam monitor demonstrator in **counter mode** without (blue color) and with (orange color) cutoff applied for different beam settings.

Table D.5.: The ⟨FWHM⟩ of the measured proton beam size in the X- and Y-directions using the beam monitor demonstrator in **counter mode without cutoff** applied for different beam settings. The $\Delta_{\mathrm{FWHM_x}}$ and $\Delta_{\mathrm{FWHM_y}}$ represent the relative difference of the estimated mean beam size measured with the demonstrator and the nominal value from the LIBC of HIT.

Setting	$\langle \mathrm{FWHM_x} \rangle$ (mm)	$\langle \mathrm{FWHM_y} \rangle$ (mm)	$\Delta_{\mathrm{FWHM_x}}$ (%)	$\Delta_{\mathrm{FWHM_y}}$ (%)
E1, I2	36.80 ± 0.43	37.29 ± 0.41	13.6	15.1
E1, I7	37.07 ± 0.18	37.95 ± 0.19	14.4	17.1
E18, I2	27.32 ± 0.16	27.32 ± 0.15	14.8	14.8
E18, I7	27.80 ± 0.17	27.79 ± 0.12	16.8	16.7
E255, I2	10.04 ± 0.21	9.76 ± 0.20	23.9	20.5
E255, I7	9.63 ± 0.22	9.31 ± 0.19	18.9	14.9

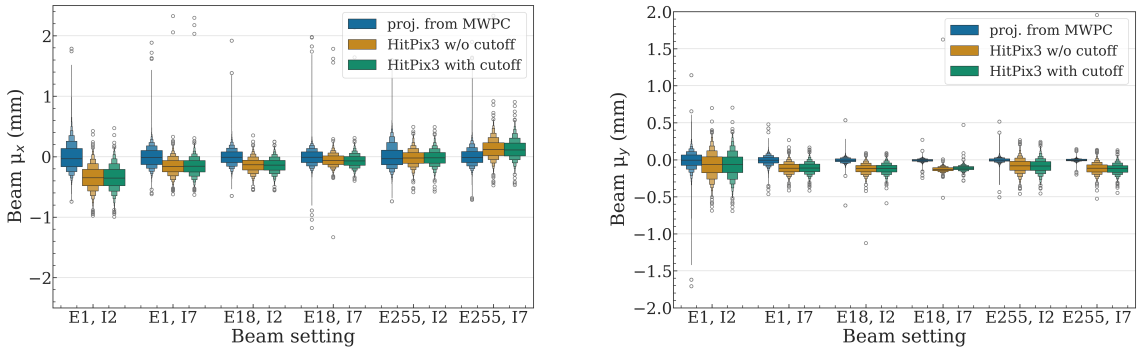


Figure D.13.: Measured distributions of proton beam position μ_x (left) and μ_y (right) using the projected MWPC values (blue color) and the beam monitor demonstrator in **counter mode** without (orange color) and with (green color) cutoff applied for different beam settings.

Table D.6.: The ⟨μ⟩ of the measured proton beam position in the X- and Y-directions using the beam monitor demonstrator in **counter mode without cutoff** applied for different beam settings. The $\Delta\mu_x$ and $\Delta\mu_y$ represent the difference of the estimated mean beam position measured with the MWPC and the demonstrator. Units: mm

Setting	$\langle \mu_{\mathrm{xref}} \rangle$	$\langle \mu_{\mathrm{yref}} \rangle$	$\langle \mu_x \rangle$	$\langle \mu_y \rangle$	$\Delta\mu_x$	$\Delta\mu_y$
E1, I2	-0.04 ± 0.22	0.00 ± 0.10	-0.35 ± 0.20	-0.07 ± 0.16	0.31	0.07
E1, I7	-0.01 ± 0.17	0.00 ± 0.06	-0.16 ± 0.14	-0.11 ± 0.08	0.15	0.11
E18, I2	-0.01 ± 0.13	-0.01 ± 0.03	-0.14 ± 0.12	-0.12 ± 0.07	0.13	0.11
E18, I7	-0.01 ± 0.13	0.00 ± 0.02	-0.06 ± 0.11	-0.13 ± 0.03	0.05	0.13
E255, I2	-0.04 ± 0.16	0.00 ± 0.02	-0.02 ± 0.13	-0.08 ± 0.09	−0.02	0.08
E255, I7	-0.01 ± 0.13	0.00 ± 0.01	0.11 ± 0.15	-0.11 ± 0.07	−0.12	0.11

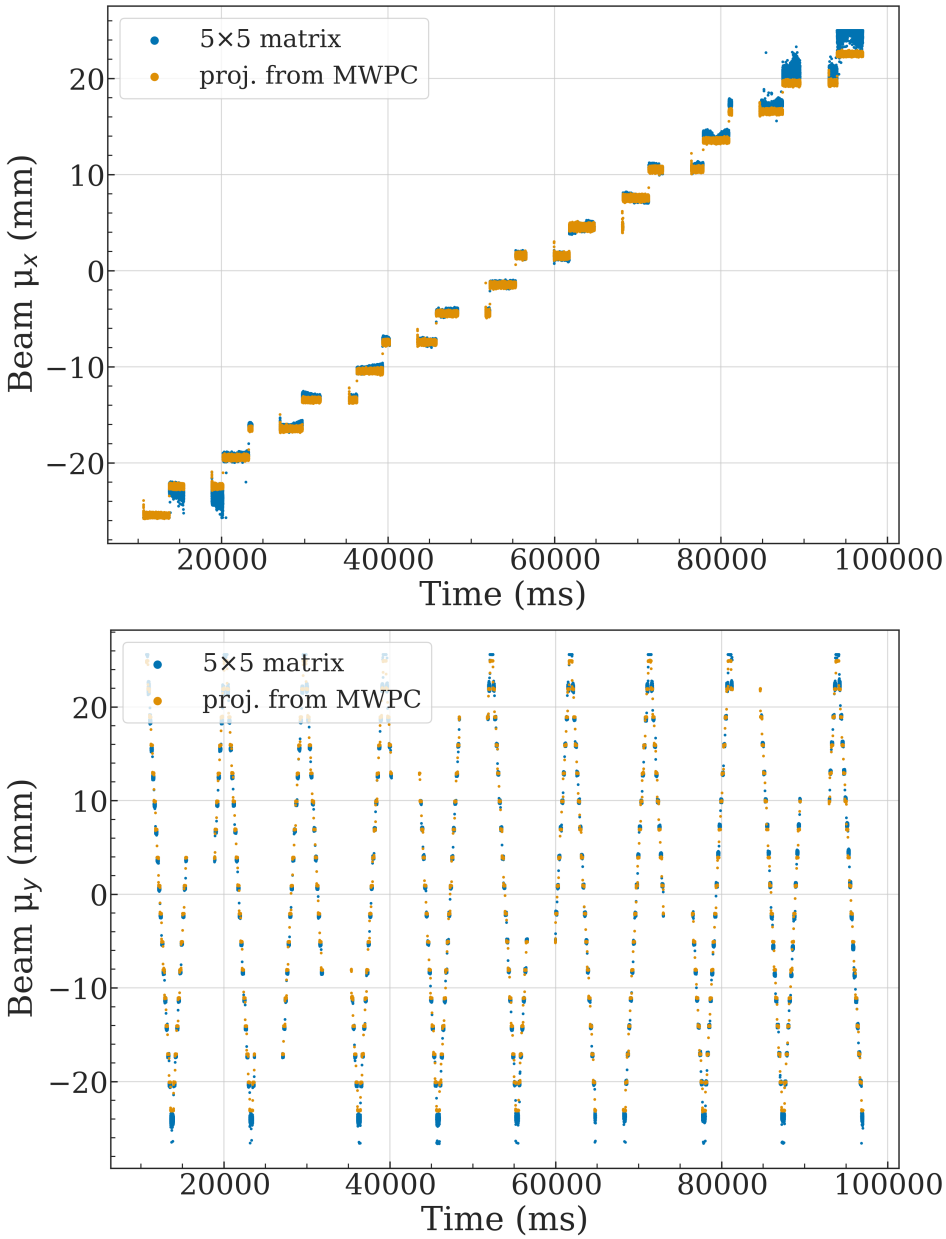


Figure D.14.: Proton beam (E255, I3) position in the X- (top) and Y- (bottom) directions versus time measured during a raster scan with a 3 mm grid step size using the beam monitor demonstrator in **adder mode without cutoff applied** (blue points) and the projected values from the MWPC (orange points).

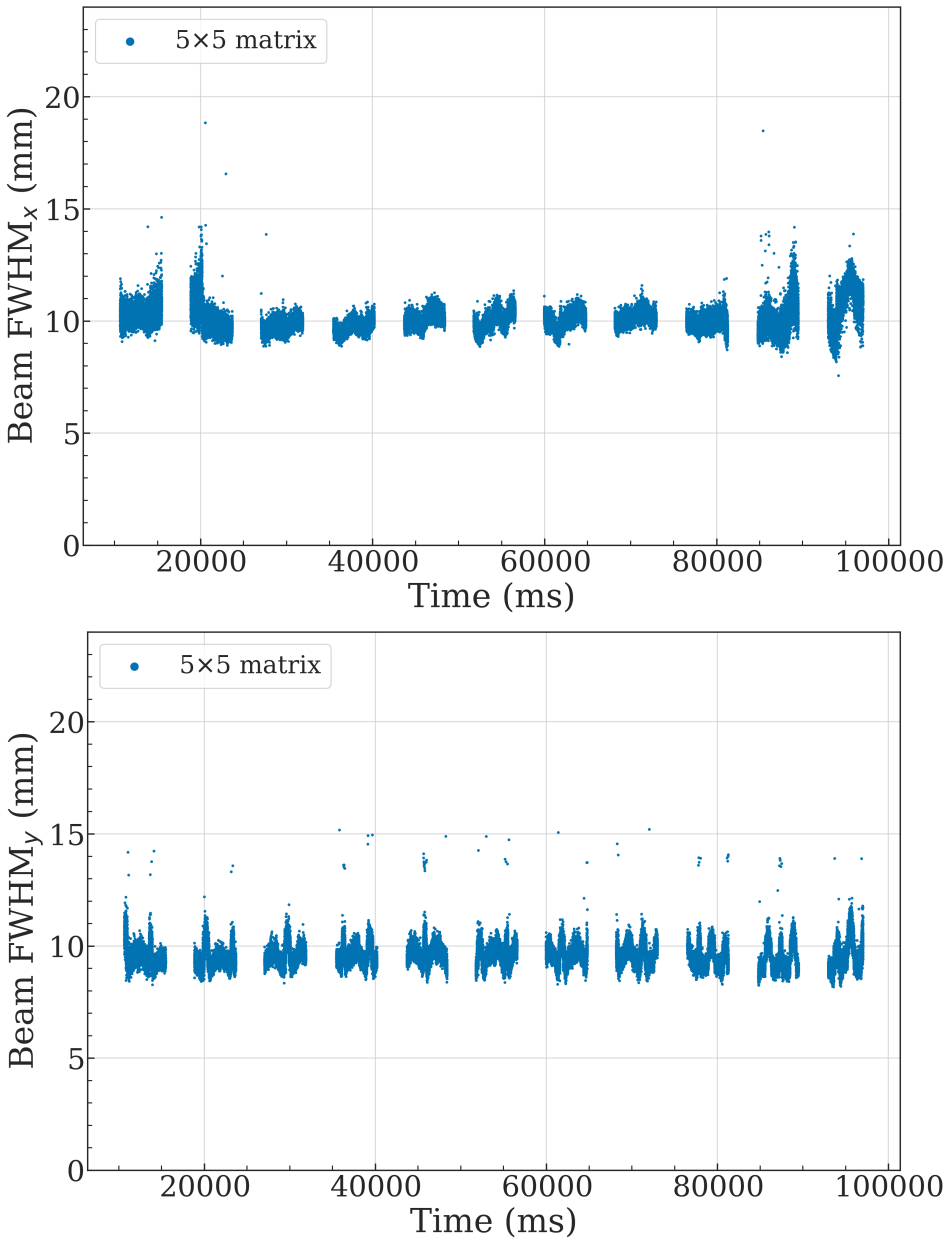


Figure D.15.: Proton beam (E255, I3) size in the X- (top) and Y- (bottom) directions versus time measured during a raster scan with a 3 mm grid step size using the beam monitor demonstrator in **adder mode without cutoff applied**.

Acronyms

ADC Analog-to-Digital Converter.

ADL ASIC and Detector Laboratory.

ASIC Application-Specific Integrated Circuit.

BAMS Beam Application and Monitoring System.

bias-DAC bias-Digital-to-Analog Converter.

CMOS Complementary Metal–Oxide–Semiconductor.

COBS Consistent Overhead Byte Stuffing.

CSA Charge-Sensitive Amplifier.

CSDA Continuous Slowing Down Approximation.

CT Computed Tomography.

DAC Digital-to-Analog Converter.

DAQ Data Acquisition.

ENC Equivalent Noise Charge.

ESTAR Electron Stopping Powers and Range Tables.

ETP Institute of Experimental Particle Physics.

FPGA Field-Programmable Gate Array.

FWHM Full Width at Half Maximum.

GECCO GEneric Configuration and COntrol.

GSI Helmholtzzentrum für Schwerionenforschung.

GUI Graphical User Interface.

HIT Heidelberg Ion Beam Therapy Center.

HV-CMOS High-voltage CMOS.

I-V Current versus Voltage.

IC Ionization Chamber.

IC Integrated Circuit.

IPE Institute for Data Processing and Electronics.

IR LED Infrared Light-Emitting Diode.

ISO-MWPC isocentric-MWPC.

KIRA Karlsruhe Infrared Array.

KIT Karlsruhe Institute of Technology.

LGAD Low Gain Avalanche Detector.

LIBC List of Ion Beam Characteristics.

LPC-FMC Low Pin-Count FPGA Mezzanine Card.

LVCMOS Low-Voltage CMOS.

LVDS Low-Voltage Differential Signaling.

MAPS Monolithic Active Pixel Sensor.

MIP Minimum Ionizing Particle.

MOSFET Metal–Oxide–Semiconductor Field Effect Transistor.

MPV Most Probable Value.

MRI Magnetic Resonance Imaging.

MWPC Multi-Wire Proportional Chamber.

nMOS n-channel MOSFET.

PCB Printed Circuit Board.

PCIe Peripheral Component Interconnect Express.

PISO Parallel In Serial Out.

pMOS p-channel MOSFET.

R&D Research and Development.

RAM Random Access Memory.

SBB Stud Bump Bonding.

ScanFF Scan Flip-Flop.

SEU Single Event Upset.

SIPO Serial In Parallel Out.

SNR Signal-to-Noise Ratio.

SOBP Spread-out Bragg peak.

spTAB single-point Tape Automated Bonding.

TDC Time-to-Digital Converter.

TOT Time-Over-Threshold.

VW Vacuum Window.

WET Water Equivalent Thickness.

ZAG Zyklotron AG.

List of Figures

2.1. Dependence of relative deposited dose on penetration depth deposited by different particles and spread out Bragg peak region generated by proton beams at different energies . . . 8
2.2. Schematic view of the magnetic raster-scanning system. . . . 8
2.3. Illustration of the Heidelberg Ion Beam Therapy Center facility . . . 9
2.4. Treatment plans for photon and proton radiotherapy. . . . 10
2.5. Possible configurations of an MRI proton therapy system with a horizontal fixed gantry beamline. . . . 11
2.6. Visual concept of the ARTEMIS project . . . 12

3.1. Simplified lattice and energy bands structures of intrinsic, p-doped and n-doped silicon material . . . 13
3.2. Simplified view of the pn-diode and its energy bands in thermal equilibrium and with applied reverse bias voltage . . . 15
3.3. Operational modes of the nMOS transistor . . . 17
3.4. Drain current versus drain to source voltage of an nMOS transistor at different values of $V_{\mathrm{GS}} - V_{\mathrm{TH}}$. . . . 18
3.5. Mass stopping power for a positive muon in copper . . . 19
3.6. Energy loss for 500 MeV pions in silicon with different thicknesses. . . . 20
3.7. Simplified view of signal generation in a silicon detector. . . . 20
3.8. General processing chain of a silicon detector signal. . . . 22
3.9. Simplified schematic of the charge-sensitive amplifier. . . . 22
3.10. Simplified schematic of the CR-RC pulse shaper. . . . 23
3.11. Simplified cross-section of HV-CMOS pixel with standard and isolated topologies. 25
3.12. Examples of silicon lattice defects induced by a traversing particle. . . . 26
3.13. Examples of defect levels locations in the electronic energy band structure and their macroscopic effects. . . . 27

4.1. The existing beam monitoring system based on MWPCs and ICs installed at HIT beam nozzle . . . 34
4.2. The 3D rendering of the proposed beam monitor based on HV-CMOS active pixel sensors . . . 36
4.3. General concept of a HitPix sensor with $N \times N$ pixels . . . 37
4.4. Simplified HitPix sensor architecture . . . 38
4.5. Stopping power of protons, carbon ions and muons in silicon material . . . 38
4.6. Block diagram of the data acquisition system . . . 39
4.7. Block diagram of the main project stages . . . 42

5.1. Layout and photograph of HitPix2 sensor . . . 43
5.2. Functional diagram and layout of HitPix2 pixel . . . 44
5.3. Simplified cross-section of a HitPix2 pixel . . . 45
5.4. Simplified schematic of HitPix2 pixel . . . 45
5.5. Simplified schematic of single HitPix2 scan flip-flop . . . 46
5.6. Simplified schematic of HitPix2 configuration/data shift register . . . 47
5.7. HitPix2 sensor under the probe card needles . . . 48
5.8. ADL-KIT chip probe station . . . 49
5.9. Flowchart of HitPix2 sensors testing procedure . . . 49

5.10. Example of a measured I-V curves for functional and malfunctional HitPix2 sensors . . . 50
5.11. Example of charge injection measurements of functional and malfunctional HitPix2 sensors. . . . 51
5.12. Pixel threshold distributions and mean μ_{thr} of these distributions of a functional sensor at different threshold voltages. . . . 52
5.13. Example of averaged number of adder counts per frame of functional and malfunctional sensors . . . 52
5.14. Example of a measured latency scan . . . 53
5.15. Simplified view of a daisy chain and a bus readout architectures . . . 55
5.16. Assembled 2×5 HitPix2 matrix. . . . 56
5.17. Pixel coordinate map of 2×5 HitPix2 matrix. . . . 56
5.18. 2×5 HitPix2 matrix and reference ISO-MWPC installed at the isocenter of HIT beamline. . . . 57
5.19. Proton beam profile measured using the 2×5 HitPix2 matrix in one 350 µs frame (**counter mode**) without and with cutoff applied. . . . 59
5.20. Measured distributions of proton beam size $FWHM_x$ and $FWHM_y$ using the ISO-MWPC, 2×5 HitPix2 matrix without and with applied cutoff for different beam focus settings. . . . 60
5.21. Measured distributions of proton beam position μ_x and μ_y using the ISO-MWPC, 2×5 HitPix2 matrix without and with applied cutoff different beam focus settings. . . . 61
5.22. Total number of hits per frame of carbon and proton beams measured using the HitPix2 sensor at different beam intensities. . . . 64
5.23. Measured and expected ⟨Hit rate⟩ distribution across HitPix2 pixels for the carbon beam with intensity I3. . . . 65
5.24. Measured versus expected pixel ⟨Hit rate⟩ of a HitPix2 sensor at different carbon beam intensities. . . . 66
5.25. Measured versus expected pixel ⟨Hit rate⟩ of a HitPix2 sensor at different proton beam intensities. . . . 67
5.26. In-pixel CSA and comparator operation. . . . 67
5.27. Measured HitPix2 pixel CSA output signals using proton beams. . . . 68
5.28. Measured HitPix2 pixel CSA output signals using carboon beams. . . . 68
5.29. ⟨Hit rate⟩ of pixels illuminated by a pulsed infrared LED. . . . 70
5.30. Microbeam nozzle and HitPix2 sensor carrier and pixels scanning procedure. . . . 71
5.31. Linearly interpolated f_{drop} map for a single HitPix2 pixel. . . . 71
5.32. Multi-carrier board PCB layout and 3D render. . . . 73
5.33. Irradiated sensors inside the cooling box at the isocenter of HIT beamline and multi-carrier board populated with HitPix2 sensors. . . . 73
5.34. I-V curves of reference and irradiated HitPix2 sensors. . . . 74
5.35. Measured ⟨Hit rate⟩ distributions of reference unirradiated sensor with resistivity of $\rho = 300\,\Omega\,\text{cm}$ and irradiated sensors with $\rho = 300\,\Omega\,\text{cm}$ using the carbon beams with different energies. . . . 75
5.36. Calculated detection efficiency of cooled irradiated HitPix2 samples. . . . 76
5.37. climatic chamber setup. . . . 77
5.38. Fraction of noisy pixels of Hitpix2 sensor before and after irradiation. . . . 78

6.1. Layout and photograph of a HitPix3 sensor . . . 81
6.2. Simplified concept of two-dimensional projection calculation . . . 82
6.3. Functional diagram and layout of HitPix3 pixel . . . 83

6.4. Simplified HitPix3 pixel cross-section . . . 84
6.5. Simplified schematic of a HitPix3 pixel electronics . . . 84
6.6. CSA feedback circuit with the feedback boost feature and simplified examples of the CSA output signals . . . 85
6.7. Simplified schematic of the HitPix3 peripheral readout. . . . 86
6.8. Simplified schematic of single HitPix3 scan flip-flop . . . 87
6.9. Single HitPix3 sensor carrier layout, 3D render, and photograph after an assembly. 88
6.10. Example of a measured I-V curve for an unirradiated HitPix3 sensor at room temperature. . . . 89
6.11. Example of a measured latency scan for HitPix3 sensor. . . . 90
6.12. Simplified geometries of the experimental setups simulated in Geant4. . . . 91
6.13. Simulated emission probability distribution of electrons from Sr-90 decay in Geant4. . . . 92
6.14. Simulated energy deposition in a HitPix3 sensor from a Sr-90 source and a mono-energetic proton beam at different energies. . . . 93
6.15. Simplified geometry of the X-ray laboratory setup. . . . 93
6.16. Examples of CSA output signals using the Sr-90 source and enabled/disabled feedback boost circuit . . . 95
6.17. CSA output signal height distributions using the Sr-90 source and enabled/disabled feedback boost circuit . . . 96
6.18. CSA output signal height distributions using the proton beam with nominal energies of 221.06 MeV u^{-1}, 156.35 MeV u^{-1}, and 94.54 MeV u^{-1}. . . . 97
6.19. Calibration curves for the charge injection circuit based on Sr-90 source and proton beam data. . . . 97
6.20. CSA output signal height distributions measured using photons emitted from different targets irradiated by the X-ray tube . . . 98
6.21. Calibration curves for the charge injection circuit based on the proton beam and X-ray setup data. . . . 100
6.22. Example of charge injection measurement of HitPix3 sensor pixel. . . . 100
6.23. Flowchart of the pixel threshold tuning algorithm. . . . 101
6.24. Measured pixel threshold distribution before and after pixel threshold tuning at different threshold voltages. . . . 102
6.25. Standard deviation of the HitPix3 pixel threshold distribution before and after pixel threshold tuning at different threshold voltages. . . . 103
6.26. Pixel noise distribution of HitPix3 before (blue) and after (orange) pixel threshold tuning at different threshold voltages. . . . 104
6.27. ⟨Hit rate⟩ of HitPix3 pixels measured using a collimated Sr-90 source centered at pixel 35. . . . 106
6.28. Output characteristics of pixel CSA configured with different gains and their calibration curves for the pixel charge injection circuit . . . 107
6.29. Measured pixel threshold distribution before and after pixel threshold tuning at different threshold voltages. . . . 108
6.30. CSA output signal height distributions using the Sr-90 source and enabled/disabled feedback boost circuit at different threshold voltages. . . . 109
6.31. Output characteristics of different pixel CSAs and their calibration curves for the charge injection circuits . . . 109
6.32. Cumulative Sr-90 source profile measured using the HitPix3 sensor in counter mode before and after pixel threshold tuning. . . . 111

6.33. Cumulative proton beam profile with a nominal energy of 221.06 MeV u^{-1} measured using the HitPix3 sensor in counter mode before and after pixel threshold tuning. . . . 111
6.34. Cumulative Sr-90 source profile measured using the HitPix3 sensor in adder mode before and after pixel threshold tuning. . . . 112
6.35. Cumulative proton beam profile with a nominal energy of 221.06 MeV u^{-1} measured using the HitPix3 sensor in adder mode before and after pixel threshold tuning. . . . 113
6.36. Cumulative Sr-90 source profile measured using the HitPix3 sensor in counter mode with a masking pattern applied. . . . 113
6.37. Total number of hits per frame of carbon and proton beams measured using the HitPix3 sensor at different beam intensities. . . . 114
6.38. Measured and expected ⟨Hit rate⟩ distribution across HitPix3 pixels for the carbon beam with intensity I7. . . . 115
6.39. Measured versus expected pixel ⟨Hit rate⟩ of a HitPix3 sensor at different carbon beam intensities. . . . 116
6.40. Measured versus expected pixel ⟨Hit rate⟩ of a HitPix3 sensor at different proton beam intensities. . . . 118
6.41. Measured versus expected pixel ⟨Hit rate⟩ of a HitPix3 sensor at different carbon beam intensities with enabled feedback boost circuit. . . . 119
6.42. Total number of hits per frame of carbon measured using the irradiated HitPix3 sensor at different beam intensities. . . . 120
6.43. Measured versus expected pixel ⟨Hit rate⟩ of an irradiated HitPix3 sensor at different carbon beam intensities. . . . 121
6.44. HitPix3 sensor under the needle probe card. . . . 122
6.45. Flowchart of the HitPix3 sensors testing procedure 123
6.46. 2 × 5 HitPix3 matrix PCB layout and its 3D render. . . . 125
6.47. Simplified block diagram of the LVDS 2 × 2 cross-point switch. . . . 126
6.48. Assembled single row of 2 × 5 HitPix3 matrix. . . . 126
6.49. Measured pixel threshold distribution for a single row of 2 × 5 HitPix3 matrix before and after pixel threshold tuning. . . . 128
6.50. Cumulative Sr-90 source profile measured using a single row of 2 × 5 HitPix3 matrix in counter mode before and after pixel threshold tuning. . . . 129
6.51. Cumulative Sr-90 source profile measured using a single row of 2 × 5 HitPix3 matrix in adder mode before and after pixel threshold tuning. . . . 129
6.52. Cumulative frames of measured Sr-90 profile with HitPix3 1 × 5 matrix in counter mode with applied mask pattern 130

7.1. 3D render of the HitPix2 5 × 5 bump-bonding PCB. . . . 135
7.2. Simplified view of the bump-bonding assembly for the 5 × 5 HitPix2 matrix. . 136
7.3. The HitPix2 pads with applied gold studs and measured gold studs heights . . 136
7.4. Four HitPix2 sensors assembled on the 5 × 5 bump-bonding PCB. . . . 137
7.5. Simplified view of the wire-bonding assembly for the 5 × 5 HitPix2 matrix. . . 137
7.6. Top and bottom 3D render views of the HitPix2 5 × 5 matrix wire-bonding PCB. 138
7.7. Assembled 5 × 5 HitPix2 matrix. . . . 139
7.8. 3D render of the assembled beam monitor demonstrator. . . . 141
7.9. 3D render of the assembled 1 × 5 strip in isometric view. . . . 142
7.10. 1 × 5 strip PCB layout (top) and 3D render of the bottom view (bottom). . . 142
7.11. Motherboard PCB layout and its 3D render. . . . 144
7.12. Simplified schematic of the LVDS repeater. . . . 145

7.13. Simplified scheme of the 5 × 5 HitPix3 matrix parallel readout. 146
7.14. Strip testing module PCB layout (top) and its 3D render (bottom). 147
7.15. Block diagram of production and quality control workflow of the beam monitor demonstrator. 148
7.16. Diagram of the 1 × 5 strip assembly flow. 150
7.17. An assembled 1 × 5 strip connected to the strip testing module. 150
7.18. Wire bonds before and after encapsulation 151
7.19. Block diagram of the testing flow of assembled 1 × 5 strip. 151
7.20. I-V tests of each 1 × 5 strip. 152
7.21. Measured pixel threshold distribution for each 1 × 5 strip before and after pixel threshold tuning. 153
7.22. Cumulative Sr-90 source profiles measured using each sensor of every 1 × 5 strip after pixel threshold tuning in counter mode. 154
7.23. Assembled HitPix3 beam monitor demonstrator connected to the FPGA board. 155
7.24. Pixel coordinate map of the HitPix3 beam monitor demonstrator. 156
7.25. Zoomed pixel coordinate map of four neighboring sensors in the matrix. 156
7.26. Coordinate assignment for adders of HitPix3 sensor without (left) and with (right) local sensor rotation. 157
7.27. Adder coordinate map of HitPix3 beam monitor demonstrator for projections in the X- and Y-directions. 158
7.28. Projection coordinate assignment for the 5 × 5 matrix in the X-direction for an ideal and a real case. 158
7.29. The HitPix3 beam monitor demonstrator installed at the isocenter of the HIT beamline. 159
7.30. Normalized intensity of four spills and the zoomed structure of the second spill for the carbon beam (E18, I10) measured using the reference IC and beam monitor demonstrator in adder mode. 161
7.31. Normalized intensity of four spills and the zoomed structure of the first spill for the carbon beam (E1, I10) measured using the reference IC and beam monitor demonstrator in adder mode. 161
7.32. Carbon beam profile (E18, I10) measured using the beam monitor demonstrator in one 500 µs frame (counter mode) and its 2D-Gaussian fit without and with beam profile cutoff applied. 163
7.33. Projections in the X- and Y-directions of carbon beam profile (E18, I10) measured using the beam monitor demonstrator in one 500 µs frame (adder mode) without and with beam profile cutoff applied. 164
7.34. Measured distributions of carbon beam size $FWHM_x$ and $FWHM_y$ using the beam monitor demonstrator in adder mode without and with beam profile cutoff applied for different beam settings. 164
7.35. Measured distributions of carbon beam position μ_x and μ_y using the projected MWPC values and the beam monitor demonstrator without and with beam profile cutoff applied for different beam settings. 166
7.36. Normalized intensity of four spills and the zoomed structure of the first spill for the proton beam (E1, I7) measured using the reference IC and beam monitor demonstrator in adder mode. 167
7.37. Proton beam profile with nominal parameters E1 and I7 measured using the beam monitor demonstrator in one 500 µs frame (counter mode) and its 2D-Gaussian fit without and with beam profile cutoff applied. 168

7.38. Proton beam (E1, I7) profile projection in the X- and Y-directions measured using the beam monitor demonstrator in one 500 µs frame (adder mode) without and with beam profile cutoff applied. . . . 169
7.39. Carbon beam (E255, I7) positions in the X- and Y-directions versus time measured during a raster scan with a 3 mm step size using the beam monitor demonstrator in adder mode without cutoff applied and the projected values from the MWPC. . . . 171
7.40. Carbon beam (E255, I7) size in the X- and Y-directions versus time measured during a raster scan with a 3 mm grid step size using the beam monitor demonstrator in adder mode without cutoff applied. . . . 172
7.41. Grid of the carbon beam (E255, I7) raster scan measured using the beam monitor demonstrator in adder mode without cutoff applied and the projected values from the MWPC. . . . 173
7.42. Grid of the proton beam (E255, I3) raster scan measured using the beam monitor demonstrator in adder mode without cutoff applied and the projected values from the MWPC. . . . 174
7.43. General and zoomed views of the HitPix3 beam monitor demonstrator installed at the isocenter of HIT MRI setup. . . . 175
7.44. Cumulative profiles of the carbon and proton beams measured using the beam monitor demonstrator inside the static magnetic field of the MRI setup. . . . 176
7.45. Simplified views of the sensor interconnection cable design based on spTAB (left) and wire-bonding (right) methods . . . 178

B.1. Cumulative 430.10 MeV u^{-1} carbon beam profile measured using the 2×5 HitPix2 matrix (**counter mode**) without cutoff applied. . . . 192
B.2. Zoomed spill structure of low-intensity carbon and proton beams measured using the HitPix2 sensor. . . . 193
B.3. Measured versus expected pixel ⟨Hit rate⟩ of a HitPix2 sensor at different proton beam intensities with energy 156.35 MeV u^{-1}. . . . 193
B.4. Measured signal of KIRA IR LED after optical-to-electrical conversion and corresponding CSA output signal of HitPix2 pixel . . . 194
B.5. Measured ⟨Hit rate⟩ distributions of reference unirradiated sensor with resistivity of $\rho = 300\,\Omega\,\text{cm}$ and irradiated sensors with $\rho = 5000\,\Omega\,\text{cm}$ using the carbon beams with different energies. . . . 194
B.6. Measured ⟨Hit rate⟩ distributions of reference unirradiated sensor with resistivity of $\rho = 300\,\Omega\,\text{cm}$ and irradiated sensors with $\rho = 20\,\Omega\,\text{cm}$ using the carbon beams with different energies. . . . 195

C.1. CSA output calibration curve based on simulated and measured MPVs of proton beam with nominal energies of 221.06 MeV, 156.35 MeV, and 94.54 MeV. . . . 198
C.2. Output characteristic of the pixel CSA, fitted with a linear function for the bias-DAC settings A and B. . . . 198
C.3. CSA output calibration curve based on tabulated data of K_α emission lines for different target materials irradiated by the X-ray tube. . . . 199
C.4. Measured pixel threshold distribution for the thinned and unthinned HitPix2 sensors at different threshold voltage values. . . . 199
C.5. Measured ⟨Hit rate⟩ distribution for the thinned and unthinned HitPix2 sensors at different threshold voltage values using the Sr-90 source. . . . 200
C.6. Measured pixel threshold distribution before and after pixel threshold tuning at different threshold voltage values. . . . 200

C.7. Standard deviation of the HitPix3 pixel threshold distribution before (blue) and after (orange) pixel threshold tuning at different threshold voltage values. 201
C.8. Pixel noise distribution of HitPix3 before (blue) and after (orange) pixel threshold tuning at different threshold voltage values. 201
C.9. CSA output signal height distributions measured using photons emitted from different targets irradiated by the X-ray tube for the sensor configured with the high CSA gain. 202
C.10. Average pixel hit rate measured using the HitPix3 sensor in counter mode without the Sr-90 source at threshold voltage of 154 DAC units and 160 DAC units before pixel threshold tuning. 203
C.11. Cumulative carbon beam profile with a nominal energy of 430.10 MeV measured using the HitPix3 sensor in counter mode before and after pixel threshold tuning. 203
C.12. Measured versus expected pixel ⟨Hit rate⟩ of a HitPix3 sensor at different proton beam intensities with energy 156.35 MeV u^{-1}. 204
C.13. Measured HitPix3 pixel CSA output of 430.10 MeV u^{-1} carbon beams with disabled and enabled feedback boost circuit. 204
C.14. Pixel CSA output of the irradiated HitPix3 sensor in response to 430.10 MeV u^{-1} carbon beams with intensity I3. 205
C.15. Example of a measured latency scan for a single row of 2×5 HitPix3 matrix. 205
C.16. Pixel coordinate map of a single row of 2×5 HitPix3 matrix. 205

D.1. Layout of the 5×5 HitPix2 bump-bonding PCB 207
D.2. Layout of the 5×5 HitPix2 wire-bonding PCB 208
D.3. Measured latency scan for each 1×5 strip. 208
D.4. Cumulative Sr-90 source profile projection in the X- and Y-directions measured using each sensor of every 1×5 strip after pixel threshold tuning in adder mode. 209
D.5. Local rotation angle distribution of the HitPix3 sensors in the beam monitor demonstrator. 209
D.6. Measured distributions of carbon beam size $FWHM_x$ and $FWHM_y$ using the existing ISO-MWPC detector for different beam settings. 210
D.7. Measured distributions of carbon beam size $FWHM_x$ and $FWHM_y$ using the beam monitor demonstrator in counter mode without and with cutoff applied for different beam settings. 211
D.8. Measured distributions of carbon beam position μ_x and μ_y using the projected MWPC values and the beam monitor demonstrator in counter mode without and with cutoff applied for different beam settings. 211
D.9. Normalized intensity of four spills for the proton beam (E18, I7) measured using the reference IC and beam monitor demonstrator in adder mode. 212
D.10. Measured distributions of proton beam size $FWHM_x$ and $FWHM_y$ using the beam monitor demonstrator in adder mode without and with cutoff applied for different beam settings. 213
D.11. Measured distributions of proton beam position μ_x and μ_y using the projected MWPC values and the beam monitor demonstrator without and with cutoff applied for different beam settings. 213
D.12. Measured distributions of proton beam size $FWHM_x$ and $FWHM_y$ using the beam monitor demonstrator in counter mode without and with cutoff applied for different beam settings. 213
D.13. Measured distributions of proton beam position μ_x and μ_y using the projected MWPC values and the beam monitor demonstrator in counter mode without and with cutoff applied for different beam settings. 214

D.14. Proton beam (E255, I3) position in the X- and Y-directions versus time measured during a raster scan with a 3 mm grid size using the beam monitor demonstrator in adder mode without cutoff applied and the projected values from the MWPC. 215
D.15. Proton beam (E255, I3) size in the X- and Y-directions versus time measured during a raster scan with a 3 mm grid size using the beam monitor demonstrator in adder mode without cutoff applied and the projected values from the MWPC. 216

List of Tables

2.1. Available range of nominal ion beam parameters used at HIT. 10

5.1. Results of HitPix2 characterization campaign at the probe station. 54
5.2. Nominal beam parameters in the measurements with 2×5 HitPix2 matrix. . . 59
5.3. The $\langle$FWHM$\rangle$ of the measured proton beam size in the X-direction using the ISO-MWPC and 2×5 HitPix2 matrix. 60
5.4. The $\langle$FWHM$\rangle$ of the measured proton beam size in the Y-direction using the ISO-MWPC and 2×5 HitPix2 matrix. 60
5.5. The $\langle\mu\rangle$ of the measured proton beam position in the X-direction using the ISO-MWPC and 2×5 HitPix2 matrix. 61
5.6. The $\langle\mu\rangle$ of the measured proton beam position in the Y-direction using the ISO-MWPC and 2×5 HitPix2 matrix. 62
5.7. Nominal beam intensity settings for proton and carbon beams at HIT. 63
5.8. Fit parameters for the original and modified Takács' formulas for the HitPix2 sensor in $430.10\,\mathrm{MeV\,u^{-1}}$ carbon beam measurements. 65
5.9. Fit parameters for the original and modified Takács' formulas for the HitPix2 sensor in $221.06\,\mathrm{MeV\,u^{-1}}$ proton beam measurements. 66
5.10. The f_{drop} for different HitPix versions in 3 MeV proton microbeam. 72
5.11. The lowest achieved temperature for the tested unirradiated and irradiated HitPix2 sensors during the beam test at HIT. 74

6.1. Simulated MPVs of the deposited charge in HitPix3 depletion region using the Sr-90 source and mono-energetic proton beam. 92
6.2. The photon energies for K_α transition in the target material used in the X-ray setup. 94
6.3. Measured MPVs (in mV) of the CSA output signal height distribution of HitPix3 using a Sr-90 source and proton beam. 96
6.4. Measured MPVs (in mV) of the CSA output signal height distribution of HitPix3 using photons emitted from different targets irradiated by the X-ray tube. . . 99
6.5. Measured MPVs of the collected charge in HitPix3 using the Sr-90 source and proton beam based on the X-ray calibration. 99
6.6. Measured MPV and calibration factor of HitPix3 pixel 35 using the Sr-90 source at different CSA gain. 106
6.7. Calibration curve parameters for HitPix3 pixel 35 injection circuit at different CSA gain. 108
6.8. Fit parameters for the original and modified Takács' formulas for the HitPix3 sensor in $430.10\,\mathrm{MeV\,u^{-1}}$ carbon beam measurements. 115
6.9. Fit parameters for the original and modified Takács' formulas for the HitPix3 sensor in $221.06\,\mathrm{MeV\,u^{-1}}$ proton beam measurements. 117
6.10. Fit parameters for the original and modified Takács' formulas for the irradiated HitPix3 sensor in $430.10\,\mathrm{MeV\,u^{-1}}$ carbon beam measurements. 120
6.11. Results of HitPix3 characterization campaign. 123
6.12. The stack-up of the 2×5 HitPix3 matrix PCB. 125

7.1. Measured outer dimensions of the HitPix2 sensors selected for the 5×5 matrix assembly. 134

7.2. Measured outer dimensions of the HitPix3 sensors selected for two 5×5 matrix assemblies. 141
7.3. Measured difference between the actual and designed sensor positions within the 1×5 strip. 154
7.4. Measured distances in the X- and Y-directions between edge pixels of neighboring sensors. 155
7.5. Nominal beam parameters for the measurements with the HitPix3 beam monitor demonstrator. 160
7.6. The $\langle$FWHM$\rangle$ of the measured carbon beam size in the X- and Y-directions using the beam monitor demonstrator in adder mode with cutoff applied. . . . 165
7.7. The $\langle$FWHM$\rangle$ of the measured carbon beam size in the X- and Y-directions using the ISO-MWPC. 165
7.8. The $\langle\mu\rangle$ of the measured carbon beam position in the X- and Y-directions using the beam monitor demonstrator in adder mode with cutoff applied. 167
7.9. The $\langle$FWHM$\rangle$ of the measured proton beam size in the X- and Y-directions using the beam monitor demonstrator in adder mode with cutoff applied. . . . 168
7.10. The $\langle\mu\rangle$ of the measured proton beam position in the X- and Y-directions using the beam monitor demonstrator in adder mode with cutoff applied. 169
7.11. The raster scan parameters extracted from measurements with the beam monitor demonstrator in adder mode without cutoff applied. 175

A.1. Input and output voltage ranges of LVCMOS18 and LVDS logic standards. . . 189

B.1. The bias-DAC block shift register bits assignment of the HitPix2 sensor. . . . 191

C.1. The bias-DAC block shift register bits assignment of the HitPix3 sensor. . . . 197
C.2. The bias-DAC settings used in measurements. 198
C.3. Measured MPV and calibration factor of HitPix3 pixels using the Sr-90 source. 202
C.4. Calibration curve parameters for HitPix3 pixel injection circuits. 202

D.1. The $\langle$FWHM$\rangle$ of the measured carbon beam size in the X- and Y-directions using the beam monitor demonstrator in adder mode without cutoff applied. . 210
D.2. The $\langle$FWHM$\rangle$ of the measured carbon beam size in the X- and Y-directions using the beam monitor demonstrator in counter mode without cutoff applied. 211
D.3. The $\langle\mu\rangle$ of the measured carbon beam position in the X- and Y-directions using the beam monitor demonstrator in counter mode without cutoff applied 212
D.4. The $\langle$FWHM$\rangle$ of the measured proton beam size in the X- and Y-directions using the beam monitor demonstrator in adder mode without cutoff applied. . 212
D.5. The $\langle$FWHM$\rangle$ of the measured proton beam size in the X- and Y-directions using the beam monitor demonstrator in counter mode without cutoff applied. 214
D.6. The $\langle\mu\rangle$ of the measured proton beam position in the X- and Y-directions using the beam monitor demonstrator in counter mode without cutoff applied. . . . 214

Bibliography

[Adv] Advanced Micro Devices, Inc. (AMD). *Artix-7 FPGA Data Sheet: DC and AC Switching Characteristics*. Advanced Micro Devices, Inc. (AMD). URL: http://docs.amd.com/v/u/en-US/ds181_Artix_7_Data_Sheet (visited on 03/27/2025) (cited on p. 189).

[Ago+03] S. Agostinelli et al. *Geant4 – a simulation toolkit*. In: Nuclear Instruments and Methods in Physics Research Section A: Accelerators, Spectrometers, Detectors and Associated Equipment 506.3 (July 2003), pp. 250–303. DOI: 10.1016/S0168-9002(03)01368-8 (cited on p. 90).

[Akb+23] A. F. Akbar et al. *Acoustic Noise Levels in High-field Magnetic Resonance Imaging Scanners*. In: OTO Open 7.3 (2023), e79. ISSN: 2473-974X. DOI: 10.1002/oto2.79 (cited on p. 12).

[Bar25] B. Bartels. *Beam position monitoring with a 5x5 HitPix3 matrix for ion-beam therapy*. ETP-KA/2025-08. Master's thesis. Karlsruher Institut für Technologie (KIT), 2025 (cited on p. 40).

[Ben+18] M. Benoit et al. *Testbeam results of irradiated AMS H18 HV-CMOS pixel sensor prototypes*. In: Journal of Instrumentation 13.02 (2018), P02011–P02011. ISSN: 1748-0221. DOI: 10.1088/1748-0221/13/02/p02011 (cited on p. 35).

[Ber+17] M. Berger et al. *Stopping-Power & Range Tables for Electrons, Protons, and Helium Ions*. NIST Standard Reference Database 124. National Institute of Standards and Technology (NIST), 2017. DOI: 10.18434/T4NC7P (cited on p. 104).

[BLP18] R. Blanco, R. Leys, and I. Perić. *Integrated readout electronics for Belle II pixel detector*. In: Journal of Instrumentation 13.03 (2018), p. C03001. ISSN: 1748-0221. DOI: 10.1088/1748-0221/13/03/C03001 (cited on p. 48).

[BM20] S. Basu and E. Mccutchan. *Nuclear Data Sheets for A = 90*. In: Nuclear Data Sheets 165 (2020), pp. 1–329. ISSN: 0090-3752. DOI: https://doi.org/10.1016/j.nds.2020.04.001 (cited on p. 92).

[Bra20] J. Braach. *Functional Tests of 2S Detector Modules for the CMS Phase 2 Outer Tracker Upgrade including the Development of an IR LED Array*. ETP-KA/2020-29. Master's thesis. Karlsruher Institut für Technologie (KIT), 2020. URL: https://publish.etp.kit.edu/record/22024 (cited on p. 69).

[Cas+16] M. Caselle et al. *Low-cost bump-bonding processes for high energy physics pixel detectors*. In: Journal of Instrumentation 11.01 (2016), p. C01050. ISSN: 1748-0221. DOI: 10.1088/1748-0221/11/01/C01050 (cited on p. 135).

[Des+05] R. Deslatte et al. *X-Ray Transition Energies Database*. NIST Standard Reference Database 128. National Institute of Standards and Technology (NIST), 2005. DOI: 10.18434/T4859Z (cited on p. 94).

[Die+23] A. Dierlamm et al. *A Beam Monitor for Ion Beam Therapy Based on HV-CMOS Pixel Detectors*. In: Instruments 7.1 (2023), p. 9. ISSN: 2410-390X. DOI: 10.3390/instruments7010009 (cited on pp. 33–36, 38–40, 42, 62, 64, 65, 78, 184).

[Die+24] K. A. Dietrich et al. *An essentially radiation-transparent body coil integrated with a patient rotation system for MR-guided particle therapy*. In: Medical Physics 51.6 (2024), pp. 4028–4043. ISSN: 2473-4209. DOI: 10.1002/mp.17065 (cited on p. 12).

[Dig20] Digilent, Inc. *Nexys Video™ FPGA Board Reference Manual*. Rev. A. Digilent, Inc. 2020. URL: https://digilent.com/reference/programmable-logic/nexys-video/reference-manual (visited on 04/03/2025) (cited on pp. 39, 140).

[DP16] M. Durante and H. Paganetti. *Nuclear physics in particle therapy: a review*. In: Reports on Progress in Physics 79.9 (2016), p. 096702. ISSN: 0034-4885. DOI: 10.1088/0034-4885/79/9/096702 (cited on pp. 7, 8).

[Ehr21] F. M. Ehrler. *Characterization of monolithic HV-CMOS pixel sensors for particle physics experiments*. PhD thesis. Karlsruher Institut für Technologie (KIT), 2021. DOI: 10.5445/IR/1000133748 (cited on pp. 17, 39, 50, 98, 145).

[Eic+03] H. Eickhoff et al. *HICAT - the German hospital-based light ion cancer therapy project*. In: Proceedings of the 2003 Particle Accelerator Conference 1 (2003). ISSN: 1063-3928, pp. 694–698. DOI: 10.1109/PAC.2003.1289012 (cited on p. 35).

[Eli21] U. Elicabuk. *Development of an Iterative Irradiation Setup and Online Beam Monitor for Silicon Sensor Irradiation Studies*. ETP-KA/2021-16. Master's thesis. Karlsruher Institut für Technologie (KIT), 2021. URL: https://publish.etp.kit.edu/record/22080 (cited on p. 57).

[Gea22] Geant4 Collaboration. *Radioactive Decay in Physics Reference Manual, Geant4 Release 11.1*. 2022. URL: https://geant4-userdoc.web.cern.ch/UsersGuides/PhysicsReferenceManual/BackupVersions/V11.1b/html/hadronic/Radioactive/radDecay.html (visited on 06/27/2025) (cited on p. 104).

[Gei+] H. Geissel et al. *ATIMA*. Version: 1.4. GSI Helmholtzzentrum für Schwerionenforschung. URL: https://web-docs.gsi.de/~weick/atima/ (visited on 03/21/2025) (cited on p. 38).

[Ger] German Cancer Research Center (DKFZ) and Heidelberg University Hospital (UKHD). *ARTEMIS - Adaptive Radiotherapy with MR-guided Ion Beams*. URL: https://www.dkfz.de/en/forschung/netzwerk/nationale-kooperationen/heidelberg-institute-for-radiation-oncology-hiro/artemis-adaptive-radiotherapy-with-mr-guided-ion-beams (visited on 02/21/2025) (cited on p. 12).

[GHT01] F. Guarino, C. Hauviller, and M. Tavlet. *Compilation of radiation damage test data*. CERN Yellow Reports: Monographs. Geneva: CERN, 2001. DOI: 10.5170/CERN-2001-006 (cited on p. 88).

[GMS01] D. E. Groom, N. V. Mokhov, and S. I. Striganov. *MUON STOPPING POWER AND RANGE TABLES 10 MeV–100 TeV*. In: Atomic Data and Nuclear Data Tables 78.2 (2001), pp. 183–356. ISSN: 0092-640X. DOI: https://doi.org/10.1006/adnd.2001.0861 (cited on p. 38).

[Gon23] A. M. González. *TCAD Simulations and Characterization of High-Voltage Monolithic Active Pixel Sensors*. PhD thesis. Heidelberg University, 2023. DOI: 10.11588/heidok.00033792 (cited on p. 99).

[GRG15] H. Giap, D. Roda, and F. Giap. *Can proton beam therapy be clinically relevant for the management of lung cancer?* In: Translational Cancer Research 4.4 (2015). ISSN: 2219-6803, 2218-676X. DOI: 10.3978/j.issn.2218-676X.2015.08.15 (cited on p. 10).

[Gut+12] M. Guthoff et al. *Geant4 simulation of a filtered X-ray source for radiation damage studies*. In: Nuclear Instruments and Methods in Physics Research Section A: Accelerators, Spectrometers, Detectors and Associated Equipment 675 (2012), pp. 118–122. ISSN: 0168-9002. DOI: 10.1016/j.nima.2012.01.029 (cited on p. 93).

[GW18] M. Garcia-Sciveres and N. Wermes. *A review of advances in pixel detectors for experiments with high rate and radiation*. In: Reports on Progress in Physics 81.6 (2018). Publisher: IOP Publishing, p. 066101. ISSN: 0034-4885. DOI: 10.1088/1361-6633/aab064 (cited on pp. 24, 35).

[Hab+93] T. Haberer et al. *Magnetic scanning system for heavy ion therapy*. In: Nuclear Inst. and Methods in Physics Research, A 330.1-2 (1993), pp. 296–305. DOI: 10.1016/0168-9002(93)91335-K (cited on p. 8).

[Hah23] L. Hahn. *Characterization of HitPix2 Sensors for an Ion Beam Therapy Monitoring System*. ETP-KA/2023-18. Bachelor's thesis. Karlsruher Institut für Technologie (KIT), 2023. URL: https://publish.etp.kit.edu/record/22211 (cited on pp. 48, 54, 134).

[Har24] F. Hartmann. *Evolution of Silicon Sensor Technology in Particle Physics*. 3rd ed. Springer, Dec. 7, 2024. ISBN: 978-3-031-59720-6. DOI: 10.1007/978-3-031-59720-6 (cited on pp. 17, 19, 24, 26–28, 99).

[Hil47] R. Hilsch. *The Use of the Expansion of Gases in a Centrifugal Field as Cooling Process*. In: Review of Scientific Instruments 18.2 (1947), pp. 108–113. ISSN: 0034-6748. DOI: 10.1063/1.1740893 (cited on p. 72).

[Hun24] Huntsman International LLC. *Araldite 2011*. Product information for Araldite 2011 adhesive. Huntsman International LLC. 2024. URL: https://products.huntsman.com/products/araldite-2011-a-b (visited on 06/16/2025) (cited on pp. 88, 150).

[INT05] INTERNATIONAL ATOMIC ENERGY AGENCY. *Radiation Oncology Physics*. Non-serial Publications. Vienna: IAEA, 2005. ISBN: 92-0-107304-6. URL: https://www.iaea.org/publications/7086/radiation-oncology-physics (cited on p. 7).

[Jak+16] M. Jakšić et al. *In-air ion beam analysis with high spatial resolution proton microbeam*. In: Nuclear Instruments and Methods in Physics Research Section B: Beam Interactions with Materials and Atoms 371.03 (2016), pp. 185–188. DOI: 10.1016/j.nimb.2015.11.012 (cited on p. 70).

[JKK22] O. Jäkel, G. Kraft, and C. P. Karger. *The history of ion beam therapy in Germany*. In: Zeitschrift für Medizinische Physik 32.1 (2022), pp. 6–22. ISSN: 0939-3889. DOI: 10.1016/j.zemedi.2021.11.003 (cited on pp. 8–10).

[Kei10] Keithley Instruments, Inc. *2410 and 2410-C SourceMeter Specifications Rev. E*. Mar. 22, 2010. URL: https://www.tek.com/en/documents/specification/models-2410-and-2410-c-sourcemeter-specifications (visited on 06/16/2025) (cited on p. 89).

[KOW09] C. Kleffner, D. Ondreka, and U. Weinrich. *The Heidelberg Ion Therapy (HIT) Accelerator Coming into Operation*. In: AIP Conference Proceedings 1099.1 (2009), pp. 426–428. ISSN: 0094-243X. DOI: 10.1063/1.3120065 (cited on pp. 9, 62).

[Krä+00] M. Krämer et al. *Treatment planning for heavy-ion radiotherapy: Physical beam model and dose optimization*. In: Physics in Medicine and Biology 45.11 (2000), pp. 3299–3317. DOI: 10.1088/0031-9155/45/11/313 (cited on pp. 8, 9).

[LR16] C. Leroy and P.-G. Rancoita. *Principles of Radiation Interaction in Matter and Detection*. 4th. WORLD SCIENTIFIC, 2016. DOI: 10.1142/9167 (cited on p. 17).

[LSY23] S. A. Lane, J. M. Slater, and G. Y. Yang. *Image-Guided Proton Therapy: A Comprehensive Review*. In: Cancers 15.9 (2023), p. 2555. ISSN: 2072-6694. DOI: 10.3390/cancers15092555 (cited on p. 10).

[Lut07] G. Lutz. *Semiconductor Radiation Detectors*. ISBN: 978-3-540-71678-5 (Print) 978-3-540-71679-2 (Online). Springer, 2007. DOI: 10.1007/978-3-540-71679-2 (cited on pp. 17, 22, 26, 27).

[Mag16] M. Mager. *ALPIDE, the Monolithic Active Pixel Sensor for the ALICE ITS upgrade*. In: Nuclear Instruments and Methods in Physics Research Section A: Accelerators, Spectrometers, Detectors and Associated Equipment 824 (2016), pp. 434–438. ISSN: 0168-9002. DOI: 10.1016/j.nima.2015.09.057 (cited on p. 35).

[Mar24] P. Marchesi. *Simulation of HV-CMOS detectors for beam monitoring in particle therapy*. ETP-KA/2024-03. Master's thesis. Karlsruher Institut für Technologie (KIT), 2024. URL: https://publish.etp.kit.edu/record/22239 (cited on pp. 39, 40, 105, 134).

[Mol99] M. Moll. *Radiation damage in silicon particle detectors: Microscopic defects and macroscopic properties*. PhD thesis. University of Hamburg, 1999. URL: https://www-library.desy.de/cgi-bin/showprep.pl?desy-thesis99-040 (cited on p. 26).

[Mor24] O. Moritz. *Evaluation of the radiation hardness of HitPix3 MAPS*. ETP-KA/2024-03. Bachelor's thesis. Karlsruher Institut für Technologie (KIT), 2024. URL: https://publish.etp.kit.edu/record/22231 (cited on pp. 89, 121, 127).

[Mül91] J. W. Müller. *Generalized dead times*. In: Nuclear Instruments and Methods in Physics Research Section A: Accelerators, Spectrometers, Detectors and Associated Equipment 301.3 (1991), pp. 543–551. DOI: 10.1016/0168-9002(91)90021-H (cited on p. 64).

[Nat25a] National Cancer Institute. *Chemotherapy - NCI Dictionary of Cancer Terms*. 2025. URL: https://www.cancer.gov/publications/dictionaries/cancer-terms/def/chemotherapy (visited on 02/18/2025) (cited on p. 7).

[Nat25b] National Cancer Institute. *Radiotherapy - NCI Dictionary of Cancer Terms*. 2025. URL: https://www.cancer.gov/publications/dictionaries/cancer-terms/def/radiotherapy (visited on 02/18/2025) (cited on p. 7).

[Nat25c] National Cancer Institute. *Resection - NCI Dictionary of Cancer Terms*. 2025. URL: https://www.cancer.gov/publications/dictionaries/cancer-terms/def/resection (visited on 02/18/2025) (cited on p. 7).

[Nav+24] S. Navas et al. *Review of Particle Physics*. In: Phys. Rev. D 110 (3 2024), p. 030001. DOI: 10.1103/PhysRevD.110.030001 (cited on pp. 7, 17–20).

[Nov+24] D. Novel et al. *Tape Automated Bonding of an ALPIDE Chip with Flexible PCBs*. In: *2024 IEEE 10th Electronics System-Integration Technology Conference (ESTC)*. Sept. 2024, pp. 1–5. DOI: 10.1109/ESTC60143.2024.10712095 (cited on p. 177).

[Par+10] K. Parodi et al. *The influence of lateral beam profile modifications in scanned proton and carbon ion therapy: a Monte Carlo study*. In: Physics in Medicine & Biology 55.17 (2010), p. 5169. ISSN: 0031-9155. DOI: 10.1088/0031-9155/55/17/018 (cited on pp. 35, 57, 165).

[Par+12] K. Parodi et al. *Monte Carlo simulations to support start-up and treatment planning of scanned proton and carbon ion therapy at a synchrotron-based facility.* In: Physics in Medicine & Biology 57.12 (2012). Publisher: IOP Publishing, p. 3759. ISSN: 0031-9155. DOI: 10.1088/0031-9155/57/12/3759 (cited on pp. 34, 62, 91, 104, 105, 165).

[Par25a] Particle Therapy Co-Operative Group (PTCOG). *Particle therapy facilities in a planning stage.* 2025. URL: https://www.ptcog.site/index.php/facilities-in-planning-stage (visited on 02/18/2025) (cited on p. 7).

[Par25b] Particle Therapy Co-Operative Group (PTCOG). *Particle therapy facilities in clinical operation.* 2025. URL: https://www.ptcog.site/index.php/facilities-in-operation-public (visited on 02/18/2025) (cited on p. 7).

[Par25c] Particle Therapy Co-Operative Group (PTCOG). *Particle therapy facilities under construction.* 2025. URL: https://www.ptcog.site/index.php/facilities-under-construction (visited on 02/18/2025) (cited on p. 7).

[Pau+24] K. Paul et al. *Online MR-guided proton and ion beam radiotherapy: investigation of image quality.* In: Physics in Medicine & Biology 69.18 (2024), p. 185013. ISSN: 0031-9155. DOI: 10.1088/1361-6560/ad7453 (cited on p. 175).

[Per+21] I. Perić et al. *High-Voltage CMOS Active Pixel Sensor.* In: IEEE Journal of Solid-State Circuits 56.8 (2021), pp. 2488–2502. DOI: 10.1109/JSSC.2021.3061760 (cited on pp. 25, 46, 76, 99, 132).

[Per07] I. Perić. *A novel monolithic pixelated particle detector implemented in high-voltage CMOS technology.* In: Nuclear Instruments and Methods in Physics Research Section A: Accelerators, Spectrometers, Detectors and Associated Equipment 582.3 (2007), pp. 876–885. ISSN: 0168-9002. DOI: 10.1016/j.nima.2007.07.115 (cited on p. 25).

[Pha+22] T. T. Pham et al. *Magnetic resonance imaging (MRI) guided proton therapy: A review of the clinical challenges, potential benefits and pathway to implementation.* In: Radiotherapy and Oncology 170 (2022), pp. 37–47. ISSN: 0167-8140. DOI: 10.1016/j.radonc.2022.02.031 (cited on pp. 10, 11).

[Pit22] M. Pittermann. *Evaluation of HV-CMOS Sensors in a Beam Monitoring System for Ion Therapy.* ETP-KA/2022-11. Master's thesis. Karlsruher Institut für Technologie (KIT), 2022. URL: https://publish.etp.kit.edu/record/22127 (cited on pp. 40, 42, 46, 47, 53, 55, 56, 62, 65, 78, 140, 146, 184, 191).

[Rin+13] I. Rinaldi et al. *Experimental characterization of a prototype detector system for carbon ion radiography and tomography.* In: Physics in Medicine & Biology 58.3 (2013), p. 413. ISSN: 0031-9155. DOI: 10.1088/0031-9155/58/3/413 (cited on p. 57).

[Rin11] I. Rinaldi. *Investigation of novel imaging methods using therapeutic ion beams.* PhD thesis. Heidelberg University, 2011. DOI: 10.11588/heidok.00012605 (cited on p. 35).

[Ros+06] L. Rossi et al. *Pixel Detectors.* ISBN: 978-3-540-28333-1. Springer-Verlag, 2006. DOI: 10.1007/3-540-28333-1 (cited on p. 35).

[Sac+20] R. Sacchi et al. *Test of innovative silicon detectors for the monitoring of a therapeutic proton beam.* In: Journal of Physics: Conference Series 1662.1 (2020), p. 012002. DOI: 10.1088/1742-6596/1662/1/012002 (cited on p. 35).

[Sam19] Samtec Incorporated. *JSOM Micro Jack Screw Precision Board Stacking Standoff Product Specification (Rev. A)*. Accessed on 2025-07-21. 2019. URL: https://suddendocs.samtec.com/productspecs/jsom.pdf (cited on p. 143).

[Sam25] Samtec Incorporated. *Razor Beam™ High Speed Hermaphroditic Terminal/Socket Strip Product Specification (Rev. G)*. LSS 0.635mm. Accessed on 2025-07-21. 2025. URL: https://suddendocs.samtec.com/productspecs/lss.pdf (cited on p. 142).

[Sch+15] C. Schoemers et al. *The intensity feedback system at Heidelberg Ion-Beam Therapy Centre*. In: Nuclear Instruments and Methods in Physics Research Section A: Accelerators, Spectrometers, Detectors and Associated Equipment 795 (2015), pp. 92–99. ISSN: 0168-9002. DOI: 10.1016/j.nima.2015.05.054 (cited on pp. 34, 35, 57, 62, 63, 160).

[Sch21] R. Schimassek. *Development and Characterisation of Integrated Sensors for Particle Physics*. PhD thesis. Karlsruher Institut für Technologie (KIT), 2021. DOI: 10.5445/IR/1000141412 (cited on p. 39).

[Sei19] S. Seidel. *Silicon strip and pixel detectors for particle physics experiments*. In: Physics Reports 828 (2019), pp. 1–34. ISSN: 0370-1573. DOI: 10.1016/j.physrep.2019.09.003 (cited on p. 35).

[SG64] A. Savitzky and M. J. E. Golay. *Smoothing and Differentiation of Data by Simplified Least Squares Procedures*. In: Analytical Chemistry 36.8 (1964), pp. 1627–1639. ISSN: 0003-2700. DOI: 10.1021/ac60214a047 (cited on p. 94).

[Sim+20] M. D. Simoni et al. *FRED: a fast Monte Carlo code on GPU for quality control in Particle Therapy*. In: Journal of Physics: Conference Series 1548.1 (2020), p. 012020. ISSN: 1742-6596. DOI: 10.1088/1742-6596/1548/1/012020 (cited on p. 8).

[Spa+18] S. Spannagel et al. *Allpix2: A modular simulation framework for silicon detectors*. In: Nuclear Instruments and Methods in Physics Research Section A: Accelerators, Spectrometers, Detectors and Associated Equipment 901 (2018), pp. 164–172. ISSN: 0168-9002. DOI: 10.1016/j.nima.2018.06.020 (cited on p. 105).

[Spi05] H. Spieler. *Semiconductor Detector Systems*. OXFORD UNIV PR, Aug. 25, 2005. 489 pp. ISBN: 9780198527848. URL: https://doi.org/10.1093/acprof:oso/9780198527848.001.0001 (cited on pp. 13–17, 21–23, 28, 73, 91).

[Tes+16] T. Tessonnier et al. *Phase Space Generation for Proton and Carbon Ion Beams for External Users' Applications at the Heidelberg Ion Therapy Center*. In: Frontiers in Oncology 5 (2016). ISSN: 2234-943X. DOI: 10.3389/fonc.2015.00297 (cited on p. 35).

[Tex13a] Texas Instruments Incorporated. *DS25BR150 3.125 Gbps LVDS Buffer Datasheet (Rev. E)*. Accessed on 2025-07-08. 2013. URL: https://www.ti.com/lit/ds/symlink/ds25br150.pdf (cited on pp. 126, 145).

[Tex13b] Texas Instruments Incorporated. *DS25CP104A / DS25CP114 3.125 Gbps 4x4 LVDS Crosspoint Switch with Transmit Pre-Emphasis and Receive Equalization Datasheet (Rev. C)*. Accessed on 2025-07-21. 2013. URL: https://www.ti.com/lit/ds/symlink/ds25cp104a.pdf (cited on p. 145).

[Tex13c] Texas Instruments Incorporated. *DS25CP152 3.125 Gbps LVDS 2x2 Crosspoint Switch Datasheet (Rev. D)*. Accessed on 2025-07-08. 2013. URL: https://www.ti.com/lit/ds/symlink/ds25cp152.pdf (cited on pp. 126, 145).

[Tex18] Texas Instruments Incorporated. *High-Speed Layout Guidelines for Reducing EMI for LVDS SerDes Designs*. Application Report SNLA302. Accessed on 2025-06-16. Texas Instruments Incorporated, 2018. URL: https://www.ti.com/lit/an/snla302/snla302.pdf (cited on p. 89).

[The17] The Dow Chemical Company. *SYLGARD™ 186 Silicone Elastomer*. Accessed on 2025-07-23. 2017. URL: https://www.dow.com/en-us/document-viewer.html?docPath=/content/dam/dcc/documents/11/11-1253-sylgard-186-silicone-elastomer.pdf (cited on p. 151).

[Top+24] B. Topko et al. *Monolithic HV-CMOS sensors for a beam monitoring system of therapeutic ion beams*. In: Journal of Instrumentation 19.03 (2024), p. C03043. ISSN: 1748-0221. DOI: 10.1088/1748-0221/19/03/C03043 (cited on pp. 55, 70–76).

[Uni25a] Universitätsklinikum Heidelberg. *Heidelberg Ion Beam Therapy Center facility*. 2025. URL: https://www.klinikum.uni-heidelberg.de/interdisziplinaere-zentren/heidelberger-ionenstrahl-therapiezentrum-hit/leistungsspektrum (visited on 02/17/2025) (cited on p. 9).

[Uni25b] Universitätsklinikum Heidelberg. *Heidelberg Ion Beam Therapy Center logo*. 2025. URL: https://www.klinikum.uni-heidelberg.de/interdisziplinaere-zentren/heidelberger-ionenstrahl-therapiezentrum-hit (visited on 07/05/2025) (cited on p. 130).

[Uni25c] Universitätsklinikum Heidelberg. *Proton Beam Therapy and Carbon Ion Beam Therapy*. 2025. URL: https://www.heidelberg-university-hospital.com/diseases-treatments/cancer-and-tumor-diseases/proton-therapy-and-carbon-ion-therapy (visited on 02/20/2025) (cited on p. 9).

[VDB73] R. Van Overstraeten, G. Declerck, and G. Broux. *Inadequacy of the classical theory of the MOS transistor operating in weak inversion*. In: IEEE Transactions on Electron Devices 20.12 (1973), pp. 1150–1153. ISSN: 1557-9646. DOI: 10.1109/T-ED.1973.17809 (cited on p. 16).

[Web+22] A. Weber et al. *High-Voltage CMOS Active Pixel Sensor Chip With Counting Electronics for Beam Monitoring*. In: IEEE Transactions on Nuclear Science 69.6 (2022), pp. 1288–1298. DOI: 10.1109/TNS.2022.3173807 (cited on pp. 25, 33, 35, 40, 44–46, 49).

[Web21] A. L. Weber. *Development of Integrated Circuits and Smart Sensors for Particle Detection in Physics Experiments and Particle Therapy*. PhD thesis. Heidelberg University, 2021. DOI: 10.11588/heidok.00030650 (cited on pp. 25, 40, 43–47, 49, 71).

[WH10] N. H. Weste and D. Harris. *CMOS VLSI Design: A Circuits and Systems Perspective*. 4th. Addison-Wesley, 2010. ISBN: 978-0321547743 (cited on p. 16).

[Wik11] Wikimedia Commons contributors. *MOSFET drain current vs. drain-to-source voltage*. 2011. URL: https://commons.wikimedia.org/wiki/File:IvsV_mosfet.svg (visited on 03/21/2025) (cited on p. 18).

[Wil46] R. R. Wilson. *Radiological Use of Fast Protons*. In: Radiology 47.5 (1946), pp. 487–491. ISSN: 0033-8419. DOI: 10.1148/47.5.487 (cited on p. 7).

[Wit+25] M. Witt et al. *Proton and Carbon Ion Beam Spot Size Measurement Using 5 Different Detector Types*. In: International Journal of Particle Therapy 15 (2025), p. 100638. ISSN: 2331-5180. DOI: 10.1016/j.ijpt.2024.100638 (cited on pp. 34, 57, 58).

[ZAG25] ZAG. *Zyklotron AG (ZAG)*. 2025. URL: http://www.zyklotron-ag.de/ (visited on 02/13/2025) (cited on pp. 72, 118).

[Zha21] C. Zhang. *Development of Depleted Monolithic Active Pixel Sensors for High Energy Physics Experiments*. PhD thesis. University of Liverpool, 2021. DOI: 10.17638/03149533 (cited on pp. 69, 84).

[ZTP26] H. Zhang, B. Topko, and I. Perić. *HitPix3 — A new HV-CMOS active pixel sensor for ion beam therapy*. In: Nuclear Instruments and Methods in Physics Research Section A: Accelerators, Spectrometers, Detectors and Associated Equipment 1082 (2026), p. 171049. ISSN: 0168-9002. DOI: https://doi.org/10.1016/j.nima.2025.171049 (cited on pp. 45, 82, 84, 85, 87–89, 101–104).

Acknowledgments — Danksagung

The present work would not have been possible without the support of many people, to whom I express my deepest gratitude.

First and foremost, I would like to thank my supervisor, Prof. Dr. Ulrich Husemann, for the opportunity to conduct this research at the Institute of Experimental Particle Physics (KIT). Your continuous guidance, support, and help, especially with the proofreading of my articles and this thesis, have been invaluable.

I am also grateful to my co-supervisor, Prof. Dr. Markus Klute, for reviewing my thesis and for the support throughout these past years.

I wish to extend my sincere thanks to Dr. Alexander Dierlamm, whose help, guidance, and support during my studies were crucial. Our discussions on measurement results and analysis were very important in deepening and improving this research. Furthermore, your suggested text corrections significantly enhanced the quality of this thesis.

My special thanks go to the following people for their help and support during this research:

- Dr. Felix Ehrler and Dr. Roland Koppenhöfer for their invaluable help during many beam tests, for verifying my designs, and for many fruitful discussions.
- Prof. Dr. Ivan Perić and Dr. Hui Zhang for the discussions regarding the HitPix3 sensor design and measurement results.
- Dr. Jakob Naumann and Dr. Stephan Brons from HIT for their professional support and assistance during the beam tests, and for providing the details on the beamline operation.
- Dr. Stefan Maier, Tobias Barvich and Marius Neufeld for their help with the mechanical design and assembly.
- Bernd Berger and Jennifer Derschang for their help with the PCB production and assembly.
- Dr. Hans Jürgen Simonis, Waldemar Rehm, Benjamin Leyrer and Dr. Horacio Mateos for their help with the sensor wire-bonding.
- Dr. Michele Caselle for his help with the sensor bump-bonding.
- Dr. Lea Stockmeier for her help in transporting all devices and equipments for several beam tests.
- Martin Pittermann for his great initial design of the backend software and firmware used for the readout of the HitPix1 and HitPix2 sensors.

Additionally, I would like to thank all former and current colleagues and students from the ETP Hardware group for the incredible working atmosphere, collaborative spirit, and constant encouragement!

Большое спасибо моим друзьям, которые, несмотря ни на что, поддерживают нашу очень важную связь, делят со мной все радости и печали. Наши редкие встречи – это те сокровенные моменты, которыми я дорожу и жду непременно в будущем.

Огромное спасибо моей жене Юлии: твои любовь и забота, твои ум и мудрость освещают наш путь, приносят радость и вдохновение и даже в самые темные часы помогают найти в себе силы не останавливаться и двигаться дальше. И я верю, что впереди нас ждёт только самое лучшее! Я люблю тебя!

И конечно же, огромное спасибо моей семье, в первую очередь моей маме Оксане, папе Леониду и младшему брату Данилу, за вашу безусловную любовь и веру в меня. Невозможно представить, просто невозможно представить, чтобы мои успехи и эта работа были воплощены в жизнь без вашей поддержки.

Der Landesgraduiertenförderung des Landes Baden-Württemberg und der Karlsruhe School of Elementary Particle and Astroparticle Physics: Science and Technology (KSETA) möchte ich für die Unterstützung während der Promotion danken.

This work was supported by HEiKA – Heidelberg Karlsruhe Strategic Partnership, Heidelberg University, Karlsruhe Institute of Technology (KIT); Germany. This work was also supported by Heidelberg Ion Beam Therapy Center (HIT). I acknowledge the financial support through the German Federal Ministry of Education and Research (BMBF) within the ARTEMIS project (Grant number: 13GW0436A).

The beam tests leading to the presented results have been performed at the experimental beamline at Heidelberg Ion Beam Therapy Center (Heidelberg, Germany) and at the in-air proton microbeam setup at Ruđer Bošković Institute (Zagreb, Croatia).

Declaration

I declare that the work in this dissertation was carried out in accordance with the requirements of the University's Regulations and that it has not been submitted for any other academic award. Except where indicated by specific reference in the text, the work is the candidate's own work. Work done in collaboration with, or with the assistance of, others is indicated as such.

Karlsruhe, September 2025

Bogdan Topko